UNIVERSITÀ DEGLI STUDI DI PADOVA

DEPARTMENT OF INFORMATION ENGINEERING

Ph.D. Course on Information Engineering

Curriculum: Information Science and Technologies

XXXI Series

STUDY OF THE RELIABILITY OF GaN-BASED OPTOELECTRONIC DEVICES: UV-LEDs AND InGaN-BASED LASER DIODES

Ph.D Student

Desiree Monti

Supervisor

Dr. Matteo Meneghini

Coordinator

Ch.mo Prof. Andrea Neviani

ACADEMIC YEAR 2017/2018

Contents

I Theoretical concepts: LEDs, LDs and advanced characterization techniques 1

Acknowledgments

The works presented in Chapter 7 and 8 were partially supported by the German Federal Ministry of Education and Research (BMBF) through the consortia project "Advanced UV for Life" under contracts 03ZZ0105A and 03ZZ0105B. Further support was given by the Federal Ministry for Economic Affairs and Energy (BMWi) through the project "UV-Berlin" under contract 03EFCBE067 as well as by the Deutsche Forschungsgemeinschaft within the Collaborative Research Center "Semiconductor Nano Photonics" (CRC 787). Further support was given by Interdepartmental Centre Giorgio Levi Cases (University of Padova) under research grant 2017LC2.

The work presented in Chapter 11 of this thesis is partially supported within the research project PRELUDIUM no. 2015/17/N/ST7/03934 funded by the Polish National Science Centre, by the grants Eurostar GaNBar E!9776 and 1/POLBER/1/2014 from the Polish National Centre for Research and Development, and partly supported by the University of Padova, through project BIRD167052/16. This work was also partially supported by Interdepartmental Centre Giorgio Levi Cases, Padova, under research grant 2017LC2, “Celle solari basate su InGaN per fotovoltaico ad alta efficienza e trasmissione wireless dell’energia”.

Abstract

This thesis reports the main results obtained from the Ph.D. research activity of the candidate. The activity was focused on the study of the physical mechanisms responsible for the degradation of ultraviolet light emitting diodes (UV-LEDs) and InGaN-based laser diodes (LDs). In particular, we tried to understand the role of defects in the device degradation by means of advanced techniques such Deep-Level Transient Spectroscopy (DLTS) and Photocurrent (PC) Spectroscopy.

In the first part of the thesis, an initial overview on the most important theoretical concepts, necessary in order to understand the obtained physical results, will be given. In particular, the fundamental properties of Gallium Nitride (GaN), including important alloys and compounds such Aluminum Nitride (AlN) and AlGaN, will be briefly discussed. The discussion will be also focused on the available substrates, the doping, the realization of the contacts and the most important point defects and dislocations in these materials. After that, the main electrical and optical properties of LEDs and LDs will be presented, along with a definition of their structure. Finally, a description of the most important characterization techniques used in this work will be given. In particular, this techniques are the Capacitance DLTS and the PC spectroscopy, that allow to study the presence and the physical origin of the defects in the material.

The second part of the thesis will focus on the analysis of the degradation process affecting UV LEDs. Initially, it will be given a description of the wide range of applications of these devices and the many difficulties that the realization of these LEDs present. This will be followed by the first work carried out on four groups of UV-A LEDs, each of them with a different emission wavelength. From this study, it was possible to demonstrate that UV-A LEDs submitted to constant current stress show a gradual degradation, whose entity shows a strong dependence on the emission wavelength. The degradation process was ascribed to the generation of point defects within the active region of the device, causing an increase in the non-radiative recombination rate. The stress current level was found to have a strong impact on the degradation, in particular the increase in the stress current level caused a faster degradation. Together with the current, it was observed that also the temperature has a certain impact on the device degradation.

This part of the thesis will continue with the description of the activity carried out on a group of (In)AlGaN-based UV-B LEDs, featuring an emission wavelength centered around 308 nm. The results of this work demonstrate that, as for the UV-A LEDs, UV-B LEDs show a gradual degradation when submitted to a constant current stress. The analysis of the degradation of the optical power highlighted a stronger decrease at low measuring current levels, meaning that degradation is mainly related to an increase in the Shockley-Read-Hall (SRH) recombination. From the electrical characterization, it was possible to observe the increase of the so-called Trap-Assisted Tunneling (TAT) mechanism, due to the increase of the defect density. This process requires the presence of mid-gap states, that was confirmed thanks to the DLTS analysis and PC spectroscopy measurements carried out. These two techniques allowed the identification of a band of defects centered around 2.5 eV below the conduction band, close to the mid-gap, that can explain both the increased SRH recombination and the increase in TAT components. Moreover, DLTS measurements allowed us to identify the signature of Mg-related acceptor traps.

The analysis on these UV-B LEDs continued with the activity carried out in order to investigate on the origin of the electroluminescence peaks and of the thermal droop. By means of spectral measurements at different temperatures and current levels, information on the physical origin of the various parasitic band were extracted, and a model based on the SRH theory and the ABC rate equation, able to reproduce the experimental data, was developed. Three parasitic bands were observed and ascribed to the following processes: band-to-band recombination in the quantum wells (main peak), radiative transitions through deep levels in the quantum well barriers, and a second parasitic peak related to a radiative parasitic transition inside the p-AlGaN superlattice.

The analysis on the degradation of AlGaN-based UV-B LEDs was then concluded with the investigation on the effect of prolonged current overstress on the electrical and optical performance. The existence of two degradation mechanisms was demonstrated. These two mechanisms have a significant impact on the relative amplitude of the main peak, related to the QW emission, and of a parasitic peak at $\sim$ 340 nm, related to the electron overflow towards the last quantum barrier. The first degradation mechanism acts in the first 50 hours of stress and is caused by an increased carrier escape from the quantum wells, resulting in a decrease in the main peak amplitude, and an increase in the amplitude of the parasitic peak at 340 nm. The second degradation mechanism acts for longer stress times and is dominated by a diffusion process, that causes an increase in the defect density, and consequently in the non-radiative recombination rate. The impact on both the main and parasitic peak is highlighted by the significant decrease of them for long stress times. Finally, photocurrent spectroscopy demonstrated that defects located next to the mid-gap are responsible for degradation, by acting as non-radiative recombination centers.

The second part of thesis will be focused on the work carried out on a group of InGaN-based laser diodes (LDs) with a nominal emission wavelength around 418 nm and another group with emission wavelength between 422 nm and 426 nm.

The analysis carried out on the first group of samples was aimed at studing the relation between the degradation and the presence of defects in these devices when submitted to constant current stress. We were able to show that constant current stress induces an increase in the threshold current of the devices, moreover, from the capacitance-temperature measurements, it was possible to identify two main defects, whose physical origin, studied by means of DLTS, could be related to acceptor-like defects associated with dislocation.

The study was concluded with the results obtained from the analysis carried out on three group of InGaN-based LDs with different dislocation density. In order to have a better comprehension of the impact of dislocation on the degradation and generation of defects DLTS analysis was carried out before and after the stress. This allowed us to identify the presence of a hole trap in all the samples, whose concentration increases with the dislocation density, together with an electron trap generated after the stress, probably related to the dislocation density. Finally, devices submitted to constant current stress showed a significant decrease in their optical power, that we observed it was not related exclusively to the dislocation density.

The above-mentioned experimental results represent the most relevant and original outcomes of the three-years research activity of the Ph.D student. Useful information can be also found in the papers co-authored by the candidate and listed in the next section.

Sommario

In questa tesi si riportano i risultati principali ottenuti dall'attività di ricerca di dottorato del candidato. L'attività si è concentrata nello studio dei meccanismi fisici responsabili per il degrado di diodi emettitori di luce con emissione nell'ultravioletto (LED UV) e diodi laser basati su InGaN, in particolare, si è cercato di comprendere il ruolo dei difetti nel degrado dei dispositivi per mezzo di tecniche avanzate come Capacitance Deep-Level Transient Spectroscopy (C-DLTS) e la spettroscopia di fotocorrente.

Nella prima parte della tesi, verrà data un panoramica dei concetti teorici più importanti, necessari per comprendere i risultati fisici ottenuti. In particolare, verranno discusse le proprietà del Nitruro di Gallio (GaN), incluse altre leghe e composti come il Nitruro di Alluminio (AlN) e l'AlGaN. La discussione si focalizzerà anche sui substrati disponibili, il drogaggio, la realizzazione dei contatti e i principali difetti di punto e dislocazioni presenti nel materiale. Dopo questa parte, verranno presentate le principali proprietà elettriche e ottiche dei LED e dei diodi laser, insieme alla definizione delle loro strutture. Verrà quindi data una descrizione delle tecniche avanzate più importanti, servite per studiare la presenza e l'origine fisica dei difetti nel materiale, utilizzate in questo lavoro, ovvero C-DLTS e la spettroscopia di fotocorrente.

La seconda parte della tesi si focalizzarà sullo studio dei processi di degrado che interessano i LED UV. Inizialmente verranno descritte le principali applicazioni di questi dispositivi insieme alle diverse problematiche che sono ancora presenti in questi LED. Verrà quindi esposto il lavoro effettuato su quattro gruppi di LED con emissione nel range spettrale dell'UV-A, ciascuno dei quali con una lunghezza d'onda d'emissione differente. Da questo studio è stato possibile dimostrare che i LED UV-A sottomessi ad uno stress a corrente costante mostrano un degrado graduale e questo degrado ha una forte dipendenza dalla lunghezza d'onda d'emissione. Il processo di degrado può essere attribuito alla generazione di difetti di punto all'interno della regione attiva del dispositivo, che causano un aumento della ricombinazione non radiativa. Inoltre, la corrente di stress ha un forte impatto sul degrado, poiché all'aumentare del livello di corrente, il degrado risulta essere più veloce. Insieme alla corrente, si è osservato che

anche la temperatura risulta avere un certo impatto sul degrado del dispositivo.

Questa parte di tesi continuerà con la descrizione dell'attività effettuata su un gruppo di LED in (In)AlGaN con emissione nel range spettrale dell'UV-B, in particolare a 308 nm. I risultati di questo lavoro dimostrano che, così come per i LED UV-A, i LED UV-B mostrano un degrado graduale se sottomessi ad uno stress a corrente costante. L'analisi del degrado della potenza ottica ha sottolineato un calo maggiore di questa alle basse correnti: questo sta a significare che il degrado è legato ad un aumento nella ricombinazione Shockley-Read-Hall (SRH). Dalle caratterizzazioni elettriche, si è osservata la presenza del cosiddetto meccanismo Trap-Assisted Tunneling (TAT), dovuto all'aumento della densità di difetti. Questo processo richiede la presenza di stati a metà del band-gap proibito, presenza confermata grazie all'analisi mediante DLTS e alle misure di fotocorrente. Queste due tecniche hanno permesso di identificare una banda di difetti centrata attorno a 2.5 eV sotto la banda di conduzione, quindi vicino a meta del band-gap, che possono spiegare sia l'aumento della ricombinazione SRH che l'aumento delle componenti di TAT. Inoltre, le misure di DLTS hanno permesso di identificare la presenza di trappole di tipo accettore dovute al magnesio (Mg).

L'analisi su questi campioni continua con l'attività effettuata con lo scopo di studiare l'origine dei picchi di elettroluminescenza e il thermal droop, ovvero il calo della potenza ottica all'aumentare della temperatura. Per mezzo delle misure spettrali effettuate a diverse temperature e correnti, si sono estratte informazioni relative all'origine fisica delle diverse bande parassite, ed è stato sviluppato un modello in grado di riprodurre i dati sperimentali osservati, basato sulla teoria di SRH e l'equazione del tasso ABC. Si sono osservate tre bande parassite, le quali si sono attribuite ai seguenti processi: ricombinazione banda-a-banda nelle buche quantiche (picco principale), transizioni radiative attraverso livelli profondi nelle barriere delle buche quantiche, e un secondo picco parassita legato a transizioni parassite radiative all'interno dello strato superlattice in p-AlGaN.

L'analisi del degrado di questi LED UV-B si è conclusa con l'indagine sull'effetto che lo stress prolungato, a correnti più elevate di quella nominale, ha sulle prestazioni elettriche e ottiche. Si è così dimostrata l'esistenza di due meccanismi di degrado. Questi due meccanismi hanno un impatto significativo sull'ampiezza relativa del picco principale, associato all'emissione dalle buche quantiche, e del picco parassita intorno ai 340 nm, associato all'overflow dei portatori verso l'ultima barriera quantica. Il primo meccanismo di degrado agisce nelle prime 50 ore di stress e viene causato da un aumento della fuoriuscita dei portatori dalle buche quantiche, risultando in un calo dell'ampiezza del picco principale e un aumento dell'ampiezza del picco parassita a

340 nm. Il secondo meccanismo di degrado agisce per tempi di stress maggiori ed è dominato da un processo di diffusione, il quale causa un aumento della densità dei difetti e di conseguenza del tasso di ricombinazione non radiativa. L'impatto su entrambi i picchi è sottolineato da un calo significativo dell'ampiezza di questi per tempi di stress più lunghi. Infine, la spettroscopia di fotocorrente ha dimostrato che difetti localizzati a metà band-gap risultano essere responsabili per il degrado, agendo come centri di ricombinazione non radiativa.

La seconda parte della tesi si concentrerà sul lavoro eseguito su un gruppo di diodi laser basati su InGaN con una lunghezza d'onda nominale attorno ai 418 nm e un altro gruppo con lunghezze d'onda comprese tra 422 nm e 426 nm.

L'analisi effettuata sul primo gruppo di campioni ha avuto lo scopo di studiare la relazione tra il degrado e la presenza di difetti in questi dispositivi sottomessi ad uno stress a corrente costante. Si è mostrato che lo stress a corrente costante induce un aumento nella corrente di soglia dei dispositivi, mentre, dalle misure di capacità in funzione della temperatura, è stato possibile identificare due difetti principali, la cui origine fisica, studiata mediante DLTS, potrebbe essere legata a difetti di tipo accettore associati a dislocazioni.

Lo studio si è concluso con i risultati ottenuti dalle analisi effettuate sull'ultimo gruppo di campioni, costituito da tre gruppi di diodi laser in InGaN, ciascuno dei quali con diverse densità di dislocazioni. Con lo scopo di avere una maggiore comprensione dell'impatto che hanno le dislocazioni sul degrado e la generazione dei difetti, un'analisi di DLTS è stata effettuata prima e dopo lo stress. Questa ha permesso di identificare una trappola per lacune tutti i campioni, la cui concentrazione aumenta con la densità di dislocazioni, insieme ad una trappola per elettroni generata dopo lo stress, probabilmente legata alla densità di dislocazioni. Infine, i dispositivi sottomessi ad uno stress a corrente costante hanno mostrato un significativo calo della potenza ottica, che si è osservato non essere esclusivamente legato alla densità di dislocazioni.

I risultati sperimentali sopra esposti rappresentano i risultati originali più importanti conseguiti dallo studente di dottorato durante la propria attività di ricerca. Informazioni utili possono essere trovate negli articoli in cui ha collaborato il candidato ed elencati nella successiva sezione.

Publications

International journal paper

- C. De Santi, M. Dal Lago, M. Buffolo, D. Monti, M. Meneghini, G. Meneghesso, and E. Zanoni, "Failure causes and mechanisms of retrofit LED lamps", Microelectronics Reliability, vol. 55, pp. 1765-1769, 2015. DOI: 10.1016/j.microrel.2015.06.080
- D. Monti, M. Meneghini, C. De Santi, G. Meneghesso, and E. Zanoni, "Degradation of UV-A LEDs: Physical Origin and Dependence on Stress Conditions", IEEE Transactions on Device and Materials Reliability, vol. 16, no. 2, June 2016. DOI: 10.1109/TDMR.2016.2558473
- D. Monti, M. Meneghini, C. De Santi, G. Meneghesso, E. Zanoni, J. Glaab, J. Rass, S. Einfeldt, F. Mehnke, J. Enslin, T. Wernicke, and M. Kneissl, "Defect-Related Degradation of AlGaN-Based UV-B LEDs", IEEE Transaction on Electron Devices, vol. 64, no. 1, January 2017. DOI: 10.1109/TED.2016.2631720
- C. De Santi, M. Meneghini, D. Monti, J. Glaab, M. Guttmann, J. Rass; S. Einfeldt, F. Mehnke, J. Enslin, T. Wernicke, M. Kneissl, G. Meneghesso, and E. Zanoni, "Recombination mechanisms and thermal droop in AlGaN-based UV-B LEDs" Photonics Research, vol. 5, no. 2, April 2017. DOI: 10.1364/PRJ.5.000A44
- D. Monti, M. Meneghini, C. De Santi, G. Meneghesso, E. Zanoni, A. Bojarska, and P. Perlin, "Long-term degradation of InGaN-based laser diodes: Role of defects", Microelectronics Reliability, Vol. 76–77, September 2017, pp. 584-587, DOI: 10.1016/j.microrel.2017.06.043
- D. Monti, M. Meneghini, C. De Santi, A. Bojarska, P. Perlin, G. Meneghesso, and E. Zanoni, "Impact of dislocations on DLTS spectra and degradation of InGaN-based laser diodes", Microelectronics Reliability, Vol. 88–90, September 2018, pp. 864-867, DOI: 10.1016/j.microrel.2018.06.055

Papers in conference proceedings

- D. Monti, M. Meneghini, C. De Santi, G. Meneghesso, and E. Zanoni, "Analysis of degradation processes of UV-A light emitting diodes stressed at constant current", WOCSDICE 2016, Conference Book
- E. Zanoni, M. Meneghini, G. Meneghesso, C. De Santi, M. La Grassa, M. Buffolo, N. Trivellin, and D. Monti, "Aging behavior, reliability and failure physics of GaN-based optoelectronic components", Proceeding of SPIE, vol 9768, 2016. DOI: 10.1117/12.2225128
- D. Monti, M. Meneghini, C. De Santi, G. Meneghesso, E. Zanoni, J. Glaab, J. Rass, S. Einfeldt, F. Mehnke, T. Wernicke, and M. Kneissl, "Defect generation in deep-UV AlGaN-based LEDs investigated by electrical and spectroscopic characterization", Proceeding of SPIE, vol. 10124, 2017. DOI: 10.1117/12.2253843
- D. Monti, M. Meneghini, C. De Santi, S. Da Ruos, G. Meneghesso, E. Zanoni, J. Glaab, J. Rass, S. Einfeldt, F. Mehnke, T. Wernicke, and M. Kneissl, "Defect-generation and diffusion in deep-UV (In)AlGaN-based LEDs submitted to constant current stress", Proceeding of SPIE, vol. 10554, 2018, DOI: 10.1117/12.2292202

List of other publications (books, book chapter, patents)

- C. De Santi, D. Monti, P. Dalapati, m. Meneghini, G. Meneghesso, E. Zanoni, "Reliability of ultraviolet light emitting diodes", Springer, editor J. Li and G.Q. Zhang, to be published in Light-Emitting Diodes – Materials, Processes, Devices and Applications

Introduction

In these last years, Gallium Nitride (GaN) has proved to be an excellent material for the fabrication of optoelectronic devices that emit in the spectral region of green, blue and ultraviolet (UV), like light emitting diodes (LEDs) and laser diodes (LDs). Until the early 90's, the III-V group semiconductor-based LEDs with the shortest wavelength available on the market were weakly greened devices, primarily suited for backlighting of phones and lights. Only thanks to Shuji Nakamura [1] and other LEDs producers, it has been possible to obtain LEDs, and subsequently solid state lasers, based on Indium (In), Gallium (Ga) and Nitrogen (N), with emission wavelengths ranging from blue to the green. Using Aluminum instead of Indium in the Nitride alloys allowed the realization of solid-state emitters with ultraviolet emission, with wavelengths between 200 and 400 nm. The commercialization of these devices has greatly facilitated their development and performance improvement, with a total turnover of 45 million dollars only in 2012, out of a total of 495.4 million of the UV lamps market [2]. The first deep-ultraviolet LEDs (DUV-LEDs) were realized and analyzed at the end of the 90's [3] and thanks to the progress achieved in growth techniques and the research efforts towards innovative device structures, their performance is expected to make them attractive for use in different application fields, such as biomedical devices, environmental protection and lighting systems [4].

Despite the many progresses made for III-V based UV-LEDs, these devices exhibit external quantum efficiencies (EQE) (Figure 1) still low compared to their visible counterparts [5, 6]. Several factors contribute to this, such as the limited light extraction efficiency ($< 5\%$), due to the high mismatch between the refractive index of the semiconductor (2.5) and that of air (1). Recently, Takano et al. [7] were able to achieve EQE of 12.3% for a 275 nm flip-chip DUV LED with p-AlGaN contact layer and highly reflective Rh p-type electrode. Since the realization of an ohmic contact to p-AlGaN with Al is not possible, due to the low work function of Al, Maeda et al. [8] introduced a thin Ni layer in order to obtain electrical contact to the p-AlGaN: they found out that the reflectivity of the UV region becomes higher as the thickness of the Ni layer becomes smaller, and as a result they were able to realize a 279 nm DUV LED with optimized electrode and with an enhancement in EQE by a factor of 1.8. Other technological problems related to materials are the high number of dislocations and reticular defects, the low injection efficiency of the carriers in the active region, the high probability of carrier escape from the quantum wells and the self-heating of the device [9].

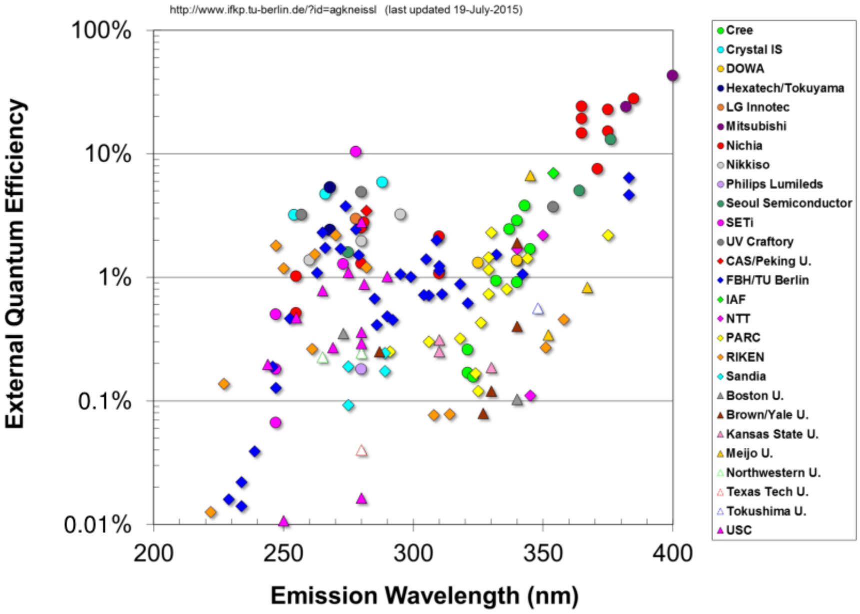

Figure 1: State of the art of external quantum efficiency for AlGaN, InAlGaN and InGaN quantum well UV-LEDs [10].

Together with UV LEDs, InGaN-based laser diodes (LDs) are becoming increasingly important in modern optoelectronics. Originally inteded to use in optical data-storage systems (BluRay), InGaN LDs are currently employed in optical projectors, white-light laser sources (e.g., car headlamps), chemical and biochemical sensing, and material processing [11, 12]. Despite the achieved progress, there are still fundamental issues that limit the accessible range of emission wavelengths and the efficiency of these devices. Since they operate at high current density, from 3 to 10 kA/cm^2 [13], these devices require high material robustness. Typically, an InGaN LD shows a degradation process that consists in the gradual increase of the threshold current, with an almost constant slope efficiency. This increase usually has a square root dependence on time [14, 15, 16, 17], suggesting the involvement of a diffusion process. Unfortunately, it is not clear which element is diffusing and which part of the laser structure is affected by degradation. Another important degradation process is the increase in the non-radiative recombination rate within the active region, due to the generation and/or propagation of defects [17, 18]. Understanding the physical origin of these defects is not a simple task, but is a critical step for improving the growth techniques for these devices.

The aim of this thesis is to study the physical mechanisms responsible for the degradation of UV-LED and InGaN-based laser diodes. By means of advanced techniques, such DLTS and PC spectroscopy, the role of defects in the device degradation was analyzed. The thesis is divided in two main parts, one regarding the work carried out on different type of UV LEDs, and a second part regarding the work on a group of InGaN-based laser diodes with emission wavelength centered around 418 nm and $422 - 426$ nm. This work is structured as follows:

- *Chapter 1: III-N semiconductors.* This first chapter will review the fundamental properties of GaN and other important alloys such AlN and AlGaN. An initial discussion on these alloys, their crystal structure and polarization fields in GaN will be given, followed by the discussion on the avalable substrates, the doping, the realization of the contacts and the most important point defects and dislocations in GaN.

- *Chapter 2: Basic principles of LEDs and LDs.* The chapter will describe the main electrical and optical properties of LEDs and LDs, as well as their typical structure.

- *Chapter 3: Advanced experimental techniques.* This chapter reports on the most important characterization techniques employed in this work in order to study the presence and the physical origin of the defects in the device under investigation. Particular attention will be focused on the Capacitance Deep-Level Transient Spectroscopy (C-DLTS) and the Photocurrent (PC) spectroscopy.

- *Chapter 4: Introduction to UV LEDs.* The chapter gives a brief introduction to these devices, their applications and their problematics, focusing in particular on the poor light extraction and typical degradation processes.

- *Chapter 5: Degradation of UV-A LEDs: physical origin and dependence on stress conditions.* This chapter is dedicated to the study of four groups of UV-A LEDs, featuring different emission wavelength. The work is focused on the study of the degradation kinetics and the physical mechanisms responsible for their degradation by means of optical/electrical/thermal measurements.

- *Chapter 6: Defect-related degradation of AlGaN-based UV-B LEDs.* In this section, the analysis carried out on a group of UV-B LEDs with emission wavelength equal to 308 nm will be described. The degradation mechanisms, also by means of DLTS and PC spectroscopy, were studied.

- *Chapter 7: Recombination mechanisms and thermal droop in AlGaN-based UV-B LEDs.* In this part, we focus on the analysis of the origin of the electroluminescence (EL) peaks and of the thermal droop in the same samples studied in the previous chapter.

- *Chpater 8: High-current stress of UV-B (In)AlGaN-based LEDs: defect-generation and diffusion process.* In this last chapter regarding the work carried out on the UV-B LEDs group, a stress at a higher current density was performed, in order to accelerate the degradation of the device. An analysis of the involved defects was performed by means of PC spectroscopy.

- *Chapter 9: Introduction to InGaN-based Laser Diodes.* The chapter gives a brief introduction on InGaN-based laser diodes, their applications and their problematics.

- *Chapter 10: Long-term degradation of InGaN-based laser diodes: role of defects.* In this section, the presence of defects and their impact on the degradation of a group of InGaN-based laser diodes, with a nominal emission wavelength of 418 nm, was studied by means of electrical/optical characterization and DLTS analysis.

- *Chapter 11: Impact of dislocations on DLTS spectra and degradation of InGaN-based laser diodes.* In this last chapter, three groups of InGaN-based laser diodes with different dislocation density were studied. This work was aimed at understanding the impact of dislocation density on the degradation and on the generation of defects within the active region of the devices.

Part I

Theoretical concepts: LEDs, LDs and advanced characterization techniques

Chapter 1

III-N semiconductors

In these last years, III-N semiconductors, i.e. semiconductor based on nitride of III-V group, had an important development (Figure 1.1). They are excellent materials for the realization of optoelectronics devices, since they allow to cover a broad range of energies, and so of wavelengths, from the ultraviolet to the infrared, that is not possible with other materials. Moreover electrically, they can withstand high breakdown voltages.

In this chapter, the structural, mechanical, thermal, chemical, electrical and optical properties of III-N semiconductors such GaN, AlN and the ternary material such AlGaN, as well as the substrates commonly used for nitride epitaxy, are discussed.

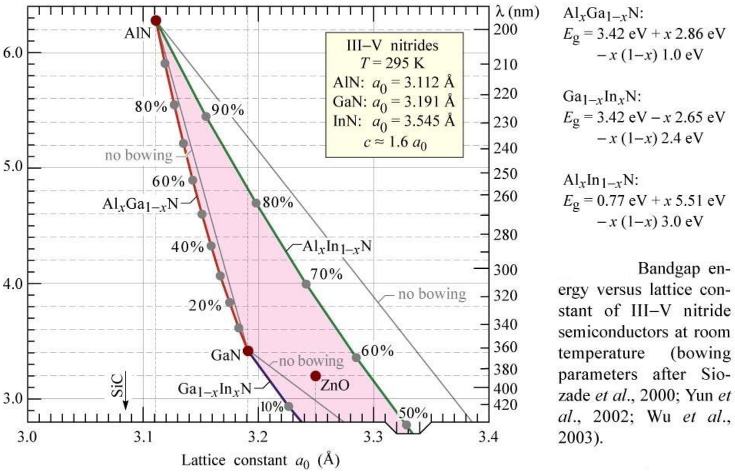

Figure 1.1: Band gap energy at room temperature as function of the lattice constant of III-N semiconductors [19].

1.1 Crystal structure of nitrides

The III-N semiconductors can be found in three common crystal structures:

- wurtzite (Wz);
- zinc blend (Zb);
- rock salt.

The latter structure does not have any importance in the realization of electronic devices, instead, for material such GaN or AlN, the thermodynamically stable structure at room temperature is the wurtzite. The zinc blende structure for GaN has been stabilized, but not for AlN. This structure has a cubic unit cell, containing four group III atoms and four nitrogen atoms. The position of the atoms within the unit cell is identical to the diamond crystal structure. Each atom in the structure may be viewed as positioned at the center of a tetrahedron, with its four nearest neighbors defining the four corners of the tetrahedron.

The wurtzite structure has a hexagonal unit cell and contains six atoms of each type. In general, the elementary cell of a crystalline lattice is characterized by three constants a, b and c, that represent the interatomic distances between the atoms. The wurtzite structure presents two equal lattice constants, a=b, thus the two considered lattice constants are c, in the perpendicular direction, and a, in the basal plane. The Wz structure consists of two interpenetrating hexagonal close-packed sublattices, each with one type of atom. Figure 1.2 reports the two structures, the wurtzite and zinc blende. The two structures are different, but present some common characteristics. In both structures, each III group atom is coordinated by four nitrogen atoms and each nitrogen atom is coordinated by four III group atoms. The main difference between the two structures lies in the stacking sequence of closest packed diatomic planes.

1.2 Gallium Nitride (GaN)

GaN is the basic material, which is typically used for devices requiring fast carrier transport with a high breakdown voltage. It can be grown as semi-insulating material with growth parameters similar to those of the semiconductor layers. Since the early studies, GaN has shown great stability and significant hardness, suitable characteristics for protective coatings. Thanks to the wide energy bandgap, it is an excellent candidate for device operation at high temperatures and caustic environments. Unfortunately, the presence of native defects and impurities and the lack of commercially available

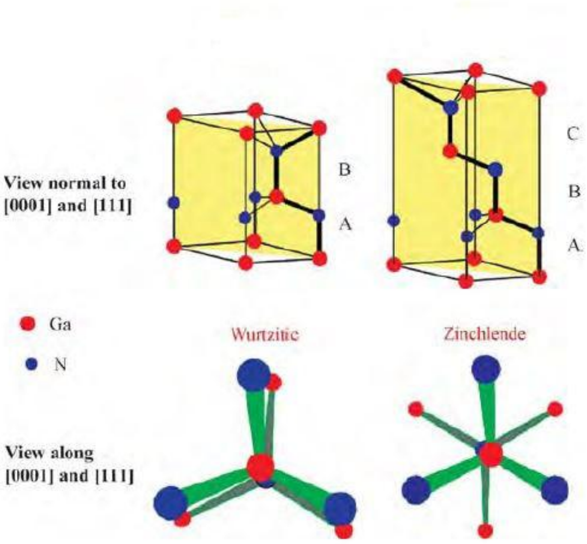

Figure 1.2: Wurtzite (a) and zinc blende (b) structures [20].

native substrates yield to many growth problematics. Moreover, it is quite difficult to obtain the p-type doping. Despite this, the interest in nitrides led to a substantial improvement in technological processes, which allowed to obtain p-n junctions for LED in ultraviolet and in other spectral ranges. The next sections will report the main physical properties of GaN.

1.2.1 Chemical and mechanical properties

GaN is a particularly stable compound, which presents a significant hardness and a good chemical stability at high temperatures. Its semiconductor characteristics have attracted the most attention. The chemical stability of GaN presents a technological challenge. Conventional wet etching techniques used in semiconductor processing have not been as successful for GaN device fabrication. In its wurtzite structure, GaN presents a molecular weight of 83.7267 $gmol^{-1}$. The lattice constant shows a dependence on growth conditions, on impurity concentration and film stoichiometry. The freestanding GaN with electron concentration of 10^{16} cm^{-3} grown on sapphire (0001) has lattice constants of $a = 3.2056 \pm 0.0002$ Å and $c = 5.1949 \pm 0.0002$ Å while for GaN platelets prepared with an electron concentration of $5 \cdot 10^{19}$ cm^{-3} under high pressure and high temperature, they are $a = 3.1890 \pm 0.0003$ Å and $c = 5.1864 \pm 0.0001$ Å at room temperature. The dielectric constant of GaN is slightly lower than in Silicon and GaAs, e.g. 9.5. Table 1.1 reports the principal properties for GaN.

Table 1.1: Principal properties of III-N semiconductors.

Properties	**Units**	**GaN**	**AlN**
Crystal structure		Wz	Wz
Bandgap type		direct	direct
Density	$\mathrm{kg\,cm^{-3}}$	6100	3230
Bandgap E_g	eV	3.43	6.2
Lattice constant a	Å	3.189	3.112
Lattice constant c	Å	5.185	3.982
Electrons mobility at 300 K	$\mathrm{cm^2V^{-1}s^{-1}}$	1400	683
Holes mobility at 300 K	$\mathrm{cm^2V^{-1}s^{-1}}$	< 20	14
Thermal expansion $\Delta a/a$	$10^{-6}\ \mathrm{K^{-1}}$	5.59	4.2
Thermal expansion $\Delta c/c$	$10^{-6}\ \mathrm{K^{-1}}$	3.17	5.3
Thermal conductivity at 300 K	$\mathrm{W\,K^{-1}cm^{-1}}$	1.3	2.85
Specific heat	$\mathrm{J\,K^{-1}kg^{-1}}$	491	748
Melting point	K	-	3273
Dielectric constant		9.5	8.5

1.2.2 Thermal properties

Lattice parameters of semiconductors depend on the temperature and this dependence is expressed by the coefficient of thermal expansion (CTE), defined as $\Delta a/a$ and $\Delta c/c$ for in-plane and out-of-plane configurations, respectively. The coefficient is important for the growth of the material and depends on the stoichiometry, extended defects, and free-carrier concentration. Measurements made over the temperature range of 300–900 K indicate the mean coefficient of thermal expansion of GaN in the c-plane to be $\Delta a/a = 5.59 \cdot 10^{-6} K^{-1}$. Similarly, measurements over the temperature ranges of $300 - 700$ and $700 - 900$ K, respectively, indicate the mean coefficient of thermal expansion in the c-direction to be $\Delta c/c = 3.17 \cdot 10^{-6}$ and $7.75 \cdot 10^{-6}\ \mathrm{K^{-1}}$. Figure 1.3 reports the coefficient of thermal expansion as function of the temperature. Having a knowledge of this parameter and its dependence on temperature is very important, since semiconductors such as GaN are grown at high temperatures and also subject to increase in the junction temperature during device operation; thus, structures like these are subjected to thermal vibrations. The bond strength in GaN is higher with respect to the conventional semiconductor like GaAs: it has a bond strength of 9.12 eV/molecule.

As already mentioned before, GaN is a perfect semiconductor in order to realize optoelectronic devices, where the thermal dissipation is a key problem. For this reason, one important property of the material is the thermal conductivity (κ_L). The transport of heat is mainly determined by the scattering between phonons and the scattering between phonons and extended defects such as vacancies and impurities. In almost all

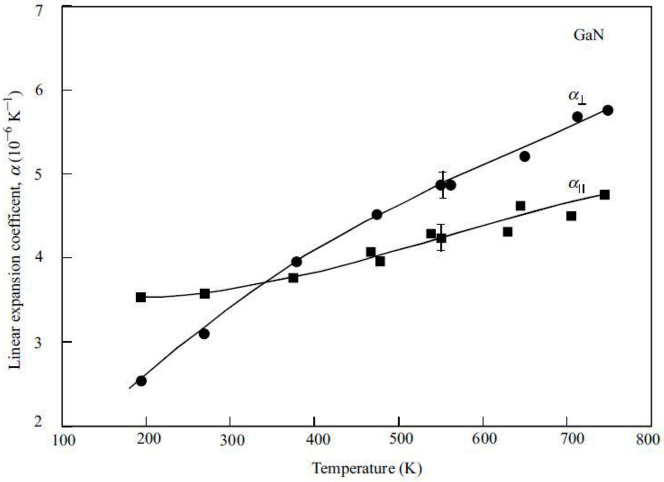

Figure 1.3: Wz GaN coefficient of thermal expansion as function of temperature for basal plane ($a_{||}$) and out of the basa plane ($a_{\perp}$) [20].

materials, the thermal conductivity first increases with temperature, until it reaches a maximum value at a given characteristic temperature, then begins to drop, as shown in Figure 1.4.

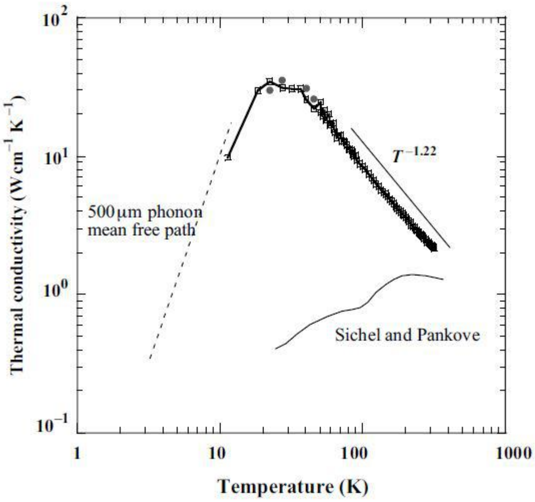

Figure 1.4: Thermal conductivity as function of temperature for a GaN layer of 200 μm [21].

1.2.3 Band structure

The GaN band structure has already been extensively studied, but it is not yet fully understood, especially with regard to the higher energy bands. The Wz GaN is a direct gap material, with an energy gap of 3.4 eV. Figure 1.5 illustrates the band diagram for GaN. The fact that GaN is a direct gap material allows the conservation of the momentum during the transition of an electron from the conduction band to the valence band: in this way, the probability of the transition is high, making GaN an excellent material for the realization of optoelectronic devices.

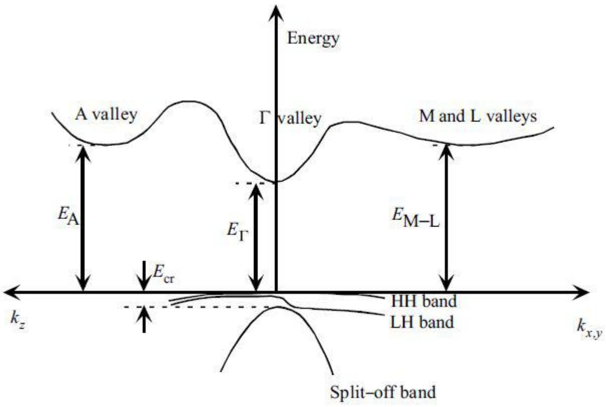

Figure 1.5: Schematic representation of band diagran for Wz GaN [20].

1.3 Aluminum Nitride (AlN)

AlN exhibits many useful mechanical and electronic properties, such as hardness, high thermal conductivity, resistance to high temperature and caustic chemicals, that combined with, in non-crystalline form, a reasonable thermal match to Si and GaAs, make AlN an attractive material for electronic packaging applications. Due to its wide bandgap and its high donor activation energy, AlN is used as an insulating material in semiconductor device applications. However, the majority of interest in this semiconductor in the context of electronic and optoelectronic device area is for its property to form alloys with GaN, producing AlGaN and allowing the fabrication of AlGaN/GaN and AlGaN/InGaN-based electronic and optical devices. Because of its high reactivity with oxygen, AlN is not a particularly easy material to investigate. Oxygen contamination during the growth can lead to modifications in the energy bandgap and, depending on the extent of contamination, in the lattice constant. Only recently, it has been possible, by creating contamination-free deposition environments, to grown high quality AlN, allowing a better study of its physical properties.

1.3.1 Chemical and mechanical properties

When crystallized in the hexagonal wurtzite structure, the AlN crystal has a molar mass of 40.9882 gmol^{-1}. The lattice parameters are in a range between 3.110 and 3.113 Å for the parameter a, and between 4.978 and 4.982 Å for the parameter c. Table 1.1 reports some of the properties of this material.

1.3.2 Thermal properties

Its high intrinsic thermal conductivity is the best compared to other semiconductors, apart from silicon carbide (SiC) and diamond. This makes AlN an attractive material for substrates. In its most commonly available form, AlN is an extremely hard ceramic material, with a melting point higher than 2000°C. Regarding the coefficients of thermal expansion, the values are $\Delta a/a = 4.2 \cdot 10^{-6}$ K^{-1} and $\Delta c/c = 5.3 \cdot 10^{-6}$ K^{-1}. The dependence on temperature of the coefficient of thermal expansion is shown in Figure 1.6.

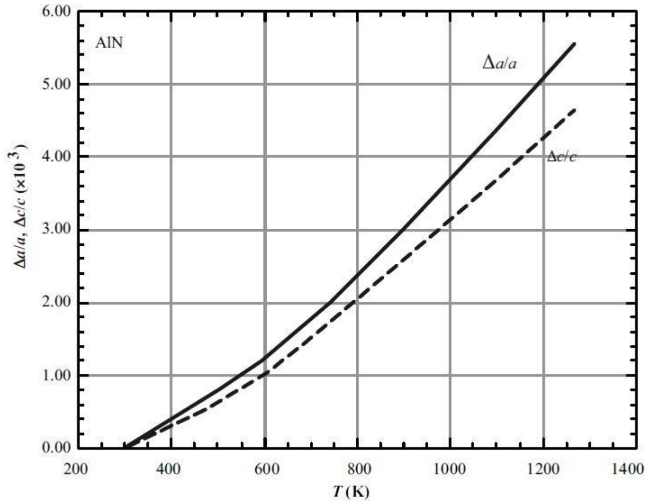

Figure 1.6: Coefficient of thermal expansion as function of the temperature [20].

Like GaN, AlN exhibits resistance to many chemical etches. For the thermal conductivity of AlN at 300 K, values such 2.5 and 2.85 W $\cdot$ cm^{-1}K^{-1} were measured. From simulations in which a material without oxygen was considered, the predicted values are around 3.2 W $\cdot$ cm^{-1}K^{-1}, but this calculation are made on measurements carried out on AlN containing oxygen. Figure 1.7 shows the dependence of the thermal conductivity on the temperature for one AlN sample with different oxygen concentration: we can notice that with increasing oxygen concentration, the thermal conductivity decreases.

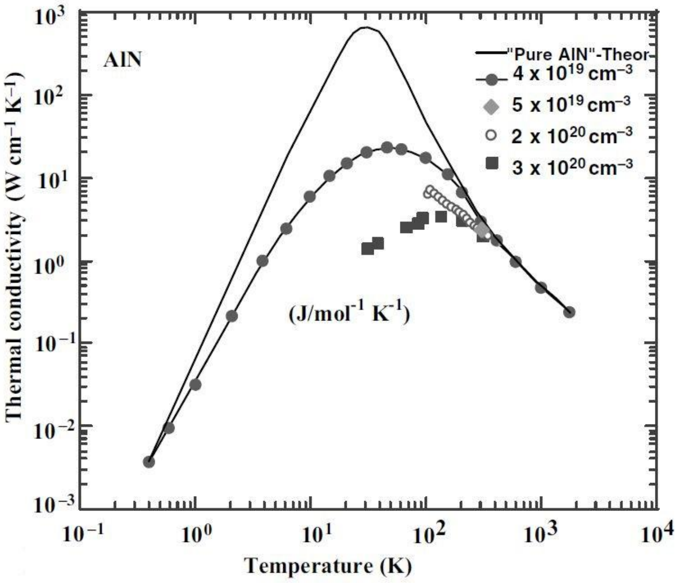

Figure 1.7: Thermal conductivity of single-crystal AlN as function of temperature. The solid line is the theoretical one, whereas the others represent measurements of AlN with different concentration of oxygen [20].

1.3.3 Band structure

Wurtzite AlN is a direct bandgap material and due to its high energy gap (6.2 eV) at room temperature, it allows to modify the energy gap of the ternary compound $Al_xGa_{1-x}N$ in a range between the one of the GaN and the one of the AlN itself. In Figure 1.8 is reported the band diagram for the Wz AlN.

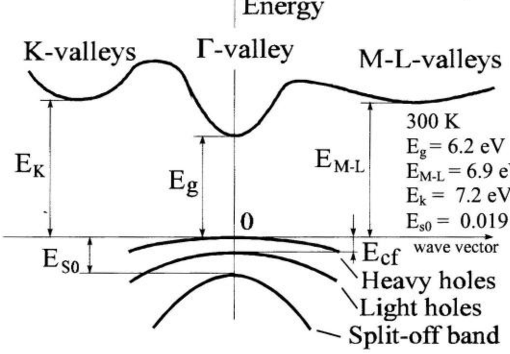

Figure 1.8: Schematic representation of the band diagram for Wz AlN [20].

1.4 The AlGaN alloy

AlN and GaN allow to realize the ternary alloy called AlGaN with a wide range of energy gaps and a small variation in the lattice constant. AlGaN is one of the most important ternary alloy, since its lattice mismatch with GaN can be controlled for almost every material compositions. This alloy allows to realize barrier layers in GaN-based devices, determining properties like carrier and light confinement, but with the introduction of short wavelength sources, the AlGaN alloy has become also a material for the realization of the active region. It is important to distinguish the Wz and Zb AlGaN, since the latter exhibits a transition from a direct bandgap to a indirect bandgap semiconductor. Considering the direct bandgap material, the energy gap at room temperature ($T = 300$ K) is in the range between 3.42 eV, when the Al concentration is zero ($x = 0$), and 6.2 eV, when we have a concentration $x = 1$. The lattice constant, the direct bandgap and the electrical properties of this alloy depend on the composition of the alloy itself. Predictions indicate that Vegard's law applies

$$a = 3.1986 - 0.0891x \text{ Å} \qquad \text{and} \qquad c = 5.2262 - 0.2323x \text{ Å} \tag{1.1}$$

where x represents the Al concentration in the alloy.

Regarding the dependence of the energy gap on the composition, the studies carried out continue to report conflicting results. It is possible to calculate the dependence by means of the following empirical expression

$$E_g(x) = xE_g(AlN) + (1-x)E_g(GaN) - bx(1-x) \tag{1.2}$$

where $E_g(GaN) = 3.4$ eV, $E_g(AlN) = 6.2$ eV, x is the AlN mole fraction and b is the bowing parameter. There are some discrepancy in the reported bowing parameters. In fact, depending on the growth techniques and the quality of the material grown, different research groups have reported very different values, which vary in a very wide range from -0.8 eV to 2.6 eV, as compiled by Yun et al. [22]. Studies performed using x-rays and analytical techniques have led to a dependence of the energy gap on the composition represented in Figure 1.9, where the $b = 1.0$ eV for the entire range of alloy compositions.

Measurements performed for $\mathrm{n-Al_{0.09}Ga_{0.91}N}$ demonstrated a carrier concentration of $5 \cdot 10^{18}\mathrm{cm}^{-3}$ and a mobility of 35 $\mathrm{cm^2V^{-1}s^{-1}}$ at 300 K [23]. This measurement did not reveal any temperature-dependent mobility. However, other measurements on Mg-doped $\mathrm{p-Al_{0.09}Ga_{0.91}N}$ grown by MOVPE revealed the temperature dependence of the mobility [24] a decrease in the holes mobility was observed with the

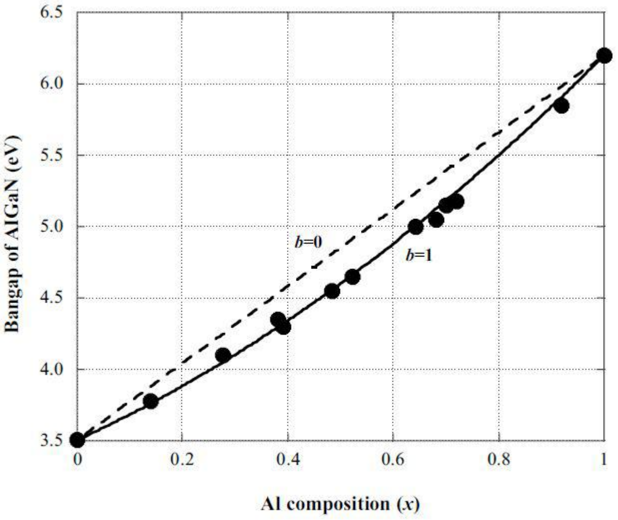

Figure 1.9: Energy gap of AlGaN as function of the Al composition (solid circle) and the least square fit (solid line). The dashed line shows the case $b = 0$ [20].

increase of the temperature, reaching values around 9 $\text{cm}^2\text{V}^{-1}\text{s}^{-1}$ for a doping density of $1.48 \cdot 10^{19}$ cm^{-3}. This low mobility is attributed to the high carrier concentration and to the intergrain scatterng present in the samples. Regarding the lattice constant, it was observed a almost linear dependence on the AlN mole fraction in AlGaN.

Until recently, the resistivity of unintentionally doped AlGaN was believed to increase so rapidly with increasing AlN mole fraction, that AlGaN became almost insulating for AlN mole fractions exceeding 20%. With increasing AlN mole fraction from 0 to 30%, the n-type carrier concentration decreased from 10^{20} to 10^{17} cm^{-3} and the mobility increased from 10 to 30 $\text{cm}^2\text{V}^{-1}\text{s}^{-1}$. One possible responsible for this variation could be an increase of the native defect ionization energies with increasing AlN. Knowledge of the doping characteristics of AlGaN is still incomplete. For example, it is not known how the dopant atoms such as Si and Mg respond to the variation of the AlN mole fraction in AlGaN. It was suggested that, with increasing of the AlN mole fraction, doping atoms move deeper into the forbidden bandgap. AlGaN with an AlN mole fraction between 50 - 60% can be doped by both n-type an p-type impurity atoms.

The band structure of GaN, $\text{Al}_\text{x}\text{Ga}_{1-\text{x}}\text{N}$ with $x = 0.25$, and AlN are reported in Figure 1.10(a), (b), and (c), respectively. Analyzing the band structure of GaN and AlN, it is possible to observe a different order in the valence bands. This causes the emitted light to be polarized with $E \parallel c$ in AlN, instead with $E \perp c$ in GaN. This particular property of AlN influences the optical properties of AlGaN, in particular for alloys with high Al concentrations. Increasing the Al mole concentration from $x = 0$

to $x = 0.25$, the valence bands are approaching until, for $x = 0.25$, the three bands degenerate into a single point.

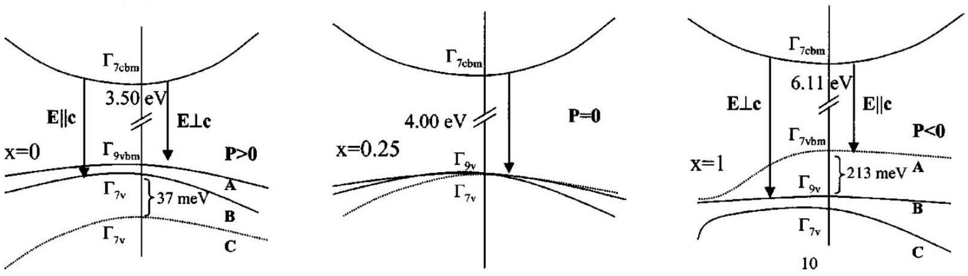

(a) (b) (c)

Figure 1.10: Band diagram of $\mathrm{Al_xGa_{1-x}N}$ with $x = 0$ (a), $x = 0.25$ (b) and $x = 1$ (c) [25].

1.5 Polarization effects

The most common epitaxial growth direction for III-N semiconductors is the c plane of the hexagonal wurtzite structure, in particular, gallium nitride layers can be grown either Ga-faced or N-faced, as shown in Figure 1.11. Grown in the c plane direction, these semiconductors show polarization charges located on each of the two surfaces of the layer. As a result of these charges, an internal electric field is generated, which has a significant effect on the optical and electrical properties of these semiconductors. The two charges affecting these materials are due to spontaneous polarization and piezoelectric polarization.

The spontaneous polarization is due to the fact that the covalent bond of GaN is characterized by a stronger ionicity compared to other III-V covalent bonds, due to the lack of electrons occupying the outer orbitals of the nitrogen atom. In fact, electrons of Ga atom involved in the metal-nitrogen covalent bond are strongly attracted by the Coulomb potential of the N atomic nucleus. The ionicity of this covalent bond, which corresponds to a microscopic polarization, results in a macroscopic polarization if the crystal has a lack of inversion symmetry, as in the case of GaN both in the wurtzite and in the zincblende structure. In the case of Ga-faced structure, the spontaneous polarization points toward the substrate, while for N-faced GaN, the polarization points toward the surface of the layer sequence.

The piezoelectric polarization is due to the mechanical deformation (strain) of the material, which can cause a reciprocal displacement of the anion-sublattice and cation-

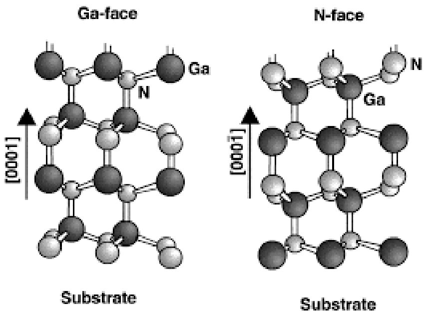

Figure 1.11: Crystal structure of Wz GaN fo Ga-face (a) and N-face (b) growth.

sublattice, thus producing a polarization in the material. This strain, in a heterostructure, is mainly due to the reticular mismatch between the active region material and the barrier material. The strain in the epitaxial layer can be tensile or compressive: for example, AlGaN is subjected to a tensile strain when it is grown over a GaN buffer layer. The direction of the internal electric field depends on the mechanical deformation and on the growth direction; Figure 1.12 reports different cases. Typically, both spontaneous and piezoelectric polarization contribute to the overall polarization field in a GaN semiconductor. Without any applied external field, the total macroscopic polarization P can be expressed as the sum of spontaneous polarization P_{SP} (i.e. the polarization at zero strain) and the piezoelectric polarization P_{PZ}

$$P = P_{SP} + P_{PZ} \tag{1.3}$$

These internal polarization fields have consequences on quantum well structures. Inside the quantum well, an electric field separates electrons and holes spatially, i.e. the electrons and holes wavefunctions are located in opposite angles of the quantum well, thus presenting a reduced overlap, which in turn reduces the efficiency of radiative recombination. This effect is evident especially for thick quantum wells, as shown in Figure 1.13. To avoid this, it is necessary to maintain the thickness of the quantum well very thin. This effect is called Quantum Confined Stark Effect (QCSE) [26] and it causes a red-shift of the quantum well emission in heterostructures, i.e. a shift of the emission towards longer wavelengths (towards the red).

These large electric fields due to the effects of polarization can be shielded by a high concentration of free carriers, which can be achieved by high doping of the active region or a high injection current. In fact, as the injection current increases, a blue-shift is obtained, i.e. a shift of the emission peak towards shorter wavelengths (towards the blue); this effect was often observed in InGaN-based LEDs [27]. However, it can be also advantageous in order to reduce ohmic contact resistances in GaN-based devices.

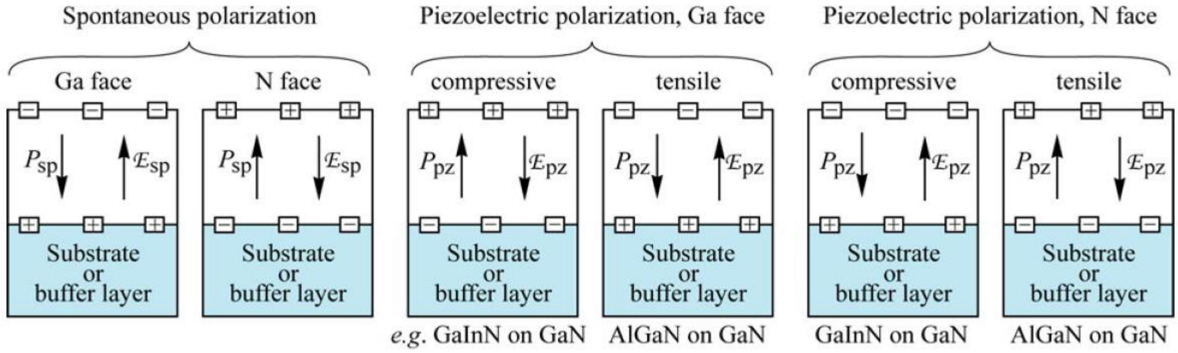

Figure 1.12: Direction of polarization field and electric field for spontaneous and piezoelectric polarization in Ga-faced and N-faced III-V nitrides [19].

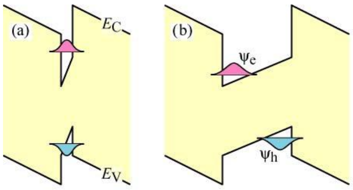

Figure 1.13: Schematic band diagram of a thin (a) and a thick (b) quantum well with internal polarization fields. In (b), the electric fields cause a severe bending of the conduction and valence bands, resulting in a reduced overlap of the electron/hole wavefunctions [19].

Table 1.2: Main properties of the considered substrates.

Material	Lattice constant a (Å)	Lattice mismatch with GaN (%)	CTE (10^{-6} K^{-1})	κ_L (Wm^{-1}K^{-1})	Isolation (Ω cm)
GaN	3.189	0	5.59	130	$\geq 10^9$
Sapphire	$4.758/\sqrt{3}$	13	7.5	50	insulating
6H SiC	3.08	3.4	4.2	490	$\geq 10^{11}$
Silicon	5.4301	17	3.59	150	$1 - 3 \cdot 10^4$
AlN	3.112	1	4.2	200	$\geq 10^{12}$

1.6 Substrates

Thanks to the development and improvement of the growth techniques, great improvements in the quality of films based on III-V group materials such as GaN, were obtained. Unfortunately, one of the main disadvantages of GaN is the lack of native substrates available in large quantities. The availability of affordable, large-diameter and high-quality substrates determines the final quality of the material that will be grown on top of it, which is the reason why it is very important to choose the right substrate. Therefore, it will be necessary to examine some properties in order to evaluate the actual suitability of the material under exam; some of these properties are:

- the lattice mismatch respect to the material we want to grow;
- the thermal conductivity and coefficient of thermal expansion;
- the maximum electrical insulation, at different temperatures;
- the price per area and availability;
- the crystalline quality and the density of residual defects;
- surface properties;
- curvature and deformation of the wafer;
- chemical and mechanical properties in terms of thinning and stretching.

Table 1.2 reports some physical properties of the principal substrate used for III-N based devices. Up to now, the best alternatives as substrates are sapphire, silicon carbide (SiC) and silicon. There is a certain interest also in substrates in AlN, due to the small lattice mismatch with the sapphire and its high thermal conductivity. GaN is also a very suitable material as substrate, but unfortunately, there are no substrates of sufficient diameter and quality.

One of the main problems in the use of non-native substrates is the lattice mismatch between substrate and grown material: this mismatch leads to the formation of defects and dislocations, which are directly or indirectly responsible for the creation of non-radiative recombination centers. Moreover, the presence of point and structural defects favors the spread of impurities through dislocations and obstructs the carrier transport. The use of these materials has therefore led to the development of unconventional methods using compliant substrates and techniques such as ELO (epitaxial lateral overgrowth) in order to reduce the density of defects.

1.6.1 Sapphire

Sapphire (Al_2O_3) has become the dominant material in the production of substrates, due to its relatively low cost, availability in large area (substrates of 2 - 4 inches in diameter) and for continual improvements in its quality, both in terms of bulk and surface properties. Moreover, it is transparent for most of the bandgaps of nitride alloys, a property that affords great benefits in the realization of devices such as LEDs. Figure 1.14 shows a schematic representation of sapphire unit cell.

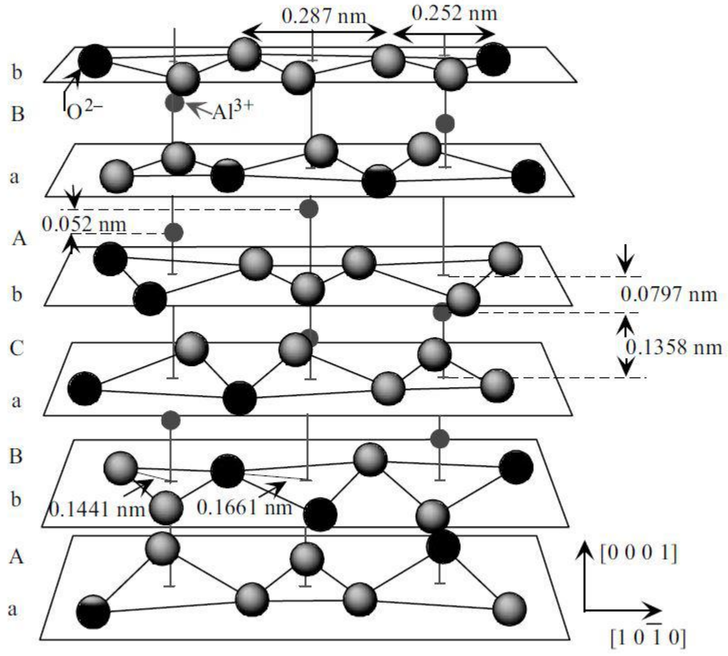

Figure 1.14: Schematic diagram of the Al_2O_3 unit cell; there are six oxygen layers in the unit cell and the distances between the various atomic layer change [20].

Before growth, the surface of the sapphire substrate must be prepared to receive the top layer, as it may have scratches and damage. In this case, it has been seen that etching by means of chemical products is not effective and for this reason, in order to eliminate these superficial alterations, a high temperature treatment is carried out in a controlled environment, which allows to smooth the surface.

Sapphire presents some problems, such as the break of the wafer during the thinning processes, the wafer curvature induced by the mismatch, thus further problems from the lithographic point of view, and obviously the lattice mismatch with materials such as GaN, and therefore with AlGaN. The mismatch makes it more difficult to produce high quality materials, due to the formation of defects and the relaxation of the lattice at the growth temperatures, even for the thinner layers. In these cases, in order to reduce the defects, the material is grown not directly on the substrate, but on another layer, called buffer layer, which has a lattice parameter that is not too different from that of the material to be grown. This growth technique is defined as metamorphic.

1.6.2 SiC

Because of its high conductivity and availability of substrates with high resistivity, silicon carbide has gained recognition as a good substrate for making optical and electrical devices. As for the dimensions, it is possible to reach a substrate with a diameter of up to 4 inches. The base unit of crystalline SiC has a tetrahedral shape, with covalent bonds, in which one atom is bound to four Si atoms, or vice versa, as shown in Figure 1.15(a). It has more than 250 polytypes, but the most used are 4H- and 6H-SiC. The growth method of this material is based on the physical vapor transport deposition (PVT) technique, but growth can also occur through high-temperature CVD (HTCVD); depending on the growth method used, however, the substrate will have different properties.

The main disadvantages of this material are related to the preparation of the surface before growth, i.e. the cleaning of the surface, in order to remove defects and reduce roughness, the presence of micropipe defects, defects such polytype inclusions, Si segregation, the dimensions and the costs. The micropipes have always been considered the main obstacle for high quality SiC substrates: these are screw defects that can stretch through the entire crystal during bulk growth. Subsurface damage and grain boundaries, especially in the periphery of the crystal, are of significant importance for III-N device performance. Subsurface damage is not visible to some characterization methods, but it becomes visible after significant thermal or chemical treatment and can be removed by the application of chemical-mechanical polishing [28].

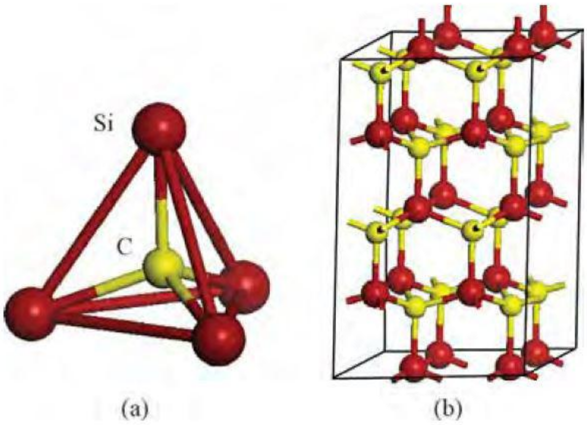

Figure 1.15: Tetragonal bondig of a carbon atom with its four nearest silicon neighbors (a). Three-dimensional structure of 2H-SiC structure (b) [20].

1.6.3 Si

Silicon is the most perfect and least expensive substrate available in sizes up to 300 mm. It has a good thermal stability under conditions used for GaN epitaxy. However, Wz GaN and AlN grown on Si (111) show high defect density. Despite this, the incentives for using Si substrates remain high, and good progress has been achieved in reducing defect density.

Si has a diamond-lattice structure, where each atom in the lattice is surrounded by four other equidistant atoms that lie at the corners of a tetrahedron (Figure 1.16). The crystalline Si ingots are produced by the Czochralski (CZ) method and eventually become thin Si wafers through the processes of shaping, slicing, lapping, etching, polishing and cleaning. By introducing impurities, it is possible to create p-type and n-type silicon.

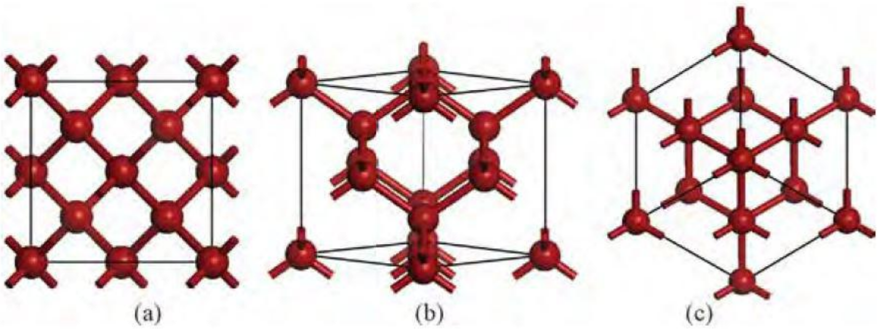

Figure 1.16: Perspective view along the (001) (a), (011) (b) and (111) (c) directions of a Si cell [20].

For GaN growth in its wurtzite structure, the plane (111) is used. Si surface is already excellent for growth, it is sufficient to remove a thin surface layer by etching and then to carry out the hydrogenation of the surface dangling bonds.

However, the use of Si introduces a number of critical issues and engineering challenges for III-N devices, including: (i) the impact of the lattice mismatch relative to GaN, which can generate defects in the material, worsen the quality and therefore impact on the reliability of the device; (ii) the difference in the coefficients of thermal expansion; (iii) the availability and cost of insulating silicon substrates, with dimensions between 2 and 6 inches, with isolation levels of $10 - 30$ kΩcm.

1.6.4 GaN and AlN substrates

Only recently, native GaN and AlN substrates have been developed and used for electronic applications. The use of native substrates allows to completely eliminate the lattice mismatch. GaN substrates are only recently available in semi-insulating and n-conductive forms, with diameters suitable for electronic devices fabrication. Often, to reduce the defect density for optoelectronic devices, a GaN template is grown by MOCVD technique over a host substrate, such as sapphire, and subsequently a quasi-GaN substrate is grown over the template. After that, the host substrate is removed. Another possibility is to grow GaN boules by HVPE, followed by Si-based n-doping in order to realized conductive substrates, or Fe doping to obtain semi-insulating substrates with a resistivity of 10^6 Ωcm. In Figure 1.17 is reported the dislocation density as function of the lattice mismatch with respect to GaN. It is possible to notice that, only with GaN substrates or with epitaxial regrowth techniques (ELO) techniques, a very low defect density can be obtained.

In addition to native GaN substrates, native AlN substrates are also under discussion for optoelectronic applications. AlN itself has a high resistivity and has a better thermal conductivity than GaN, actually very similar to that of SiC. Furthermore, compared with other non-native substrates, it has the lowest lattice mismatch, as shown in Figure 1.17. For the use of AlN for GaN-based lasers, even the residual AlN mismatch with respect to GaN lattice constant is too high in order to provide reliable GaN lasers without the use of additional concepts, such as ELO technique, that reduces the defect concentration [30]. The AlN material is particularly attractive for the growth of AlGaN layers in the UV LEDs fabrication: AlN substrates are promising candidate to achieve good quantum efficiency, as they allow the incorporation of compressive strain into the epitaxial growth of AlGaN layers, counteracting the formation of cracks, reducing the density of dislocations and therefore the component of loss of

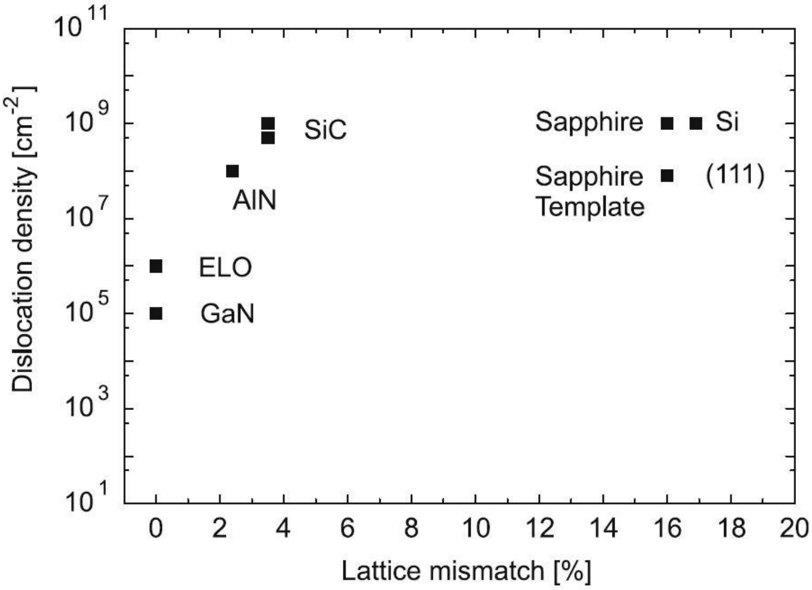

Figure 1.17: Dislocation density as function of lattice-mismatch relative to GaN [29].

efficiency given by non-radiative recombination [3]. Despite this, the available AlN substrates still exhibit significant light absorption due to contaminants such as oxygen, and this requires process steps to remove them, such as removing the substrate during the device fabrication. For this reason, sapphire substrates remain until now the most competitive substrates for AlGaN growth in the UV LEDs fabrication.

One of the main impediments in the fabrication of native substrates is the high vapor pressure of N on the AlN and on the GaN, together with its low solubility in molten metals at reasonable temperatures and pressures. Furthermore, the thermodynamic properties of GaN, in particular its melting conditions, are so extreme that it is not possible to apply common growth methods that use stoichiometric solutions.

1.7 GaN doping

III-N devices are intrinsically doped due to the presence of impurities, such as nitrogen vacancies, and the intrinsic polarization of the material; in fact, intentional doping is often based entirely on polarization mechanisms. Despite this, conventional doping by impurities is still used and presents difficulties in controlling it, both for n-type and p-type doping.

1.7.1 n-type doping

For the fabrication of n-type GaN-based devices, it is necessary to minimize unintentional doping, which often has a level around 10^{16} cm^{-3}. For the realization of intentionally n-type GaN, Si is the major used dopant, since the electron concentration can be controllably changed from $\sim 10^{17}$ to $2 \cdot 10^{19}$ cm^{-3} by varying the flow rate of SiH_4 in OMVPE growth [1]. Moreover, its solubility in GaN results to be on the order of 10^{20} cm^{-3}, making it suitable for group III-N doping. In GaN, Si replaces a Ga atom in the lattice by providing an electron free of bonds. Other possible doping agents of n-type are germanium (Ge), that allowed to produce material with electron concentrations of $7 \cdot 10^{16} - 10^{19}$ cm^{-3}, selenium (Se) and oxygen, even though silicon still remains the most used. It has been observed [31] that an increase in the flow of NH_3 during growth can significantly increase the conductivity of the n-type GaN; this effect is probably due to passivation, by hydrogen, of the acceptors in the material during growth.

1.7.2 p-type doping

There has been much effort aimed at doping GaN and its p-type ternaries by incorporating group II and group IV elements. P-type doping has been a big obstacle for GaN-based LEDs, until Akasaki and Amano made the major breakthrough by using the low energy electron beam irradiation (LEEBI) on the Mg-doped GaN [32, 33]. Later Nakamura et al. [34] also successfully obtained p-type GaN by thermal annealing. Achievement of p-type doping represented the turning point for GaN. This milestone took GaN from a low-level laboratory curiosity and placed it among the most important technology, the applications of which are constantly expanding.

Typically, the acceptable materials used as agents for p-type doping are magnesium (Mg) and zinc (Zn), even if they are not very efficient acceptors. Although Mg_{Ga} is a relatively shallow acceptor [35, 36, 37], early attempts of Mg doping were unsuccessful, presumably for two reasons: (i) hydrogen, always present in OMVPE and HVPE growth environments, passivates Mg, causing the formation of electrically and optically inactive complexes [38]; (ii) heavily Mg-doped GaN is subject to self-compensation due to donor-like defects that are created [39].

Later, it was understood that the passivation with hydrogen during growth is favorable for the formation of highly conductive p-type GaN, since the shift of the Fermi level towards the conduction band facilitates the incorporation of the Mg. An important step forward was made through the use of LEEBI [33], which allowed the conversion of compensated Mg-doped GaN into a conductive p-type material, with hole concentrations as high as $3 \cdot 10^{18}$ cm^{-3} and resistivity of 0.2 Ωcm [40]. Afterwards, it was verified that even through thermal annealing at 700°C under N2 environment, it was possible to obtain the same conversion into p-type; furthermore, the process results to be reversible.

One problem of Mg acceptors in GaN and AlGaN is their activation energy, much larger than kT at 300 K: $160 - 200$ meV in GaN, which increases as the Al mole fraction increases. This results in low activation and therefore low conductivity in p-type GaN and AlGaN, degrading the performance of devices such as LEDs, lasers and hetero-junction bipolar transistors.

1.8 Contacts on GaN

The formation of ohmic contacts requires the solution of a number of issues, including the increase of the density of states at the interface for wide bandgap semiconductors ($\geq$ 3.4 eV), the pretreatment of the semiconductor surface before metal deposition, the control of the metal morphology, due to the high annealing temperatures (600°C), which includes control of vertical diffusion of metal and of the lateral diffusion of contact metals.

A high density of states near the interface is required for the formation of ohmic contacts at a semiconductor surface, to push the Fermi level in the semiconductor close to the conduction band. This operation is made more difficult by the wide bandgap of III-N semiconductors, while it is possible to exploit the polar properties to increase the density of states at the interface. There are two types of low resistivity ohmic contacts: the Schottky contacts with very low barrier height, where the carriers inside the material can flow towards the semiconductor thanks to the thermal activation even at room temperature, and the contacts that exploit the tunneling effect, in which the presence of a very doped semiconductor means that the potential barrier is very thin, allowing the carriers to cross it through tunneling. The annealing procedures have the purpose of providing strong vertical material diffusion, while the lateral one must be minimized; moreover, the contact resistance has the trend to decrease with increasing annealing temperature.

We want to report some examples of materials used as ohmic contacts for III-N semiconductors, distinguishing between n-type and p-type ohmic contacts.

1.8.1 Ohmic contacts on n-GaN

For the realization of ohmic contacts on n-type GaN it is possible to use metallizations in Al and gold (Au), with contact resistances between 10^{-4} and 10^{-3} Ωcm^2. The metals are deposited by evaporation and modeled by photolithography. The simple deposition of Au for the realization of the contact is not enough, since the contact turns out to be rectifying, and for this reason a treatment by annealing at 575°C is necessary to make it ohmic. Among the possible n-type ohmic contacts, contacts made with mixtures of titanium (Ti) and Al are reported at an annealing temperature of 900°C for 30 s, with contact resistances of $8 \cdot 10^{-6}$ Ωcm^2. Whereas, with Ti and Au contacts, resistances of $7.8 \cdot 10^{-5}$ Ωcm^2 [31] are reported.

Improved ohmic contact stability is reported for Ti/Al/Pt/Au multilayer contacts to n-type GaN compared to Ti/Al/Au contacts, with annealing temperatures in the range of $750 - 950$°C. Platinum is used as a diffusion barrier for Au penetration. Contacts in Ti/Al/Ni/Au, instead, allow the formation of a contact resistance of 0.75 Ωcm. The use of highly Al-doped-sputtered zinc oxide (ZnO) layers on top of AlGaN/GaN heterostructures allows to obtain a poor ohmic contact resistance of 2.7 Ωcm, without any further annealing process.

1.8.2 Ohmic contacts on p-GaN

The p-type ohmic contacts on GaN are of great importance for optoelectronic devices. Because of the intrinsic properties of GaN, the p-type ohmic contact resistances are typically two orders of magnitude higher than that for the best n-type contacts. Among the possible materials, Ni/Au contacts are reported with annealing temperatures of 600 and 450°C. For contacts derived from this metal system using Ni/Pd/Au layer, low resistances are reported: for Mg-doped GaN, resistances of $1 \cdot 10^{-4}$ Ωcm^2 were obtained, while very low values, $4.5 \cdot 10^{-6}$ Ωcm^2, are reported for heavily Be-doped GaN samples [41]. With transparent Ag-based contacts, contact resistances of $5 \cdot 10^{-4}$ Ωcm^2 were obtained.

1.9 Defects, impurities and related complexes in GaN

No matter how perfect semiconductors are or would be, defects are still present, particularly in semiconductors like GaN, due to high lattice mismatch between this semiconductor and the typical substrates used for the growth. The investigation of the presence of defects is one of the main topic of discussion. As already mentioned before, GaN epitaxial layers have been grown on substrates such sapphire, SiC and Si and to improve the quality of layers, much attention has been devoted to the understanding of particulars heteroepitaxy.

Electrical and optical properties of the semiconductor material depend strongly on the density and nature of point defects. Furthermore, crystallographic defects can act as non-radiative recombination centers, which strongly reduce the efficiency of the devices. For this reason, it is important to deeply understand the origins of defects in GaN.

In this section, point defects, extended defects and their charge nature will be discussed from a theoretical point of view, in terms of their formation energies and manifestation of defect.

1.9.1 Point defects

Point defects are the most common defects occuring in semiconductors. They are also known as native defects or intrinsic defects and manifest themselves as background doping or autodoping, and compensated dopants. Point defects play an important role in the electrical and optical activity in nitride semiconductors and interfer in the efforts to increase efficiency of LEDs, increase laser operation lifetime, and eliminate anomalies observed in electronic devices. Carrier lifetime is influenced by the type and density of these defects, consequently, point defects play an important role in the radiative quantum efficiency and the longevity of GaN-based laser diodes and light emitting diodes.

Several papers report the formation energy and corresponding energy level for major native defects in III-N, theoretically and experimentally [42]. Figure 1.18 shows the formation energies for all native point defects in GaN. The Fermi level determines the charge state of a particular point defect. There are three basic type of native point defects: vacancies, self-interstitials and antisites. Vacancies correspond to a missing atom in the lattice; they present low energy, enough to be present in significant concentrations in GaN. They are common, especially at high temperatures when atoms change frequently and randomly their positions, leaving behind empty lattice sites. An example of vacancies in GaN is represented by nitrogen vacancies, V_N which act as donors. Self-interstitials are additional atoms between the lattice sites. An example of interstitial defect on gallium nitride is represented by hydrogen, that can passivate magnesium dopant in p-type layers. Antisites are cations sitting on anion sites and vice versa, and are unique to compound semiconductors. Figure 1.18 shows that self-interstitial and antisite defects are high-energy defects in GaN, and thus are unlikely to occur during growth, but they may be created under non-equilibrium conditions (for example by electron irradiation or ion implantation).

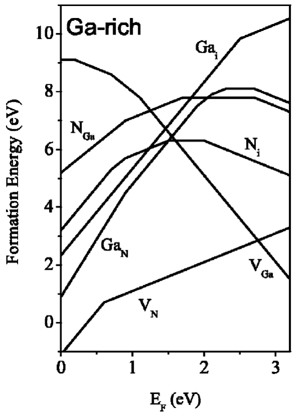

Figure 1.18: Formation energies as function of Fermi level for point defects in GaN under Ga-rich conditions. The zero of Fermi level corresponds to the top of the valence band. The graph shows only segments corresponding to the lowest-energy charge states and the slope of these segments indicates the charge state. Curves present kinks that indicate transitions between different charge states [42].

When Si donors are introduced into GaN, the lattice may attempt to create Ga vacancies, V_{Ga}, which are acceptors. V_{Ga} is the lowest energy defects in n-type GaN and plays a role in donor compensation as well in the yellow luminescence. The yellow luminescence is a broad luminescence band centered around 2.2 eV, that it has been observed in bulk GaN crystals as well as in epitaxial layers grown by different techniques [42].

This is one possibility, through which point defects like vacancies may be formed. Another way is through defective or incomplete kinetic processes on the growing surface of an epitaxial layer. An example are the N vacancies, V_N, created due to insufficient N flux at the growing surface. When purposely created, nitrogen vacancies will increase the electron concentration [43]. However, their high formation energy in n-type makes their spontaneous formation very unlikely during growth of non-intentionally doped GaN and hence they cannot be responsible for the n-type conductivity.

Point defects may also originate from impurities and relative complexes. The main foreign species used to obtain p-doped GaN is Mg, which is an acceptor in III-nitrides. Figure 1.19 shows calculated formation energies for impurities and defects relevant for p-type GaN. Mg acceptor has low formation energy and can easily incorporate into GaN. Considering Ga-rich conditions, the ionization energy of the Mg acceptor level corresponds to a value of 0.2 eV [44]. It is in reasonable agreement with experimental value of 0.208 eV determined by Götz et al. [45].

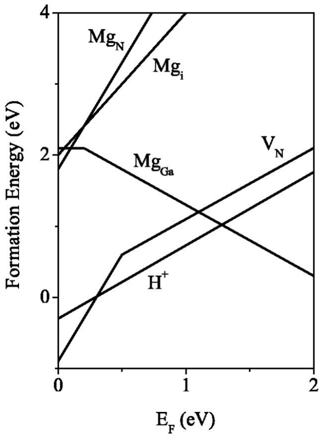

Figure 1.19: Formation energy as function of Fermi level for Mg in different configurations. Ga-rich conditions and equilibrium with Mg_3N_2 are assumed [42].

Hydrogen forms complexes with defects in GaN, and often the formation energies of the hydrogenated defects are lower. As already mentioned, in Mg-doped GaN, hydrogen is known to passivate the Mg acceptor. In particular, the electrically neutral Mg-H complex has a binding energy of 0.7 eV, with the H atom located in an antibondig site behind the N neighbor of the acceptor [46]. Hydrogen bonding with the Mg acceptors to form neutral complexes during grwoth is widley belived to be the main cause of the failure to get p-type conductivity in GaN early experiments, particularly in the case of layers prepared by MOCVD [47]. In order to break Mg-H complexes and obtain high hole concentrations, high-temperature annealing, in a hydogen-free atmosphere, is a common routine procedure for GaN films where a hydrogen carrier gas was used [47]. During the postgrowth annealing, the Mg-H complex dissociates and H diffuses either to the surface or to the extended defects.

High levels of n-type conductivity have always been found in GaN bulk crystals grown at high temperature and high pressure [48]. It has been established that the characteristics of these samples are very similar to epitaxial films which are intentionally doped with oxygen [49]. The n-type conductivity of bulk GaN can therefore be attributed to unintentional oxygen incorporation.

1.9.2 Dislocations in GaN

The large difference in lattice mismatch and in the coefficient of thermal expansion among the materials involved results in a large number of dislocations. GaN films typically have threading dislocation density of $10^8 - 10^{10}$ cm^{-2} and these may cause the formation of non radiative recombination and scattering centers [50, 51, 52].

In general, dislocations are areas where the atoms are out of positions in the crystal structure. Dislocations can be divided in two main groups, misfit dislocations and threading dislocations (TDs). Misfit dislocations are confined to the interface, between the GaN epitaxial layer and the substrate interface. To a first extent, misfit dislocations are not supposed to thread up into the layer, but it has been shown that TD can be interconnected to the misfit dislocation network [53].

TD propagate through the layer, reach the surface of the film and can be detrimental to the electrical and optical properties of epitaxial layers. TEM investigations have shown that these dislocations originate at the interface and the large majority propagates to the sample surface [54, 55]. Among the TDs are pure edge, pure screw and mixed dislocations. Due to their importance, TDs in GaN have been studied for more than a decade, often leading to contradictory results. Pure screw dislocations, pure edge dislocations, and mixed dislocations (having screw and edge components) are considered as extended defects that thread through the crystal. In literature, it is possible to find conflicting reports regarding whether extended defects are or are not electrically active. However, many works lead to the conclusion that extended defects directly or indirectly cause electrically active centers and they can do so by trapping impurities and point defects and by forming complexes due in part to large local strain induced.

Elsner et al. in [56] reported that pure screw dislocations in an eightfold ring are not electrically active, but left the possibility that the associated strain field may trap point defects and impurities. He also reported that these dislocations form a band of deep levels located between 0.9 eV and 1.6 eV above the valence band, and relatively shallow states about 0.2 eV. The open core and implicitly the electrical neutrality predicted by Elsner in [56] are consistent with some experimental investigations that point to open-core screw dislocations [57]. In a subsequent work, the same group argued that TDs in GaN produce strain fields strong enough to lead to impurities segregation, with oxygen being the most likely impurity involved [58]. Using correlated techniques in the scanning transmission electron microscope, Arslan et al. [59] reported experimental observations of oxygen segregation to screw dislocations in GaN.

In another work, Northrup [60] found that under Ga-rich growth conditions, screw dislocations with Ga-filled core produce metallic-like energy levels over the whole bandgap and the Fermi level inside the dislocation core is pinned at about 1.4 eV above the valence band. Such dislocations may affect the electrical properties by both enhancing the leakage current through their metallic-like core and by encouraging non-radiative recombination.

Lee et al. [61] investigated atomic and electronic structures of threading pure edge dislocations in GaN. Full-core, open-core, Ga-vacancy, and N-vacancy edge dislocations have been assumed to be fully relaxed in the computations. The Ga-vacancy dislocation core variety was found to be the most stable in a wide range of Ga chemical potentials. The full-core and open-core dislocation core structures were found to be more stable than the others in the Ga-rich growth regime. Figure 1.20 reports the energies of all edge dislocations reported in the mentioned paper. The lines with filled circles depict the occupied states.

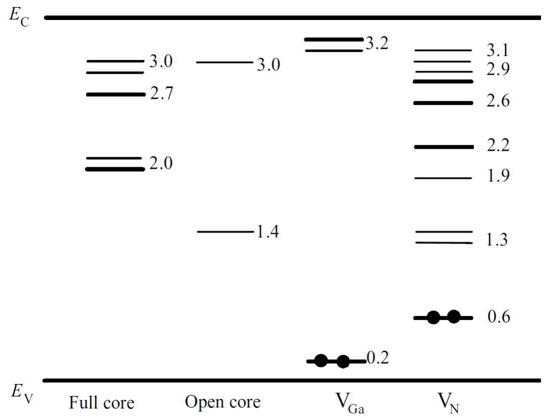

Figure 1.20: Schematic diagram of energy levels in the bandgap for various types of edge dislocations: full-core, open core, V_{Ga} and V_N. Filled circles indicate the occupied states [61].

In essence, all edge dislocations can act as deep trap centers, the energies of which are illustrated schematically in Figure 1.20.

All these results on threading dislocations in GaN reported in the literature are quite complex. Comparison with experimental data shows that the deep states associated to dislocations are often similar to those traps due to point defects, suggesting that point defects decoration of dislocations is one of the main factors that determines the electronic properties of dislocations [62].

Chapter 2

Basic principles of LEDs and LDs

The mechanism at the base of the operation of a Light Emitting Diode (LED) is the spontaneous emission of photons from the active region of a pn junction. One of the main aim in the realization of LEDs is to maximize this emission, that turns out to be the useful part of the so-called electron-hole recombination process. However, electron-hole pairs can also recombine non-radiatively, resulting in this case in the emission of a phonon. It is important to maximize the radiative recombination and limit the non-radiative recombination. In laser diodes (LDs) spontaneous emission is no more the dominant emission mechanism, since stimulated emission is the relevant one. Moreover, a particular cavity, such the Fabry-Perot cavity, is needed in order to favor this emission.

The chapter presents the basic principles of operation of LEDs and LDs, focusing on the recombination mechanisms that occur in these devices, their electrical and optical properties and the main problems that are encountered when trying to increase their efficiency.

2.1 Radiative recombination

Any doped or undoped semiconductor has two kind of free carriers, electrons and holes. Under equilibrium condition, the law of mass action controls the concentration of these carriers with the following equation:

$$n_0 p_0 = n_i^2 \tag{2.1}$$

where n_0 and p_0 are the electron concentration and the hole concentration at equilibrium, respectively, and n_i is the intrinsic carrier concentration. In order to generate excess carriers in a semiconductor, it is possible to take advantage of the light absorption or of the current injection, meaning that the total carrier concentration will be equal to the sum of the concentration at equilibrium and of that of excess carrier:

$$n = n_0 + \Delta n \quad \text{and} \quad p = p_0 + \Delta p \tag{2.2}$$

where Δn and Δp are the excess electron and hole concentrations, respectively.

Since we are interested in the carrier recombination, it is useful to define some parameters. The first one is the recombination rate R, i.e. the rate at which the carrier concentration varies. This parameter is defined as:

$$R = -\frac{dn}{dt} = -\frac{dp}{dt} = Bnp \tag{2.3}$$

In order to have the electron-hole recombination, a free electron must be in the conduction band and a hole in the valence band (i.e. a free energy level for holes in the valence band). The probability that an electron recombines with a hole is proportional to the hole concetration p; moreover, the number of recombination occurences is also related to the electron concentration n. For this reason, the R rate is proportional to the electron and hole concentrations by means of a B constant, defined as bimolecular recombination coefficient. For semiconductors III-V with direct band-gap, its typical value is in the range between 10^{-11} and 10^{-9} cm^3/s.

In the next section, the recombination dynamics as function of time will be discussed.

2.1.1 Radiative recombination for low-level excitation

Considering a semiconductor under photoexcitation, since electrons and holes are generated and annihilated in pairs, the steady state electron and hole excess concentrations are equal:

$$\Delta n(t) = \Delta p(t) \tag{2.4}$$

Equation 2.3 can be rewritten:

$$R = B[n_0 + \Delta n(t)][p_0 + \Delta p(t)] \tag{2.5}$$

In case of low-level excitation, the photogenerated carrier concentration is very low with respect to the majority carrier concentration, that means $\Delta n \ll (n_0 + p_0)$, and 2.5 becomes:

$$R = Bn_i^2 + B(n_0 + p_0)\Delta n(t) = R_0 + R_{excess} \tag{2.6}$$

where R_0 is the equilibrium recombination rate and R_{excess} is the excess recombination rate. In this way, the time-dependent carrier concentration can be calculated:

$$\frac{dn(t)}{dt} = G - R = (G_0 + G_{excess}) - (R_0 + R_{excess}) \tag{2.7}$$

where G_0 is the equilibrium generation rate, that is $G_0 = R_0$.

We assume an illuminated semiconductor and excess carrier have been generated, at time $t = 0$ we suppose to interrupt the carrier generation ($G_{excess} = 0$). Using equation 2.6 in 2.7, we obtain the following differential equation:

$$\frac{dn(t)}{dt} = -B(n_0 + p_0)\Delta n(t) \tag{2.8}$$

Solving this last equation, we are able to find the following result:

$$\Delta n(t) = \Delta n_0 e^{-B(n_0+p_0)t} = \Delta n_0 e^{-t/\tau} \tag{2.9}$$

where $\Delta n_0 = \Delta n(t = 0)$ and $\tau = \frac{1}{B(n_0+p_0)}$ is the carrier lifetime.

Figure 2.1 reports the majority and minority carrier concentration in a p-type semiconductor. The majority carrier concentration also decays with a time constant τ, though only a small fraction of carriers disappear due to recombination. In fact, the mean time for a majority carrier to recombine is higher than minority carrier lifetime; for this reason, the majority carrier lifetime is assumed to be infinitely long.

Equation 2.9 shows that, once photoexcitation is terminated, the minority carrier concentration decays exponentially with a constant time τ, that is the mean time between generation and recombination of minority carriers.

2.1.2 Radiative recombination for high-level excitation

In case of high-level excitation, the photogenerated carrier concentration is higher than the one at equilibrium, that means $\Delta n \gg (n_0 + p_0)$; in this way equation 2.3 becomes:

$$\frac{dn}{dt} = -B\Delta n^2 \tag{2.10}$$

that yields the solution:

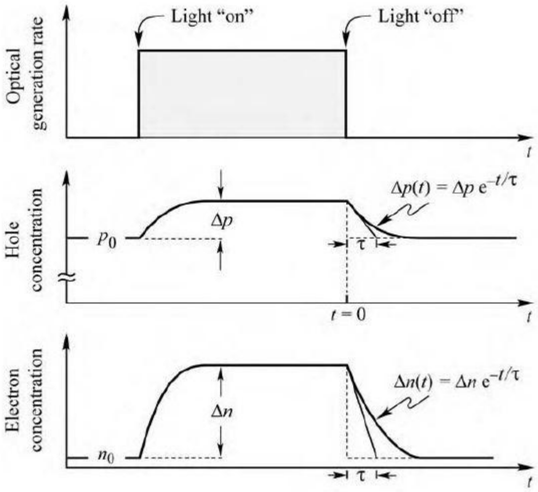

Figure 2.1: Carrier concentration as function of time before, during and after an optical excitation pulse. The semiconductor is assumed to be p-type [19].

$$\Delta n(t) = \frac{1}{Bt + \Delta n_0^{-1}} \tag{2.11}$$

In this case the carrier concentration decay is no more exponential, and for this reason the time constant is calculated from the slope of the decay using the following equation:

$$\tau = t + \frac{\Delta n(t)}{\frac{d\Delta n(t)}{dt}} \tag{2.12}$$

that yields to

$$\tau = t + \frac{1}{B\Delta n_0} \tag{2.13}$$

Note that for a non exponential decay, the time constant depends on the time itself and in this way the minority carrier lifetime increases with time. For sufficiently long times, the low-level excitation condition will be reached again.

2.1.3 Luminescence decay

Since the luminescence intensity is proportional to the recombination rate, it is possible to measure the carrier decay from the luminescence decay after optical excitation by a short pulse. Figure 2.2 shows schematically the luminescence decay after a short excitation pulse, in the case of low excitation and high excitation density (Figure 2.2(a)), together with the time constants in both cases(Figure 2.2(b)).

The carrier recombination dynamic is one of the factors that limits the time needed to switch an LED on and off. For this reason, it is important to reduce the carrier lifetimes with different precautions, such increasing the doping in the active region or the injected carrier concentration.

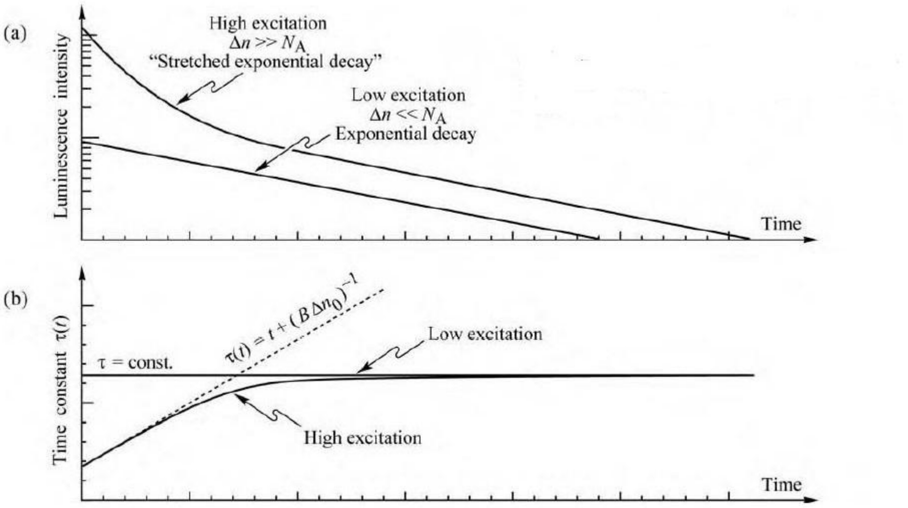

Figure 2.2: Luminescence decay for low and high excitation densities (a). Time constants for low and high excitation densities (b) [19].

2.2 Non-radiative recombination

As already mentioned before, in a semiconductor, together with the radiative recombination, non-radiative recombination processes may happen and these processes are not desired. During these processes, the electron energy is converted to vibrational energy of lattice atoms, i.e. phonons, that is dissipated in heat. There are different physical mechanisms that may cause non-radiative recombination and these mechanisms will be described in the following paragraphs.

2.2.1 Non-radiative recombination in the bulk

Defects in the crystal structure are the most common cause for non-radiative recombination. These defects may include unwanted foreign atoms, native defects and dislocations. All these defects introduce energy levels within the band-gap of the semiconductor.

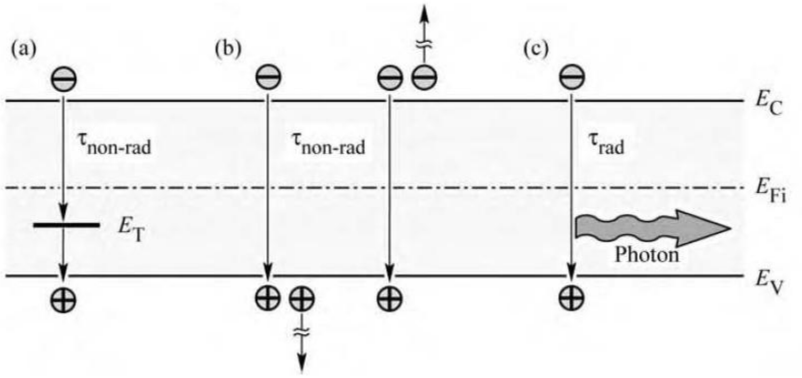

Figure 2.3: Band diagram illustrating non-radiative recombination via deep levels (a), non-radiative via Auger process (b) and radiative (c) [19].

Figure 2.3(a) reports schematically the carrier recombination through deep levels. A first study on recombination of free carriers via deep levels was performed by Shockley, Read and Hall in 1952. The non-radiative recombination rate via deep levels with energy level E_T and concentration N_T is given by

$$R_{SRH} = \frac{p_0\Delta n + n_0\Delta p + \Delta n\Delta p}{(N_T\nu_p\sigma_p)^{-1}(n_0 + n_1 + \Delta n) + (N_T\nu_n\sigma_n)^{-1}(p_0 + p_1 + \Delta p)} \tag{2.14}$$

where $\Delta n = \Delta p$; ν_n and ν_p are the electron and hole thermal velocities, respectively, and σ_n and σ_p are capture cross section of the traps. Parameters n_1 and p_1 are electron and hole concentrations, in case the Fermi level is located at the trap level; these two are:

$$n_1 = n_i \exp\left(\frac{E_T - E_{Fi}}{kT}\right) \quad \text{and} \quad p_1 = n_i \exp\left(\frac{E_{Fi} - E_T}{kT}\right) \tag{2.15}$$

where E_{Fi} is the Fermi level in an intrinsic semiconductor. Knowing that $R_{SRH} = \Delta n/\tau$, the non-radiative lifetime of the excess electron can be extrapolate from 2.14. As a consequence, we obtain:

$$\frac{1}{\tau} = \frac{p_0 + n_0 + \Delta n}{(N_T\nu_p\sigma_p)^{-1}(n_0 + n_1 + \Delta n) + (N_T\nu_n\sigma_n)^{-1}(p_0 + p_1 + \Delta p)} \tag{2.16}$$

Assuming that the semiconductor is p-type, where majority carriers are holes, i.e. $p_0 \gg n_0$ and $p_0 \gg p_1$, and a small deviation from equilibrium, i.e. $\Delta n \ll p_0$, the minority carrier lifetime is

$$\frac{1}{\tau} = \frac{1}{\tau_{n_0}} = N_T \nu_n \sigma_n \tag{2.17}$$

Instead, if electrons were majority carriers, meaning a n-type semiconductor, then we would obtain:

$$\frac{1}{\tau} = \frac{1}{\tau_{p_0}} = N_T \nu_p \sigma_p \tag{2.18}$$

From the previous equations, we can deduce that the SRH recombination rate is limited by the minority carrier capture rate; in fact, the capture of majority carriers is a more likely event with respect to the capture of minority carriers. Equation 2.16 becomes:

$$\frac{1}{\tau} = \frac{p_0 + n_0 + \Delta n}{\tau_{p_0}(n_0 + n_1 + \Delta n) + \tau_{n_0}(p_0 + p_1 + \Delta p)} \tag{2.19}$$

Assuming that $\nu_n \sigma_n = \nu_p \sigma_p$, $\tau_{n_0} = \tau_{p_0}$ and remembering that $\Delta n \ll p_0$, we obtain:

$$\tau = \tau_{n_0}\left(1 + \frac{p_0 + p_1}{p_0 + n_0}\right) \tag{2.20}$$

Considering a further semplification, that is the case of an intrinsic material $n_0 = p_0 = n_i$, equation 2.20 simplifies to:

$$\tau_i = \tau_{n_0}\left(1 + \frac{p_1 + n_1}{2n_i}\right) = \tau_{n_0}\left[1 + \cosh\left(\frac{E_T - E_{Fi}}{kT}\right)\right] \tag{2.21}$$

From equation 2.21 we can deduce that, since the cosh function has a minimum when its argument is equal to zero (in our case when $E_T = E_{Fi}$), the non-radiative lifetime is minimized when the trap level is near the center of the band gap. In this case, the lifetime is given by $\tau = 2\tau_{n_0}$.

Inspection of equation 2.21 also reveals a temperature T dependence of the non-radiative recombination lifetime, more precisely as T increases the non-radiative recombination lifetime decreases. This implies that, at higher temperature the radiative band-to-band recombination efficiency decreases.

2.2.2 Auger recombination

Another important non-radiative recombination mechanism is Auger recombination. In this type of process, the excess energy due to the electron-hole pair recombination is dissipated through the excitation of a free electron in the conduction band, or a hole in the valence band. This process is reported in Figure 2.3(b). The excited carrier will lose its energy by multiple phonon emission, until it will reach the edge of the band. The recombination rates associated to the Auger process are:

$$R_{Auger} = C_p n p^2 \tag{2.22}$$

in the case of energy given to a hole in valence band (this process is more likely to happen in p-type semiconductors), while:

$$R_{Auger} = C_n n^2 p \tag{2.23}$$

in the case of energy given to an electron in the conduction band (process more likely to happen in n-type semiconductors). From these two equations, we can evince that Auger recombination is proportional to the square of the carrier concentration, since we need two carriers of the same type during the process. In general, coefficients C_n and C_p are different due to the different structure of the conduction band and of the valence band.

In high-excitation condition, where the photogenerated carrier concentration is higher than the one of carriers at equilibrium, the two previous equations reduce to:

$$R_{Auger} = (C_p + C_n) n^3 = C n^3 \tag{2.24}$$

where C is defined as Auger coefficient, and presents typical values around 10^{-28} - 10^{-29} cm^6/s for III-V semiconductors.

Auger recombination reduces the luminescence efficiency in semiconductor only at high excitation intensity or at high injection currents, thus for high carrier concentrations, due to the cubic carrier concentration dependence. At lower carrier concentrations, the Auger recombination rate can be neglected.

2.2.3 Non-radiative recombination at surfaces

Non-radiative recombination can occur also at semiconductor surfaces that introduce strong perturbation in the periodicity of a crystal lattice. Since the band diagram model is based on the latter, it will need to be modified at the semiconductor surface. This modification includes the addition of electronic states within the band gap of the semiconductor. From a chemical point of view, atoms at the surface cannot have the same bonding structure like the atoms in the bulk due to the lack of neighboring atoms. For this reason, some of the valence orbitals do not form chemical bonds, giving origin to the so-called dangling bonds, partially filled electron orbitals that introduce electronic states within the band gap and act as recombination centers. These states can be as acceptor-like or donor-like states, depending on the charge state of these valence orbitals. It is possible that some of these dangling bonds rearrange themselves and form bonds between neighboring atoms in the same surface plane, causing the formation of new atomic structures with different energy states with respect to those in the bulk. It is difficult to predict the energetic localization of surface states, even with powerful theoretical models, thus usually phenomenological models of surface recombination are used.

Considering a p-type semiconductor subjected to illumination, it is possible to calculate the effect of surface recombination on the carrier distribution. Assuming a uniform generation rate G, the continuity equation for electrons is given by:

$$\frac{\partial n(x,t)}{\partial t} = G - R + \frac{1}{q}\frac{\partial J_n}{\partial x} \tag{2.25}$$

where J_n is the current density due to the electrons flowing to the surface. In the bulk there is no dependence on space, thus the continuity equation reduces to $G = R$ under steady-state conditions. Since the semiconductor is p-type, the recombination rate is given by:

$$R = -\frac{d\Delta n(t)}{dt} = \frac{\Delta n(x,t)}{\tau_n} \tag{2.26}$$

The excess carrier concentration in the bulk is given by $\Delta n_\infty = G\tau_n$. Moreover, assuming that the current density J_n is a diffusion current density with this form:

$$J_n = qD_n\frac{\partial \Delta n(x,t)}{\partial x} \tag{2.27}$$

and using this in equation 2.25, the continuity equation becomes:

$$\frac{\partial \Delta n(x,t)}{\partial t} = G - \frac{\Delta n(x,t)}{\tau_n} + D_n\frac{\partial^2 \Delta n(x,t)}{\partial x^2} \tag{2.28}$$

At the semiconductor surface, the boundary condition is given by:

$$J_n\big|_{x=0} = qD_n\frac{\partial \Delta n(x,t)}{\partial x}\bigg|_{x=0} = qS\Delta n(x,t)\big|_{x=0} \tag{2.29}$$

where S is the surface recombination velocity (cm/s). This equation shows that carriers recombine rapidly at the surface with velocity equal to S. Finally, assuming a time constant generation rate G, thus the minority carrier concentration has no time dependence, we can find the steady state solution to the continuity equation:

$$n(x) = n_0 + \Delta n(x) = n_0 + \Delta n_\infty \left[1 - \frac{\tau - NS \exp(-x/L_n)}{L_n + \tau_n S}\right] \tag{2.30}$$

where $L_n = \sqrt{D_n \tau_n}$ is the diffusion length of the minority carriers in the semiconductor, that in our case are electrons. Figure 2.4 shows the band diagram and the majority and minority carrier concentrations next to the surface for a p-type semiconductor. For $S \to 0$, the minority carrier concentration at the surface is equal to the bulk value, i.e. $n(0) \to n_0 + \Delta n_\infty$, while for $S \to \infty$ the minority carrier concentration at the surface tends to decrease, approaching the value at equilibrium, $n(0) \to n_0$. Typical value for S in GaN is $5 \cdot 10^4$ cm/s.

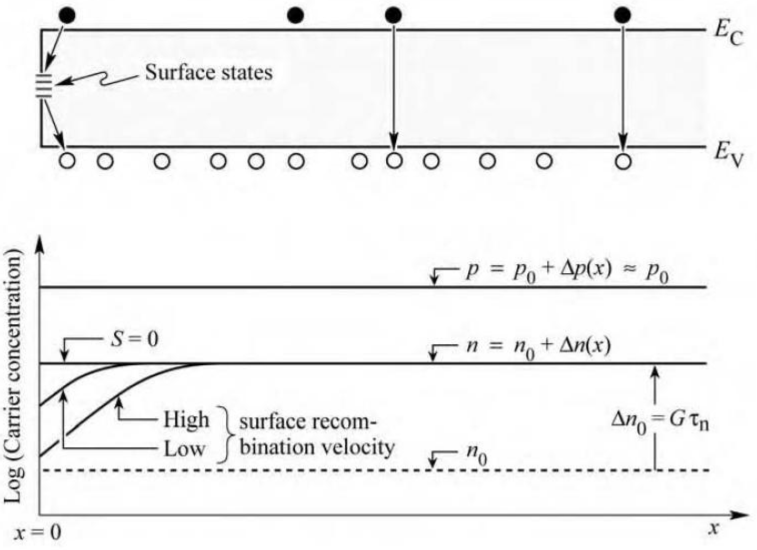

Figure 2.4: Band diagram and minority and majority carrier concentrations next to the surface, assuming an uniform carrier generation due to illumination [19].

Surface recombination causes undesired effects, like the luminescence efficiency reduction and the surface heating. In order to have this process, both carriers are needed. The device realization requires that active region, where both carriers are needed, is far from the surface. Different passivation techniques have been developed in order to reduce this non-radiative recombination mechanism, like treatments with sulfur and other chemicals.

2.3 Internal quantum efficiency

In the previous sections, different non-radiative recombination mechanisms have been presented; though this process can be reduced with different techniques, it is not possible to eliminate it completely. We can define internal quantum efficiency (IQE) the ratio between the number of emitted photons inside the semiconductor and the number of carriers undergoing recombination that means the probability to have radiative recombination; this efficiency allows us to evaluate the impact of the non-radiative recombination on the radiative one. In order to calculate it, we define τ_r as the radiative lifetime, and τ_{nr} as the non-radiative lifetime. Thus, the total probability of recombination is given by the sum of these two probabilities:

$$\tau^{-1} = \tau_r^{-1} + \tau_{nr}^{-1} \tag{2.31}$$

The internal quantum efficiency is given by:

$$\eta_{IQE} = \frac{\tau_r^{-1}}{\tau_r^{-1} + +\tau_{nr}^{-1}} \tag{2.32}$$

Not all photons emitted internally are able to escape from the semiconductor due to reflection problems and reabsorption mechanisms in the substrate.

In the next section, the electrical properties of LEDs will be presented, in order to better understand the mechanisms that cause the reduction of the efficiency in these devices.

2.4 Electrical properties of LEDs

The basic structure of an LED is the p-n junction. In this section we will explain the principal electrical properties of a diode, analyzing the structure and the current-voltage (IV) characteristic, considering also the non-ideal case.

2.4.1 P-n junction

The p-n junction is one of the most important junctions in solid state electronic. It is made by two semiconductors, one of p-type and the other one of n-type, put together. Then, a metal contact is put on both the two semiconductors in order to have the anode and the cathode.

Let's consider an abrupt p-n junction, that means the transition from the n-type material to the p-type material is abrupt, obtained by a step variation in the doping at the junction sides. The donor concentration is N_D and the acceptor concentration is N_A. All dopants are assumed to be fully ionized, thus the free electron concentration is $n = N_D$, while the free hole concentration is $p = N_A$. Finally, is assumed that no compensation of the dopants occurs by unintentional impurities and defects.

The big difference in the electron concentration in the two materials causes the electrons diffusion from the n-side to the p-side and the holes diffusion from the p-side to the n-side. Moving to the material with the opposite doping, carriers leave behind them doping atoms not compensated, near the junction, giving birth to the depletion of electrons in this region. This last region is called depletion region. Without electrons in the depletion region, the only present charge is given by ionized acceptors and donors. In this region it is assumed that the semiconductor can be divided in two distinct zone, one on the n-side where donors dispose, the other one on the p-side, where acceptor dispose, like Figure 2.5 reports.

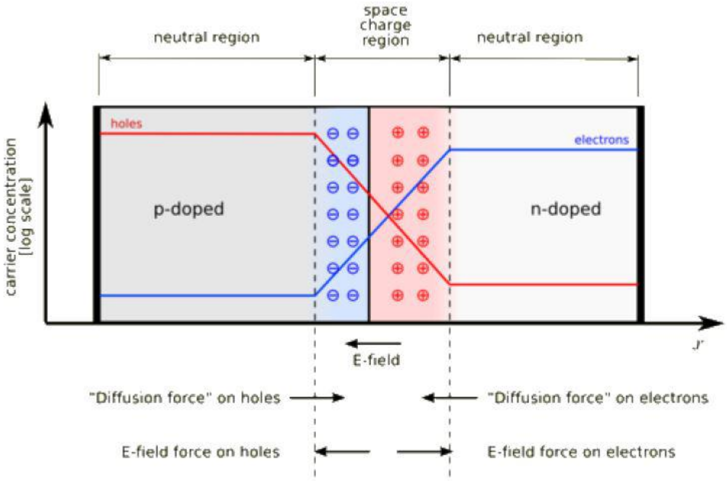

Figure 2.5: p-n junction, where the depletion region is shown.

An electric field is associated to the depletion region, called built-in, that creates a potential barrier between the two materials. At equilibrium, the electric field amplitude is such that the electrons trend to diffuse from the n-side to the p-side is balanced from the drift trend of the electrons in the opposite direction under the electric field influence. The built-in electric field generates a voltage defined as diffusion voltage, given by:

$$V_D = \frac{kT}{q} \ln \frac{N_A N_D}{n_i^2} \tag{2.33}$$

This voltage represents the barrier that the free carriers need to pass in order to reach the neutral region with the opposite conductivity. Figure 2.6(a) reports the band diagram of a p-n junction under zero bias and shows the diffusion voltage.

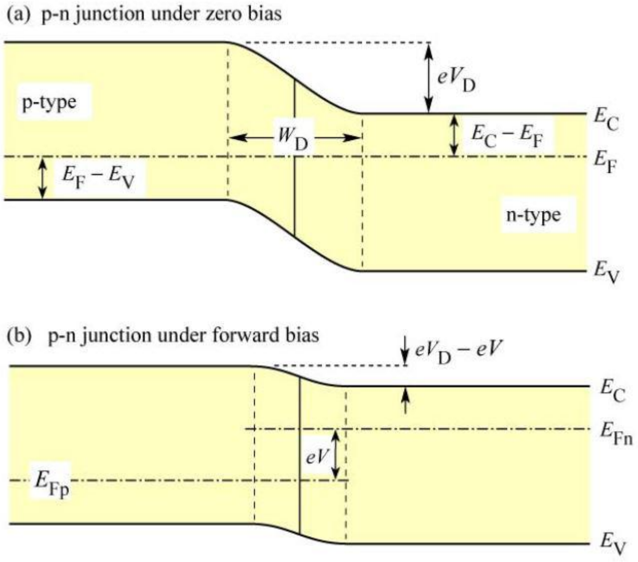

Figure 2.6: Band diagram of a p-n junction under zero bias (a) and under forward bias (b). Under forward bias conditions, minority carriers diffuse into the neutral regions where they recombine [19].

From the diffusion voltage, it is possible to extrapolate the width of the depletion region: in fact, these two quantities, together with the charge in the depletion region, are bound together by the Poisson equation. The width of the depletion region is:

$$W_D = \sqrt{\frac{2\varepsilon}{q}\left(\frac{1}{N_A} + \frac{1}{N_D}\right)(V_D - V)} \tag{2.34}$$

where $\varepsilon = \varepsilon_r \varepsilon_0$ is the dielectric permittivity of the semiconductor and V is the diode polarization voltage.

In general, two types of currents flow through the diode and these are the drift current and the diffusion current of the electrons and holes. When no voltage is applied, these two currents eliminate each other. In fact, considering as an example the hole current density:

$$J_p(x) = q\left[\mu_p p(x)E(x) - D_p\frac{dp(x)}{dx}\right] = 0 \tag{2.35}$$

where the first term represents the hole drift current, $J_{p_{drift}} = q\mu_p p(x)E(x)$, due to the electric field, instead the second term is the diffusion current, $J_{p_{diff}} = qD_p\frac{dp(x)}{dx}$, due to the hole concentration gradient in the p-type region. Similar considerations can be done for electrons.

If a voltage is applied to the p-n junction, it is possible to observe a potential drop on the depletion region. This region is highly resistive, since it is depleted of free carriers, and for this reason the voltage drop will be entirely on this region. If an external reversed bias voltage is applied, this will cause an increase in the potential barrier, blocking the carrier injection. Instead, applying an external forward voltage (Figure 2.6(b)), the potential barrier will decrease, promoting the carrier injection and causing an increase in the total current. Carriers diffusing in region with opposite type of conductivity will recombine giving place to a photon emission.

2.4.2 I-V characterisitc

The first who studied I-V characteristic of a p-n junction was Shockley, from which it derives the equation that describes the diode I-V curve, that is the Shockley equation:

$$I = I_S(e^{qV/kT} - 1) \tag{2.36}$$

where I_S is defined as saturation current

$$I_S = qA\left(\sqrt{\frac{D_p}{\tau_p}}\frac{n_i^2}{N_D} + \sqrt{\frac{D_n}{\tau_n}}\frac{n_i^2}{N_A}\right) \tag{2.37}$$

A is the diode area, while $D_{n,p}$ and $\tau_{n,p}$ are the diffusion constants and minority carrier lifetimes of electrons and holes, respectively. Equation 2.36 can be rewritten:

$$I = qA\left(\sqrt{\frac{D_p}{\tau_p}}\frac{n_i^2}{N_D} + \sqrt{\frac{D_n}{\tau_n}}\frac{n_i^2}{N_A}\right)(e^{qV/kT} - 1) \tag{2.38}$$

Under typical forward bias conditions, where the applied voltage is $V \gg kT/q$ in order to have $[\exp(qV/kT) - 1] \approx \exp(qV/kT)$, equation 2.38 becomes:

$$I = qA\left(\sqrt{\frac{D_p}{\tau_p}}N_A + \sqrt{\frac{D_n}{\tau_n}}N_D\right)e^{q(V-V_D)/kT} \tag{2.39}$$

From equation 2.39 we can notice that current increases significantly when the diode voltage is close to the value of the diffusion current, and for this reason it is defined as threshold voltage $V_{th} \approx V_D$.

Considering the band diagram of the p-n junction under forward bias (Figure 2.6(b)), it is evident the separation of the Fermi level from the conduction and valence band. For this reason, the following sum of energies is zero:

$$qV_D - E_g + (E_F - E_V) + (E_C - E_F) = 0 \tag{2.40}$$

In heavily doped semiconductor, this separation is very small with respect to the energy gap and for this reason equation 2.40 becomes:

$$V_{th} \approx V_D \approx \frac{E_g}{q} \tag{2.41}$$

that is an approximate value of the threshold voltage.

Figure 2.7 reports the forward voltage at a current of 20 mA as function of the energy gap for LEDs with different emission wavelength, in the range from the ultraviolet to the infrared. The solid line represents the expected forward diode voltage. Analyzing the figure, it is possible to observe that LEDs based on III-V nitrides do not follow the line. This is caused by different factors: (i) nitride material system presents large band gap discontinuities, which cause an additional voltage drop; (ii) the contact technology is not yet completely mature in nitride-based structures, which causes an additional voltage drop at the ohmic contacts; (iii) the low p-type conductivity in bulk GaN; (iv) it is possible that a negative parasitic voltage drop occurs in the n-type buffer layer.

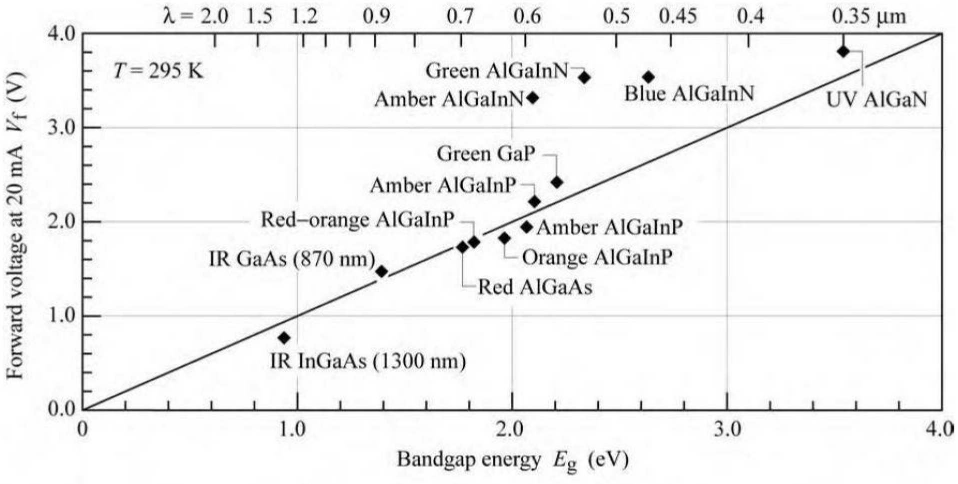

Figure 2.7: Diode forward voltage as function of energy gap for LEDs made by different materials [19].

2.4.3 Non ideality in the I-V characteristic

The Shockley equation gives us the first theoretical I-V characteristic for a p-n junction, but in order to describe the experimentally measured characteristics, the equation becomes:

$$I = I_S e^{qV/(\eta_{ideal} kT)} \tag{2.42}$$

where η_{ideal} is the ideality factor of the diode. For an ideal diode this factor is equal to 1, but for a real diode η_{ideal} can assume values between 1.1 - 1.5, though higher values have been found for III-V arsenide and phosphide diodes (2.0) and for GaN/InGaN diodes (7.0).

Another unwanted effect in a real diode is the presence of parasitic resistances, in particular the series resistance and the parallel resistance. The first one could be ascribed to an excessive contact resistance or the resistance of the neutral regions, instead, the second one can be caused by any parasitic channel through the p-n junction. This last condition can be ascribed to the degradation of the p-n junction or to the generation of surface defects. Figure 2.8 reports the effects on the I-V characteristic due to these parasitic resistances. In order to take in account these, it is necessary to modify the Shockley equation.

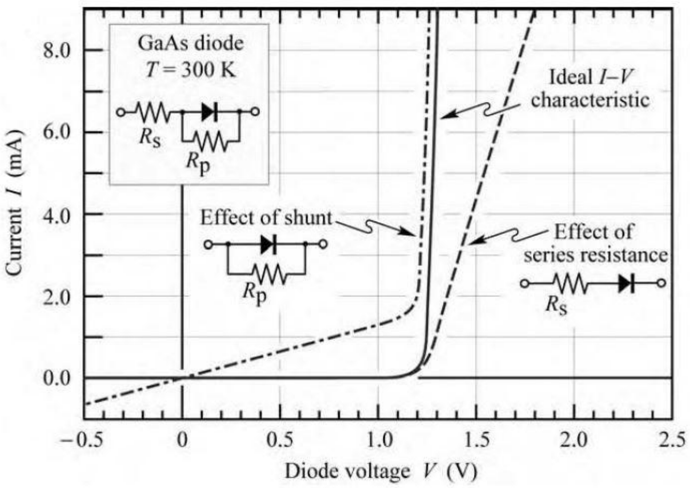

Figure 2.8: Effect of series and parallel resistance on the I-V characteristic [19].

Assuming to have a shunt resistance R_P, parallel to the ideal diode, and a series resistance R_S, in series with the ideal diode and R_P, the relation between the current and the voltage becomes:

$$I - \frac{(V - IR_S)}{R_P} = I_S e^{q(V-IR_S)/(\eta_{ideal} kT)} \tag{2.43}$$

There are further deviations of the I-V curve from the ideal conditions, that are not taken into account in equation 2.43. One of this is the abrupt turn-on of the diode, referred as sub-threshold turn-on or premature turn-on: in some conditions, the diode turn-on voltage is distributed over a voltage range instead of having a precise value. In this way, a sub-threshold current is observed before the hypothetic turn-on voltage. This current can be caused by carrier transport through surface states or deep levels in the semiconductor bulk.

Carrier generation and recombination in the depletion region are two other important events that can occur in real diodes, due to the presence of trap levels in this region (Figure 2.9). This implies an increase in the current when a forward and a reversed voltage is applied. The recombination current dominates at low voltages and an ideality factor of 2.0 is associated to this current, instead the diffusion current dominates at high voltages and presents an ideality factor equal to 1.0. From Figure 2.10, we can distinguish three main region in the I-V characteristic, from these the two regions related to the generation and recombination current.

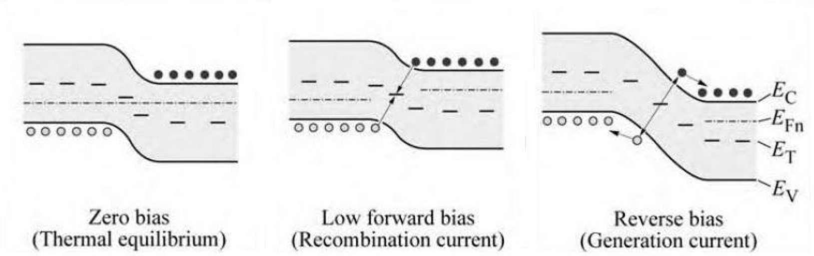

Figure 2.9: Effect of carrier generation and recombination in the depletion region.

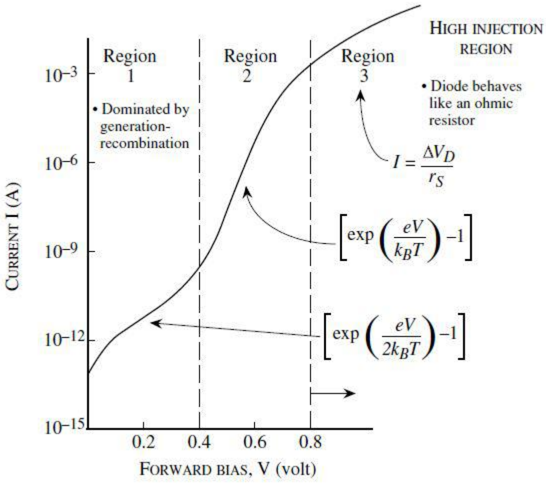

Figure 2.10: Diode current in forward voltage. The generation current dominates in the first region, the diffusion current dominates in the second, instead in the third region the current presents a resistive behavior [63].

When a reversed bias is applied, current is dominated by carrier generation in the depletion region; this current increases if a higher reverse voltage is applied, due to the increase in the depletion region width.

I-V measurements are carried out in the dark, since light may generate photocurrent in the diode. There should be no photocurrent in dark conditions, but a very small value is always measured (such 10^{-12} A), due to the limited accuracy of the instruments.

2.4.4 Carrier distribution in homojunction and heterojunction

Until now, p-n homojunctions were considered, that means p-n junctions consisting of a single material. In these p-n junctions, the carrier distribution depends on the diffusion constant of carriers, that can be inferred from the mobility thanks to the Einstein relation, which, for a non-degenerate semiconductor is given by:

$$D_n = \frac{kT}{q}\mu_n \quad \text{and} \quad D_p = \frac{kT}{q}\mu_p \tag{2.44}$$

Carriers injected into a semiconductor, with no external electric field applied, propagate by diffusion. Carriers will pass through the depletion region and will reach the region with opposite conductivity where they will eventually recombine. The mean distance a minority carrier diffuses before recombination is the diffusion length. Diffusion lengths for electrons and holes are

$$L_n = \sqrt{D_n \tau_n} \quad \text{and} \quad L_p = \sqrt{D_p \tau_p} \tag{2.45}$$

where τ_n and τ_p are the electron and hole lifetimes, respectively. In typical semiconductors, the diffusion length is in the order of several micrometers, since the minority carriers are distributed in a region several micrometers thick. In Figure 2.11 the carrier distribution in a p-n junction under zero bias (2.11(a)) and forward bias (2.11(b)) is shown. Minority carriers are distributed over a large distance, thus recombination occurs over a large region and this is not beneficial for an efficient recombination.

The typical structure used, in order to realized high-intensity LEDs, is the heterojunction. In these devices, two type of semiconductor are used, one with a small bandgap, that will be the active region, and another one with a large bandgap, that will be the barrier region. It is possible to realize a structure with two barriers, i.e. an active region enclosed between two large-bandgap semiconductors: in this case, the structure is called double heterojunction. Figure 2.12 reports the band diagram of a double heterojunction and its carrier distribution: in this case, the injected carriers are confined within the active region by the barriers. The active region will define the thickness of the region in which carriers recombine, rather than the diffusion length. Usually the length of the active region is smaller than the diffusion length, and this

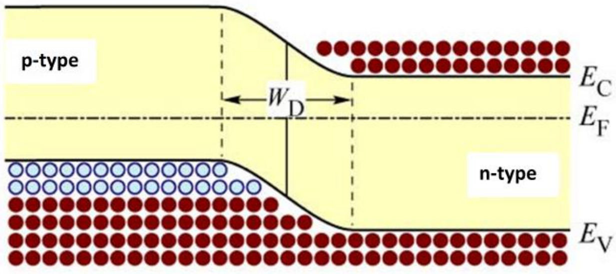

(a)

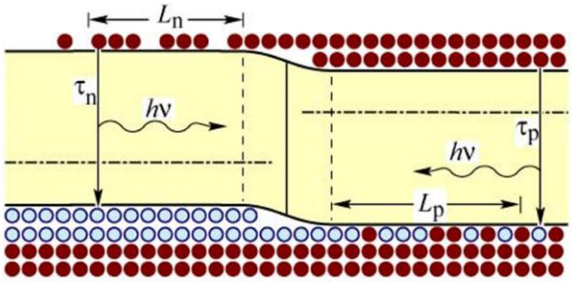

(b)

Figure 2.11: Carrier distribution in a p-n homojunction under zero bias (a) and forward bias (b) [19].

allows an increase in the carrier concentration with respect to the homojunction case. Moreover, since the radiative recombination rate is given by $R = Bnp$, having a high carrier concentration in the active region allows an increase in the radiative recombination rate.

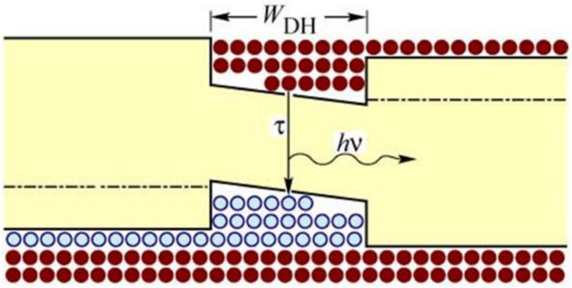

Figure 2.12: Carrier distribution in a double heterojunction under forward bias [19].

2.4.5 Heterojunctions characteristics

Using heterojunction in order to realize LEDs allows to better improve the performances of these devices, thanks to the carrier confinement in the active region and avoiding the minority carrier diffusion on long distances. The double heterojunction introduces a potential well where carriers are trapped and, if the well is narrow, the allowed energy levels within it are quantized. The structure is called quantum well (QW) (Figure 2.13).

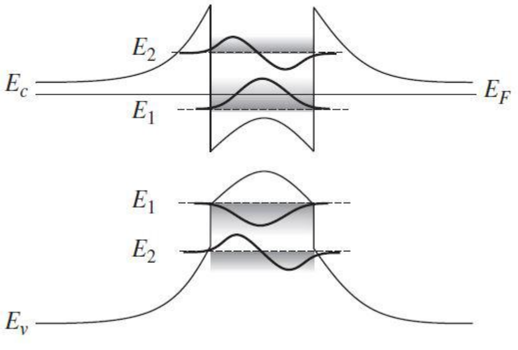

Figure 2.13: Quantized energy level in a quantum well, where the carrier wave functions are shown.

Carriers behavior in QWs is described by Schrödinger, which solution allows to evaluate the energy levels and the sub-bands, giving the potential profile of the well. Despite the heterostructures contribute to the improvement of the LEDs efficiency, however, there are still several problems. In the following sections, the main mechanisms that contribute to reducing efficiency and the possible structure optimizations to limit these loss mechanisms are reported.

Effect of heterojunctions on device resistance

As already mentioned before, the employment of heterostructures allows to improve the efficiency of LEDs by confining carriers into the active region; the heterostructures can be used to confine light to waveguide regions. Modern LEDs present many heterojunctions. One of the problems that the heterojunction introduces is the resistance at the heterostructure interface. Considering a heterostructure made by two semiconductors with different band-gap and assuming both of n-type, there will be the diffusion of carriers from the large-bandgap material to the small-bandgap material. As a result of this transfer, an electrostatic dipole will be formed, followed by a band bending, as Figure 2.14(a) shows. Carriers transferring from one semiconductor to the other must overcome this barrier by either tunneling or by thermal emission over the barrier. The thermal power generated from this resistance leads to a reduction in the radiative efficiency, since it causes the heating of the active region.

This kind of structure is obtained when the passage from a material to another is abrupt. A way to eliminate these barriers is to make graded heterojuncton, changing

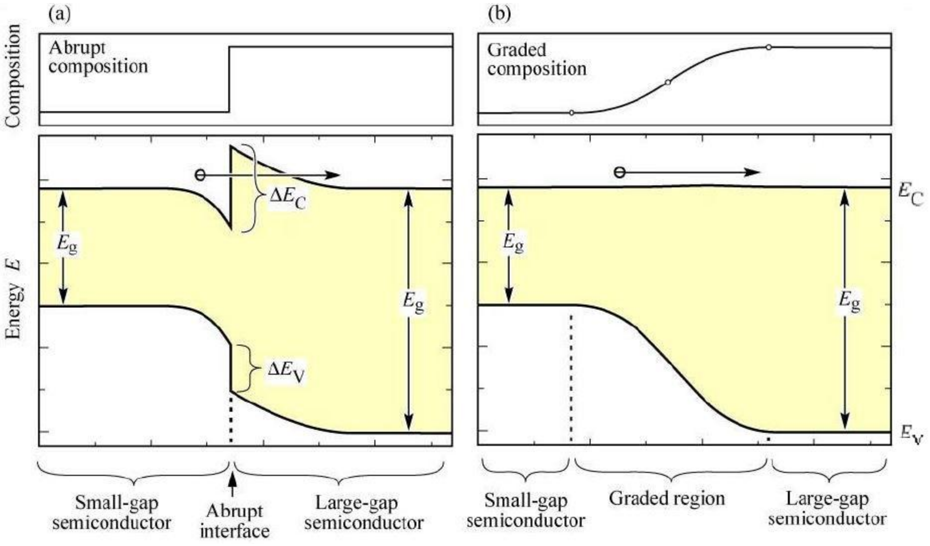

Figure 2.14: Band diagram of an abrupt heterojunction (a) and a graded one (b) of two n-type semiconductors with different bandgap energy [19].

the chemical composition of the semiconductor in the proximity of the interface, as shown in Figure 2.14(b). It has been shown that, the shape of the graded region should be parabolic: in this way, the large-bandgap material will be depleted of free carriers due to electron transfer to the small-bandgap material. For this reason, the carrier concentration in the first material will be equal to the donor concentration N_D. Assuming that this concentration is constant, the electrostatic potential is:

$$\Phi = \frac{qN_D}{2\varepsilon}x^2 \tag{2.46}$$

The equation shows that the potential depends on the position x with a parabolic shape. In order to compensate for the parabolic shape of the depletion potential, the composition of the semiconductor is varied parabolically as well, so that an overall flat potential results, assuming that the bandgap energy depends linearly on the chemical composition. An approximate design rule for the grading of a heterostructure is given by:

$$x_d = \sqrt{\frac{2\varepsilon \Delta E_C}{q^2 N_D}} \tag{2.47}$$

where x_d is the depletion region thickness in the large-bandgap semiconductor and ΔE_C is the discontinuity of the conduction band of the abrupt heterojunction. The heterostructure interface should be graded over the distance x_d in order to minimize the resistance at the interface.

Carrier escape

In an ideal LED, the injected carriers should be confined within the active region thanks to the presence of the lateral barriers. The energy barriers are usually in the order of several hundred meV, i.e. much larger than kT. Despite this, some carriers will be able to escape from the QW, moving in the barrier regions. In fact, free carriers in the active region are distributed according to the Fermi-Dirac distribution, thus some carriers could have higher energy than the height of the confining barrier. This mechanism is shown in Figure 2.15. This carrier escape causes the recombination in the barrier regions, reducing the radiative recombination. The concentration of electrons with energy higher than the barriers is given by:

$$n_B = \int_{E_B}^{\infty} \rho_{DOS} f_{FD}(E) dE \tag{2.48}$$

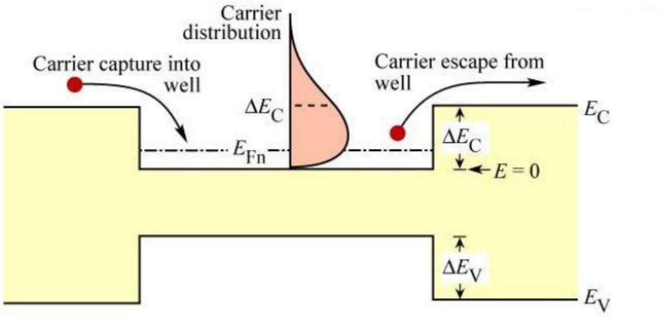

Figure 2.15: Capture and escape of one carrier in a double heterojunction. The figure shows also the carrier distribution in the active region [19].

where ρ_{DOS} is the state density, f_{FD} is the Fermi-Dirac distribution function, and E_B is the height of the barrier.

The electron loss over the barrier generates a leakage current that depends on the carrier concentration at the edge of the barrier. This leakage increases exponentially with the temperature, causing a decrease of the radiative efficiency.

Carrier overflow

Carrier overflow is another loss mechanism that occurs at high injection current densities. In this way, the carrier concentration in the active region increases, followed by an increase in the Fermi level; the latter will rise to the top of the barrier and when it will be within the conduction band, the semiconductor will be in degeneration condition

(Figure 2.16). At this point, the active region is flooded with carriers, causing a saturation of the optical intensity, since a further increase in injection current density will not increase the concentration in the active region. Carriers are now able to overcome the quantum well, as Figure 2.17 shows.

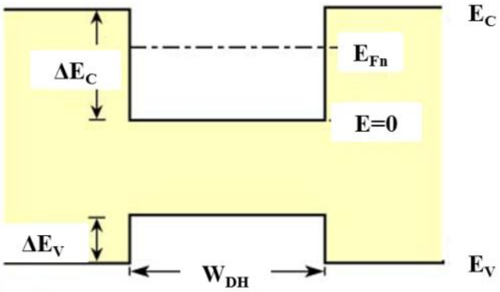

Figure 2.16: Fermi level in a double heterostructure [19].

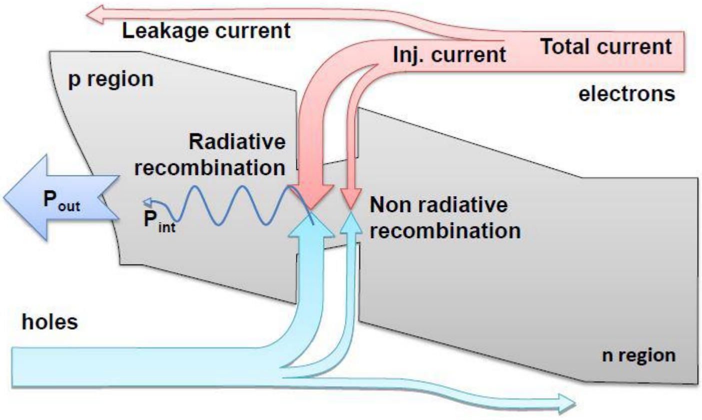

Figure 2.17: Carrier overflow in a double heterostructure.

The current density at which the active region overflows can be obtained as follows. Consider a double heterostructure LED with an active region of thickness W_{DH}, the equation that describes the variation of the electron concentration in the active region is:

$$\frac{dn}{dt} = \frac{J}{qW_{DH}} - Bnp \tag{2.49}$$

This equation is given by two terms, one is due to the electron injection in the active region, the other one is given by the recombination. Solving the equation in steady state conditions, i.e. $dn/dt = 0$, and in high injection conditions, i.e. $n = p$, we obtain:

$$n = \sqrt{\frac{J}{qBW_{DH}}} \tag{2.50}$$

In high-density approximation, the Fermi energy is given by:

$$\frac{E_F - E_c}{kT} = \left(\frac{3\sqrt{\pi}}{4}\frac{n}{N_C}\right)^{2/3} \tag{2.51}$$

When the Fermi level reaches the top of the barrier, no more carriers will be confined. At that point $E_F - E_C = \Delta E_C$. Using this value, the current density at which the active region overflows is:

$$J = qW_{DH}Bn^2 = \left(\frac{4}{3}\frac{N_C}{\sqrt{\pi}}\right)^2 \left(\frac{\Delta E_C}{kT}\right)^3 qBW_{DH} \tag{2.52}$$

In general, this problem is more severe in structures with a small active region volume, like single quantum well structures and quantum dot active regions. A possible solution is the realization of structures with multiple quantum wells (MQWs). In fact, as reported in Figure 2.18, as the number of quantum well is increased, the current level at which saturation occurs is increased, together with the optical saturation intensity.

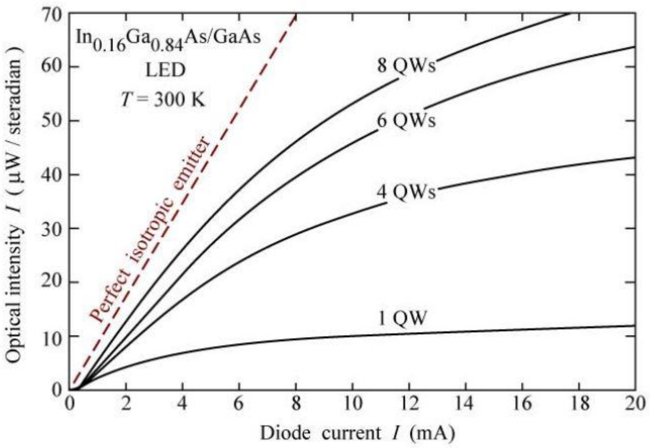

Figure 2.18: Optical intensity as function of the diode current varying the number of quantum wells [19].

Another possibility is to increase the height barrier ΔE_C, but this requires the employment of material with appropriate band gap. It is also possible to realized a quantum well with a larger thickness, but this solution is rare.

Electron blocking layer

The carrier escape from the active region has a strong impact in double heterostructures with low barrier height. Moreover, since the diffusion constant of electrons in semiconductor III-V is higher than the one of holes, the electron leakage current will be higher than the hole leakage current. To reduce carrier leakage, carrier-blocking layers are used: these structures are called electron blocking layers (EBL). These layers present a high band gap energy and are located at the confinement-active interface, i.e. at the interface between the active region and the barrier region on the p-side. In order to not obstruct the passage of holes coming from the p-type region, the EBL will be doped. Figure 2.19 shows an example of band diagram of an InGaN-based LED with an AlGaN-based EBL and an active region made by InGaN/GaN MQWs. The insert shows the presence of a potential spike (hole depletion layer in the electron blocker) and notch (hole accumulation layer in the p-type confinement layer), forcing holes to tunnel through the potential spike in order to reach the active layer. The valence band edge can be completely smoothed out by compositional grading at the interface between the EBL and the barrier layer so that the EBL does not impede the hole flow. The total band discontinuity is located in the conduction band, that means

$$\Delta E = E_{C,confinement} - E_{C,active} + \Delta E_g \tag{2.53}$$

where ΔE is the barrier height for electrons and ΔE_g is the difference in band gap energy between the barrier layer and the EBL.

Diode voltage

When an electron is injected, its energy is converted into optical energy upon electron-hole recombination. The drive voltage or forward voltage is given by the ratio between the band gap energy and the elementary charge

$$V = h\nu \approx E_g/q \tag{2.54}$$

There are some mechanisms that can cause a voltage variation. A first mechanism is the presence of a series resistance: this can be due to a contact resistance, by abrupt heterostructures and by bulk resistance, occurring particularly in materials with low carrier concentration or low carrier mobilities. A second mechanism is related to the energy loss of carriers due to non-adiabatic injection, as shown in Figure 2.20. An electron injected in the quantum well can lose an energy equal to $\Delta E_C - E_0$, where

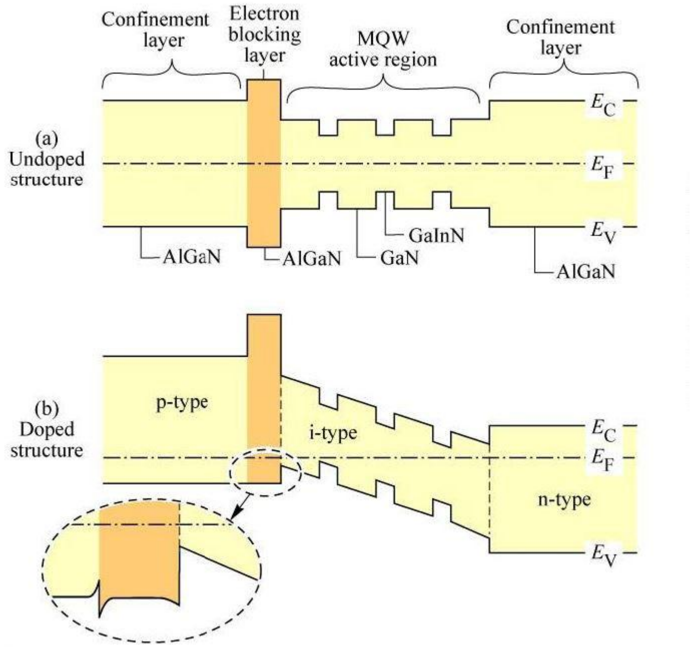

Figure 2.19: Band diagram of an LED with a MQWs structure, with (a) and without (b) doping [19].

ΔE_C is the band discontinuity and E_0 is the energy of the lowest quantized state in the conduction band. Similar consideration can be made for holes.

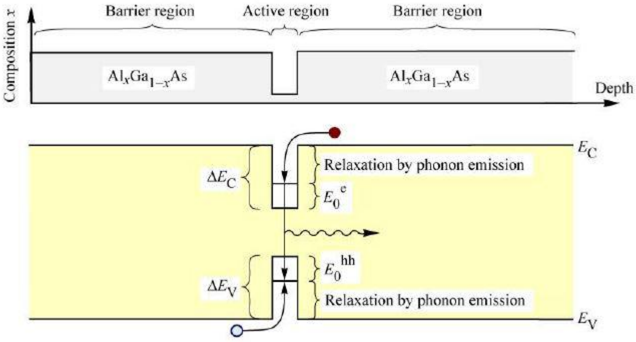

Figure 2.20: Chemical composition and band diagram of a quantum well structure. The figure shows the energy loss of carriers as they are captured into the quantum well [19].

The total voltage drop across the LED is:

$$V = \frac{E_g}{q} + IR_S + \frac{\Delta E_C - E_0}{q} + \frac{\Delta E_V - E_0}{q} \tag{2.55}$$

where E_g/q is the theoretical voltage minimum, IR_S is the contribution due to the series resistance and $(\Delta E_C - E_0)/q + (\Delta E_V - E_0/q)$ is the contribution due to the adiabatic injection.

2.5 Optical properties of LEDs

In this section, the optical properties of LEDs will be discussed. In particular, the emission spectrum, the optical power-current characteristic and different ways in order to improve the light extraction will be discussed. First, it is important to define the efficiencies in a LED.

2.5.1 LED efficiency

The internal quantum efficiency is defined as the ratio between the number of photons emitted from the active region per second and the number of injected electrons per second, that means:

$$\eta_{IQE} = \frac{P_{int}/h\nu}{I/q} \tag{2.56}$$

where P_{int} is the optical power emitted from the active region and I is the injected current. An ideal LED has unity internal quantum efficiency, since each injected electron produces a photon. In a real LED, this is not possible, due to the presence of non-radiative recombination processes, already explained.

The extraction efficiency is defined as the ratio between the number of photons emitted outside the LED per second and the number of photons emitted from the active region per second:

$$\eta_{ext} = \frac{P/(h\nu)}{P_{int}/(h\nu)} \tag{2.57}$$

where P is the optical power emitted into free space. In an ideal LED, all the photons emitted from the active region are able to escape from the LED die, having an unity extraction efficiency. In a real LED not all the power emitted from the active region is emitted in the free space: in fact, some photons may not escape from the semiconductor due to several loss mechanisms, that will be discussed in the next paragraphs. In general, the extraction efficiency can strongly limit the LED performances.

The external quantum efficiency (EQE) is defined as the ration between the number of photons emitted outside the LED per second and the number of electrons injected into the LED per second:

$$\eta_{EQE} = \frac{P/(h\nu)}{I/q} = \eta_{IQE} \cdot \eta_{ext} \tag{2.58}$$

The power efficiency is defined as:

$$\eta_{power} = \frac{P}{IV} \tag{2.59}$$

where IV is the electrical power provided to the LED.

2.5.2 Emission spectrum

The spontaneous recombination of electron-hole pairs is the physical mechanism responsible for the light emission from a LED. The energy obtained from this process is transferred to a photon. The optical properties of LEDs are determined by the physical mechanism of spontaneous emission. Figure 2.21 reports a schematic of the electron-hole pair recombination process. The electron and hole energy distributions are defined by the Fermi statistic: at a temperature above the absolute zero, electrons and holes will occupy a certain number of energy state higher than the minimum value. Electrons and holes are assumed to have a parabolic dispersion relation:

$$E = E_C + \frac{\hbar^2 k^2}{2m_e^*} \tag{2.60}$$

for electrons, instead

$$E = E_V - \frac{\hbar^2 k^2}{2m_h^*} \tag{2.61}$$

for holes. m_e^* and m_h^* are defined as the effective masses of electron and hole, respectively, $\hbar$ is the Planck constant divided by 2π, k is the carrier wave number, and E_C and E_V are, respectively, the conduction and valence band edges.

Energy conservation is required and for this reason the photon energy will be given by the difference between the electron energy E_e and the hole energy E_h. Electrons and holes present an average kinetic energy equal to kT and since $kT \ll E_g$, the photon energy will be approximately equal to the bandgap energy E_g:

$$h\nu = E_e - E_h \approx E_g \tag{2.62}$$

For this reason, the emission wavelength of a LED is determined by choosing a semiconductor material with an appropriate band gap energy.

Together with energy conservation, momentum conservation is required. Compar-

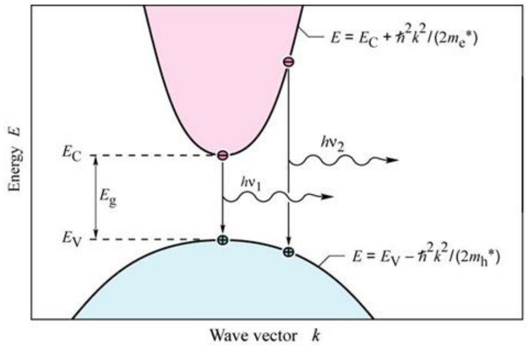

Figure 2.21: Parabolic dispersion relation for electrons and holes: figure shows the vertical recombination between an electron and a hole with the emission of a photon [19].

ing the momentum of a photon, $p = \hbar k = h\nu/c = E_g/c$, with the average carrier momentum, $p = \sqrt{2m^* kT}$, yields that the carrier momentum is orders of magnitude larger than the photon momentum. In this way, during a transition from the conduction to the valence band, the electron momentum does not change significantly. The transitions are therefore "verticals", i.e. electrons will recombine only with holes that have the same value of k. Assuming that electrons and holes momentum are equal, the photon energy can be rewritten as:

$$h\nu = E_C + \frac{\hbar^2 k^2}{2m_e^*} - E_V + \frac{\hbar^2 k^2}{2m_h^*} = E_g + \frac{\hbar^2 k^2}{2m_r^*} \tag{2.63}$$

where m_r^* is the reduced mass given by:

$$\frac{1}{m_r^*} = \frac{1}{m_e^*} + \frac{1}{m_h^*} \tag{2.64}$$

Equation 2.63 is defined as joint dispersion relation and using it, the joint density of states can be calculated:

$$\rho(E) = \frac{1}{2\pi^2}\left(\frac{2m_r^*}{\hbar^2}\right)^{3/2} \sqrt{E - E_g} \tag{2.65}$$

The Boltzmann distribution is used to determine the distribution of carriers in the allowed bands:

$$f_B(E) = e^{-E/(kT)} \tag{2.66}$$

The emission intensity of an LED as function of the energy (Figure 2.22) is proportional to the product of equations 2.65 and 2.66:

$$I(E) \propto \sqrt{E - E_g} e^{-E/(kT)} \tag{2.67}$$

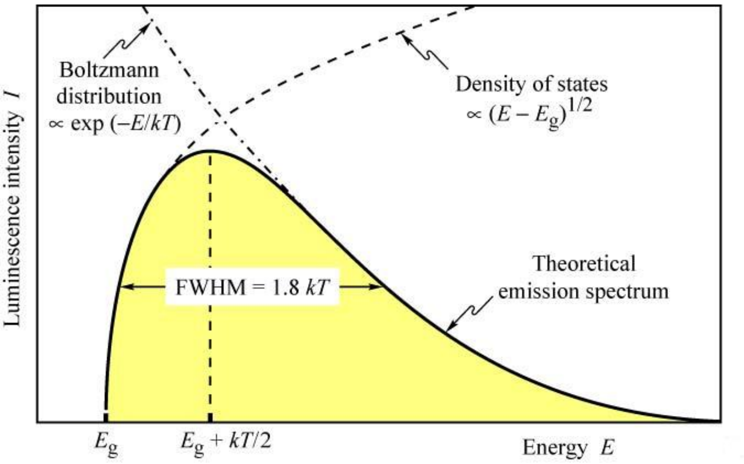

Figure 2.22: Theoretical emission spectrum of an LED [19].

From Figure 2.22 it is possible to observe that the maximum emission intensity occurs at:

$$E = E_g + \frac{1}{2}kT \tag{2.68}$$

and the full-width at half maximum (FWHM) of the emission is:

$$\Delta E = 1.8kT \tag{2.69}$$

or, in terms of wavelength:

$$\Delta\lambda = \frac{1.8kT\lambda^2}{hc} \tag{2.70}$$

The linewidth of an LED is relatively narrow compared with the range of the entire visible spectrum, even narrower than the spectral width of a single color as perceived by the human eye. For this reason, the LED emission is perceived by the human eye as a monochromatic source.

2.5.3 L-I characterisitc

The optical power-current characteristic will be analyzed. Knowing the connection between these two magnitudes is useful in order to obtain information regarding recombination mechanisms at a certain current level. Using the ABC model, where

- B is the bimolecular recombination coefficient;
- A is the non radiative recombination coefficient due to SRH processes;
- C is the Auger recombination coefficient;

under steady state conditions, the rate equation for the LED is:

$$\frac{dn}{dt} = \frac{J}{qd} - (Bnp + AN_T n) = 0 \tag{2.71}$$

where J is the current density through the active region, d is the active region width, N_T is the density of non-radiative recombination centers, and p and n are the electron and hole concentrations in the active region, respectively.

Under high injection conditions, where $n \gg N_a, N_d$, the previous equation becomes:

$$Bn^2 + AN_T n - \frac{J}{qd} = 0 \tag{2.72}$$

In case the radiative recombination dominates on the non-radiative recombination processes, i.e. $AN_T n \ll Bn^2$, we get

$$L = Bn^2 \approx \frac{J}{qd} \tag{2.73}$$

where L is the light intensity, since Bn^2 is related to the radiative recombination. In the other case, where the non-radiative recombination processes dominates on the radiative recombination, i.e. $AN_T n \gg Bn^2$, we get

$$AN_T n = \frac{J}{qd} \tag{2.74}$$

In this case, since n is proportional to the injected current, the light intensity (Bn^2) is proportional to the square of the injected current ($L \sim J^2$).

Figure 2.23 reports the L-I characteristic, where we can distinguish two regions:

- in the first region, the non-radiative recombination dominates; the light intensity has a square dependence on current, but since the latter is very low, the emitted light is low;
- in the second region, the radiative recombination dominates, and the relation between the optical power and the current is linear.

For very high current levels, the relation between the light intensity and the current will result in a sub-linear trend, since the Auger recombination will start to participate.

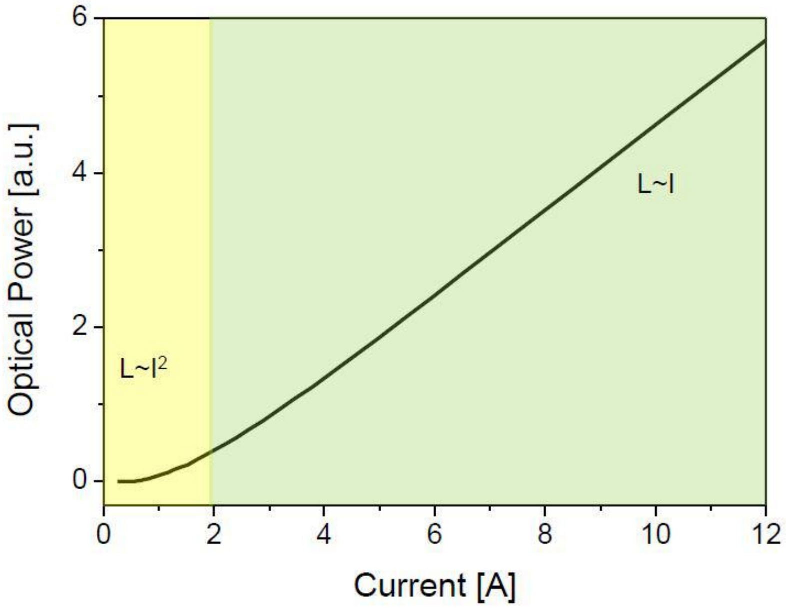

Figure 2.23: L-I characteristic of an LED.

2.5.4 Light extraction

As already explained, the photon extraction can be a limiting factor for LEDs performances, if no good encapsulations are realized. Considering an LED with a simple planar heterostructure, photons are emitted from the active region with different angles of incidence. If the angle of incidence is close to normal incidence, light can escape from the semiconductor. However, if a photon arrives at the semiconductor-air interface with oblique or grazing-angle incidence, total internal reflection can occur, which reduces significantly the external efficiency, in particular for LED made with high-refractive-index materials.

Defining ϕ the angle of incidence in the semiconductor at the semiconductor-air interface, by means of the Snell law, the angle of incidence of the refracted ray Φ can be inferred:

$$\bar{n}_s \sin\phi = \bar{n}_{air} \sin\Phi \tag{2.75}$$

where $\bar{n}_s$ and $\bar{n}_{air}$ are the refractive indices of the semiconductor and air, respectively. The critical angle for total internal reflection is defined as the angle beyond which the photons are completely reflected, as shown in Figure 2.24(a). In order to calculate it, we set $\Phi = 90°$ in the Snell law

$$\sin\phi_c = \frac{\bar{n}_{air}}{\bar{n}_s}\sin 90^\circ = \frac{\bar{n}_{air}}{\bar{n}_s} \tag{2.76}$$

from which we obtain:

$$\phi_c = \arcsin\frac{\bar{n}_{air}}{\bar{n}_s} \approx \frac{\bar{n}_{air}}{\bar{n}_s} \tag{2.77}$$

where this last approximation is valid since the refractive indeces of semiconductors are quite high (for example GaAs has a refractive index of 3.4).

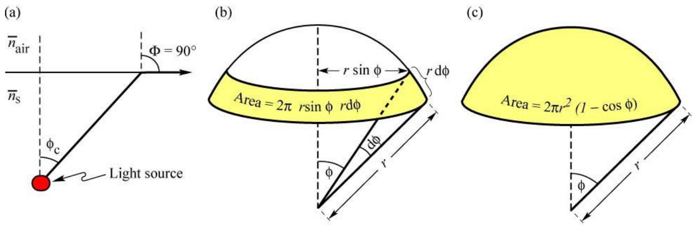

Figure 2.24: Definition of the critical angle (a), area element dA (b), and area of calotte-shaped section of the sphere (c) [19].

The angle of total internal reflection defines the light escape cone: light emitted into the cone can escape from the semiconductor, whereas light emitted outside the cone is subject to total internal reflection. It is possible to calculate the number of photons that are able to escape from the semiconductor that means the total fraction of light emitted into the light escape cone. The escape cone is projected in three dimensions: the spatial distribution of photons can be represented by means of a calotte-shaped surface with amplitude lower than the critical angle. Figure 2.24(c) shows the surface area of the calotte-shaped surface, defined as:

$$A = \int dA = \int_{\phi=0}^{\phi_c} 2\pi r\sin(\phi) r d\phi = 2\pi r^2(1-\cos\phi_c) \tag{2.78}$$

In order to calculate the emission efficiency, it will be necessary to calculate the ration between the area of the calotte-shaped section of the sphere and the total area of the sphere. Assuming that light is emitted from a point-like source in the semiconductor with a total power of P_{source}, then the power that can escape from the semiconductor is given by:

$$P_{escape} = P_{source}\frac{2\pi r^2(1-\cos\phi_c)}{4\pi r^2} \tag{2.79}$$

where $4\pi r^2$ is the entire area of the sphere with radius r.

The fraction of light emitted that can escape from the semiconductor is:

$$\frac{P_{escape}}{P_{source}} = \frac{1}{2}(1 - \cos\phi_c) \tag{2.80}$$

The cosine term can be expanded into a power series, since the critical angle of total internal reflection for high-index materials is relatively small. Neglecting higher-than-second-order terms we obtain:

$$\frac{P_{escape}}{P_{source}} \approx \frac{1}{2}\left[1 - \left(1 - \frac{\phi_c^2}{2}\right)\right] = \frac{1}{4}\phi_c^2 \approx \frac{1}{4}\frac{\bar{n}_{air}^2}{\bar{n}_s^2} \tag{2.81}$$

In many semiconductors, the refractive index is > 2.5, thus it is high enough so that only a small percentage of the light generated by the semiconductor manage to get out.

2.6 From LED to laser diode

Both the LED and the laser diodes (LDs) exploit radiative recombination of electron–hole pairs in a forward-biased junction to emit light, implying broad linewidth. However, LEDs are based on spontaneous emission, instead the dominant emission mechanism in lasers is stimulated emission: photons of a specific energy and wavenumber stimulate the emission of coherent photons: all electron-hole pairs recombine to generate coherent photons, and narrow linewidth results. Another important feature of laser diodes that differentiates it from an LED, is the presence of mirrors in order to keep stable the radiation field within the active region. In this section, the structure and the basic principles of LDs will be described.

2.6.1 Stimulated emission

The stimulated emission process is not ordinarily observed in nature. In this process, an electron in excited state relaxes to the ground state by the interaction of the electron with an incident photon. In this way, there will be two photons, both of which occupy the same quantum state. Photons obey to the Bose-Einstein statistics, in which the number of particles occupying a given energy state is not limited, in this way photons tends to accumulate in a particular energy state and if stimulated emission were to occur enough times, the number of photons occupying that particular energy state would be enormous. This is manifested in the phenomenon of coherence, i.e. light emitted from a laser exhibits coherence.

Stimulated emission competes with absorption (Figure 2.25): if the electron is in the ground state when the photon is incident, the photon will be absorbed and the electron excited. This will cause a reduction in the number of photons comprising the optical field. Usually, in thermal equilibrium, the number of electrons in the ground state far exceeds the number in the excited state: this will promote absorption. In order to promote stimulated emission, the population of the two states have to be inverted, i.e. there must be more electrons in the excited state than in the lower.

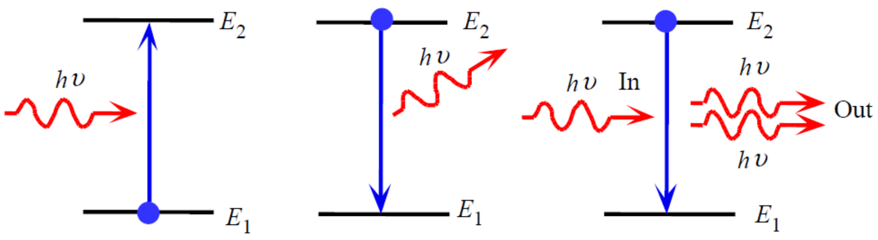

(a) Absorption (b) Spontaneous emission (c) Stimulated emission

Figure 2.25: Schematic of the absorption (a) and emission (b,c) processes.

The analytical relations on the process of absorption, stimulated emission and spontaneous emission where developed by Einstein. The Fermi-Dirac statistics describes the populations of two energy levels E_1 and E_2 ($E_2 > E_1$) in thermal equilibrium, but under certain conditions it is possible to use the Boltzmann approximations. The two population densities are then related by:

$$n_2 = n_1 e^{(E_1 - E_2/kT)} \tag{2.82}$$

and equilibrium is maintained by spontaneous and stimulated relaxation from the excited state to the ground state, with the emission of radiation. The rate of absorption of radiation which causes transitions between levels 1 and 2 in the body is:

$$R_{12} = B_{12} n_1 \rho(h\nu) \tag{2.83}$$

where B_{12} is the Einstein coefficient and $\rho(h\nu)$ is the energy density of photons per frequency unit. The rate of emission has both stimulated and spontaneous components, that means:

$$R_{21} = A_{21} n_2 + B_{21} n_2 \rho(h\nu) \tag{2.84}$$

where A_{21} is the Einstein coefficient for spontaneous emission and B_{21} is the coefficient for stimulated emission. In a simple two-level system, the energy of the upward transition is identical to the energy of the downward transition, so in thermal equilibrium $R_{12} = R_{21}$, hence:

$$\rho(h\nu) = \frac{A_{21}}{B_{12}e^{h\nu/kT} - B_{21}} \tag{2.85}$$

The energy density as function of frequency of photons at equilibrium is given by Planck's black body law:

$$\rho_{eq}(h\nu) = \frac{8\phi\nu^2}{c^3}\frac{h\nu}{e^{h\nu/kT} - 1} \tag{2.86}$$

From the previous equations we obtain:

$$B_{12} = B_{21} = B \quad \text{and} \quad \frac{A_{21}}{B_{21}} = \frac{8\pi h\nu^3}{c^3} \tag{2.87}$$

The ratio between stimulated emission and spontaneous emission is given by:

$$\frac{R_{21,stim}}{R_{21,spon}} = \frac{B_{21}N_2\rho(h\nu)}{A_{21}N_2} = \frac{B_{21}\rho(h\nu)}{A_{21}} \tag{2.88}$$

and using equation 2.88 it becomes:

$$\frac{R_{21,stim}}{R_{21,spon}} = \frac{c^3}{8\pi h\nu^3}\rho(h\nu) \tag{2.89}$$

Instead, the ration between stimulated emission and absorption is:

$$\frac{R_{21,stim}}{R_{12}} = \frac{n_2}{n_1} \tag{2.90}$$

From these two last equations we can say that, in order that the stimulated emission prevails over the spontaneous emission, a high photon density is needed; to have optical amplification (stimulated emission that prevails on absorption), the inversion of population is needed, that means $n_2 > n_1$. In general, population inversion cannot be achieved using the simple two-level system so far described. At best, the populations will be equal, so at least three levels are required to realize inversion.

A semiconductor with an inverted population behaves like a four-level system where the pumping is supplied by the current (Figure 2.26). If we assume that the only electrons that recombine are those at the bottom of the conduction band, then electrons injected at the quasi-Fermi level must lose kinetic energy in order to reach the band edge: this is achieved by the emission or absorption of phonons so that both energy and momentum are lost to the lattice. The electrons, therefore, cascade through the states to occupy those made empty by recombination. This cascade process is extremely fast (of the order of ps).

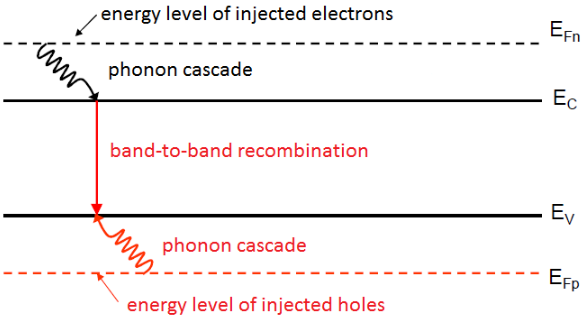

Figure 2.26: An equivalent four-level scheme for a diode laser with phonon cascade for the electrons and holes [64].

2.6.2 Laser oscillation conditions

Together with the stimulated emission, in order to realize a laser, we need a mechanism able to foster stimulated rather than spontaneous recombination at a certain photon energy, i.e. a frequency-selective structure such as an optical resonator or cavity. The optical cavity is compatible with a discrete set of photon states, whose density is large within the cavity, and which operate as positive feedback with respect to stimulated emission.

The spectral position of the laser modes for a cavity with length L is given by the condition:

$$L = \frac{m\lambda}{2n} \tag{2.91}$$

where m is the natural number and n is the dispersion of the index of refraction. The distance of neighboring modes is given by (for large m):

$$\Delta\lambda = \frac{\lambda^2}{2nL\left(1 - \dfrac{\lambda}{n}\dfrac{dn}{d\lambda}\right)} \tag{2.92}$$

The dispersion $dn/d\lambda$ can sometimes be neglected. The above modes are controlled by the length L of the optical cavity along its axis and are called longitudinal axial modes.

Optical gain coefficient

We consider a general laser medium which has an optical gain for coherent radiation along some direction x, as shown in Figure 2.27. This means that the medium is appropriately pumped. Then, we consider an electromagnetic wave propagating in the medium along the x-direction. As it propagates, its power increases due to greater stimulated emissions over spontaneous emissions and absorption across the same two energy levels $E_2 - E_1$, as in Figure 2.27(a). The intensity of the light beam increases with $\exp(gx)$, where g is the optical gain per unit length and is called the optical gain coefficient of the medium (fractional increase in light power per unit distance). Optical power P along x at any point is proportional to the concentration of coherent photons N_{ph} and their energy $h\nu$. These coherent photons travel with a velocity c/n, where n is the refractive index. In time ∂t they travel a distance $\partial x = (c/n)\partial t$ in the tube. Then

$$g = \frac{\partial P}{P\partial x} = \frac{\partial N_{ph}}{N_{ph}\partial x} = \frac{n}{c\partial t}\frac{\partial N_{ph}}{N_{ph}} \tag{2.93}$$

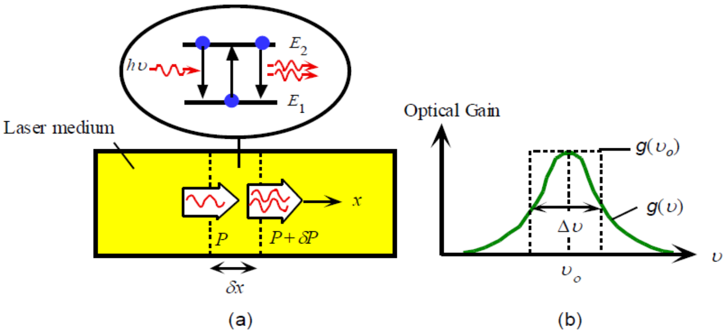

Figure 2.27: A laser medium with an optical gain (a). The optical gain curve of the medium (b); the dashed line is the approximate deviation [65].

From the theory of stimulated emission, the net rate of stimulated photon emission is:

$$\frac{dN_{ph}}{dt} = N_2 B_{21}\rho(h\nu) - N_1 B_{21}\rho(h\nu) \tag{2.94}$$

We can express $\rho(h\nu)$ in terms of N_{ph} by noting that $\rho(h\nu)$ is the radiation energy density per unit frequency so that:

$$\rho(h\nu) \approx \frac{N_{ph}h\nu}{\Delta\nu} \tag{2.95}$$

where $\Delta\nu$ is the widening in frequency due to Doppler broadening or broadening of the energy levels E_2 and E_1. Using equation 2.95 together with 2.93 we can obtain the optical gain coefficient at the center frequency ν_0:

$$g(\nu_0) = (N_2 - N_1)\frac{B_{21}nh\nu_0}{c\Delta\nu} \tag{2.96}$$

Threshold gain

We consider an optical cavity with mirrors at the ends, as reported in Figure 2.28. The optical cavity acts as optical resonator. Then, we consider an electromagnetic wave with an initial optical power P_i starting at some point in the cavity and traveling towards the cavity face 1 shown in the figure. This will travel the length of the cavity, become reflected at face 1, travel back to face 2, become reflected at 2 and arrive at the starting point with a certain final optical power P_f. Under steady state conditions, oscillations do not build up or do not die out. To built the oscillation, there should be no optical power loss, i.e. the net round-trip optical gain $G_{op} = P_f/P_i = 1$ must be unity ($P_f = P_i$). The optical power in the cavity increases according to the $\exp(gx)$. However, there are a number of losses in the cavity medium acting against the stimulated emission gain. The optical power decreases through reflections at mirrors (R_1 and R_2) and due to absorption of the medium (interaction with defects, inhomogeneites) as $\exp(-\gamma x)$, where γ is the attenuation or loss coefficient of the medium. The latter parameter represents all losses in the cavity and its walls, except light transmission losses through the end mirrors and absorption across the energy levels involved in stimulated emissions.

The power P_f of the electromagnetic radiation after one round trip of path length $2L$ is given by:

$$P_f = P_i R_1 R_2 \exp[g(2L)] \exp[-\gamma(2L)] \tag{2.97}$$

The round trip otpical gain is:

$$G = \frac{R_1[R_2 I_0 e^{(g-\gamma)L}]e^{(g-\gamma)L}}{I_0} = R_1 R_2 e^{2(g-\gamma)L} \tag{2.98}$$

If $G > 1$, light (at the characteristic frequency of the laser) will be amplified. The threshold condition is therefore:

$$G = R_1 R_2 e^{2(g_{th}-\gamma)L} = 1 \tag{2.99}$$

from which we can calculate the threshold gain:

$$g_{th} = \gamma + \frac{1}{2L}\ln\left(\frac{1}{R_1 R_2}\right) \tag{2.100}$$

Equation 2.100 gives the optical gain needed in the medium to achieve a continuous wave lasing emission.

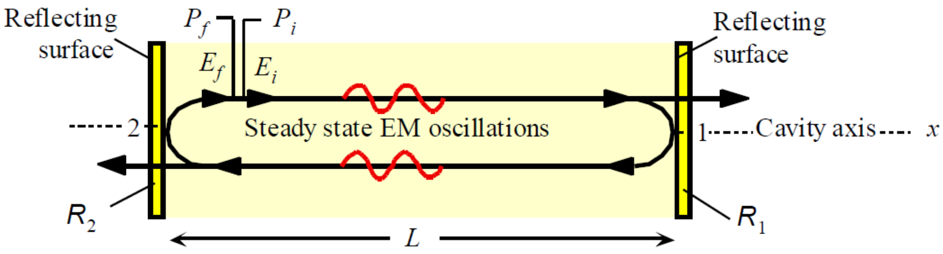

Figure 2.28: Optical cavity resonator [65].

The necessary g_{th} has to be obtained by suitably pumping the medium so that N_2 is sufficiently greater than N_1. Considering that the optical gain of the material is:

$$g(\nu_0) = (N_2 - N_1)B_{21}\frac{h\nu_0}{\Delta\nu}\frac{n}{c} \tag{2.101}$$

the population inversion at threshold is equal to

$$(N_2 - N_1)_{th} = N_{th} = g_{th}\frac{c\Delta\nu}{B_{21}nh\nu_0} \tag{2.102}$$

The examination of the output power P_0 and the population difference $(N_2 - N_1)$ in a laser as function of the pump rate would reveal the behavior reported in Figure 2.29. Until the pump rate can bring $(N_2 - N_1)$ to the threshold value $(N_2 - N_1)_{th}$, there would be no coherent radiation output. When the pumping rate exceeds the threshold value, $(N_2 - N_1)$ remains clamped at $(N_2 - N_1)_{th}$ because this controls the optical gain g which must remain at g_{th}. Additional pumping increases the rate of stimulated transitions and hence increases the optical output power P_0.

2.6.3 Elementary laser diode characteristics

One important and useful laser diode parameter is the slope efficiency, which determines the optical power P_0 of the output coherent radiation in terms of the diode current above threshold current I_{th}. If I is the diode current, the slope efficiency η_{slope} is

$$\eta_{slope} = \frac{P_0}{I - I_{th}} \tag{2.103}$$

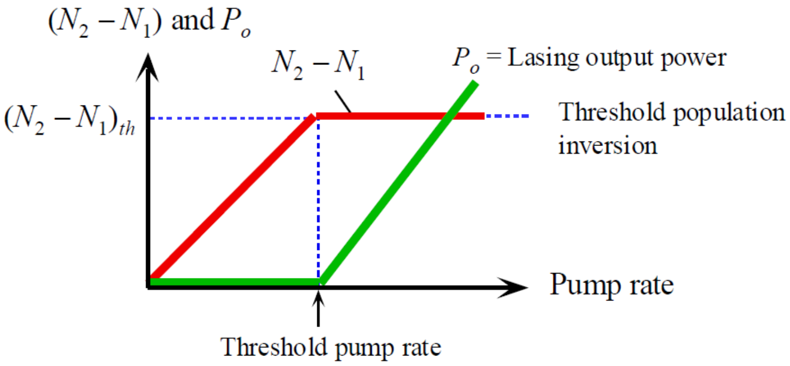

Figure 2.29: $(N_2 - N_1)$ and coherent output power (P_0) as function of the pump rate under continuous wave steady state operation [65].

and is measured in W/A or in W/mA. This parameter depends on the structure as well as the semiconductor packaging, and typically values for commonly available LDs are less then 1 W/A.

Another parameter is the conversion efficiency, that is the ratio between the output optical power and the input electrical power. In some modern LDs this may be as high as $30 - 40\%$.

We consider a double heterostructure LD under forward bias with a structure reported in Figure 2.30. The current carries the electron into the active layer where they recombine with holes radiatively. We define d as the thickness, L as the length and W as the width of the active layer. Under steady state operation, the rate of electron injection into the active layer by current I is equal to their rate of recombination by spontaneous and stimulated emissions (neglecting non-radiative recombinations), that is:

$$\frac{I}{qdLW} = \frac{n}{\tau_{sp}} + CnN_{ph} \tag{2.104}$$

where n is the electron concentration, N_{ph} is the coherent photon concentration in the active layer, τ_{sp} is the average time for spontaneous recombination and C is a constant that depends on B_{21}.

Under steady state conditions, the rate of coherent photon loss in the cavity is equal to the rate of stimulated emission

$$\frac{N_{ph}}{\tau_{ph}} = CnN_{ph} \tag{2.105}$$

where τ_{ph} is the average time for a photon to be lost from the cavity due to transmission through the end-faces, scattering and absorption in the semiconductor.

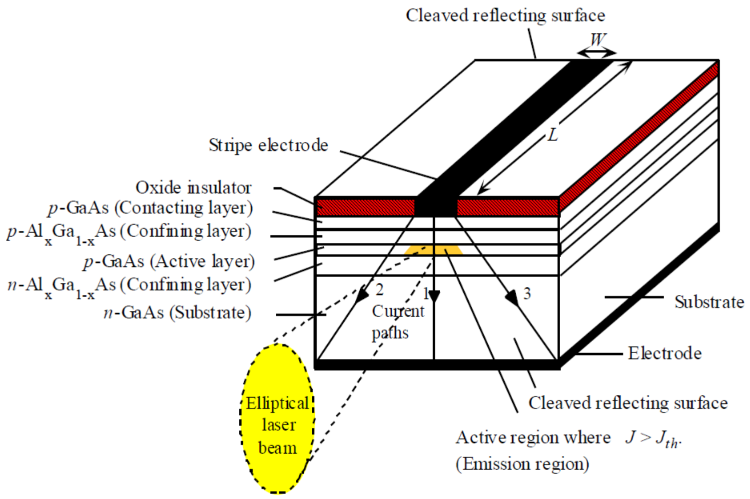

Figure 2.30: Schematic illustration of the structure of a double heterojunction stripe contact laser diode [65].

In semiconductor laser science, the threshold electron concentration n_{th} and the threshold current I_{th} refer to that condition when the stimulated emission just overcomes the spontaneous emission and the total loss mechanisms in τ_{ph}. This occurs when the injected n reaches n_{th}:

$$n_{th} = \frac{1}{C\tau_{ph}} \tag{2.106}$$

When the current exceeds I_{th}, the output optical power increases sharply with the current (Figure 2.31), so we can consider $N_{ph} = 0$ when $I = I_{th}$, which gives:

$$I_{th} = \frac{n_{th} qdLW}{\tau_{sp}} \tag{2.107}$$

The threshold current decreases with d, L and W, which explains why it is better to avoid homojunction lasers.

When $I > I_{th}$, the excess carriers above n_{th} brought by the current recombine by stimulated emission, since above the threshold the active layer has optical gain and therefore builds up coherent radiation quickly and stimulated emission dependes on N_{ph}. The steady state electron concentration remains constant at n_{th} though the rates of carriers injection and stimulated recombination have increased. Above threshold, with $n \sim n_{th}$

$$\frac{I}{qdLW} = \frac{n_{th}}{\tau_{sp}} + Cn_{th}N_{ph} \tag{2.108}$$

as a consequence

$$\frac{I - I_{th}}{qdLW} = Cn_{th}N_{ph} \tag{2.109}$$

so using 2.106 and defining $J = I/WL$ we can find

$$N_{ph} = \frac{J - J_{th}}{qd}\frac{1}{Cn_{th}} = \frac{\tau_{ph}}{qd}(J - J_{th}) \tag{2.110}$$

A photon needs $\Delta t = nL/c$ seconds in order to cross the laser cavity lenght L, with refractive index n. Only $1/2N_{ph}$, that means half of the photons in the cavity, would be moving towards the output face of the crystal, and only a fraction equal to $(1 - R)$ of this will escape. Thus, the optical power P_0 is:

$$P_0 = \frac{\text{energy}}{\Delta t} = \frac{\frac{1}{2}N_{ph}(WLd)(h\nu)(1-R)}{\Delta t} \tag{2.111}$$

and using N_{ph} we obtain the laser diode equation:

$$P_0 = \frac{\frac{1}{2}\frac{\tau_{ph}}{qd}(J - J_{th})(WLd)(h\frac{c}{\lambda})(1-R)}{\frac{nL}{c}} = \frac{hc^2\tau_{ph}W(1-R)}{2qn\lambda}(J - J_{th}) \tag{2.112}$$

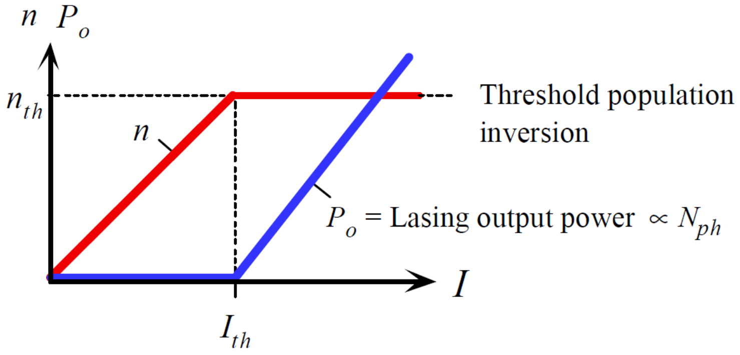

Figure 2.31: Injected electron concentration n and coherent radiation output power P_0 as function of diode current I [65].

The LD output characteristics tend to be temperature sensitive. Figure 2.32 shows the changes in the optical power as function of the diode current with the case temperature. As the temperature increases, the threshold current increases typically as the exponential of the absolute temperature. The threshold current can be approximately modeled by $I_{th}(T) = I_0e^{T/T_0}$, where T_0 is an overall characteristic temperature. This formula takes into account global changes such as the changes in the gain spectrum, the increased SRH and the stronger escape at high temperatures.

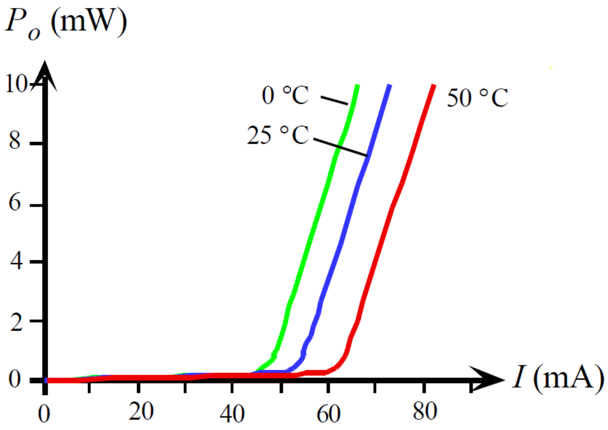

Figure 2.32: Output optical power as function of diode current for three different temperatures. The threshold current shifts to higher temperatures [65].

2.6.4 Heterostructure laser diodes

In homojunction lasers, carrier confinement is not sufficient. Optical confinement is obtained thanks to the contrast between the refractive indices of the two materials. In homojunction laser diodes this contrast originates from the difference in carrier density, that is very small, causing in fact a no effective optical confinement. Since the confinement is poor, there is only a small overlapping between the volume where photons can propagate, and the region where population inversion takes place. Thus, light amplification is not efficient. Moreover, the threshold current density J_{th} is too high for practical uses. The reduction requires improving the stimulated emission rate and also improving the efficiency of the optical cavity. First, we can confine the injected electrons and holes to a narrow region around the junction. This narrowing of the active region means that less current is needed to establish the necessary concentration of carriers for population inversion. Secondly, we can build a dielectric waveguide around the optical gain region to increase the photon concentration and hence the probability of stimulated emission. This way we can reduce the loss of photons traveling off the cavity axis.

Both the requirements of carrier and photon confinement are achieved in modern laser diodes by the use of heterostructured devices as in the case of high-intensity double heterostructure LEDs. However, in the case of laser diodes, there is an additional requirement for maintaining a good optical cavity that will increase stimulated emission over spontaneous emission.

Figure 2.33 shows a double heterostructure (DH) device based on two junctions between different semiconductor materials with different bandgaps. The p-GaAs region constitutes the active layer in which lasing recombination takes place. Both p-GaAs and p-AlGaAs are heavily p-type doped and are degenerate with E_F in the valence band. When a sufficiently large forward bias is applied, E_C of n-AlGaAs moves above E_C of p-GaAs, which leads to a large injection of electrons in the conduction band of n-AlGaAs into p-GaAs, as shown in Figure 2.33(b). However, these electrons are confined to the conduction band of p-GaAs since there is a barrier ΔE_C between p-GaAs and p-AlGaAs due to the change in the bandgap. The concentration of injected electrons in the p-GaAs layer can be increased quickly even with moderate increases in forward current, and this reduces the threshold current. Thus, even moderate forward currents can inject sufficient a number of electrons into the conduction band of p-GaAs to establish the necessary electron concentration for population inversion in this layer.

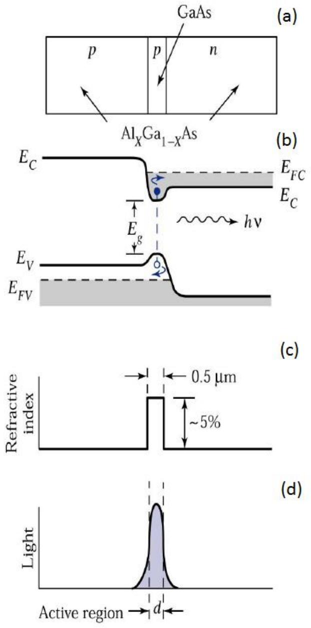

Figure 2.33: A double heterostructure diode has two junctions which are between two different bandgap semiconductors (a). Simplified energy band diagram under forward bias (b); the lasing recombination takes place in the p-GaAs layer, the active layer. Higher bandgap materials have a lower refractive index (c). Confinement of light (d).

A wider semiconductor, like AlGaAs in our case, has a lower refractive index, that means AlGaAs has a lower refractive index than that of GaAs. The change in the refractive index defines an optical dielectric waveguide, as depicted in Figure 2.33(c), that confines the photons to the active region of the optical cavity, reducing photon losses and increasing photon concentration (Figure 2.33(d)). This increase in the photon concentration increases the rate of stimulated emissions. In this way, both carrier and optical confinement lead to a reduction in the threshold current density.

A typical structure of a double heterostructure laser diode is similar to a double heterostructure LED, as shown in Figure 2.30. An important feature of this laser diode is the stripe geometry, or stripe contact on p-GaAs. The current density J from the stripe contact is not uniform laterally. J is greatest along the central path 1 and decreases away from path 1, towards 2 or 3. The current is confined to flow within paths 2 and 3. The current density paths through the active layer where J is grater than the threshold value J_{th} define the active region where population inversion, and hence optical gain, takes place. The lasing emission emerges from this active region. The width of the active region is therefore defined by the current density from the stripe contact. Optical gain is highest where the current density is greatest. Such laser is called gain guided. Stripe geometry allows to have two advantages: (i) the reduced contact area also reduces the threshold current; (ii) the reduced emission area makes light coupling to optical fibers easier.

The laser efficiency can be further improved by reducing the reflection losses from the rear crystal facet. By fabricating a dielectric mirror and the rear facet, that is a mirror consisting of a number of quarter wavelength semiconductor layers of different refractive index, it is possible to bring the reflectance close to unity and thereby improve the optical gain of the cavity. This corresponds to a reduction in the threshold current.

The width of the optical gain region in the stripe geometry DH laser in Figure 2.30 is defined by the current density and changes with the current. Moreover, the lateral optical confinement of photons to the active region is poor because there is no marked change in the refractive index laterally. It would be advantageous to laterally confine the photons to the active region to increase the rate of stimulated emissions. This can be achieved by shaping the refractive index profile in the same way the vertical confinement was defined by the heterostructure. The structure of such a DH laser diode is illustrated schematically in Figure 2.34, where the active layer is bound both vertically and laterally by a wider bandgap semiconductor, which has a lower refractive index. Since the active layer is buried within a wider bandgap material, the structure is called buried double heterostructure laser diode. The active layer behaves as a dielectric waveguide and ensures that the photons are confined to the active region, increasing the rate of stimulated emission, thus the efficiency of the diode. Since the optical power is confined to the waveguide defined by the refractive index variation, these diodes are called index guided. With the right dimensions of the buried heterostructure, compared with the wavelength of the radiation, only the fundamental mode can exist in this waveguide structure and in this case it will be call single mode laser diode.

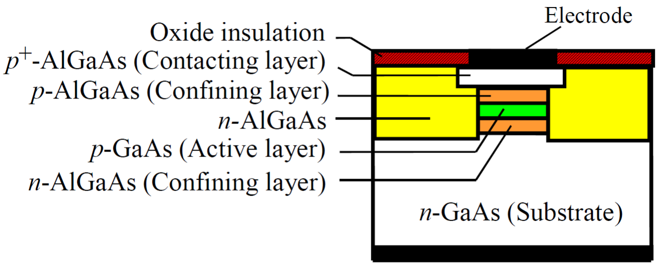

Figure 2.34: Schematic illustration of the cross sectional structure of a buried heterostructure laser diode [65].

2.6.5 Quantum well deivices

Figure 2.35 illustrates a quantum well device that has a narrow bandgap semiconductor sandwiched between two wider bandgap semiconductors. Assume that the two semiconductors are lattice matched, that means same lattice parameter a, in order to have a reduced number of interface defects due to mismatch of crystal dimensions between the two semiconductor crystals. At the interface there are discontinuities ΔE_C and ΔE_V, that depends on the semiconductor materials and their doping. Because of the potential energy barrier ΔE_C, conduction electrons in the thin GaAs layer are confined in the x-direction. Since the confinement length d is small, we can treat the electron as in an one-dimensional potential energy (PE) well in the x-direction but if it were free in the yz plane.

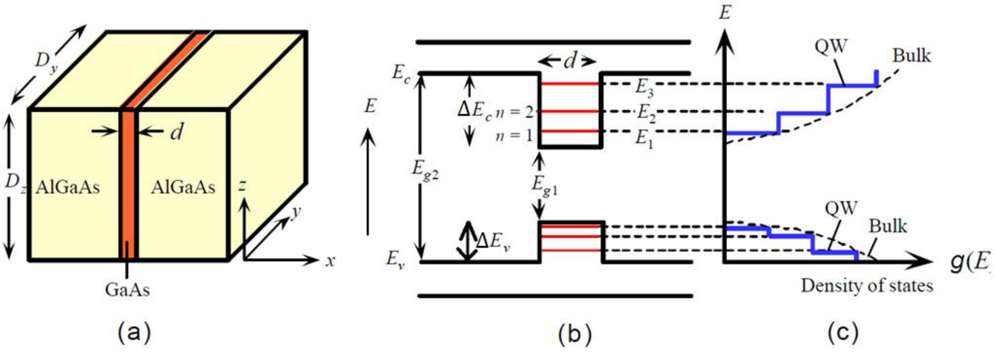

Figure 2.35: Schematic illustration of a quantum well structure in which a thin layer of GaAs is sandwiched between two wider bandgap semiconductors (AlGaAs) (a). Electrons in the GaAs layer are confined in the x-direction to a small length d so that their energy is quantized (b). Density of state of a two dimensional QW (c) [65].

We can appreciate the confinement effect by considering the energy of the conduction electron that is bound by the size of the GaAs layer which is d along x and D_y and D_z along y and z as shown in Figure 2.35(b). The energy of the conduction electron will be the same as that in a three dimensional PE well of size d, D_y and D_z and it is given by:

$$E = E_C + \frac{h^2 n^2}{8 m_e^* d^2} + \frac{h^2 n_y^2}{8 m_e^* D_y^2} + \frac{h^2 n_z^2}{8 m_e^* D_z^2} \tag{2.113}$$

where n, n_y and n_z are the quantum numbers having the values $1, 2, 3....$ The minimum energy E_1 corresponds to $n = 1$ and is above E_C of GaAs as shown in Figure 2.35(b). We have a two-dimensional electron gas confined in the x-direction. The holes in the valence band are confined by the potential energy barrier ΔE_V and behave similarly as indicated in Figure 2.35(b).

The densities of states for the confined electron and that in the bulk semiconductor are shown in Figure 2.35(c). The density of electronic states for the two dimensional electron system is not the same as that for the bulk semiconductor. For a given electron concentration n, the density of states $g(E)$, number of quantum states per unit energy per unit volume, is constant and does not depend on the energy. $g(E)$ is constant at E_1 until E_2, where it increases as a step and remains constant until E_3, where again it increases as a step by the same amount and at every value of E_n. In the valence band, the density of states behaves similarly.

On the other hand, in the bulk semiconductor the density of states at E_C is zero and increases slowly with $E^{1/2}$, which means that the electrons are spread more deeply into the conduction band, searching for states. A large concentration of electrons can easily occur at E_1, whereas this is not the case in the bulk semiconductor.

Under forward bias, electrons are injected into the conduction band of the active layer and populate the wide number of states at E_1, which means that the electron at E_1 increases rapidly with the current. Thus, population inversion occurs quickly without the need for a high current. Stimulated transitions of electrons lead to a lasing emission. There are two main advantages: (i) the threshold current for population inversion is reduced with respect to that for bulk semiconductor devices; (ii) since the majority of the electrons are at and near E_1 and holes are at and near E_1' (the minimum hole energy in the valence band), the range of emitted photon energies are very close to $E_1 - E_1'$, consequently the spread in the wavelength, the linewidth, in the output spectrum is narrower than in the bulk semiconductor laser. In multiple quantum well (MQW) lasers, the advantage of the single quantum well (SQW) can be extended to a larger volume.

Chapter 3

Advanced experimental techniques

In this chapter, we present two advanced experimental techniques useful to characterize defects in the semiconductors. The first technique is the Capacitance-Deep Level Transient Spectroscopy (DLTS) technique, that allows to measure the concentration of defects in a pn junction and to extract the signature of these defects, namely their activation energy and capture cross-section. It consists in applying a voltage pulse to the device under test and measure the associated capacitance transients over time, iterating the procedure at diferent temperatures. The second technique is the Photocurrent (PC) spectroscopy technique, that allows to excite carriers, with a monochromatich light, trapped in deep levels in the bandgap, and collect the excited carriers at the electrode, obtaining the PC signal.

3.1 Deep Level Transient Spectroscopy (DLTS)

The DLTS techniques was developed in 1974 by D.V. Lang [66] and allows to study the deep energy levels in semiconductors. In the following section, we will analyze this measurement technique, starting from the basic theoretical principles and then describing the experimental procedure.

3.1.1 Capacitance Transient

For simplicity, we will consider a p^+n-junction; the results are the same for the case of a n^+p-junction, with only trivial changes in the notation. For this reason, in our discussion we will consider only those traps in the low-doped n-side of the junction.

Figure 3.1 is a schematic summary of the emission and capture processes, which

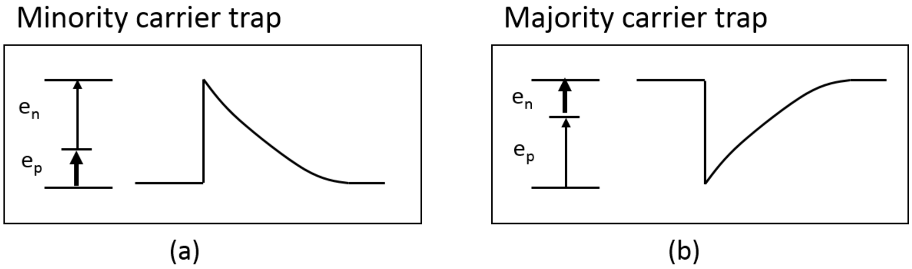

Figure 3.1: Capacitance transients in a p^+n junction in case of (a) minority-carrier traps and (b) majority-carrier traps. The larger arrows indicate that emission is the dominant process during the transient [66].

characterize a particular trap. The capture and thermal emission rates for minority carriers, that in our case are holes, are c_p and e_p, respectively. Instead, for the majority carriers, in our case electrons, are c_n and e_n, respectively. The occupation state of a deep level can be described by a differential equation that takes into account the capture/emission processes:

$$\frac{\partial n_T}{\partial t} = (c_n n p_T - e_n n_T) - (c_p p n_T - e_p p_T) \tag{3.1}$$

where n_T and p_T indicate the concentration of traps filled with an electron and a hole, respectively, n and p are the electrons and holes density. By defining the total concentration of traps at the considered energy level $N_T = n_T + p_T$, the previous equation can be rewritten as:

$$\frac{\partial n_T}{\partial t} = (c_n n + e_p)(N_T - n_T) - (c_p p + e_n) n_T \tag{3.2}$$

which is a first-order differential equation on n_T. Under quasi-equilibrium conditions the carrier density is constant and one can obtain:

$$n_T(t) = n_T(0) e^{-t/\tau} + \frac{(c_n n + e_p) N_T}{c_n n + e_p + c_p p + e_n}(1 - e^{-t/\tau}) \tag{3.3}$$

where $n_T(0)$ is the initial density of occupied trap states and τ is defined as:

$$\tau = \frac{1}{c_n n + e_p + c_p p + e_n} \tag{3.4}$$

The density of states filled with an electron in steady-state is:

$$n_T(t = \infty) = \frac{c_n n + e_p}{c_n n + e_p + c_p p + e_n} N_T \tag{3.5}$$

The latter expression can be further simplified by considering than in a reverse biased p-n junction, the carrier concentration is low, therefore capture events are unlikely. This allows to rewrite the previous equation in a more usable form:

$$n_T(t=\infty) = \frac{e_p}{e_p + e_n} N_T \tag{3.6}$$

We define an electron trap as one which tends to be empty ($n_T = 0$) of electrons and thus capable to capture them. Likewise, a hole trap is one which tends to be full ($n_T = N_T$) of electrons and thus capable of having a trapped electron recombine with a hole, i.e. capture a hole. The emission rates of electrons and holes are proportional to a Boltzmann factor, and thus strongly depend on the position of trap level with respect to the conduction and valence band. In case of an electron trap at energy E_T located in the upper half of the bandwidth, $|E_t - E_C| < |E_t - E_V|$ and therefore $e_p \ll e_n$. Instead, for a hole trap $e_n \ll e_p$. If the initial density of traps occupied by electrons is $n_T(0)$, the under reverse bias conditions 3.2 becomes:

$$\frac{dn_T}{dt} = -e_n n_T \tag{3.7}$$

which has solution

$$n_T(t) = n_T(0)e^{-e_n t} \tag{3.8}$$

Once electrons are emitted from the deep level, the strong electric field inside the space charge region (SCR) pushes them towards the n-side of the junction. Each electron emission, therefore, corresponds to a net increase of the total store charge. To maintain the total charge constant (the external bias is constant), the SCR shrinks and this results in an increase in the capacitance. The relationship between the junction capacitance and the density of occupied traps in the case of an ideal junction can be written as:

$$C = \epsilon A \left[\frac{q(N_D - n_T)}{2\epsilon(V_{bi} - V_R)} \right]^{1/2} \tag{3.9}$$

where A is the junction area, V_{bi} and V_R the built-in and bias voltage, respectively, N_D the n-type dopant concentration and the ϵ the dielectric constant. The previous equation can be rewritten as:

$$C = C_\infty \left(1 - \frac{n_T(t)}{N_D} \right)^{1/2} \quad , \quad C_\infty = \epsilon A \left[\frac{qN_D}{2\epsilon(V_{bi} - V_R)} \right]^{1/2} \tag{3.10}$$

where steady-state capacitance C_∞, i.e. the capacitance value after any detrapping process occurred, is decoupled. This expression can be further simplified by considering that the defects density is much lower than the dopant concentration, i.e. $n_T \leq N_T \ll N_D$. Under this condition, using the approximation $(1+x)^n \approx 1 + nx$ which is valid for $x \lesssim 0.1$, one obtains:

$$C(t) = C_\infty\left(1 - \frac{n_T(t)}{2N_D}\right) = C_\infty\left(1 - \frac{n_T(0)}{2N_D}\exp\left(-\frac{t}{\tau_n}\right)\right) \tag{3.11}$$

where $\tau_n = 1/e_n$ is the trap's emission time constant of electrons. This formula shows that the capacitance transient due to the emission of trapped electrons is an exponential function with a time constant equal to the inverse of the emission rate. Similar considerations can be used to analyze the case of hole traps, obtaining an exponential capacitance transient having time constant $\tau_p = 1/e_p$.

The sign of the capacitance change depends on whether the electron occupation of the trap had been increased or decreased by the bias pulse given in order to cause the capacitance change. An increase in trapped minority carriers, that in our case means holes, causes an increase in the junction capacitance (the total charge in the SCR decreases). As shown in Figure 3.1, the shape of the capacitance transient is an indicator of the type of traps under investigation: capacitance transient due to a minority carrier trap is always positive, whereas the transient due to a majority-carrier trap (electrons) is always negative.

The concentration of the trap can be obtained directly from the capacitance change. Assuming $n_T(0) = N_T$ and $n_T(\infty) = 0$, one obtains:

$$\frac{C_\infty - C(0)}{C_\infty} = \frac{n_T(0) - n_T(\infty)}{2N_D} = \frac{N_T}{2N_D} = \frac{\Delta C}{C} \tag{3.12}$$

where ΔC is the capacitance change at $t = 0$. Therefore, the concentration of defects is:

$$N_T \approx 2\frac{\Delta C}{C}N_D \tag{3.13}$$

This estimation of the defects density could lead to inaccurate results for small values of the reverse bias V_R, as will be discussed later in this section. However, in practical applications, this approach is often preferred over more accurate methods whose application is not trivial. Moreover, most of the times the effective dopant concentration N_D is not precisely known, thus further justifying a simpler approach for the defects density estimation.

3.1.2 Bias Voltage Pulses

By applying the adequate filling voltage pulses, it will allow the traps to capture carriers. There are two main types of filling pulses, namely, a minority-carrier pulse, which momentarily drives the diode into forward bias and injects minority carriers into the region of observation, and a majority-carrier filling pulse, which momentarily reduces the diode bias and introduces only majority carriers into the region of observation. As Figure 3.2 shows, we start applying a reverse bias voltage V_R at the beginning; after that, the majority-carrier filling pulse V_f, where $|V_f| < |V_R|$, is applied for a certain time t_{FP}. After the filling pulse, the voltage returns to V_R in order to observe the capacitance transient. As a result, the SCR shrinks and some of the traps previously located inside of it are now in the quasi-neutral region, where the free-carrier concentration n is high. As a consequence, the capture process dominates and the traps can be filled with electrons. The total amount of captured carriers depends on the duration of the filling pulse t_{FP}: a longer pulse will result in a higher number of filled traps. As already mentioned before, after the filling pulse, the voltage returns to V_R and the SCR width increases. However, due to the presence of trapped carriers, the initial width of the SCR will be different from its steady-state value and this difference corresponds to the initial capacitance peak ΔC introduced in the previous paragraph. The subsequent emission of trapped carriers gives rise to the capacitance transient previously discussed.

In order to study a minority-carrier defect, it is necessary to previously fill it with carriers and this is achieved by applying a positive filling pulse. However, during such pulse, both minority and majority carriers are flowing through the junction, therefore the initial occupation state of the traps will be a function of both the capture rates c_n and c_p.

3.1.3 DLTS measurement procedure

The DLTS measurement apparatus consists in a temperature-controlled cryostat, where the sample is mounted, connected to a capacitance monitor and a waveform generator. The latter applies the reverse bias V_R and the filling pulse V_f for a certain period, while the capacitance meter records the capacitance transient. The measurement is then repeated for several times by changing the temperature. One important feature of the DLTS technique is the ability to set an emission rate window such that the measurement apparatus only responds when it sees a transient with a rate within this window. Thus, if the emission rate of a trap is varied by varying the sample

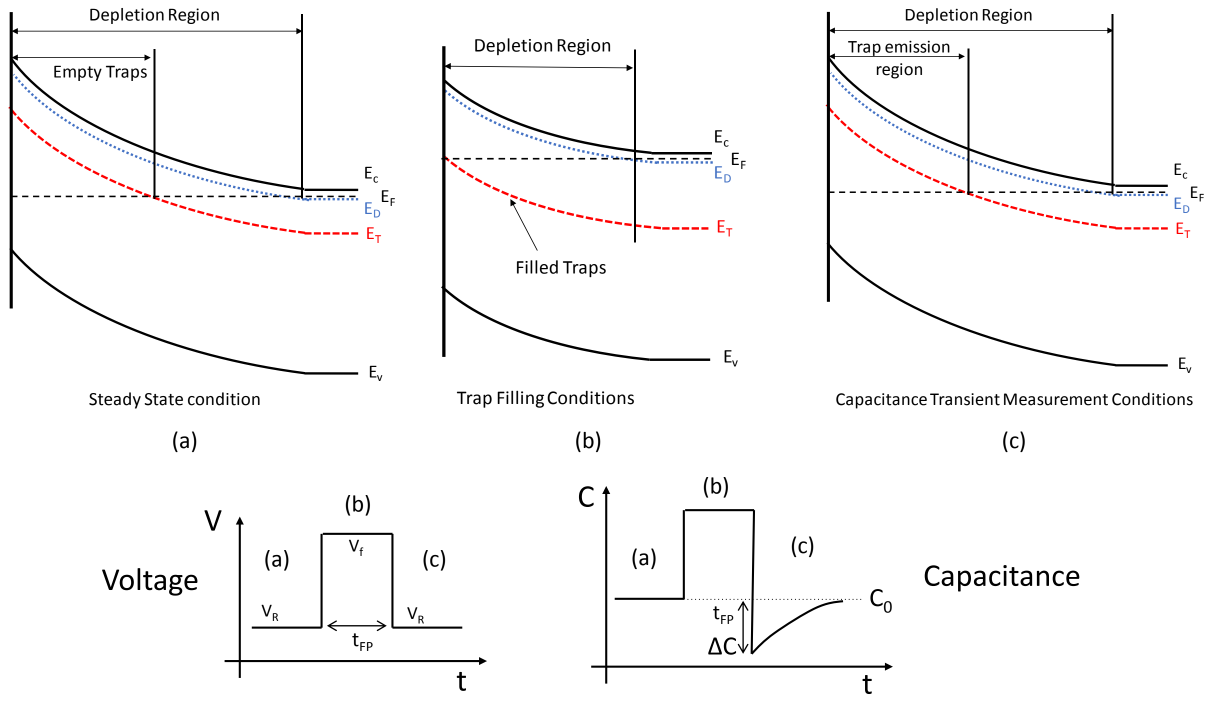

Figure 3.2: Evolution of band diagram during the capacitance transient measurement for a p^+n junction characterized by the presence of a majority-carrier trap localized at the energy level E_T in the bandgap. The figure shows only the band diagram of the n-side.

temperature, the instrument will show a response peak at the temperature where the trap emission rate is within the window. These emission rates are thermally activated and, considering an electron emitted by a deep level located at $(E_C - E_t)$ eV below the conduction band, the emission probability is given by:

$$e_n = \upsilon_{th}\sigma_n N_C \exp\left[\frac{E_t - E_C}{kT}\right] \tag{3.14}$$

where υ_{th} is the thermal velocity, σ_n is the capture cross section of the deep level, N_C is the effective density of states, k is the Boltzmann constant, T is the temperature, E_t and E_C are the energies of the deep level and the conduction band, respectively. An exactly similar equation holds for e_p. Neglecting the capture of a hole from the valence band, which is unlikely inside the SCR, the emission time constant $\tau_n = 1/e_n$ is therefore an exponential function of temperature. Thermal velocity and density of states are also temperature-dependent and for this reason the 3.14 can be rewritten as:

$$\tau_n T^2 = \frac{\exp[(E_C - E_t)/kT]}{\gamma\sigma_n} \quad , \quad \gamma = \left(\frac{\upsilon_{th}}{T^{1/2}}\right)\left(\frac{N_C}{T^{3/2}}\right) \tag{3.15}$$

Applying the logarithm, the previous equation becomes:

$$\ln(\tau_n T^2) = (E_C - E_t)\frac{1}{kT} - \ln(\sigma_n\gamma) \tag{3.16}$$

A standard means of characterizing the depth of a trap is to construct a plot $\ln(\tau_n T^2)$ vs $1/kT$, that means the emission time constant of each recorded transient, along with the corresponding temperature, represents a data point of an Arrhenius plot. The slope of the resulting linear fit represents the distant between the conduction band and the deep level, called activation energy, while the capture cross section can be extracted from the intercept value b, that is:

$$b = \ln\left(\frac{1}{\gamma\sigma_n}\right) \quad , \quad \sigma_n = \frac{1}{\gamma e^b} \tag{3.17}$$

The very same arguments still apply in case of a hole trap, but the activation energy indicates the distance $E_t - E_V$ and γ parameter needs to be recalculated properly.

3.1.4 The dual-gate integrator (double boxcar)

The DLTS apparatus presented here makes use of a dual-gate integrated method, also called double boxcar, to determine the emission rate window and to provide signal averaging capability to enhance the signal-to-noise ratio for the detection of low-concentration traps. The use of a double boxcar to select the rate window is illustrated in Figure 3.3. According to this method, each capacitance transient is sampled at two times t_1 and t_2 after the filling pulse. The difference between the capacitance values at these two times, $C(t_1) - C(t_2)$, gives the so-called DLTS signal. This quantity goes through a maximum when the time constant of the transients becomes comparable with the time interval $t_2 - t_1$. Instead, the signal will be negligible for both very fast and slow transients, corresponding to high and low temperatures, respectively, as shown in Figure 3.3.

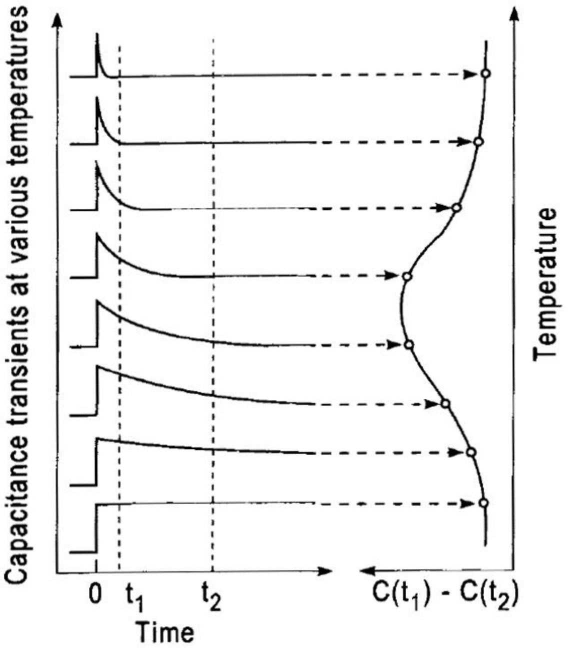

Figure 3.3: Illustration of how a dual-gate integrator (or double-boxcar integrator) is used to define the rate window. The left-hand side shows the capacitance transients at different temperatures, and the right-hand side shows the corresponding DLTS signal resulting from using the double boxcar to display the difference between the capacitance at t_1 and the capacitance at t_2 as function of temperature [66].

It is possible to derive the relationship between τ_{max}, the value of τ at the maximum of the DLTS signal for a particular trap, and the position of the two times t_1 and t_2. The parameter that we called rate window is now defined to be τ_{max}^{-1}. Let's define the normalized DLTS signal $S(T)$ as:

$$S(T) = [C(t_1) - C(t_2)]/\Delta C \tag{3.18}$$

where ΔC is the capacitance change due to the pulse at $t = 0$, already introduced in paragraph 3.1.1. Assuming exponential capacitance transients:

$$S(T) = \exp(-t_1/\tau) - \exp(-t_2/\tau) = \exp(-t_1/\tau)[1 - \exp(-\Delta t/\tau)] \tag{3.19}$$

where $\Delta t = t_2 - t_1$. The relationship between τ_{max} and t_1 and t_2 is simply determined by differentiating $S(T)$ with respect to τ and setting the result equal to zero. The final result is:

$$\tau_{max} = (t_1 - t_2)[\ln(1_1/t_2)]^{-1} \tag{3.20}$$

Thus, the temperature that corresponds to the peak in the DLTS signal together with the corresponding time constant τ_{max} may be used in constructing the semilog activation energy plot as expressed by equation 3.16. Other data points can similarly be obtained from other scans made by varying the sampling instants t_1 and t_2 and finding the temperatures that maximize the corresponding DLTS signals.

3.1.5 Trap concentration profile

Another important information that we can obtain from the capacitance transient is the trap concentration as function of the position inside the SCR. We suppose that in an asymmetric p^+n junction the space-charge region has width W when all traps are empty. Consider an interval between x and $x + \Delta x$ having $n(x)$ electrons trapped in a deep level, where $0 < x < W$. Assuming that Δx is small, the trapped negative charge will cause an increase in the space-charge width ΔW and a consequent variation in the electric field ΔE. The latter consists in two terms, one related to the new ionized donors $\Delta E'$ and one related to the trapped electrons $\Delta E''$:

$$\Delta E' = \frac{q}{\epsilon} N_D \Delta W \quad , \quad \Delta E'' = -\frac{q}{\epsilon} n(x) \Delta x \tag{3.21}$$

From the Possion equation, each of these two contributes leads to a voltage drop variation equal to:

$$\Delta V' \approx \frac{q}{\epsilon} N_D \Delta W (W + \Delta W) \approx \frac{q}{\epsilon} N_D W \Delta W \quad , \quad \Delta V'' = -\frac{q}{\epsilon} n(x) x \Delta x \tag{3.22}$$

The total voltage variation is expressed as:

$$\Delta V = \frac{q}{\epsilon}[N_D W \Delta W - n(x) x \Delta x] \tag{3.23}$$

Since we are interested in capacitance changes at constant bias, we set $\Delta V = 0$ and thus:

$$\frac{\Delta W}{W} = \frac{n(x) x \Delta x}{N_D W^2} \tag{3.24}$$

Knowing the expression of the junction capacitance under reverse bias, $C = \epsilon A/W$, we finally obtain:

$$\left[\frac{\Delta C}{C}\right]_x \approx \left[-\frac{\Delta W}{W}\right]_x = -\frac{n(x)}{N_D W^2} x \Delta x \tag{3.25}$$

It is interesting to observe that the sensitivity of the junction to trapped charge varies linearly from zero at the junction ($x = 0$) to a maximum at the edge of the depletion region ($x = W$). This means that capacitance measurements are very insensitive to traps located at the junction or at the surface of the semiconductor for the Schottky barrier diode.

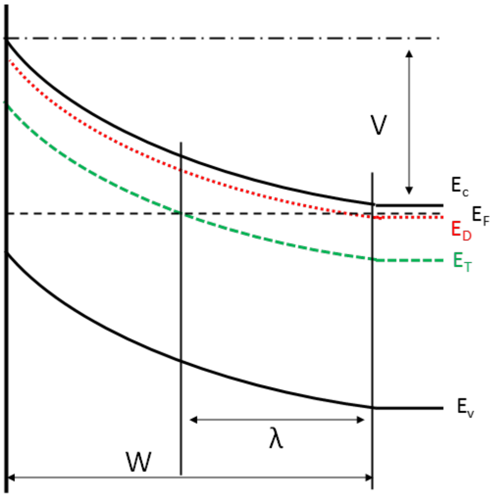

Figure 3.4: Band diagram of a p^+n junction showing the parameter λ.

In order to calculate the capacitance transient amplitude ΔC, we must integrate equation 3.25 over the region of the space-charge layer where emission takes place, that is the region where the traps are filled during the filling pulse. Figure 3.4 shows the band diagram for a p^+n junction having a uniformly doped n region with a deep level located at E_T. The space charge region can be divided into two sections: the central region closest to the junction, where both the shallow donors and the deep levels lies above the Fermi level, that is depleted; the second region, defined from the point where the Fermi level crosses the trap energy level to the edge of the depletion region, where all the traps are filled with electrons. The width of this region, called "edge region", is defined as:

$$\lambda = \sqrt{\frac{2\epsilon(E_F - E_T)}{q^2 N_D}} \tag{3.26}$$

which does not depend on the polarization voltage, but on the energy difference between the Fermi level E_F and the trap level E_T. Although there are sufficient carriers in the edge region to affect the trap occupation and so the capacitance transient amplitude, there are not enough to affect the band bending and they can be ignored in the calculation of the depletion width. This approach can be justified since the error in the depletion width W is negligible [67]. The total signal $\Delta C/C$ produced by a filling voltage pulse V_{FP} long enough to fill all the traps is obtained integrating 3.25 between $W(V_{FP} - \lambda)$ and $W(V_R) - \lambda$:

$$\frac{\Delta C}{C} = -\frac{N_T}{2N_D}\left[1 - 2\frac{\lambda}{W(V_R)}\left(1 - \frac{C(V_R)}{C(V_{FP})}\right) - \left(\frac{C(V_R)}{C(V_{FP})}\right)^2\right] \tag{3.27}$$

If the edge region is neglected ($\lambda = 0$), like also the quadratic term, this equation simplifies in:

$$\frac{\Delta C}{C} \approx -\frac{N_T}{2N_D} \tag{3.28}$$

and therefore we can obtain the usual equation for the defects concentration:

$$N_T \approx \left|2\frac{\Delta C}{C}N_D\right| \tag{3.29}$$

This equation is the same obtained in 3.13, which was calculated neglecting the edge region. We still have to neglect the quadratic term in order to obtain the same result, since equation 3.13 assumes that the filled traps are distributed along the whole extension of the SCR, which corresponds to perform the integration from 0 instead of $W(V_{FP})$. Applying this, at $W = 0$ the capacitance will be $C = \infty$, the quadratic term is zero and we obtain again 3.13. However, neglecting the edge region may cause significat understimation of the trap concentration, especially at low reverse bias voltages.

Knowing the variation of the depletion width with applied bias, we are able to estimate the deep level concentration profile. Basically, the concentration profile of a trap can be determined by using the difference in transients that result from two slightly different filling pulses. The difference between the transient amplitude measured at two filling pulse voltages is a measure of the trap concentration from the region corresponding to the deep level depletion at each of the filling pulses. We assume that during the filling pulse all traps get filled. Starting from the equation 3.25, the total capacitance variation can be written as:

$$\frac{\Delta C}{C} = \int_{z_n}^{W} -z\frac{N_T(z)}{N_D W^2}dz \tag{3.30}$$

where z_n is the width of the SCR during the filling pulse V_{FP}. Differentiating the latter equation leads to:

$$\delta\left(\frac{\Delta C}{C}\right) = \frac{N_T(z_n)}{N_D W^2}z_n\delta z_n \tag{3.31}$$

with δz_n defined as the variation of the SCR edge induced by a variation of the filling pulse δV_{FP}. Using the relation $C(z_n) = \epsilon A/z_n$ and taking into account the definition of capacitance:

$$C(z_n) = \frac{dQ}{dV_{FP}}\bigg|_{W(V_{FP})=z_n} = \frac{qAN_D(z_n)dz_n}{dV_{FP}} \tag{3.32}$$

we obtain that the incremental change in the relative capacitance signal, due to the traps filled by the small change in voltage δV_{FP} is:

$$\delta\left(\frac{\Delta C}{C}\right) = \frac{N_T(z_n)}{N_D(z_n)}\left(\frac{\epsilon}{qN_D W^2}\right)\delta V_{FP} \tag{3.33}$$

where W is the depletion width where $V = V_R$, $N_D(z_n)$ is the dopant concentration at position z_n and N_D is the average dopant concentration. $N_D(z_n)$ is typically measured using C-V profiling methods, that means measuring the capacitance-voltage characteristics and then extracting the apparent charge profile along the depletion width, assuming an asymmetric junction.

Basically, during this measurement a reverse bias voltage V_R is applied in order to determine the steady-state depletion width W. After that, the filling pulse voltage V_{FP} is varied of an amount equal to δV_{FP}, starting from a minimum value grater or at least equal to V_R, and a measurement of $\Delta C/C$ is performed. Usually, δV_{FP} is kept constant between measurements. Finally, the defects concentration profile can be estimated as:

$$N_T(z_n) = N_D(z_n)\left(\frac{qN_D W^2}{\epsilon}\right)\frac{\delta(\Delta C/C)}{\delta V_{FP}} \tag{3.34}$$

3.1.6 Capture process characterization

There are different type of defects in semiconductor. We can divide these in two pricipal categories: point-defects and extended defects. Studying the capture kinetic behavior allows one to distinguish what kind of defect is under investigation

Comparison of the pulse width dependence of the capacitance transient amplitude to the expected behavior for various capture mechanisms will show what the closest match is for the trapping process. In other words, the analysis consists in measuring the initial ΔC capacitance peak at varying filling pulse duration t_{FP}, while keeping the sample at the temperature corresponding to the peak in the DLTS signal associated to the deep level that we want to study. A capture process at a simple point defect is described by the following equation:

$$\Delta C(t_p) = \Delta C_{max}(1 - \exp(-n\sigma_n \upsilon t_{FP})) \tag{3.35}$$

where ΔC_{max} is the amplitude of the transient, n is the shallow carrier concentration, υ is the thermal velocity, σ_n is the capture cross section and t_{FP} is the filling pulse width.

Capture by a point defect with a fixed capture barrier modifies the capture process by introducing an exponential term to the capture cross section according to:

$$\Delta C(t_{FP}) = \Delta C_{max}(1 - \exp(-c_n t_{FP})) \quad , \quad c_n = \upsilon n \sigma_n^{\infty} \exp\left(\frac{-\Delta E_b}{kT}\right) \tag{3.36}$$

where the terms are the same as before, except σ_n^{∞} is the high temperature capture cross section, and ΔE_b is the capture barrier energy. A capture barrier is shown schematically in Figure 3.5, where the red line represents the capture barrier.

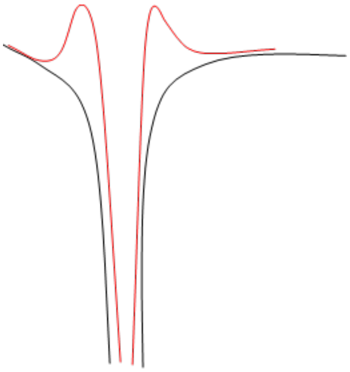

Figure 3.5: Energy pit due to a point defect (black line) with the presence of the capture barrier (red line).

A third possibility is that the trap is related to a dislocation. Charge build-up along a dislocation line produces a Coulombic repulsion, resisting capture of further charges, described by:

$$n_T(t_{FP}) = \sigma_n v \tau n N_T \ln\left(\frac{t_{FP}+\tau}{\tau}\right) \tag{3.37}$$

where N_T is the trap concentration, τ is the inverse of the capture rate ($n\sigma_n v$) scaled by he ratio of the equilibrium trap occupation to the barrier energy, where the barrier energy is proportional to the trap occupation.

Plotting the transient amplitude ΔC as function of the natural log of the filling pulse width will show that, in case of linearly arranged extended defect, the dependence will be linear: this means that we have a slow increase in occupied traps with increase in filling pulse, consistent with trapping along a dislocation.

3.2 Photocurrent spectroscopy

Photocurrent spectroscopy is a useful tool to analyze the presence of defects in optoelectronic devices. This technique allows to excite carriers within the QWs with light of a defined wavelength, and to measure the corresponding variation in the PC signal. In an ideal LED, photons with energies below the energy gap of the material with the smallest bandgap would not excite carriers, i.e., there would be no PC. But the presence of defects introduces energy levels within the bandgap, allowing the transfer of electrons from these levels to the conduction band, where they generate a PC. With increasing photon energy, more carriers will be generated when the photon energy is high enough to excite electrons from additional deeper energy levels. Furthermore, every step in the PC spectrum corresponds to a specific transition, from a defect band to the conduction band, or from the valence band to the conduction band.

In general, it allows to spectrally separate the contributions to the generated photocurrent into carriers generated inside the QW system and carriers generated in the other layers. The high energy part of the spectrum, above the bandgap of the QW material, is due to carriers generated in the QWs, whereas the low energy part of the spectrum, is due to carriers trapped in deep levels within the bandgap.

3.2.1 Measurement apparatus

Figure 3.6 shows a schematic of the PC spectroscopy setup. The setup is characterized by the following instruments:

- xenon arc lamp;
- chopper;
- monochromator (Oriel Cornerstone 130);
- filter wheel;
- lens with a certain focal length (in our case 35 mm), in order to focus the monochromatic light;
- lock-in amplifier (Oriel Merlin).

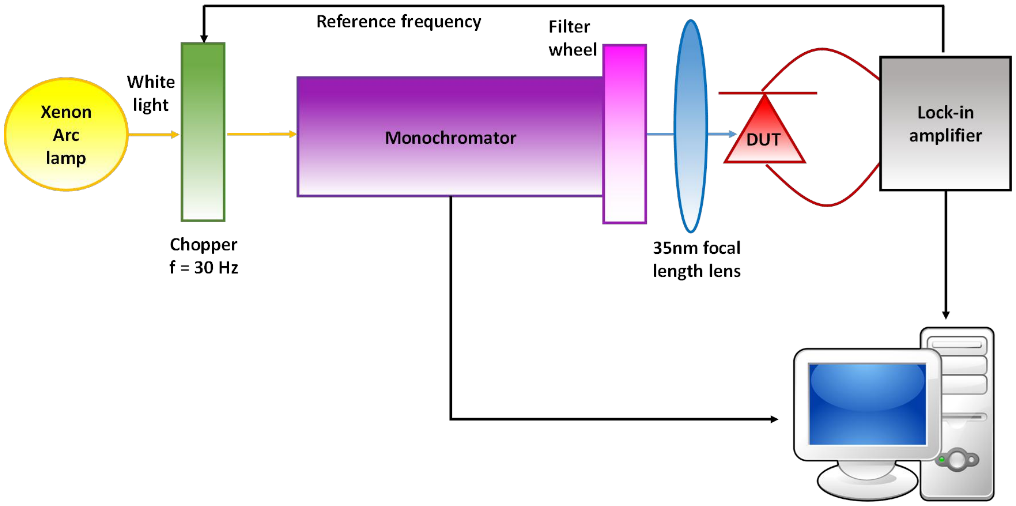

Figure 3.6: Schematic of the PC spectroscopy setup.

The xenon arc lamp generates a white light that covers a high spectral range, from the UV (around 280 nm) to the infra-red (1100 nm). The monochromator allows us to select the wavelength of the incident light. The monocrhomator used in our setup is shown in Figure 3.7. The optical design of the Cornerstone 130 is based on an out-of-plane version of an Ebert-Fastie monochromator. This configuration consists of a single large spherical mirror and one plane diffraction grating. The input and output ports are in line with each other, to simplify the system alignment. A motor is used to select the desired wavelength and switch between diffraction gratings quickly. Figure 3.8 shows the optical configuration of the monochromator. Light passing through the entrance slit will be reflected by a first mirror to the spherical mirror, in order to direct the beam towards the grating. At the grating, the light is dispersed and reflected back towards the mirror. This reflected beam will again be collimated, thanks to the first plane mirror, to the exit slit, where a monochromatic light will pass. The light obtained at the exit of the monochromator could be not exactly at the desired wavelength. The ideal transfer function of a monochromator is a triangular shape. The peak of the triangle is at the nominal wavelength selected. The intensity of the nearby colors decreases linearly on either side of this peak until some cutoff value is reached. This level is called stray light level. In order to reduce the stray light, a filter wheel is used between the exit of the monochromator and the lens. This filter allows to cut the highest orders of the monochromator wavelengths.

Figure 3.7: Oriel Cornerstone 130.

The light coming from the filter wheel is then focused on the sample thanks to a lens; in our case we used a lens with a 35 mm focal length.

Considering that we are promoting carriers from deep levels to the conduction band and the ammount of these carriers is very low, since they are proportional to the deep level density, the PC signal collected is very weak, usually below the noise level. The lock-in amplifier allows to read this signal. The lock-in amplifier used in this setup is the Oriel Merlin Control unit, shown in Figure 3.9, that drives the optical chopper and acts as a lock-in amplifier to retrieve the signal and reject unmodulated background radiation. The optical chopper is s a rotating disc, which periodically interrupts the light beam and modulates the intensity of it. In this way, the light incident on the sample is superimposed to the frequency at which the chopper is rotating. This means that also the PC signal is at the same chopper rotation frequency. The lock-in amplifier decomposes the PC signal in its spectral components and takes only the one at the

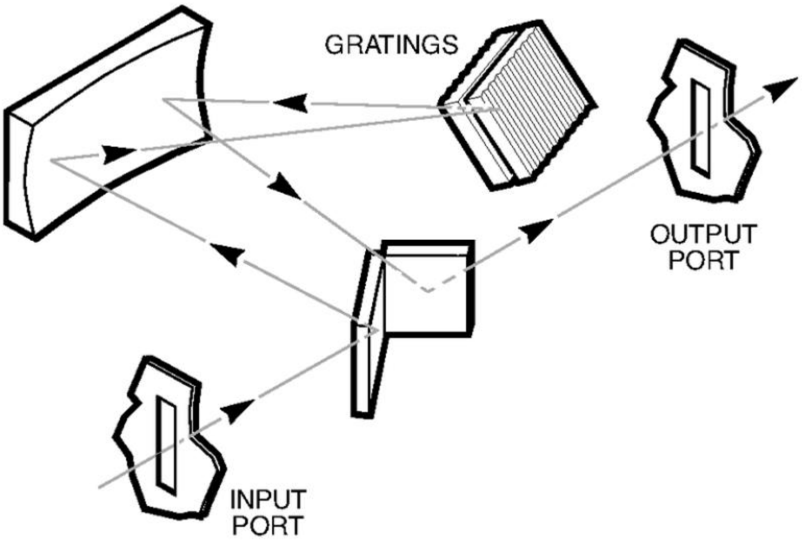

Figure 3.8: Optical configuration of the Cornerstone 130.

frequency of interest. At this point the noise level is lowered, since we have the signal at only one frequency, and so the noise. In this way, it is possible to discriminate the useful signal. It is important to select a frequency far away from the one of noises with a known frequency, in order to not include these in the useful signal. A typical frequency used is 30 Hz.

Before the real measurements, all the optical path is calibrated. In fact, it is important to know the total amount of photons incident on the samples for each wavelength, since we are measuring the photocurrent collected in order to study the presence of deep levels and how much is their concentration, and the xenon arc lamp may emit at a certain wavelength light with a stronger intensity. In order to consider the spectral response of the system, a calibration measurement is required. A calibrated photodiode, controlled in temperature, is used: the output light coming from the system is focused on the useful area of the photodiode and the signal is read.

3.2.2 Photocurrent signal

The PC signal collected allows to identify the presence of deep levels within the bandgap. An example of PC signal is reported in Figure 3.10(a). In general the signal tells how many charge are extracted as function of incident photons in a certain wavelength interval $\lambda \pm \Delta\lambda$. The spectral response SR of the device is therefore defined as:

Figure 3.9: Oriel Merlin Control Unit.

$$SR(\lambda \pm \Delta\lambda) = \frac{j_Q(\lambda \pm \Delta\lambda)}{j_E(\lambda \pm \Delta\lambda)} \tag{3.38}$$

where $j_Q(\lambda \pm \Delta\lambda)$ is the current density of the sample and $j_E(\lambda \pm \Delta\lambda)$ is the energy current density in that specific wavelength interval. The PC signal is usually measured keeping the device at ground potential, in short circuit. Once the SR is known as function of wavelength, the external quantum efficiency EQE can be calculated by:

$$EQE(\lambda) = \frac{SR(\lambda)\varepsilon_\gamma(\lambda)}{e} = SR(\lambda)hc/(e\lambda) \tag{3.39}$$

EQE gives information about how efficiently photons are converted into electron–hole pairs as a function of wavelength.

When a photon with a certain energy below the band-gap reaches the device, it may be able to excite carriers trapped in deep levels with an activation energy similar to the photon one (Figure 3.10(b)), causing an increase in the carriers collected at the electrode and consequently in the photocurrent signal. More carriers will be generated when the photon energy is high enough to excite electrons from additional deeper energy levels.

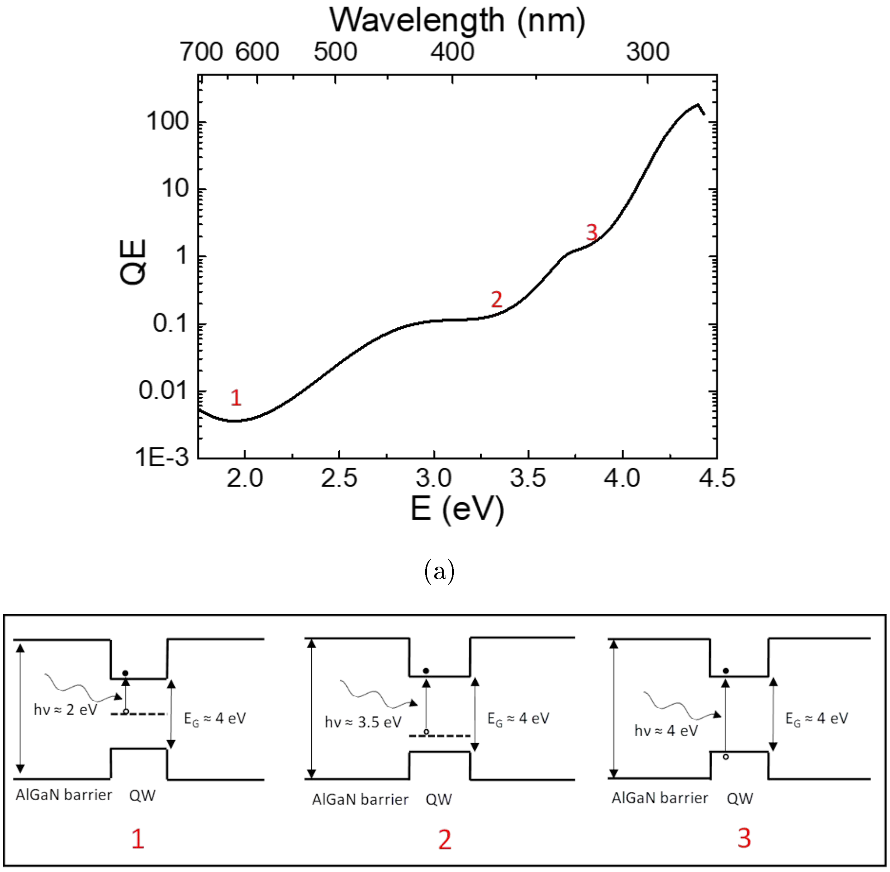

(a)

(b)

Figure 3.10: (a) Example of photocurrent signal. Each change in the slope represents a defects with a certain activation energy. (b) Schematic view of the mechanisms responsible for the photocurrent [68].

Part II

Degradation mechanisms of UV LEDs

Chapter 4

Introduction to UV LEDs

By adding aluminum nitride (AlN) to the GaN alloy system, it is possible to tune the emission wavelength of AlGaN-based LED over almost the entire UV spectral range. There are two main classifications for the UV spectral range, as Figure 4.1 reports. The first classification is based on a convention established during the Second International Congress on Light in 1932 (International, 1932) and divides the UV spectral range in: UV-A (315 – 390 nm), UV-B (280 – 315 nm) and UV-C (< 280 nm). UV-A radiation from the sun penetrates the earth's atmosphere (including clouds) and, due to the high energy of UV photons, creates damage to the skin, particularly to the deeper layers of the skin. Both UV-B (partially absorbed by the earth's ozone layer) and UV-C radiation (mostly absorbed by ozone layer) create serious damage to skin and eyes. Because no natural light with $\lambda \leq 280$ nm exists at the earth's surface, this wavelength range is also referred to as the solar-blind range.

The other possible classification has the following categories: extreme UV (10 – 100 nm); vacuum UV (100 – 200 nm); deep UV (200 – 320 nm); and near UV (320 – 390 nm).

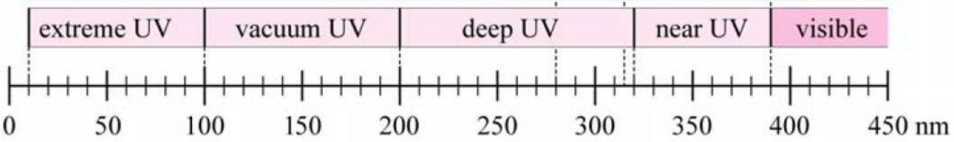

Figure 4.1: Nomenclature of UV radiation as function of the wavelenght [19].

Compared to conventional UV sources, such as mercury discharge lamps, UV LEDs present a number of advantages and they are promising candidates in order to replace these lamps. UV LEDs are extremely robust and compact, moreover, since they are mercury free, they are environmentally friendly [69]. They present long lifetimes, do not require any warm-up times and can be switched on and off within a few tens of nanoseconds [10]. Other advantages are low energy consumption, a more constant light intensity and greater easiness in controlling the temperature [70]. UV lamps are characterized by a continuous emission spectrum between 200 and 450 nm, instead UV-LEDs are characterized by almost monochromatic radiation.

Figure 4.2 reports the different applications for UV-LEDs. In general, UV LEDs can be used as fluorescent light sources for lighting and displays, but also as high-resolution light sources (for example in microscopes). In particular, UV-A LEDs are used for drying and UV curing of inks, resins and varnishes, in safety systems (for example for the identification of banknotes) and in medical applications such as blood analysis. UV-B LEDs are used in the field of phototherapy [71, 72], especially for the treatment of diseases such as psoriasis and vitiligo, and in lighting for plant growth. UV-C LEDs allow decontamination and sterilization of water [73, 74, 75], for example for wastewater treatment, recycling and disinfection of medical equipment and food. UV-B and UV-C LEDs are also used for bioagent detection and identification, since many gases, such as sulfur dioxide (SO_2), NO_x compounds and ammonia (NH_3), and several biomolecules, such as tryptophan, NADH, tyrosine, DNA and RNA, have absorption bands in these spectral ranges [76, 77, 78].

Despite their excellent potential and their advantages, there are still many factors that slow down their market penetration. The aim of this chapter is to give a description of UV LEDs state of the art and of the main problematics related to these devices.

4.1 State of the Art

The most common substrate used for UV-LED heterostrucures is (0 0 0 1) oriented c-plane sapphire, since it is available in various sizes with diameters in the range of $2-8$ inches for commercial wafers. Moreover, sapphire wafers have become very inexpensive, since they are used in large volumes for blue LEDs production. Sapphire is transparent across the entire UV spectral range, a very important feature in order to have a good extraction efficiency. Usually, metalorganic vapor phase epitaxy (MOVPE) is used in order to grow these devices. Sapphire substrate is electrically insulating and for this reason, a Si-doped n-AlGaN current spreading layer is deposited above the substrate in order to have uniform lateral current-spreading and injection of electrons into the AlGaN MQWs. The active region consists usually in a few nanometer thick AlGaN or InAlGaN QWs separated by (In)AlGaN quantum barriers, in this way the emission

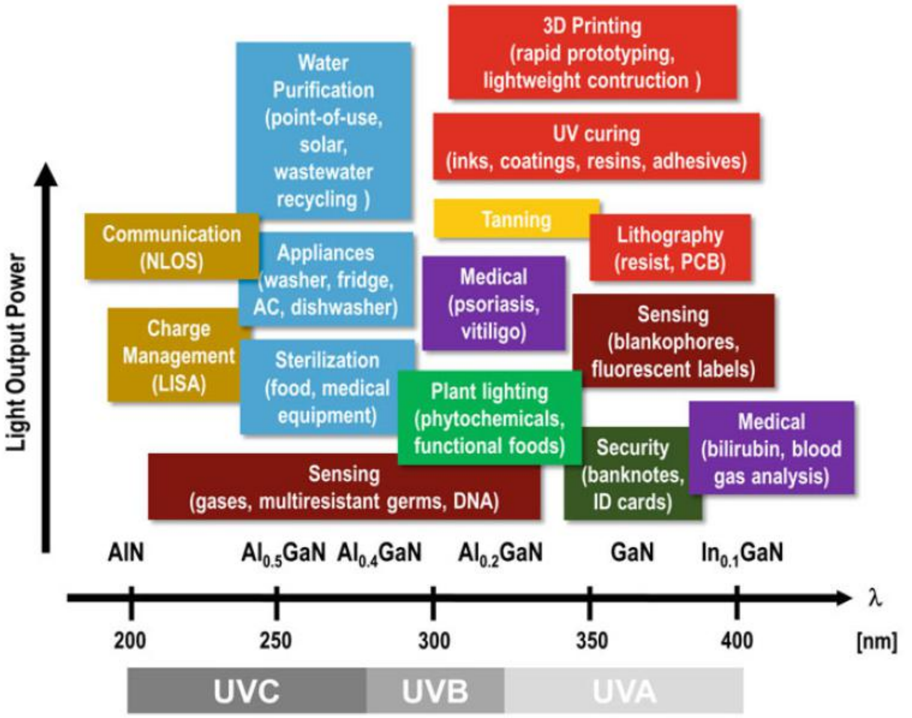

Fig. 1.2 Applications of UVA (400–320 nm), UVB (320–280 nm), and UVC (280–200 nm) LEDs

Figure 4.2: Applications of UV LEDs [10].

wavelength is related to the Al or In mole fractions. A schematic example of an (In)AlGaN MQW UV-LED heterostructure is reported in Figure 4.3.

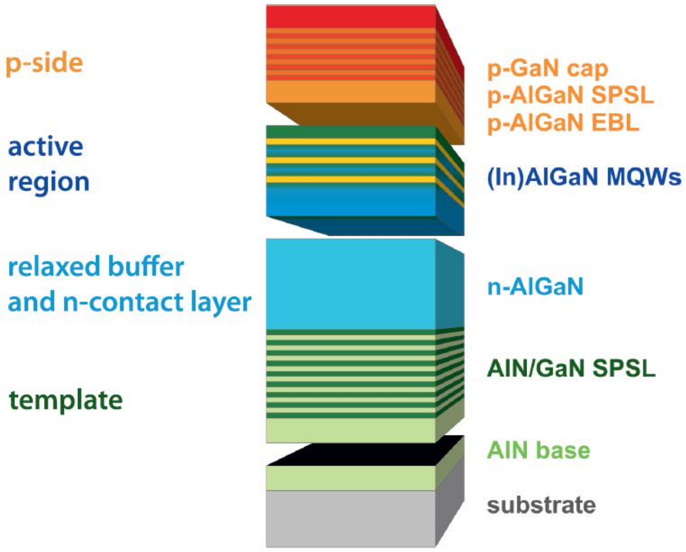

Figure 4.3: Schematic illustration of an (In)AlGaN MQW UV LED [69, 79]

Strong spontaneous and piezoelectric polarization charges arise at AlGaN heterostructure interfaces, creating polarization fields in the QWs and consequently causing the QCSE. The difference in Al mole fractions between AlGaN QWs and AlGaN barriers has a strong impact on the magnitude of the polarization field.

An Mg p-doped EBL is usually used in order to facilitate the hole injection into the QWs. This is followed by an Mg-doped short period superlattice layer (SPSL), or in other case by an Mg-doped bulk layer, that should be UV transparent in order to prevent UV absorption.

4.2 Internal and external quantum efficiency

One important factor that limits the UV LEDs market penetration is their low external quantum efficiency. UV-A LEDs are able to reach EQEs above 30%, but UV-B and UV-C LEDs still exhibit EQEs of $1-3\%$, i.e. very low efficiencies [10]. Higher values of EQE can be achieved only by improving the different terms that contribute to the EQE, remembering that

$$\eta_{EQE} = \eta_{IQE} \cdot \eta_{ext} \tag{4.1}$$

Starting from the IQE, the low values for this parameter are usually attributed to the high defect density in AlN and AlGaN layers. For example, threading dislocations may form non-radiative recombination pathways, leading to a reduction in IQE and consequently in EQE [80, 81]. These dislocations form deep levels within the bandgap that act as non-radiative recombination centers for holes and electrons. To reduce the dislocation density in AlGaN and AlN layers grown on sapphire substrate, various techniques have been developed: one of these is the use of a SPSL between the AlGaN layer and the AlN buffer layer, like Figure 4.4 reports. This layer consists of AlN/GaN layers and allows to significantly reduce the dislocation density [69].

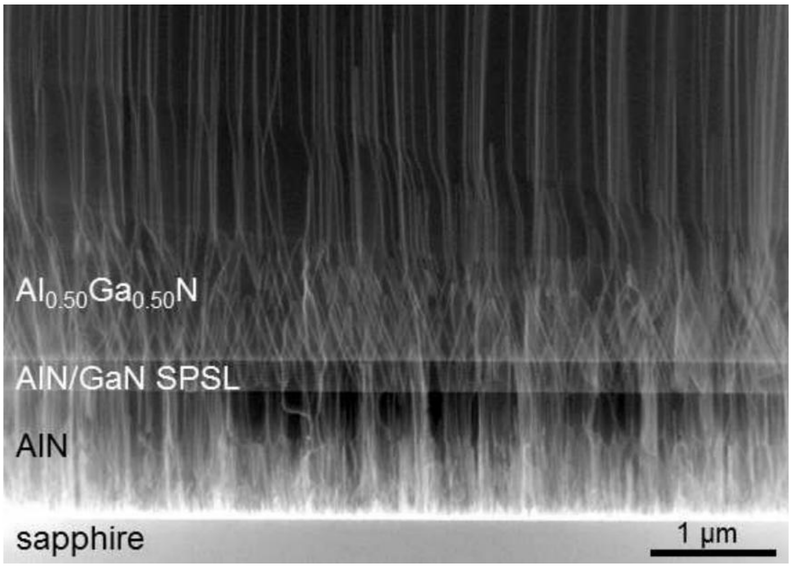

Figure 4.4: TEM image of an AlGaN-template with SPSL [69].

Together with a high value of IQE, it is also necessary a high value of extraction efficiency. As already mentioned in Chapter 2, an important problem in GaN-based LEDs is the electron escape from the active region to the p-type region, where they can recombine radiatively or not with holes. Generally, an EBL with a high Al mole fraction is located between the active region and the p-side, Mg-doped in order to allow the holes injection. However, due to the high activation energy of Mg acceptors, when a high concentrations of aluminum is present, it is very difficult to realize a p-doped AlGaN EBL: other alternative solutions to improve the carrier injection are the use of a multiquantum-barrier EBL [82] or an electron blocking heterostructure (EBH) [83]. The EBH, in particular, is placed after the active region and consists of a thin layer of Al(Ga)N with a very high aluminum content followed by a thick layer of AlGaN with a lower aluminum content.

4.3 Light extraction

The parameter that mainly limits the performance of UV LEDs is the light extraction efficiency, which has a very low value due to internal reflection on the substrate and the strong absorption of p-GaN [84]. In general, most of the methods used to improve light extraction in visible-emitting LEDs are not applicable to UV-LEDs: as a result, completely new technologies have been developed to improve light extraction, such as the use of photonic crystals [85], roughening of surfaces, patterning of substrates, chip shaping, micro-pixel LEDs and omnidirectional reflectors [85, 86, 87, 88, 89].

It is important to notice that the light extraction efficiency is heavily influenced by the design of the metal contacts. Usually, a transparent substrate (e.g. sapphire) is used for light extraction; in this way, it is easy for the light emitted in opposite directions (i.e. towards epitaxial layer and p-type metal contact) to be lost. Using, instead, metal contacts that reflect UV radiation and p-type layers that are transparent to the emitted photons, part of the emitted light can be reflected back and the chances of the light being extracted through the substrate increase. However, it is difficult to find suitable materials for the realization of such contacts: for example, even if, in the visible and near UV range, silver contacts reflect light well, this reflectivity undergoes a rapid collapse for wavelengths smaller than 350 nm. In addition, Al, which may reflect light well over the entire UV range, does not form an ohmic contact with the Mg-doped p-AlGaN layer, due to its low work function. An approach in order to obtain ohmic contacts that are able to reflect UV is the use of nano-pixel LEDs [90].

Another big challenge is to find suitable materials for encapsulation and packaging. LED encapsulation leads to several advantages: it protects the chip and bonding wires from mechanical damage, and also prevents contact oxidation. Besides this, another fundamental property of an encapsulation is the increase in extraction efficiency, since it allows to obtain a more extended light extraction cone. For example, the extraction efficiency of LEDs emitting in the visible spectral range can be improved by using dome-shaped encapsulations; these encapsulations are called epoxies, since they consist of materials such as plastics or resins, and present a refraction index between that of the air and the semiconductor. The use of polymers for the encapsulation of UV LEDs is not easy to achieve, since many resins absorb in the near UV, causing the degradation of the package: for example, in the visible the polymethylmethacrylate (PMMA) is used, which is characterized by a strong absorption in the ultraviolet range. Therefore, it is critical the research for UV-transparent, long stable and high index encapsulation materials, in order to improve the light extraction and the output power of UV LEDs. Currently, polymers based on dimethyl chains, such the polydimethylsiloxane (PDMS) have been used as LED encapsulants [91].

Another method to increase the extraction efficiency is to realize the LED using the technology called flip chip bonding [92]: the bonding wires, normally used to fix the LED to the printed circuit board, are eliminated and replaced by spheres distributed over the whole area below the active surface of the chip. As shown in Figure 4.5, the chip has an inverted structure, i.e. it is mounted on a support and the substrate is in the upper part: the light is extracted through the sapphire substrate, avoiding absorption by the p-type ohmic contact. Furthermore, if the contacts are replaced with highly reflecting mirrors, the downwardly propagating light can be returned upwards and extracted through the substrate. Another advantage is the reduction of the thermal resistance of the device, thanks to a more efficient transfer of heat through the metal pads of bonding.

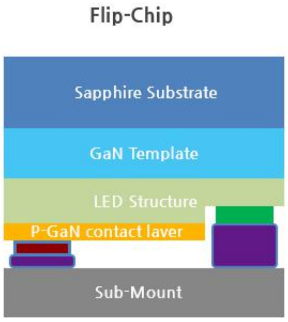

Figure 4.5: Structure of a LED realized by means of the flip chip technique; the light is collected from the transparent substrate.

4.4 Degradation of UV LEDs

Degradation is an important issue for UV LEDs. Usually the first hours of operation are critical for these devices, since they exhibit rapid degradation of the optical power, in some cases even very short lifetimes, especially for UV-B and UV-C LEDs [74, 93]. Improving lifetime is necessary in order to provide these devices for real-world applications and to replace conventional UV sources. Nowadays, state-of-the-art UV-B LEDs with emission wavelength around 310 nm and near 280 nm exhibit L50 lifetime of more than 10000 hours [94, 95] and 3000 hours [96]. Instead, for UV-C LEDs with emission wavelength below 270 nm, L50 lifetimes above 1000 hours have been reported [97]. Degradation, together with UV LEDs light output power, has a strong dependence on temperature. Many LEDs failures are caused by overheating. For this reason, thermal management is critical for high performance UV LEDs [98, 99, 100]. Again, flip chip mounting is a good solution, since it provides an excellent heat extraction for thermal management. Together with temperature, also current has a strong impact on the device degradation. The study of the impact of these parameters on the device degradation is usually carried out by means of accelerated stress test.

Many improvements have been achieved in the development of ultraviolet LEDs. Unfortunately, these progresses are still slower compared to the ones for visible GaN-based LEDs. In this chapter, we have shown the different challenges that many researchers have run into in the development of these devices. In the following chapters, the work carried out on different types of UV LEDs will be presented. The aim of this work was to contribute to this research, in order to improve the efficiency of these devices, trying to better understand the physical mechanisms responsible for their degradation, in particular the impact of point defects in these processes. The work was carried out on a group of commercially available UV-A LEDs and a group of UV-B LEDs provided by the research group from the Ferdinand Braun Institut (FBH).

Chapter 5

Degradation of UV-A LEDs: physical origin and dependence on stress conditions

The chapter presents an extensive analysis of the degradation of four gorup of commercially available UV-A LEDs submitted to constant current stress. The study is based on combined electrical, optical, and thermal measurements. The following results were published in [101].

5.1 Introduction and motivation

Recently, high power UV-A LEDs have become commercially available; the typical optical power levels are in the range $175-500$ mW for emission wavelengths in the range between 385 nm and 420 nm. The high operating power levels may lead to a premature degradation of the devices. In the literature several papers investigated the degradation processes of visible (blue/white) GaN-based LEDs; on the other hand, only little information has been published on the physical origin and degradation kinetics of UV LEDs. As already mentioned in the previous chapter, the performance of UV-LEDs is still limited: InGaN/GaN quantum wells emitting in the range $365-420$ nm suffer from escape and overflow processes, due to the small height of the confinement barriers (in the range $0.1-0.15$ eV or even lower). The low efficiency of UV LEDs results in significant self heating and enhanced non-radiative recombination; these factors can significantly limit the reliability of the devices.

The aim of this study is to contribute to the understanding of the physical mechanisms responsible for the degradation of UV-A power LEDs; four different groups of commercially available UV-LEDs emitting at different wavelengths (between 385 nm and 420 nm) were taken into account. More specifically, the aim was (i) to investigate the physical origin of degradation by combined electrical/optical/thermal measurements, (ii) to analyze the degradation kinetics, and, therefore, extrapolate the lifetime, and (iii) to understand the dependence of time-to-failure (TTF) on wavelength and temperature. Results demonstrates that: a) the UV-A LEDs submitted to constant current stress show a gradual degradation, and the degradation rate is strongly dependent on the emission wavelength; b) the degradation process is ascribed to the generation of point defects within the active region of the devices, with a subsequent increase in the non-radiative recombination rate; and c) the time to degradation is strongly dependent on the stress current level and is thermally activated (activation energy equal to 0.36 eV).

5.2 Experimental details

The analysis was performed on four groups of commercially available GaN-based UV-LEDs, each with a different peak emission in the UV-A spectral range: the nominal peak wavelengths are 385, 395, 405, and 420 nm. The samples have a nominal operating current of 1 A. More details on the characteristics of the devices from the datasheets are reported in Table 5.1.

Electrical and optical measurements were carried out at different temperatures (in the range 15 − 85°C); a full thermal characterization was performed to extract the thermal resistance of the samples, based on the forward-voltage method. After these preliminary analysis, a set of devices for each group was submitted to constant current stress. Considering the nominal operating current of the samples (1 A dc), four different current levels were chosen: 1.0, 1.1, 1.2 and 1.3 A. Thereafter, another set of devices was stressed at different temperature levels, RT (25°C), 50°C, and 75°C, with the same current level (1 A). During stress the electrical and optical parameters of the devices were continuously monitored.

Table 5.1: Electrical and optical characteristics fo the UV-LEDs (T_j = 25°C and $I = 500$ mA).

Parameters	**385 nm**	**395 nm**	**405 nm**	**420 nm**
Forward Voltage (V)	3.2	3.1	3.0	3.0
Radiometric Power @ 500 mA (mW)	175	375	525	575
Measured Wall Plug Efficiency ($I = 1$ A, %)	6.9	23.6	34.6	34.1

5.3 Thermal characterization

The thermal resistance of the devices was characterized by means of the forward-voltage method [102]. Within the calibration phase we characterized the relation between forward voltage and junction temperature, at several current levels. The calibration measurement consists of a certain number of pulsed I-V characterization with very short pulses and low duty cycle, with the devices mounted on a Peltier-based temperature controller. Since the duty cycle of the pulsed current is very low, the heat generated by the pulsed current can be neglected and the junction temperature can be assumed , with very good accuracy, to be equal to the Peltier-based temperature controller. The same process is repeated for different (pulsed) current levels. Representative results obtained on a sample emitting at 385 nm are reported in Figure 5.1; with increasing temperature, the operating voltage of the LEDs decreases almost linearly, with a negative slope in the range 1.57 – 1.67 V/°C. After this preliminary calibration phase, we mounted the samples in their final stress fixture, and applied a constant current. The voltage reached at the end of the self-heating transient was directly converted to the corresponding junction temperature by using the results of the calibration phase. In this way it was possible to estimate the junction temperature of the devices in the final stress conditions.

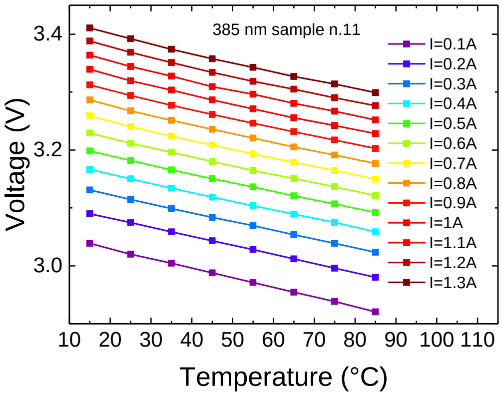

Figure 5.1: Forward voltage versus oven temperature for one of the samples emitting at 385 nm at various bias current levels.

The average results obtained on the 4 groups of LEDs are reported in Figure 5.2, that reports the relation between junction temperature and operating current. Remarkably, for the same operating current the devices with shorter wavelength reach a stronger self-heating with respect to the others. At a current level of 1 A, the difference between the junction temperature of the LEDs emitting at 385 nm and 420 nm is about 50°C. This difference can be explained by the fact that the wall plug efficiency of the LEDs decreases significantly with decreasing wavelength (from 34.1% of the LEDs emitting at 420 nm to 6.9% of the LEDs emitting at 385 nm, see Table 5.1), thus resulting in a stronger self-heating.

In Table 5.2, the thermal resistance for each group of samples is reported.

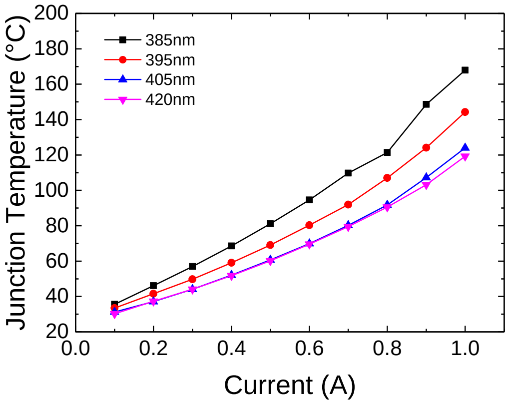

Figure 5.2: Junction temperature as a function of current for the four types of UV-LEDs. Devices emitting at 385 nm exhibit a higher junction temperature than those emitting at higher wavelengths.

Table 5.2: Extrapolated values of thermal resistance for the four UV-LEDs

	385 nm	**395 nm**	**405 nm**	**420 nm**
R_{th} (°C/W)	49.4	52.5	56.2	47.3

5.4 Electrical characterization

Figure 5.3 shows the electrical characteristics (current-voltage) at different temperatures of one of the samples emitting at 385 nm. Higher temperatures result in higher current levels, both in the low forward-bias region and under reverse-bias.

The comparison between the four groups of LEDs emitting at different wavelengths showed that the current at low forward bias (around +2 V) has a stronger dependence on temperature for the LEDs with shorter emission wavelength, i.e. for the LEDs with shallower quantum wells (see the inset of Figure 5.3). This kind of process can be ascribed to the so-called trapp-assisted-tunneling (TAT) process [103], that in this case is more pronounced for the sampes emitting at lower emission wavelength. We also have to consider a more pronounced carrier escape in these samples, due to the higher band gap energy of the quantum wells and consequently to the smaller band offset with respect to the barriers (for the devices emitting at 385 nm the offset in conduction and valence band are 0.23 eV and 0.1 eV respectively).

In order to investigate the origin of reverse leakage current, we report the reverse current at a bias of -5 V in an Arrhenius plot, as shown in Figure 5.4 for the sample emitting at 385 eV. Two mechanisms are usually considered as responsible for the reverse current conduction: variable-range hopping (VRH) [104], [105] and thermally assisted multi-step tunneling [105]. VRH has the following dependence on temperature $I \propto I_0 \exp[(T_0/T)^{1/4}]$, where T_0 is the characteristic temperature. Our data on reverse current conduction can not be effectively fitted according to the VRH mode, consistently with its usual relevance at lower temperatures [104], [105]. On the other hand, as shown in Figure 5.4, in our samples the reverse current has an Arrhenius-like dependence on temperature, $I \propto \exp[E_a/(kT)]$, where E_a is the activation energy. This result is consistent with the hypothesis that the reverse leakage current occurs through thermally assisted multi-step tunneling [105]: the electron moves from the valence band of p-GaN to the conduction band of n-GaN by a thermally-activated multi-step tunneling (Figure 5.5). A linear fit in the Arrhenius plot yields activation energy of about 0.59 eV for the devices emitting at 385 nm. As described in [105], the thermal activation energy is attributed to the excitation of electrons from deep centers to the conduction band (or to the corresponding process in the valence band).

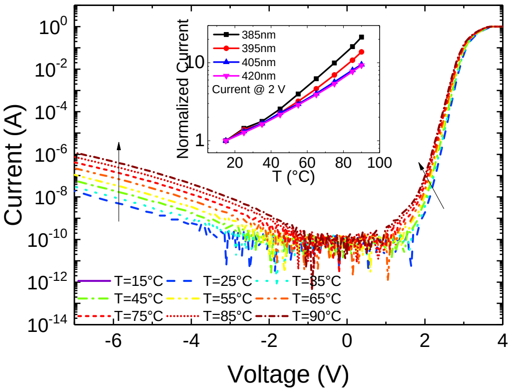

Figure 5.3: I–V characteristics measured at different temperatures on one of the analyzed samples emitting at 385 nm. Inset: variation of forward current (at +2 V) with temperature for the four groups with different emission wavelengths.

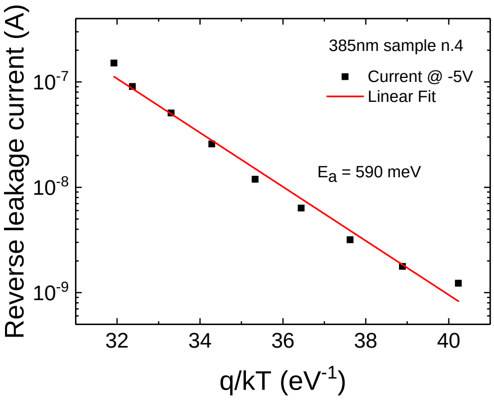

Figure 5.4: Arrhenius plot and activation energy of the reverse leakage current at 5 V of one of the samples emitting at 385 nm. A thermally assisted multi-step tunneling model is used to fit the experimental data.

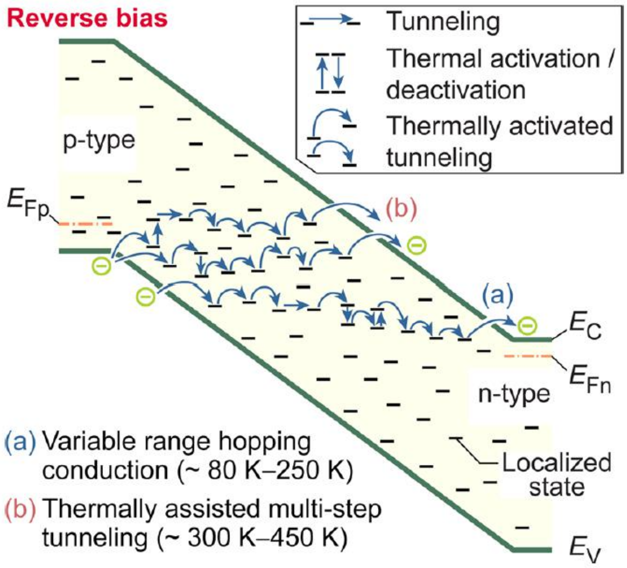

Figure 5.5: Schematic diagram of hopping conduction and thermally assisted multi-step tunneling [105].

5.5 Optical characterization

In Figure 5.6, we report the optical power measured at 1 A as function of temperature for the four different UV-LEDs. As shown in Figure 5.6, the thermal droop (i.e. the decrease in optical power with increasing temperature from 15°C to 90°C) is stronger (50%) for the devices with shorter emission wavelength, and decreases significantly for the devices with longer wavelength ($\sim$ 10% for the devices emitting at 420 nm). According to the literature, the decrease in optical power with increasing temperature can be attributed to two main factors [106]: first, a higher thermal energy of the injected carriers, which promotes the carrier escape from the QWs; second, the increase of the non-radiative recombination rate in the QWs due to the increase of the temperature. Considering the structure of the analyzed samples, the main difference between the four sets of analyzed samples is the emission wavelength (λ). The differences in λ correspond to different band offsets (ΔE_c and ΔE_v) from the quantum wells to the barriers, ranging from $\Delta E_c = 0.23$ eV for the devices emitting at 385 nm to $\Delta E_c = 0.42$ eV for the devices emitting at 420 nm. For this reason we ascribe the stronger thermal droop observed in the devices with shorter wavelength to the thermal escape of the carriers from the quantum wells (due to the poor confinement in short wavelength devices).

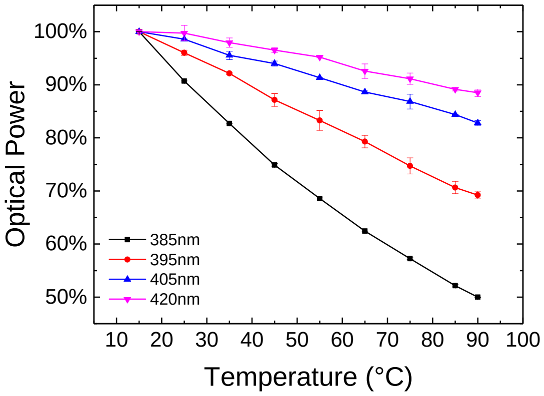

Figure 5.6: Optical power reduction (measured at 1 A) with increasing temperature for the four analyzed UV-LED groups (the error bars highlight the standard deviation).

5.6 Constant current stress

After this preliminary electrical and optical characterization, the devices were submitted to stress test at four different current levels: 1 A (nominal operating current), 1.1 A, 1.2 A, and 1.3 A. We report the results for the 1 A stress on one of the 385 nm UV-LEDs; the other sets of samples showed similar degradation modes, with different kinetics. Stress induced a significant optical power decrease (Figure 5.7(a)). Figure 5.7(b) reports the evolution of the optical power of the same sample during stress at 1 A. Stress induces a significant decrease in the optical power emitted by the device. More specifically, the degradation kinetics show a first fast decrease of the optical power during the first 100 minutes, followed by a slower drop.

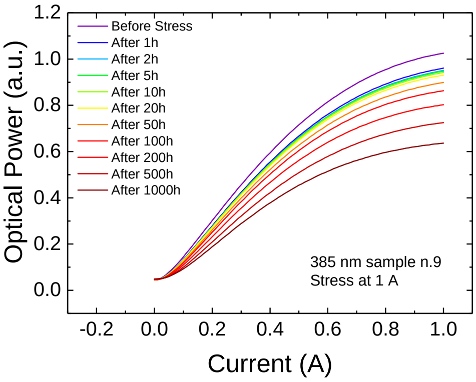

(a)

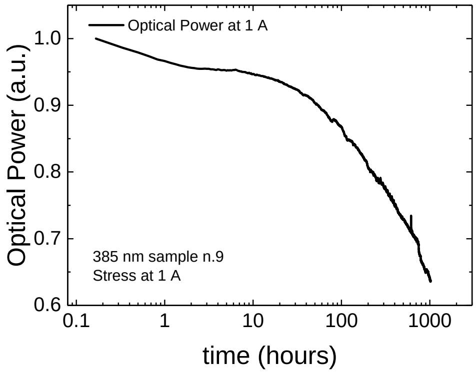

(b)

Figure 5.7: (a) L–I characteristics measured on one of the analyzed samples with a peak emission wavelength of 385 nm during stress at nominal current (1 A). (b) Normalized optical power as a function of time.

A third very fast phase of the degradation appears to be related to the increase in the power dissipated by the devices, and this can be observed especially for stress current levels higher than 1 A (see Figure 5.8(b) for stress at 1.1 A). This behavior is more evident for the samples emitting at 385 nm, probably because of their higher forward voltage, causing a higher dissipated power.

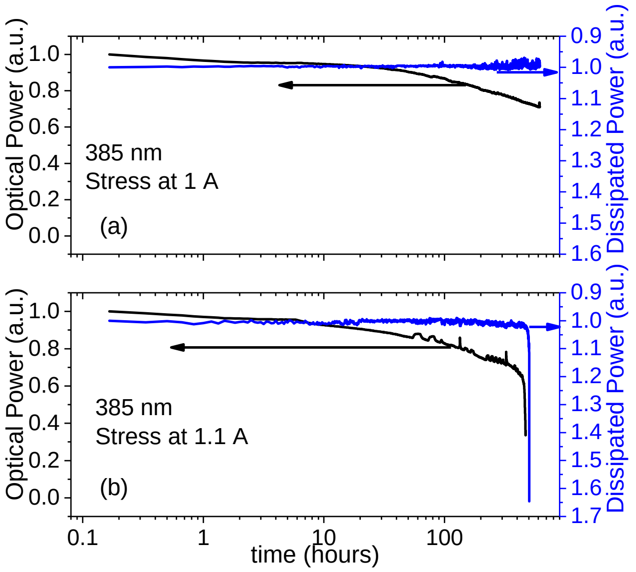

Figure 5.8: Optical power and dissipated power as a function of temperature for two of the samples emitting at 385 nm: (a) for stress current level of 1 A and (b) for stress current level of 1.1 A. The dissipated power axis is reverse to better compare it with the optical power.

To gather more accurate information on the degradation process we carried out an extensive characterization of the electrical parameters. Figure 5.9(a) shows the I–V characteristics of the same sample emitting at 385 nm. An increase in the reverse leakage current is evident with the aging of the device. Figure 5.9(b) shows this behavior at 3 V during stress: this is due to the generation of defects, within or around the active region, promoting conduction through tunneling [105], [107] and/or hopping [104], [108].

The analysis of the 385 nm I–V characteristic indicates also an increase in the sub-threshold forward current (see the region between 0 V and 2 V in Figure 5.9(a)). To better understand this behavior, we evaluated the ideality factor, that is determined by carrier transport, recombination and resistivity. The values expected from the Sah–Noyce–Shockley model [109] are 1.0 to 2.0, but GaN-based junctions generally present ideality factors higher than 2. Shah et al. [110] proposed a model where they consider two additional rectifying junctions. Therefore, the measured ideality factor is the sum of the ideality factors of the various rectifying junctions of which the LED is constituted. Other groups ascribe the high value of the ideality factor to the occurrence of tunneling processes [111, 112, 113]. In Figure 5.10(a), we report the ideality factor

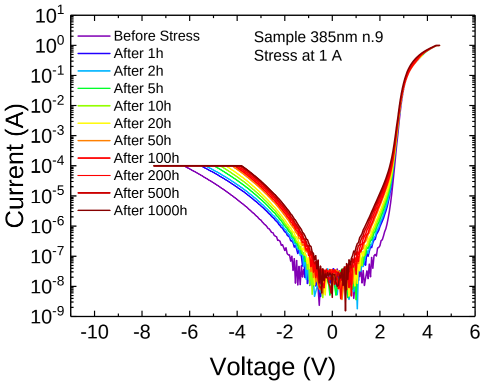

(a)

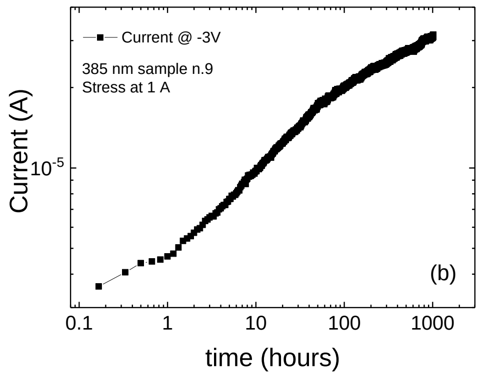

(b)

Figure 5.9: (a) Electrical degradation of one UV-LED emitting at 385 nm during stress at 1A. (b) Reverse leakage current of the same LED at3V during stress.

evaluated during the stress test. Within the first hour, the ideality factor is close to 2: in the Sah–Noyce–Shockley model this indicates that the recombination current is the major mechanism of the current transport [114]. These values are consistent with other works on GaN-based LEDs [115]. The analysis of the ideality factor provides information on the degradation process [116]: in this case, with increasing aging time, the ideality factor increases linearly. This trend is generally ascribed to the generation of point defects within the active region, that assist electron tunneling in quantum wells as well as non-radiative recombination [114]. For low current levels, it is possible to observe a correlation between the variation of the ideality factor and the decrease in optical power (Figure 5.10(b)). This result is also consistent with the hypothesis that stress induced an increase in defects responsible both for trap-assisted tunneling (TAT) and non-radiative recombination [103].

5.7 Dependence of lifetime on stress conditions

The dependence of lifetime on the stress conditions was analyzed by stressing identical devices at several current levels between 1 A and 1.3 A. The TTF was defined as the time required to reach a 30% optical power decrease. Figure 5.11 reports the results obtained on the UV-A LEDs emitting at 385 nm. For a current level of 1.3 A, the degradation is faster than at 1 A. After 900 minutes of stress, in fact, the optical power of the sample stressed at 1.3 A has dropped by almost 30% of the initial value, while for the sample stressed at 1 A the optical power is still higher than 90% of its initial value. The dependence of time-to-failure on stress current is summarized in Figure 5.12. The almost linear dependence of TTF on stress current demonstrates that current is a relevant driving force for the degradation process; this result supports the hypothesis that the generation of defects (responsible for the optical power decrease and for the changes in the I–V curves) is activated by the flow of carriers through the active region of the devices. Such carriers may have enough energy to interact with the lattice, break atomic bonds, and generate non radiative defects within the active region [117].

In the literature several types of point defects have been proposed as responsible for the degradation of GaN-based LEDs, like nitrogen antisite defects [118, 119, 120], defects related to foreign impurities, such carbon [121], and point defects related to gallium vacancies [122].

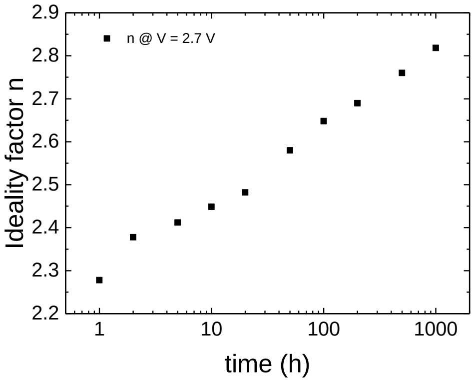

(a)

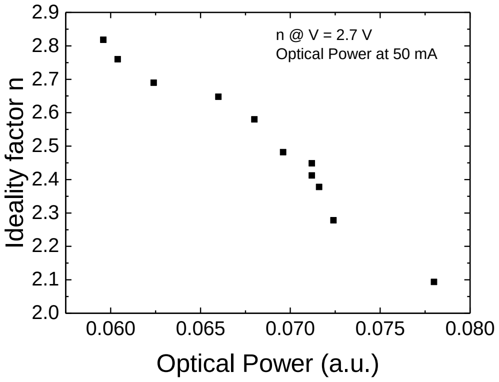

(b)

Figure 5.10: (a) Ideality factor of UV-LED emitting at 385 nm at 2.7 V during the aging process. (b) Correlation between ideality factor at 2.7 V and optical power at 50 mA.

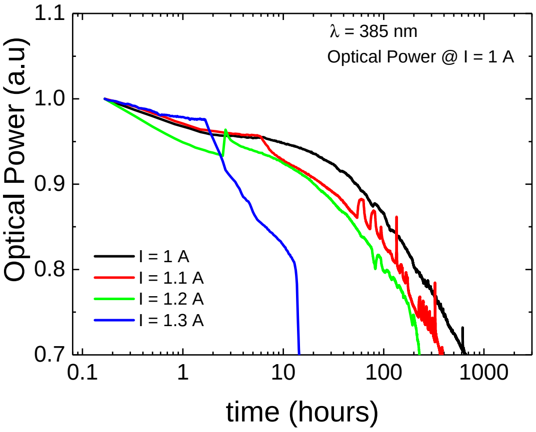

Figure 5.11: Optical power degradation of UV-LED emitting at 385 nm during the aging process for different stress current levels.

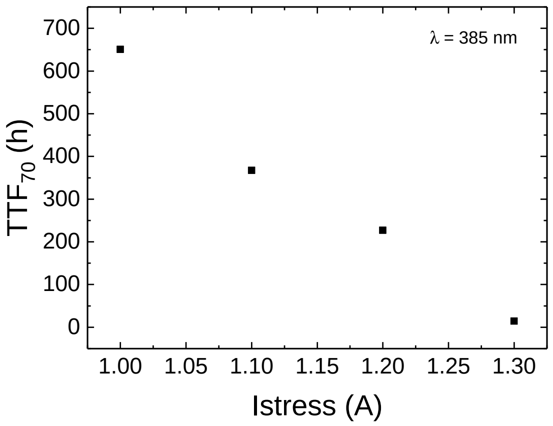

Figure 5.12: Time-to-failure (L_{70}) for one of the samples emitting at 385 nm.

To better understand the role of the temperature in the device degradation, we carried out a stress test at fixed current level (1 A) with different temperature levels on another set of samples emitting at 385 nm. We chose three stress temperature levels: 25°C (room temperature), 50°C and 75°C. As in the thermal characterization, the devices were mounted on a Peltier-based temperature controller. Figure 5.13 reports the optical power degradation during the stress for the different stress temperatures at a current level of 20 mA. For low measuring current levels we observed a more pronounced decrease of the optical power, due to an increase of the defectiveness of the active layer [123]. As shown in Figure 5.13, the optical power degradation is slightly accelerated by temperature, with an Arrhenius temperature dependence. By defining the time-to-failure (TTF80%) as the time necessary to reach a 20% decrease in optical power, we extrapolated the Arrhenius plot in Figure 5.14. The activation energy of the degradation process is equal to $E_a = 0.36$ eV, that is consistent with previous papers on the topic: Ikeda et al. [124] and Asano et al. [125] reported a similar value, 0.32 eV, while other groups found a slightly higher value, 0.5 eV [126], [127]. A low activation energy suggests a weak dependence of the degradation kinetics from temperature; the degradation process is therefore supposed to be electro-thermally activated, since the degradation rate has a linear dependence on temperature, and TTF is thermally-activated.

We also investigated the dependence of the degradation kinetics on the emission wavelength of the devices: the results indicated that the devices with longer wavelength (i.e. with higher indium content in the quantum wells) show a weaker degradation. Figure 5.15 reports the optical power degradation measured after 10000 minutes as

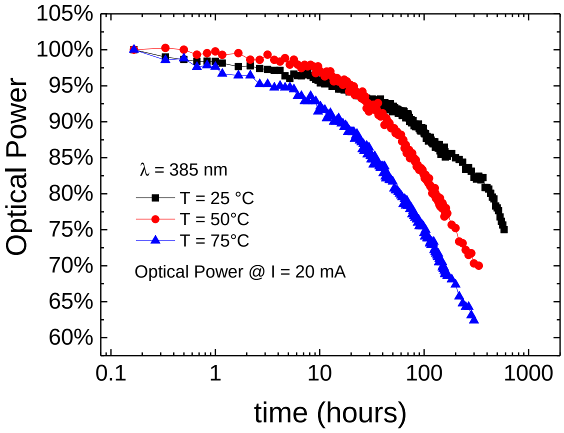

Figure 5.13: Optical power degradation of UV-LED emitting at 385 nm during the aging process for different stress temperature levels.

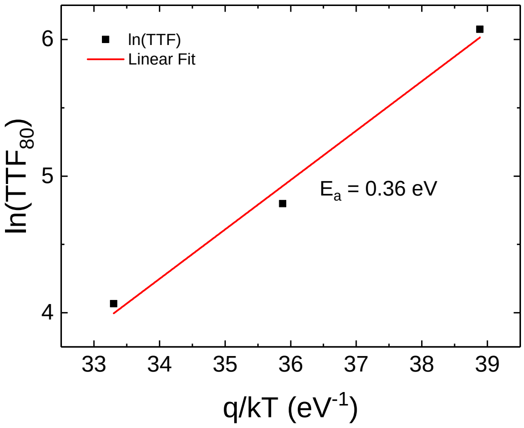

Figure 5.14: Arrhenius plot of the TTF80% during temperature aging for UV-LEDs emitting at 385 nm. The line represents the linear fitting of data.

function of wavelength for the devices stressed a 1 A, 1.1 A, and 1.2 A. The stronger degradation of the devices with shorter wavelength can be explained by the following process: as indicated in Table 5.1, the devices emitting at 385 nm have a significantly lower wall-plug efficiency (WPE = 6.9%) with respect to those emitting at 420 nm (WPE = 34.1%), due to the stronger escape/overflow of carriers out of the quantum wells. This means that the devices with shorter emission wavelength show a stronger self-heating, that can accelerate the degradation kinetics as previously described in [128], [129] (see also Figure 5.13). In addition, overflowing carriers can release their excess energy as lattice vibrations (phonons), thus accelerating the defect-generation process.

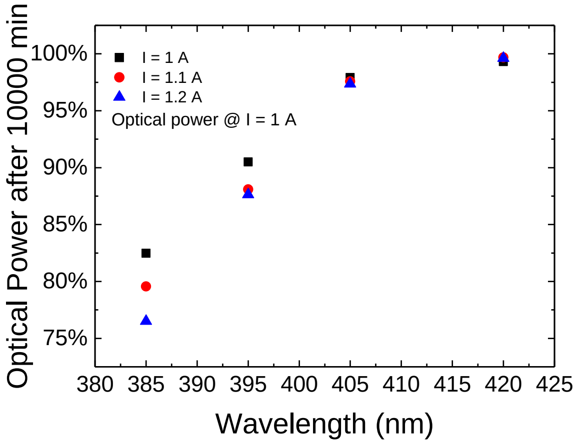

Figure 5.15: Optical power degradation after 10000 minutes as a function of wavelength for three different stress current levels.

5.8 Conclusion

We have investigated the performance of four groups of InGaN-based UV-LEDs, each of them emitting at a different wavelength. Results indicate that UV-A LEDs show optical degradation during aging, and this degradation is strongly correlated to the emission wavelength: samples emitting at 385 nm exhibit a more pronounced degradation, while degradation of samples emitting at 420 nm is almost negligible. The origin of this degradation is ascribed to the generation of point defects within the active region of the devices, that results in an increased non-radiative recombination, and in a significant change in the ideality factor. Degradation is also strongly dependent on the stress current level and is thermally activated, especially in the case of the devices emitting at 385 nm.

Chapter 6

Defect-related degradation of AlGaN-based UV-B LEDs

This chapter describes an extensive analysis of the degradation of InAlGaN-based UV-B LEDs, provided by FBH, submitted to constant current stress. The study is based on combined electrical characterization, spectral analysis of the emission, deep-level transient spectroscopy (DLTS) and photocurrent (PC) spectroscopy. The results described in this chapter were published in [130].

6.1 Introduction

During operation, UV-B LEDs can show a decrease in the efficiency, an increase in the operating voltage, and – in some cases – reach catastrophic failure [123]. The physical origin of degradation is still under investigation. Early technologies showed a relatively fast degradation, taking place in the initial few hundred hours [123, 131, 132]. In [131], the optical power reduction over time of 280 nm LEDs was investigated: the results showed a strong correlation between optical power degradation, operating current and junction temperature. The activation energy of the degradation process was found to be in the range 0.23 eV − 0.27 eV; similar values were reported in [95], in the range 0.13 eV − 0.27 eV. Other studies [123], [132] suggested that operation induced stress may favor the increase in point defect density; nitrogen vacancies or Mg-dopant atoms are known to reduce the optical power during the operation of the device.

The aim of this work is to give a contribution to the understanding of the physical origin of the degradation of InAlGaN-based UV-B LEDs. Based on combined electrical-optical measurements, deep level transient spectroscopy and photocurrent spectroscopy, we describe the role of defects in changing the electro-optical performance of the devices; more specifically, the results of this analysis demonstrate that: (i) UV-B LEDs show a gradual degradation when submitted to constant current stress; the decrease in optical power is stronger for low measuring current levels, indicating that degradation is related to the increase in SRH recombination; (ii) the current-voltage characteristics measured before/during stress show an increase in the current below the turn-on voltage, that is ascribed to the increase in trap-assisted tunneling (TAT) components; (iii) DLTS analysis and photocurrent spectroscopy measurements were carried out to identify the properties of the defects responsible for the degradation of the optical and electrical characteristics. The results indicate that stress induces or activates defects centered around 2.5 eV below the conduction band edge. These defects, close to mid-gap, can explain both the increased SRH recombination and the increase in TAT components detected after stress. Moreover, the DLTS measurements allowed to identify the signature of Mg-related acceptor traps.

6.2 Experimental details

The analysis was performed on a group of five UV-B LEDs with nominal peak wavelength around 308 nm. Devices were grown by metal-organic vaport phase epitaxy (MOVPE) on (0001) sapphire substrates. After a 700 nm thick AlN buffer layer, an AlN/GaN superlattice was introduced to relax the strain of an upper $\sim 4.5\ \mu$m thick buffer, and a Si-doped n-AlGaN current spreading layer. The active region is composed of 3x $In_{0.02}Al_{0.36}Ga_{0.62}N$ QWs (2 nm) nominally undoped, separated by AlGaN barriers. A 25 nm Mg-doped p-$Al_{0.7}Ga_{0.3}N$ EBL is employed, followed by a p-AlGaN SPSL and a p-GaN contact layer. The devices have a junction area of about $7.2 \cdot 10^{-4}$ cm^2, and are based on a standard chip processing technology [79]. Single chips were flip-chip mounted on AlN submounts using AuSn soldering without encapsulation. More details on the LEDs can be found in [69, 133].

The analyzed devices were submitted to stress at a constant current of 100 mA (nominal operating current, corresponding current-density = 140 A/cm^2) at room temperature, over approximately 1000 hours. The electrical and optical parameters were continuously monitored during stress. DLTS and PC spectroscopy measurements were carried out to investigate the processes related to the generation/propagation of defects within or close to the active region of the devices.

6.3 Optical characterization and spectral analysis

Figures 6.1 - 6.3 report the changes in the optical characteristics of the devices during stress time (the measurements were taken at room temperature). The degradation was found to be more prominent at low measuring current levels (Figure 6.1 and 6.3). This suggests that stress induces an increase in the defectiveness of the active layer, with subsequent increase in SRH recombination centers: at low measuring current levels, these centers can capture the injected carriers and promote their recombination through non-radiative processes, in contrast, at high measuring current levels, the non-radiative recombination centers are saturated by the high density of injected carriers. Therefore, the impact on the optical power degradation at high current levels is smaller [123], [134]. We can observe this behavior even better when looking at the evolution of the emission spectrum.

Figure 6.2 reports the emission spectra of a sample measured at 10 mA during stress. Stress causes a decrease of the main peak intensity (at 308 nm), with no significant modification of the peak emission wavelength. During aging, also the parasitic emission (between 330 and 380 nm) shows a decrease in intensity. This broad emission probably originates from electron-overflow from the QW region toward the p-side, where electrons recombine with holes [135]. Moreover, a previous report [136] indicated that recombination involves Mg-related acceptor levels. A better overview of the physical origin of the different parasitic peak will be given in Chapter 7. The decrease of the main (308 nm) and parasitic peak ($330 - 380$ nm) during the stress is ascribed to the increase in the SRH recombination, that causes an increase in the capture rate of the quantum wells (reduction in the 308 nm peak), and a consequent reduction in carrier overflow toward the p-side (reduction of the $330 - 380$ nm band).

Figure 6.3 shows the normalized peak intensity of the main peak during stress at different current levels: as already explained, we observed a strong decrease of the electroluminescence peak at low currents ($\sim$ 50% at 2 mA) as compared with high currents ($\sim$ 30% at 50 mA).

6.4 Electrical characterization

In order to better understand the physical mechanisms responsible for the optical power degradation, we report the I–V characteristics during the aging of the device in Figure 6.4. From the I–V curves, we can identify three main regions: 1) the reverse bias region; 2) the low-forward bias region (from 0 to $\sim$ 4 V); and 3) the bias region above

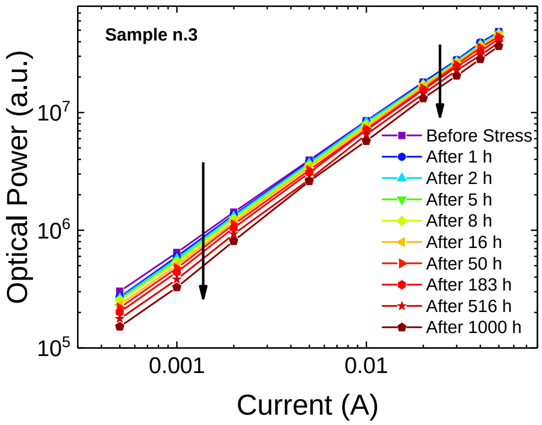

Figure 6.1: Optical power-current (L–I) characteristics measured on the analyzed sample during stress.

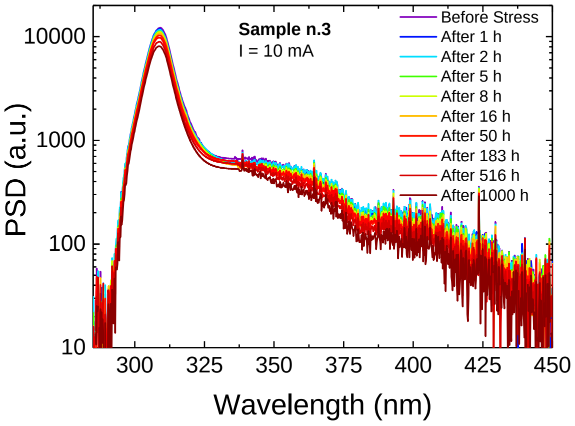

Figure 6.2: Emission spectra measured at 10 mA during stress.

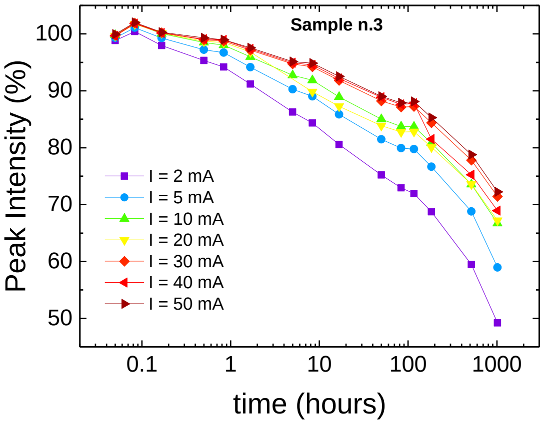

Figure 6.3: Peak intensity of the primary emission peak at different current levels during stress; the peak intensity is normalized with respect to the value at 0 h of stress.

the turn-ON voltage (from ∼ 4 V). In the first region, we observed an increase in the reverse leakage current during the aging of the device. In Figure 6.5, we report the reverse leakage current during stress measured at -3 V. After an initial stable phase ($t < 0.2$ h), the leakage current increases gradually, following a logarithmic dependence on stress time. The increase in the reverse bias leakage current has already been reported in other works [94], and, usually, is ascribed to the generation of point defects within or around the active region. This induces defect-assisted carrier transport, forming parasitic current paths across the active region. It is worth noticing that previous reports—based on in situ stress tests carried using transmission electron microscopy—indicated that degradation is not caused by dislocation multiplication [18], but more likely to the generation/activation of point defects.

In the second region (from 0 to ∼ 4 V), we observed an increase in the current below the turn-ON voltage. Previous reports indicated that the low-voltage behavior of LEDs is governed by TAT: before the LED reaches the turn-ON voltage, electrons cross the potential barrier by trap-assisted conduction, eventually recombining with a hole [103], [137]. The model assumes the presence of additional deep traps in the QWs with an energy level near mid-gap that assist the tunneling mechanism. The increase in subthreshold current (from 0 to ∼ 4 V), therefore, suggests that stress induces the generation of mid-gap states, thus leading to an increase in TAT. This hypothesis has been verified by means of PC analysis.

In the high-injection region, we observed a decrease of the drive voltage in the first 2 h, probably due to a decrease of the resistivity of the p-type material and/or

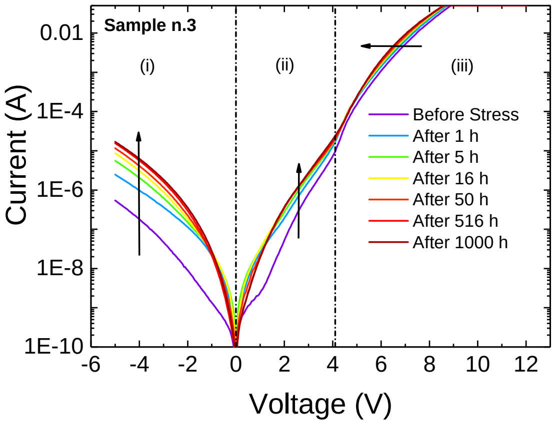

Figure 6.4: Current–voltage (I–V) characteristics of the 308 nm LED, measured at different stress times, where we can identify three main regions.

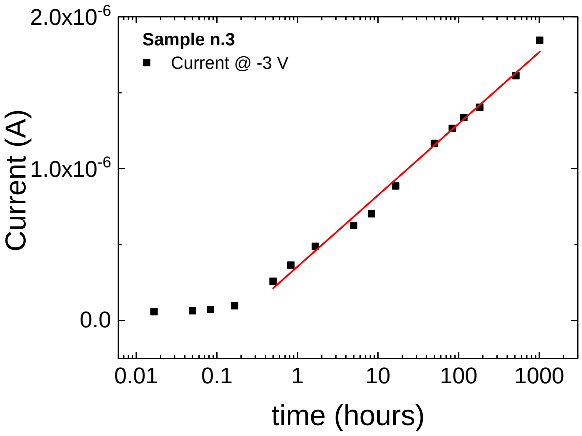

Figure 6.5: Reverse leakage current of a sample at −3 V during stress.

the resistance of the nonideal, i.e., partially Schottky-type, p-contact, followed by a gradual increase. The origin of the changes in the drive voltage is investigated in detail in the next section, based on the comparison with DLTS data.

6.5 DLTS analysis

In order to characterize the involved deep levels, we carried out a DLTS investigation during stress time. We performed two DLTS measurements (setup by Sula Technologies) between each stress step: one with a filling voltage (V_{fill}) of +1 V and a reverse measuring voltage (V_{rev}) of -1 V (that explores the semiconductor region next to the junction), and the other with a filling voltage of -3 V and a reverse measuring voltage of -5 V (in order to probe also the material toward the n-side of the junction). The duration of the filling pulse was set to 100 ms. The capacitance transient measurements were carried out with a measurement frequency of 1 MHz, in the temperature range between 83 and 440 K. It is worth noticing that due to the difference of the work-function of the p-side metal and the Fermi-level of the p-GaN cap layer, the p-side contact is not perfectly ohmic but has a partial Schottky nature. The (thin) space charge region at the p-side contact contributes to the overall device capacitance. However, the higher doping in the p-side at the contact compared with the n-side below the active region ensures that the capacitance variations are most likely dominated by the active region.

The DLTS spectra for $V_{fill} = -3$ V and $V_{rev} = -5$ V during the stress are reported in Figure 6.6. As we can see from Figure 6.6, the DLTS spectra present multiple peaks that are partially superimposed. In this case, the interpretation of the spectra could be quite complex: one possible explanation is that the positive peak, labeled as “h1,” decreases and shifts toward lower temperature during the stress, whereas a negative peak, labeled as “e2” becomes visible after 83 h of stress. A second possibility is that peak “h1” stays constant, instead peak “e2” is increasing and this produces an apparent decrease of “h1.” From the analysis of the DLTS peaks at different emission rates (not shown here for brevity), we can conclude that the first explanation is more likely. From the theory of DLTS analysis, we can say that a positive peak is related to minority-carriers trap levels, whereas a negative peak is related to majority-carriers [66], as we are considering traps in the low doped n-type layer next to the active region, where the minority carriers are the holes and the majority are the electrons. The Arrhenius plots of these deep traps are shown in Figure 6.7. During the stress, the activation energy of the trap h1 is in the range $0.11 - 0.24$ eV. The trap e2 has an activation energy in the range between 0.25 and 0.47 eV. The activation energy of trap e1 is equal to 0.14 eV.

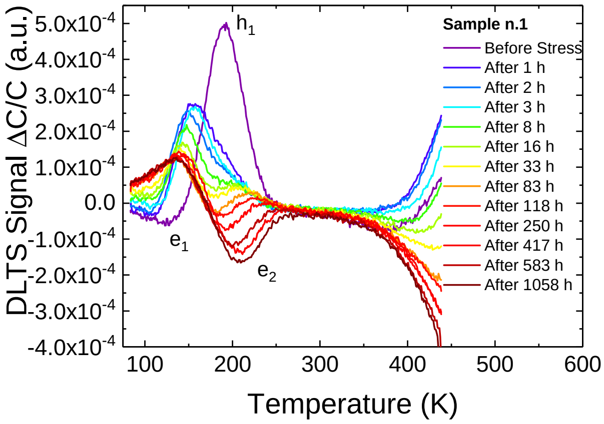

Figure 6.6: DLTS spectra obtained after successive stress steps. Spectra are collected with reverse bias $V_{rev} = -5$ V and filling pulse $V_{fill} = -3$ V. The emission rate window is 23.8 s^{-1} (it corresponds to a time window between $t_1 = 28.2$ ms and $t_2 = 69.8$ ms).

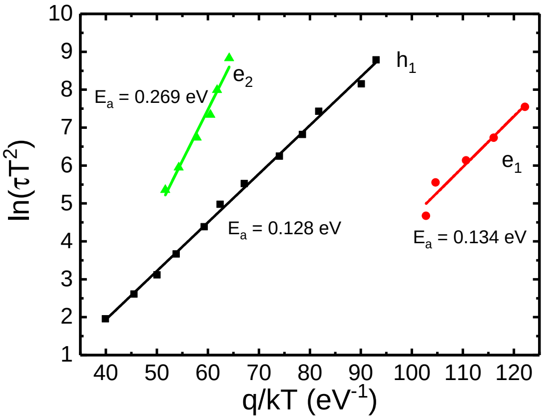

Figure 6.7: Arrhenius plot of the energy levels detected in DLTS; q is the elementary charge, T is the temperature, and τ is the emission rate corresponding to the maximum of the trap peak observed.

From a comparison with the literature [138], we conclude that the possible origin of deep level h1 could be Mg-related acceptor traps. Several activation energies have been attributed to Mg [139] Tanaka et al. [24] found 125 and 157 meV, instead Johnson et al. [140] reported 131 meV for the Mg acceptor in MOCVD-grown samples. In addition, Polyakov and Lee [62] suggested that a 0.15 eV trap could be consistent with Mg–H complexes. In a previous work, Mg diffusion into the active layer was proposed as the major gradual degradation mechanism in InAlGaN-based LEDs [141]. Regarding the two electron traps, the negative peak e1 could be ascribed to N vacancies [142], [143], instead the physical origin for trap level e2 is still unknown.

As previously explained (Figure 6.4), the drive voltage shows a decrease during the first hours of stress; this effect can be correlated with the decrease of the peak intensity of the Mg-related trap h1. This result suggests that the reduction of the Mg-related traps (or Mg–H complexes) may lead to a reduced resistivity of the p-type layers and the p-side contact, respectively, and therefore to a reduced drive voltage.

6.6 Photocurrent spectroscopy

As already mentioned in Chapter 3, PC spectroscopy is a useful tool to analyze the presence of defects in optoelectronic devices. Every step in the PC spectrum corresponds to a specific transition, from a defect band to the conduction band, or from the valence band to the conduction band (Figure 6.8 inset). For the PC measurements, we used a xenon arc lamp, a chopper (with a frequency of 30 Hz), a monochromator (Oriel Cornerstone 130), a lens with 35-mm focal length for focusing the monochromatic light, and a lock-in amplifier. The light generated by the xenon arc lamp was coupled with the monochromator, to shine monochromatic light on the sample (through the rough sapphire substrate). Before the test, the whole optical path was calibrated by using a photodiode with calibrated spectral responsivity, in order to account for the different efficiencies of the system at different wavelengths. During the measurements, the sample was kept at ground potential, in short circuit.

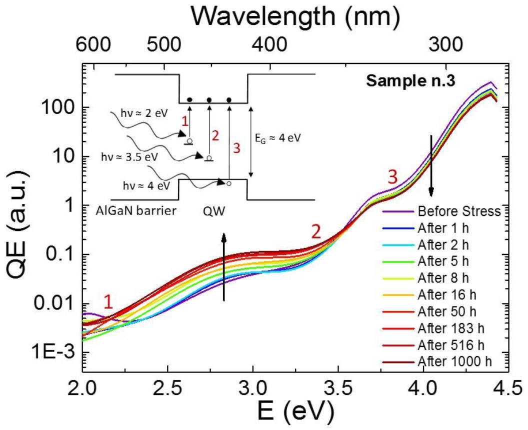

Figure 6.8: PC measurements on the sample during stress. We can identify three different steps corresponding to three different energy levels; the inset shows the mechanism responsible for the PC.

The results obtained by PC spectroscopy during stress are reported in Figure 6.8.

We can identify three steps (Figure 6.8 inset): 1) the first step is around 2 eV, representing the first band of defects in the mid-gap of the active region or of the p-GaN cap layer; 2) the second around 3.5 eV, identifying another band of defects, deeper in the gap; and 3) the last around 4 eV, related to the excitation of the carriers in the QWs. In Figure 6.9, the same data are normalized with respect to the PC measured before stress, for easier understanding of the variations introduced by the stress.

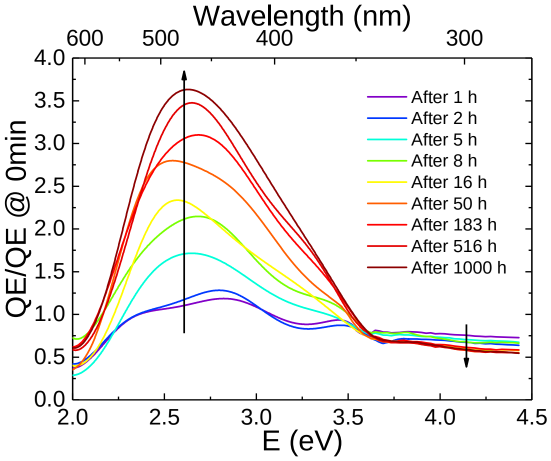

Figure 6.9: Normalized QE during stress; we can observe the increase of the signal between 2 and 3.5 eV and the decrease around 4 eV.

During the stress, we detected an increase in the signal associated with deep levels with an energy between 2 and 3.5 eV, thus close to the mid-gap (Figure 6.8 and 6.9). We observed also a decrease in the quantum efficiency (QE) of the main peak (∼ 4 eV), which can be explained by the increase of SRH non-radiative recombination within the quantum wells. Out of the total amount of hole–electron pairs photoexcited inside the quantum wells, with increasing stress time, a higher number of pairs recombine non-radiatively (due to the increased mid-gap defect density already discussed). Therefore, a lower PC can be extracted from the sample, leading to the reduction in QE. Figure 6.10 shows that the optical power decrease is correlated with the increase in the PC signal associated with deep levels located between 2 and 3.5 eV below the conduction band energy, thus confirming the important role of defects in device degradation. The results in Figure 6.8 and 6.9 demonstrate that stress induces the generation of deep levels within the active region of the devices; specifically, the deep levels located at $E_c - 2.25$ eV are very close to the mid-gap, and can behave as effective non-radiative recombination centers, as described by the SRH theory. In addition, the increase in the concentration of mid-gap states can explain the modifications in the region below the turn-ON voltage of the I–V curves (Figure 6.4), that is commonly ascribed to the increase in TAT components.

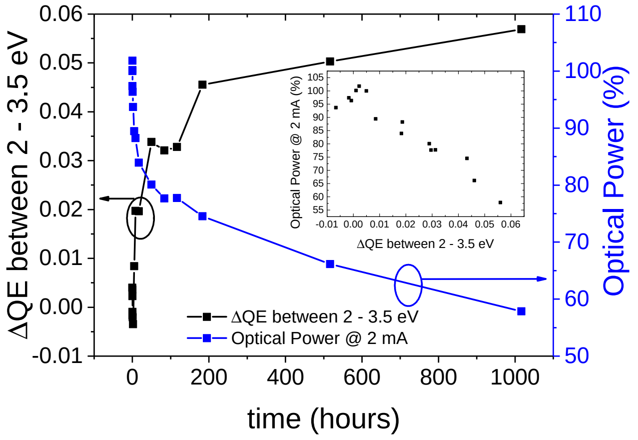

Figure 6.10: Evolution of the optical power and the QE derived from the PC signal between 2 and 3.5 eV during stress; optical power measured at 2 mA. The inset shows the direct correlation between the otpical power and the QE calculated from the PC signal.

6.7 Conclusion

In summary, we have presented an extensive analysis of the electrical and optical degradation of InAlGaN-based DUV LEDs, based on combined DLTS, PC, and EL measurements. Operation-induced stress was found to induce a gradual degradation of the optical power, especially at low measuring current levels, due to the increase in the non-radiative recombination. The QW-related luminescence peak (308 nm) and the parasitic emission band related to electron overflow ($330 - 380$ nm) decrease during the stress, indicating an increase of the SRH recombination within the active region. The results of current–voltage measurements show an increase in the reverse bias leakage current, which is ascribed to the generation of point defects; in addition, we detected an increase in the current below the turn-ON voltage, suggesting the presence of TAT mechanisms. This last hypothesis is confirmed by the PC spectroscopy measurements, where the results indicate that stress induces the increase in the concentration of mid-gap defects, located $2 - 2.5$ eV below the conduction band energy. The same defects are supposed to be responsible for the optical degradation of the devices, based on the correlation between the associated PC signal and the optical power decrease. Finally, DLTS analysis allowed to identify the presence of Mg-related acceptor traps next/within the active region, whose change in concentration has been correlated with the change of the electrical characteristics of the p-type region and/or of the ohmic contacts.

Chapter 7

Recombination mechanisms and thermal droop in AlGaN-based UV-B LEDs

This chapter continues the previous work on AlGaN-based UV-B LEDs, reporting a comprehensive analysis of the origin of the electroluminescence (EL) peaks and of the thermal droop in these devices. Spectral measurements at several temperatures and currents were carried out. The results obtained from this work were published in [144].

7.1 Introduction

As already mentioned in the introductive chapter (Chapter 4), the efficiency of UV-B LEDs is still low compared to their visible counterparts, due to the low light extraction efficiency of AlGaN-based structures [145] and partly to the non-radiative recombination losses (SRH and Auger-related) that limit the internal quantum efficiency at low and high current levels. Recent papers indicated that the reduction in optical power with increasing temperature (referred to as thermal droop) may also limit the performance of GaN-based LEDs, causing an emission decrease comparable to the more discussed efficiency droop [146, 99]. This is particularly relevant for UV LEDs, which - owing to the lower efficiency - convert most of the electrical power to heat. This effect is quantitatively ascribed to increased carrier escape or defect-related non-radiative recombination [147, 106], but no comprehensive analysis or accurate theoretical model is present in the literature.

Understanding the physical origin of the parasitic peaks is important to reduce their contribution and improve the spectral purity of the devices. With the aim of obtaining more insight on these physical processes, within this chapter we propose a new approach with the following elements: (i) the combined analysis of both spectral and temperature-dependent data, (ii) the definition of a closed-form model for the thermal droop caused by the SRH non-radiative recombination through deep levels, based on the SRH theory and on the ABC rate equation, and (iii) a complete and consistent analysis of the various effects occurring in a wide temperature and bias current range. In the samples under test, the three EL bands are ascribed to the following processes: band-to-band recombination in the quantum wells (main EL peak), a parasitic intra-bandgap radiative transition in the quantum well barriers, and a second defect-related radiative process in the p-AlGaN superlattice.

7.2 Experimental details

The devices under test were the same used for the measurements reported in Chapter 6. To understand the origin of the EL and the role of the different thermal droop mechanisms, electrical and optical characteristics were measured in a liquid nitrogen cryostat from 100 to 400 K. The spectral power distribution of the EL was collected at five different current levels, namely, 10 μA, 100 μA, 1 mA, 10 mA, and 100 mA, by means of a compact array spectrometer. The bias current was supplied by a precision parameter analyzer.

7.3 Spectral Analysis

The EL spectra collected at the various test temperatures are reported in Figure 7.1, in this case for the 1 mA bias current. Several different spectral features can be noticed, including four peaks, which are referred to as peak 1, QW, peak 3, and peak 4 in the following. In the past, complex (multi-band) emission spectra from UV devices were already reported [148, 149, 150, 151]. The strongest parasitic emission peaks at 4% at room temperature, and this is comparable to state-of-the-art commercial devices with similar performances (See, for instance, Sensor Electronic Technology Inc., "Technical Data Sheet," S-S35F-F3-310-01-4).

The wavelength of the second peak ("QW") is compatible with the nominal emission from the QWs. A detailed analysis on the effect of bias current and temperature will be given in the following sections, which will also discuss the origin and behavior of peaks 3 and 4.

Peak 1 is visible only at the lowest temperature and current levels and is not relevant

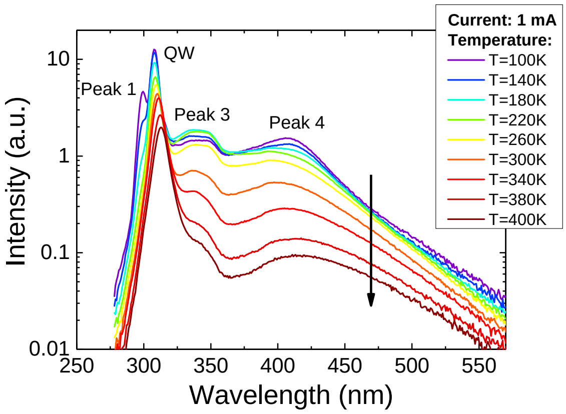

Figure 7.1: Spectral distribution of the EL at various temperatures and a current of 1 mA. The four main emission peaks are labeled in the figure.

for the room temperature performance of the devices, and, for this reason, its analysis is beyond the scope of this work. In fact, the collected experimental data do not point out a clear origin of this peak.

7.4 Analysis of the QW luminescence

The analysis of the QW emission peak as a function of temperature and measuring current is summarized in Figure 7.2. Three different thermal droop regimes can be identified. The first one is visible at $T < 200$ K for the three lower currents ($I \leq 1$ mA). In this case, a significant decrease in the optical power is detected even for small temperature variations; this effect is more prominent at low currents. The temperature dependence of the optical power was fitted according to the well-known equation

$$L = \frac{L_0}{1 + A\exp(-E_a/kT)} \tag{7.1}$$

where L_0 is the extrapolated intensity at $T = 0$ K, A a proportionality constant, E_a the activation energy of the process causing the decrease in the optical power, and k the Boltzmann constant [152]. The results reported in Figure 7.3 show a very good quality of the fit and a low value of the activation energy of about 70 meV. This behavior can be explained by taking into account the exciton delocalization inside the QWs [153]. Electrons and holes may be localized in potential minima, caused by fluctuations in the alloy composition or in the QW thickness. When the temperature is increased, the carriers can gain enough energy to overcome the small potential barrier confining them in the localized states, thus becoming delocalized in the plane of the

QWs. This lowers the probability of an electron–hole interaction and decreases the rate of radiative recombination [154, 155, 156, 157]. This hypothesis is supported by the low activation energy derived in Figure 7.3, which is comparable to values reported for exciton delocalization [158, 159, 160, 161]. Typical reported values of localization potential in AlGaN are, in some cases, lower, but the average radius of the composition fluctuation was recently shown to have a strong impact on the localization potential [161]. Additionally, our devices have a small In content in the QWs, which was shown to potentially increase the localization energy [162].

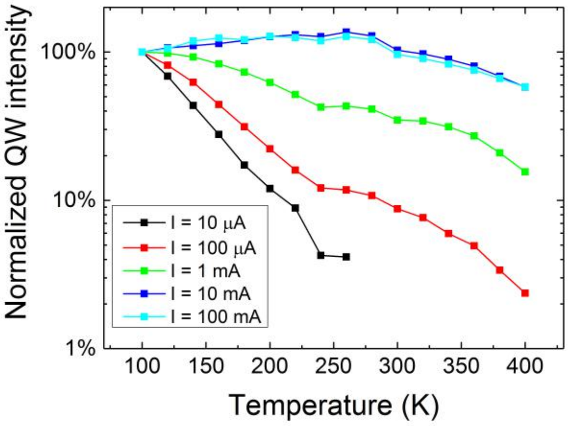

Figure 7.2: Intensity of the QW emission for different temperatures and currents.

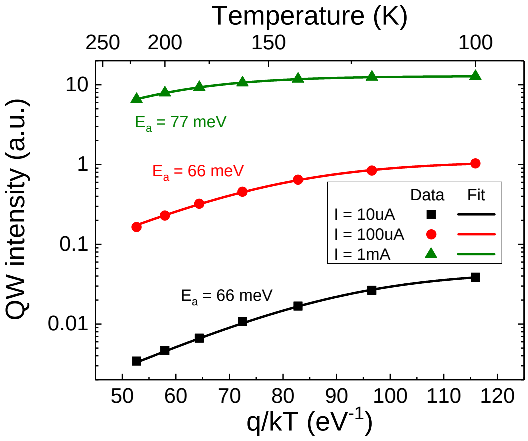

Figure 7.3: Arrhenius plot of the intensity of the QW emission and fit according to equation 7.1.

An additional confirmation that for $T < 200$ K the reduction in optical power of the QW emission with increasing temperature is caused by exciton delocalization rather than by SRH recombination is given by the analysis of the peak wavelength of the

QW emission shown in Figure 7.4. The almost constant wavelength of the emission at low temperature (from 100 to 160 K) is not consistent with an increase in SRH recombination, which would add an additional redshift to the redshift of the bandgap in accordance with Varshni's law: in fact due to the reduced density of carriers available for radiative recombination inside the QWs, carriers are not able to reach higher energy states inside the QWs. Rather, the almost constant emission wavelength corresponds to a superimposed blueshift from localized electrons and holes that are thermally excited to higher energy states. At higher temperatures ($T > 160$ K), the peak wavelength strongly shifts red, caused by the bandgap narrowing with increasing temperature and confirmed by a fitting using Varshni's law (see the inset in Figure 7.4) [102].

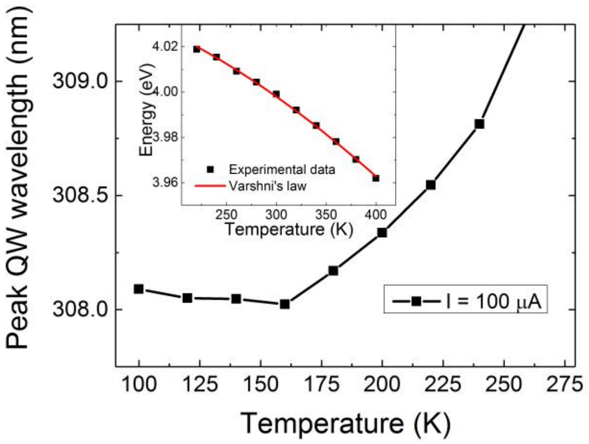

Figure 7.4: Temperature dependence of the peak wavelength of the QW emission. Inset: bandgap narrowing with increasing temperature in accordance with Varshni's law.

The second thermal droop regime is visible in Figure 7.2 for $T \geq 300$ K for all current levels. This can be clearly distinguished from the previous mechanism as a separate one due to the transition temperature range around $250 - 300$ K. We propose SRH recombination as a good candidate for explaining such a decrease in the optical power. Several reports [163, 164, 165, 166] used equation 7.1 to analyze the decrease in optical power at high temperatures. This formula is effective to investigate the thermal droop due to exciton delocalization, but it is not adequate to study the impact of SRH recombination (even if it is used sometimes in the literature [167, 168, 169]). In fact, it can be noticed from equation 7.2 that the optical power does not approach zero for infinitely high temperatures, whereas we expect this trend when the temperature increases significantly [155, 170, 171, 172]:

$$\lim_{T\to\infty} \frac{L_0}{1 + A\exp\left(-E_a/kT\right)} = \frac{L_0}{1+A} \tag{7.2}$$

Equation 7.1 is a simplification, as is clear from the theoretical background described, for example, in Ref. [173]. First, the distribution of the carriers is approximated by the Boltzmann distribution rather than described by the Fermi distribution. Moreover, the defect density, which acts as a ratelimiting element in the SRH recombination process, is not taken into account. An additional problem may arise from the assumption that the number of excitons in the QWs does not depend on temperature, which may not be reasonable over a wide temperature range due to additional temperature-dependent loss mechanisms (such as carrier escape, thermionic emission, and injection efficiency). Finally, equation 7.1 does not take into account the particular expressions of the capture and emission rates typical of the SRH process.

For this reason, we followed a novel approach based on the ABC rate equation [174, 175] and on the approximated formula for the SRH non-radiative recombination lifetime τ_{nr}:

$$\tau_{nr} = \tau_0\left(1 + \cosh\frac{E_T - E_{Fi}}{kT}\right) \tag{7.3}$$

where τ_0 is a constant that depends on the deep level density and on the carrier capture rate, E_T is the trap energy level, and E_{Fi} the intrinsic Fermi energy level [176]. According to the ABC model and assuming perfect injection efficiency, the rate equation of an LED can be written as

$$I = qV_R(An + Bn^2 + Cn^3) \tag{7.4}$$

Here, q is the electron electrical charge, V_R the recombination volume, $A = 1/\tau_{nr}$ the SRH recombination coefficient, B the bimolecular radiative recombination coefficient, C the Auger recombination coefficient, and n the carrier concentration. The internal quantum efficiency η_{IQE} can then be expressed as

$$\eta_{IQE} = \frac{Bn^2}{I/qV_R} = \frac{Bn^2}{An + Bn^2 + Cn^3} \tag{7.5}$$

Based on equations 7.3–7.5, it is possible to develop an analytical model for the thermal droop. When taking two temperatures $T_1 < T_2$, the variation in internal quantum efficiency is

$$\frac{\eta_{IQE}(T_2)}{\eta_{IQE}(T_1)} = \frac{B_2n_2^2}{A_2n_2 + B_2n_2^2 + C_2n_2^3}\frac{A_1n_1 + B_1n_1^2 + C_2n_1^3}{B_1n_1^2} \tag{7.6}$$

where the subscript number in A, B, C, and n is a reference to the corresponding temperature value. Under the assumption that the value of B is not temperature dependent and that the Auger recombination is negligible (no efficiency droop was detected up to 30 mA), equation 7.6 can be rewritten as

$$\frac{\eta_{IQE}(T_2)}{\eta_{IQE}(T_1)} = \frac{n_2^2(A_1 n_1 + B n_1^2)}{n_1^2(A_2 n_2 + B n_2^2)} \tag{7.7}$$

If the current at the two temperatures is the same, and assuming that the recombination volume does not vary with temperature, we obtain from equation 7.4

$$A_1 n_1 + B n_1^2 = A_2 n_2 + B n_2^2 \tag{7.8}$$

and therfore

$$n_2 = \frac{-A_2 + \sqrt{A_2^2 - 4B(-A_1 n_1 - B n_1^2)}}{2B} \tag{7.9}$$

where only the positive solution was kept, because the carrier concentration cannot be negative.

By using equations 7.3, 7.7, and 7.9, it is possible to fit the experimental data for every current. The results shown in Figure 7.5 demonstrate a good agreement between theory and experiment. To achieve the best fitting quality, the parameters τ_0, A_1, B, n_1, and $E_T - E_{Fi}$ had to be fitted independently for each current (but are kept constant, when not explicitly stated, for every temperature), which may partly result from the simplicity of the model. The increase in the density of carriers at different bias levels is expected, and the variation in the recombination coefficients is consistent with several reports [174, 177, 178, 179, 180, 181]. The parameters remained within a reasonable range, if the variation of the parameters with current density mentioned above is taken into account [177] (e.g., B from $2.63 \cdot 10^{-13}$ to $7.99 \cdot 10^{-13}$ cm^{3}s^{-1}, n_1 from $2.7 \cdot 10^{17}$ to $14.5 \cdot 10^{17}$ cm^{-3}), when compared to data available for InGaN-based devices [174, 182] (given the lack of experimental reports on these values for AlGaN LEDs), confirming that the model achieves good fitting quality with meaningful parameters, comparable to experimental ones. The fitting indicated that the deep levels responsible for SRH recombination are located close to mid-gap ($E_T - E_{Fi}$ in the range between 165 and 342 meV). Therefore, we conclude that above 300 K (i.e., at realistic temperatures of device operation), the thermal droop is caused by the increased SRH recombination.

The third region of interest in Figure 7.2 is the part at low temperature (100 K $<$ $T <$ 250 K) and high current ($I \geq$ 10 mA). In this case, the optical power emitted by the QW increases (instead of decreasing) with increasing temperature. This effect

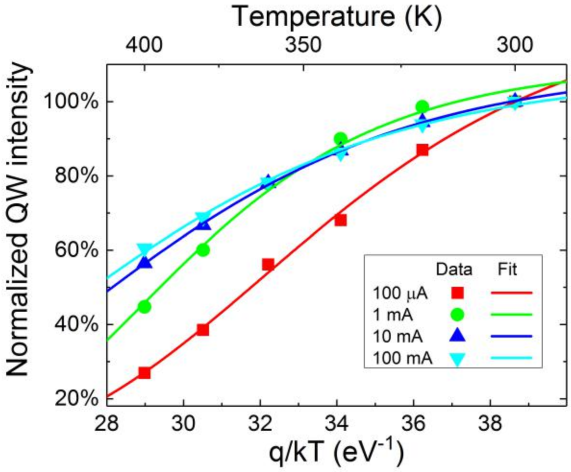

Figure 7.5: Intensity of the QW emission for different temperatures and currents fitted by equations 7.3, 7.7, and 7.9.

can be related to an enhanced hole injection from the p side to the QWs, as previously proposed for similar samples [69, 133]. The enhanced hole injection at higher temperature is confirmed by numerical simulations based on a one-dimensional drift-diffusion model of the band structure and carrier concentration (Simulations are based on the software package SiLENSe 5.2.1, STR Group, Ltd.), as shown in Figure 7.6. Here, the temperature dependence of the bandgap is described by Varshni's empirical expression, and the charge carrier mobility is set constant in the temperature range. When the temperature is increased from 140 to 300 K, the electron concentration in the QWs is not expected to vary significantly, but the hole concentration in the farthest QW is expected to increase. The higher hole density causes the detected increase in optical power.

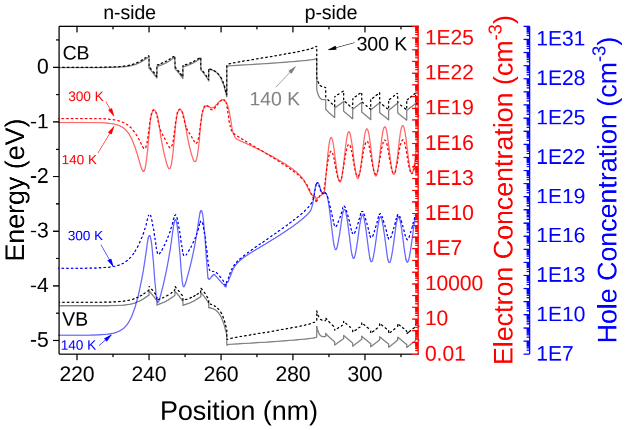

Figure 7.6: Numerical simulation of the band diagram and of electron and hole concentration at 140 and 300 K at a current of 10 mA.

The presence of excitons and excitonic recombination has been shown to play an important role in time-resolved photoluminescence (TRPL) studies, even at high temperature and high excitation densities [183, 184]. As reported in [184], the exciton density rapidly decreases in hundreds of picoseconds (even without self-heating), more rapidly than the e-h plasma. Both studies analyze TRPL with (at most) picosecond-long laser pulses, and there is no evidence that this process would impact the longer timescale of CW operation (the condition of our thermal droop analysis), especially if the self-heating of the device is taken into account. Even if we assume that excitons are present, their very low binding energy (50 meV at most, according to [183, 184]) would lead to a significant dissociation in the long term, due to multi-phonon processes and to the energy distribution of the phonons. During a capacitance deep level transient spectroscopy experiment, it is possible to detect, at room temperature, thermal emission from deep levels about $0.6 - 0.8$ eV below the conduction band and about $0.2 - 0.3$ eV at 100 K [185, 186, 187, 138, 188, 189]. For all these reasons, excitonic effects are probably negligible in our thermal droop analysis.

7.5 Peak 3 analysis

The EL intensity of peak 3 as a function of temperature and current is summarized in Figure 7.7. In this case, at low current levels we do not observe the double-slope behavior highlighted in Figure 7.2 for the QW peak. The analysis of the thermal droop reveals that the intensity of peak 3 can also be fitted according to the complete SRH model based on equations 7.3, 7.7, and 7.9. For this reason, non-radiative recombination through deep levels inside the bandgap is the likely cause for the reduction in the optical power of peak 3 with increasing temperature.

Information on the physical origin of peak 3 was obtained by the behavior at low temperature for the three highest currents. As can be noticed in Figure 7.7, the optical power increases with increasing temperature, as already found for the QW peak. Therefore, peak 3 is also affected by the hole injection efficiency, and the layer responsible for this EL has to be located beyond the p side of the device. By using this information and by comparing the peak emission wavelength with the nominal bandgap values of the different layers in the heterostructure, we suggest that peak 3 originates from radiative transitions through deep levels, as confirmed by the broad shape of the peak (see Figure 7.1), which is a common signature of parasitic intra-gap emission. This radiative recombination is most probably occurring in the quantum

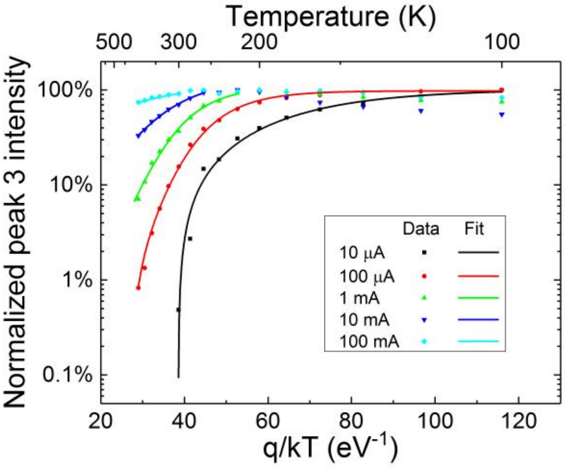

Figure 7.7: Arrhenius plot of the peak 3 intensity for different currents fitted by the complete SRH model (equations 7.3, 7.7, and 7.9).

barrier next to the EBL and not inside the QWs, because no effect of exciton delocalization is detected, whereas it is present for the main QW peak. This hypothesis is supported when multiplying the hole and electron concentration shown in Figure 7.6, because this product is directly proportional to the recombination rate. The results of the product show (not shown here), besides strong peaks within the QWs, an increased value in that part of the band structure.

7.6 Analysis of peak 4

The analysis of the origin of peak 4 and of its thermal droop is more complex than for the other peaks. In this case, the SRH model does not fit the experimental data adequately (see Figure 7.8 for three representative current values). For this reason, we suggest that a different mechanism may play an important role. The first information originates from the behavior at low temperature: contrary to the QW peak and peak 3, no increase in the optical power is detected with increasing temperature, suggesting that this emission process is not limited by hole injection and, therefore, that its source is probably located in the p-side. Comparing the wavelength of peak 4 with the layer structure of the p-side as well as considering the spectral width of peak 4 (see Figure 7.1) suggests that peak 4 is likely related to a radiative parasitic transition inside the region with the lowest energy gap in the p side, i.e., the AlGaN/AlGaN SPSL, where the density of holes available for the emission is highest.

These assumptions can be supported by again analyzing the simulation results of the band structure, carrier densities, and recombination rates as partially shown in

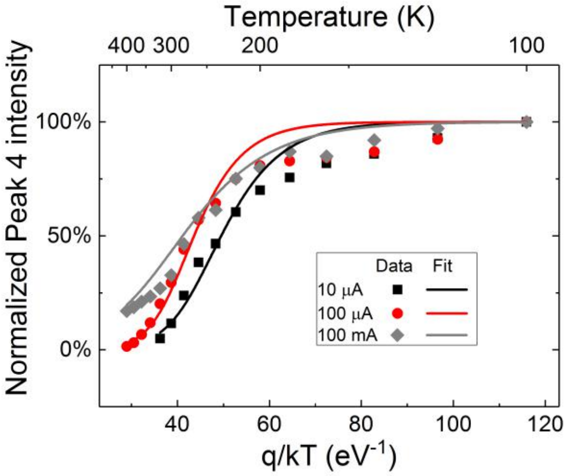

Figure 7.8: Arrhenius plot of the peak 4 intensity for different currents fitted by the complete SRH model (equation 7.7).

Figure 7.6. Taking the radiative recombination rate in the p-superlattice for different temperatures, a similar dependence can be recognized, as it is observed in the normalized intensity of peak 4 as a function of q/kT shown in Figure 7.8. It should be noted, however, that the simulation does not take into account hole injection mechanisms at the p contact and, therefore, only partially reflects the experiment. The simulation shows that at low temperatures the band bending in the EBL is lower, because fewer acceptors are ionized and a higher external voltage is needed to maintain the current flow (mainly electrons at low temperature). Thus, more electrons overcome the EBL, penetrate into the p-side, and recombine radiatively there. At higher temperatures more acceptors are ionized, a lower voltage is needed to inject holes in the active region, and, hence, the EBL works more efficiently preventing electron leakage into the p-side.

The presence of various radiative transitions in the p-side was already reported in the past, and qualitatively ascribed to several origins, such as band-to-band recombination promoted by defect-assisted electron tunneling [147] and radiative recombination through deep acceptor levels [190, 191] or complexes [151].

An extended analysis of the temperature dependence of peak 4 becomes even more complex if the temperature and current dependence of the electron leakage across the EBL is taken into account. Additionally, the broad peak 4 may be the composition of several defect-related radiative recombination channels, given the asymmetric shape of peak 4 (see Figure 7.1). All these aspects prevent a clear identification of the physical mechanism of the thermal droop. Given the short periodicity of the superlattice, it could also include field- or trap-assisted escape processes, such as phonon-assisted tunneling, trap-assisted tunneling, or more accurate models [146].

7.7 Conclusion

In summary, we showed that the temperature and current dependence of AlGaN UV-B LEDs can provide useful information on the physical origin of multiple EL peaks. Moreover, we developed a new closed-form model based on the SRH recombination lifetime and on the ABC model, that can be used to closely fit the decrease of the optical power with increasing temperature caused by the non-radiative recombination through deep levels.

With increasing temperature, the QW emission showed three different trends that have been investigated in detail. At low temperature and high currents an increase in the optical power, caused by an enhanced hole injection from the p-side to the n-side, was found. At high temperature, the optical power is reduced due to a more common increase in the SRH recombination rate, whereas at low temperature and low current, the reduction is likely caused by exciton delocalization from potential minima inside the QWs.

A second emission peak (peak 3) originates most likely from parasitic intra-bandgap radiative transitions beyond the p-side of the device and is influenced by the enhanced hole injection with increasing temperature at high currents. A possible location is in the quantum barrier next to the EBL, because we have not detected any exciton delocalization effect.

The third emission peak (peak 4) is the most complex one. It is attributed to a parasitic radiative transition, possibly in the p-AlGaN superlattice and assisted by a charge transfer mechanism.

7.8 Appendix: simplified SRH model

The fitting algorithm based on equations (7.3), (7.7), and (7.9) is complex and requires some computation time. The model can be simplified considering that for $T_1 < T_2$ the carrier concentration n_2 is slightly lower than n_1 (due to the increased SRH recombination), and we can write this difference as

$$n_1 = n_2 + \Delta n \tag{7.10}$$

By using equation (7.10) in equation (7.7), we obtain

$$\frac{\eta_{IQE}(T_2)}{\eta_{IQE}(T_1)} = \frac{A_1 n_2^3 + A_1 n_2^2 \Delta n + B n_1^2 n_2^2}{A_2 n_2^3 + 2A_2 n_2^2 \Delta n + A_2 n_2 \Delta n^2 + B n_1^2 n_2^2} \tag{7.11}$$

If the variation B in carrier concentration between two subsequent temperature points is small ($\Delta n < n_2$), equation (7.11) can be approximated as

$$\frac{\eta_{IQE}(T_2)}{\eta_{IQE}(T_1)} \cong \frac{A_1 n_2 + B n_1^2}{A_2 n_2 + B n_1^2} \tag{7.12}$$

By using equation (7.12) instead of equation (7.7) together with equations (7.3) and (7.9), we can obtain a simpler and quicker fitting algorithm. As can be noticed in Figure 7.9 for the representative current of 10 mA, the fitting quality obtained by using the approximated equation (7.12) (red line) is lower than the more accurate equation (7.7) (blue line), but agreement is still acceptable.

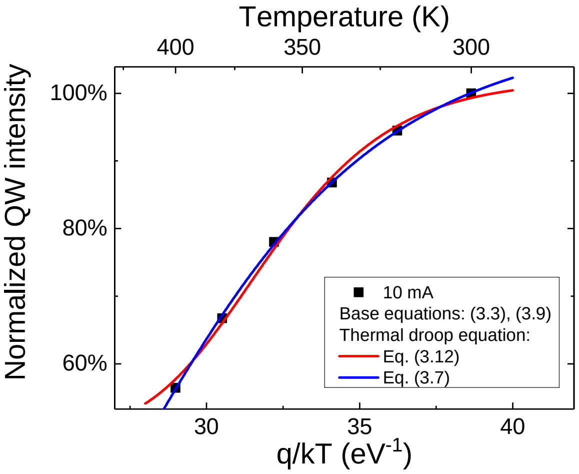

Figure 7.9: Intensity of the QW emission at different temperatures fitted by the complete SRH model (equation (7.7)) and the approximated model (equation (7.12)), respectively.

Chapter 8

High-Current Stress of UV-B (In)AlGaN-based LEDs: defect-generation and diffusion processes

In this chapter, we continue to investigate the degradation mechanisms of UV-B AlGaN-based light-emitting diodes (LEDs) submitted to constant current stress, but in this case the stress current level is beyond the typical application conditions. The work described in this chapter was published in [192].

8.1 Introduction

The degradation of UV-B LEDs is mostly current- and temperature-driven [131, 95, 132]. Over the last years, a number of groups investigated the physical origin of this degradation. The reports published so far [4, 193, 194] indicate that point defects play an important role, since their concentration can increase over stress time, leading to enhanced non-radiative recombination.

In this chapter we investigate the degradation processes induced by operation at high current densities (350 A/cm^2, significantly higher than typical current densities of UV-B LEDs which are below 100 A/cm^2). This allows us to significantly accelerate the involved degradation mechanisms compared to previous papers in the field. More specifically, by studying the relative variations of the main QW peak at 310 nm (4.00 eV) and of a parasitic peak at 340 nm (3.65 eV), related to carrier escape towards the p-side, we demonstrate the existence of two different degradation mechanisms: (i) in the first 50 hours of stress, carrier escape from the quantum wells is promoted, which leads to a significant decrease in the QW peak, and to an increase in the parasitic peak at 340 nm; (ii) for stress times longer than 50 hours, a defect-diffusion process leads to a significant decrease in the luminescence of both the QW and the parasitic peak. These mechanisms are thoroughly investigated by means of electrical and optical measurements, and by PC spectroscopy.

8.2 Experimental details

A group of UV-B LEDs with nominal emission wavelength of 310 nm was analyzed. Again, the structure of these LEDs is described in Chapter 6. These devices are typically run at a maximum current of 100 mA which corresponds to a nominal current density of 140 A/cm^2. In this study, the LEDs were submitted to a constant current stress of 250 mA (current density = 350 A/cm^2), at 25°C, in order to significantly accelerate the degradation processes. In order to control the temperature, the devices were mounted on a Peltier-based temperature controller. Electrical and optical parameters were continuously monitored, in particular EL spectra; all measurements were carried out at various temperatures (from 15°C to 85°C, with 10°C steps). In order to have more information on the presence of defects, during the stress PC spectroscopy was performed. The setup used is the same described in Chapter 6.

8.3 Optical characterization

Relevant information regarding the drop of the optical power and its correlation with the presence of defects was collected by measuring the EL spectra at different temperatures, as a function of stress time. Figure 8.1 shows the emission spectra (measured at 5 mA and room temperature) for one of the analyzed LEDs at different stages of the stress at 250 mA. From the analysis of the main peak during the stress (Figure 8.2), it is evident that the overall degradation is more prominent at low measuring currents. This result suggests that the stress is inducing an increase in the defectiveness of the active region. At low measuring currents, such defects can efficiently act as non-radiative recombination centers, thus limiting the optical power of the device. At higher current, the SRH centers are saturated, and their impact on the optical power is significantly reduced [123, 134].

The EL spectra (Figure 8.1) reveal the presence of a parasitic peak between 325 nm and 355 nm (3.5 – 3.8 eV). Consistent with the previous work reported in Chapter

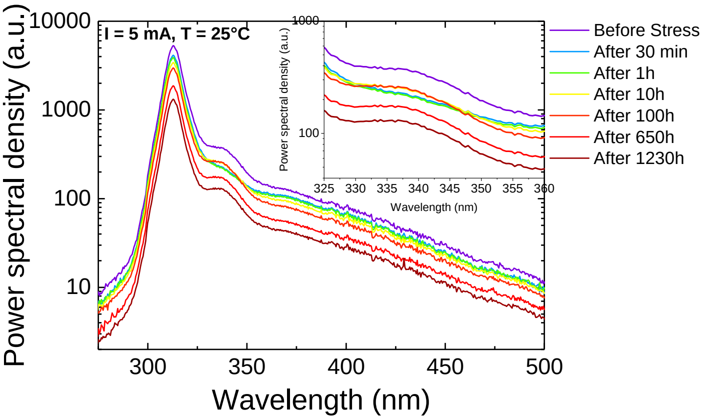

Figure 8.1: Emission spectra measured at 5 mA and room temperature after different stress times. The inset shows in details the parasitic peak during the stress.

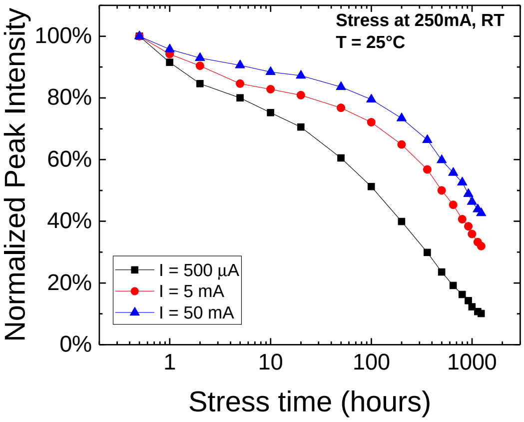

Figure 8.2: Peak intensity of the main emission peak at different currents (measured at 25°C) during stress. The peak intensity is normalized with respect to the value at 30 minutes of stress.

7, such a peak can be ascribed to electrons that escape from the quantum wells, and undergo radiative transitions through deep levels in the quantum barrier next to the EBL. In order to study the behavior of the main and parasitic peaks during the stress in more details, Figure 8.3 reports the variation of these two peaks during the stress measured at a current of 50 mA and at different temperatures. The following trends can be observed:

- In the first 50 h of stress, the main QW peak decreases, while the intensity of the parasitic peak increases, but only at high measuring currents; in fact, as Figure 8.4 shows, this behavior is not evident at low measuring currents.
- For stress times longer than 50 h, both peaks decrease.
- For stress times longer than 50 h, the variation of the QW peak and of the parasitic peak are linearly correlated (see Figure 8.5), indicating a common degradation process when considering an only small overlap of the QW peak with the parasitic peak.
- For stress times longer than 50 h, the decrease of the main QW peak and of the parasitic peak have a square-root dependence on time. Compare Figure 8.6, where the curves at 5 mA and 50 mA, for a temperature of 15°C, are plotted as a function of the square-root of time ($\sqrt{t}$).

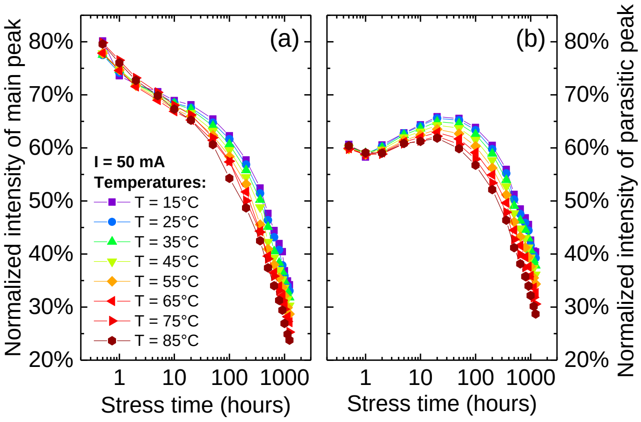

Figure 8.3: Main peak (a) and parasitic peak (b) intensities (normalized at 0 hour of stress) measured at 50 mA during stress.

Based on these findings, we can identify two different degradation processes (see Figure 8.7). The first process dominates in the first hours of stress (first 50 hours) and causes an increase in the parasitic peak at high measuring currents (see Figure 8.3):

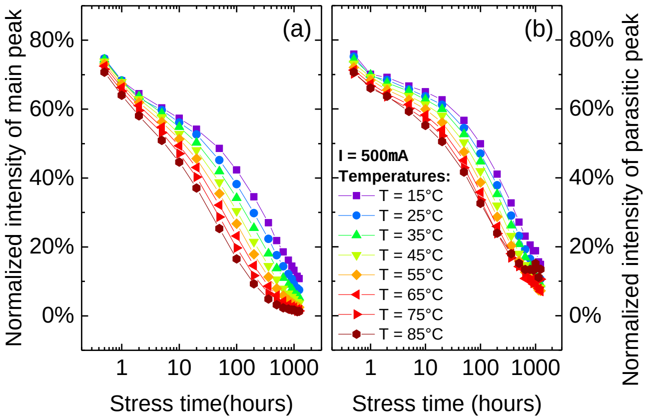

Figure 8.4: Main peak (a) and parasitic peak (b) intensities (normalized at 0 hours of stress) measured at 500 μA during stress.

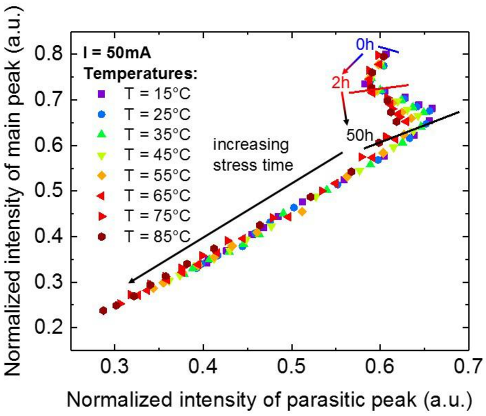

Figure 8.5: Correlation between main peak and parasitic peak intensity measured at 50 mA and different temperatures. The peak intensities are normalized at 0 hour of stress.

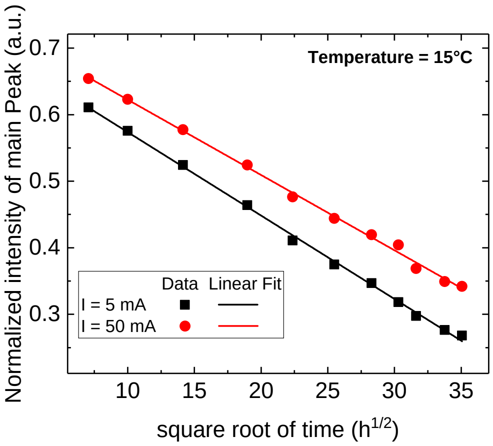

Figure 8.6: Peak intensity measured at 5 mA and 50 mA, at 15°C, normalized at 0 hour, as a function of square root of time (symbols). The solid lines are fits by a linear fit dependences.

this could be ascribed to an increase in carrier escape from the quantum wells. Such an escape can be caused by the following factors: (i) a first possibility is an increase in the net positive charge next to the last quantum barrier (which would attract electrons towards the EBL), due to the emission of electrons trapped at pre-existing defects or by the generation of new positively charged defects; (ii) a second possibility is the formation of defects which promote trap-assisted tunneling out of the quantum wells. Further studies are needed to identify the dominant process.

The second degradation process dominates after 50 hours of stress and later, when both the main and the parasitic peak decrease similarly. This degradation mode is ascribed to a diffusion process, which increases non-radiative recombination in the sample. As a consequence, both the parasitic peak and the main emission peak decrease over time. In this second degradation mechanism there could be also the contribution due to the self-heating of the device and as consequence the thermal droop, as already seen in the previous chapter.

8.4 Electrical characterization

The degradation processes described above have a significant impact also on the electrical characteristics of the devices. In this section, the main changes of the I-V curves identified during long-term stress are described (see Figure 8.8). Three main regions can be identified, as already observed in Chapter 6: (i) the reverse bias region, (ii) the region below the turn-on voltage (from 0 V to ~ 4 V), and (iii) the region above the

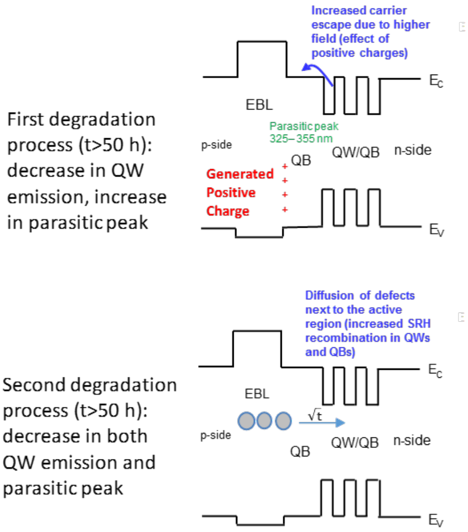

Figure 8.7: Schematics of the two proposed degradation processes. Band bending due to polarization is not shown.

turn-on voltage (above ∼ 4 V).

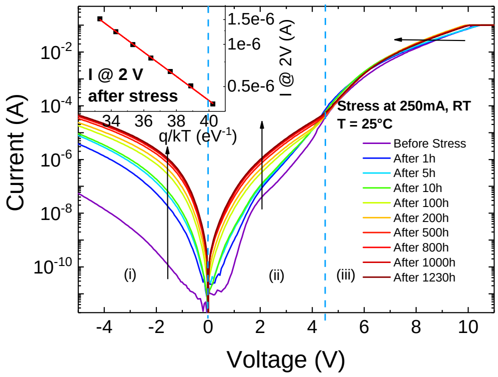

Figure 8.8: I-V characteristics, in semi-logarithmic scale, of one of the analyzed samples after different stress times. The inset shows the Arrhenius plot of the current at 2 V after the stress (symbol); the data is fitted in accordance with the Arrhenius law (solid line).

The reverse-bias leakage current increases during stress time: this is ascribed to the generation of point defects inducing parasitic current paths across the active region, and/or an increase in the generation current components [105, 195]. The reverse-bias leakage current at −4 V as a function of the reciprocal temperature (Arrhenius plot) for various stress times is shown in Figure 8.9. A reverse bias at −4 V was chosen to minimize possible impact from the non-ohmic p-contact. The current can be reasonably described by the temperature dependence $I \propto \exp[-E_a/kT]$ (here E_a is the activation energy), which fits to a carrier transport by thermally assisted multi-step tunneling [105, 104]. According to this transport model, electrons are moving from the valence band in the p-type region to the conduction band in the n-type region by tunneling via deep levels. This process is enhanced at elevated temperature if not all of the deep levels along the tunneling path have the same energy. The activation energy derived by fitting the data shown in Figure 8.9 represents (in a first order approximation) the average energy of the thermally-assisted component of this multi-step process. This energy increases during the first 50 hours of stress (Figure 8.10), and decreases afterwards. Here, the untreated sample does not follow this trend most likely due to additional burn-in effects during the first minutes of operation. In agreement with the explanation given above (see also the schematic in Figure 8.7), the generation of net positive charges next to the EBL on the p-side of the device during the first 50 hours may reduce the electric field across the unintentionally-doped QW region, thus reducing the tunneling probability. As a consequence, the apparent activation energy E_a increases during this period of stress. For longer stress times, the defect density in the active region increases due to a diffusion process: this reduces the distance, both in space and energy, between the deep levels. Resonant tunneling is enhanced with respect to thermally activated tunneling, i.e. the transport process will show a weaker dependence on the temperature, and the apparent activation energy E_a will decrease.

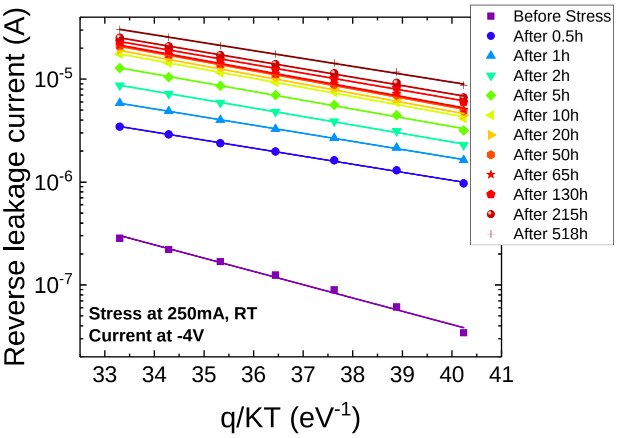

Figure 8.9: Arrhenius plot of the reverse leakage current at −4 V of one of the analyzed samples after different stress times (symbols). The data is fitted in accordance with the thermally-assisted multi-step tunneling mode (solid lines).

In the second region of the I-V characteristic (from 0 V to $\sim$ 4 V), the current below the turn-on voltage increases during stress, as shown in Figure 8.8. This increase is more prominent for stress times longer than $20 - 50$ h (see Figure 8.11), and it follows

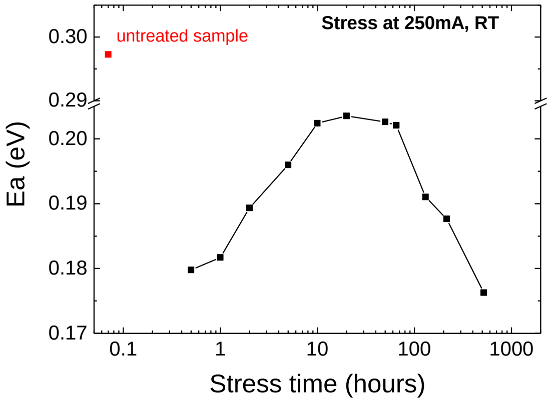

Figure 8.10: Activation energy of the reverse leakage current at −4 V during the stress derived from the Arrhenius plots in Figure 8.9.

a square-root dependence on stress time. This effect confirms the hypothesis on the presence of a diffusion process. In general, the increase of the current below the turn-on voltage can be attributed to the trap-assisted tunneling (TAT) mechanism [103, 137], assuming the presence of deep levels in the QWs, which was verified in previous studies [196]. The TAT mechanism is also temperature dependent. For this reason, we can confirm the presence of this process by looking at the inset in Figure 8.8, where the Arrhenius plot for the current at 2 V after stress shows a linear correlation according to Arrhenius law. It is also important to consider the fact that the p-side contact has a Schottky-behavior, that could impact on the current transport (this is especially true when the LED is forward-biased, i.e. when the metal/p-GaN junction is reversely biased).

In the third region ($V > 4$ V), we observed a decrease in drive voltage in the first 20 hours of stress, followed by a small increase. This change was already studied in Chapter 6, and is ascribed to a change in the electrical properties of the p-side and/or at the interface with the p-metal contact. Assuming the number of traps to be small, their impact on the current well above the turn-on voltage should be small.

8.5 Photocurrent spectroscopy

To characterize the defects involved in the device degradation, PC spectroscopy was performed during stress, with the same setup used for the measurements reported in Chapter 6. Several photon energies (between 2.0 eV and 4.2 eV) were investigated, in order to cover the whole spectral region between mid-gap (2 eV) and the band-gap

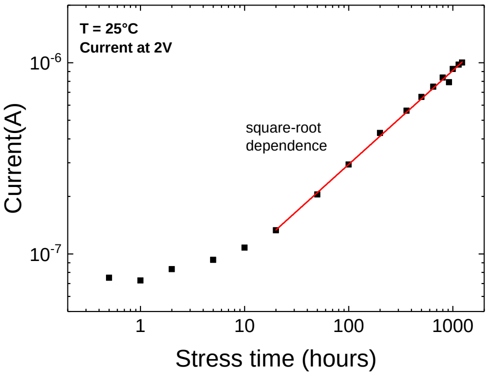

Figure 8.11: Forward current at 2 V, i.e. below the turn-on voltage, during stress. The solid line is a fit of the data beyond 20 hours of stress using a square-root time dependence.

energy in the QWs (4 eV).

Figure 8.12 shows the PC signal collected at different stress times. Two main bands at $2 - 2.5$ eV and at 3.2 eV (identified by the presence of two steps in the PC signal) were found. The first band at $\sim 2 - 2.5$ eV is usually associated to deep levels of defects such as V_{Ga} or complexes of $V_{Ga} - H$ [197, 198]. Instead, the 3.2 eV band could be attributed to C_N substitutional defects [199]; it is worth noticing that the 3.2 eV edge could originate also from band-to-band transitions within the GaN layers. During the stress the PC signal increases, especially between $2 - 2.5$ eV and 3.2 eV. Figure 8.13 reports the variation of the photocurrent signal as measured at different photon energies.

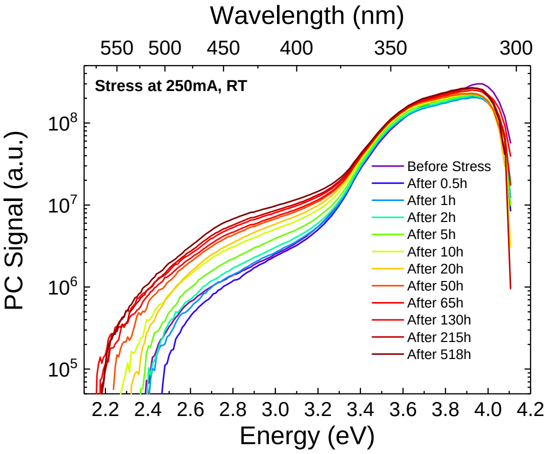

Figure 8.12: PC spectrum for one of the analyzed sample kept at ground potential, after different stress times.

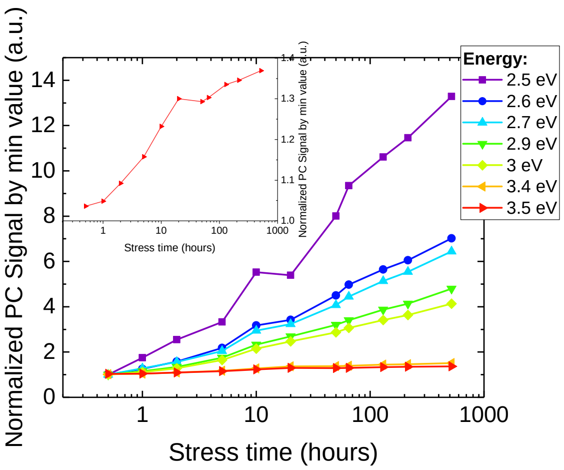

Figure 8.13: Normalized photocurrent signal (by the minimum value) at different energies during stress. The inset shows the photocurrent signal at 3.5 eV

The increase in the signal associated to deep levels (especially in the range 2 – 3.2 eV) is consistent with the hypothesis that stress induces the diffusion of defects within the active region of the devices, with a consequent increase in non-radiative recombination rate. This hypothesis is consistent with the Shockley-Read-Hall theory, that specifies that the most effective non-radiative recombination centers are those located near the middle of the energy-gap, in this case around 2 – 2.5 eV. The PCS data of Figure 8.12 was not evaluated with respect to a possible dependence on the square-root of time as was done for the emission intensity, because of the different spatial sensitivity of the two parameters. The emission intensity is depending directly on the concentration of diffused impurities inside the active region, i.e. in a narrow and localized position. Therefore, it closely follows the square root of time dependence expected for the concentration of diffusing elements at a given position predicted by the diffusion model based on the solution of Fick's second law in one dimension [200]. Conversely, the PC signal originates from deep levels present in the entire space charge region (and a second parasitic one is present at the p-side contact), leading to an averaging in space of the diffusion effect and then to a non-ideal square root of time dependence, as in this case.

8.6 Conclusion

In summary, (In)AlGaN-based UV-B LEDs with a nominal emission wavelength at 310 nm were stressed under highly accelerated conditions. By analyzing the variation of the amplitude of a parasitic emission band centered at 340 nm and of the main emission from the QWs during the stress, two main degradation mechanisms were found. The first degradation mechanism takes place in the first 50 hours of stress, and is ascribed to an increased carrier escape from the quantum wells, due to the generation of a positive charge density at the interface with the EBL. The second degradation process takes place after 50 hours of stress and is ascribed to a defect-diffusion process, with a consequential increase in non-radiative recombination. From the electrical characterization we observed an increase in the reverse leakage current during operation, ascribed to the generation of point defects. In addition, the electrical characterization allowed to confirm the hypothesis on the role of defects in the degradation processes: an increase in the current at low-forward voltages was found and attributed to an increase in the TAT components, and the current in reverse-bias shows similar defect-related current conduction increase. Such changes were found to have a square root dependence on time, thus supporting the hypothesis on the presence of a diffusion process. Information on the physical origin of the defects was collected by photocurrent spectroscopy: the measurements allowed to identify two main absorption bands at least one of which was attributed to defects forming states near the mid-gap, and increasing in concentration after stress.

Part III

Degradation mechanisms of InGaN-based laser diodes

Chapter 9

Introduction to InGaN-based Laser Diodes

Laser diodes are small and efficient sources of laser light. They are well-suited for a wide range of applications, and at the beginning of their market penetration the most popular were optical fiber communications and data storage on CDs and DVDs. During these last years, laser diodes with short wavelength, based on the III-N group, have reached remarkable progress. The possibility of covering a wide spectral range by changing the indium content of the InGaN active region has become one of the key advantages of these optoelectronic devices: GaN-based laser diodes are able to cover a spectral range from near-UV to green. The first prototype high brightness ($>$ 100 times greater than previous alternatives) blue LEDs were developed in 1993 by S. Nakamura [201], followed then, in 1996, by the first III-V nitride based violet LDs with an emission wavelength around 400 nm [202] (Figure 9.1). Since this first demonstration, great improvements have been achieved concerning efficiency, device lifetime, output power and beam quality. Violet laser diodes reach output powers of up to 8 W in pulsed operation [203], and the maximum wavelength in continuous wave (CW) operation demonstrated with GaN-based green laser diode is 525 nm [204].

Besides the application in Blu-ray optical drives, which have a five times higher data density than the DVD, InGaN-based laser diodes are suitable for various applications in consumer electronics, optical lithography, sensing, medical treatment [12], but also optical projectors, white-light laser sources, chemical and biochemical sensing [11], photochemical processing and environmental monitoring [205]. In particular, the availability of laser diodes for the three basic colors allows the realization of ultra-compact, energy efficient laser projectors for integration in mobile devices. Furthermore, short pulse operations give access to a wider range of additional applications in bio-photonics, like fluorescence lifetime microscopy (FLIM) or fluorescence resonance energy transfer (FRET). Despite the achieved progress, there remain fundamental issues, limiting the accessible range of emission wavelengths and the efficiency of GaN-based laser diodes. In this chapter, we will give a brief introduction on the problematics of InGaN-based laser diodes, discussing the current knowledge of degradation processes in these devices.

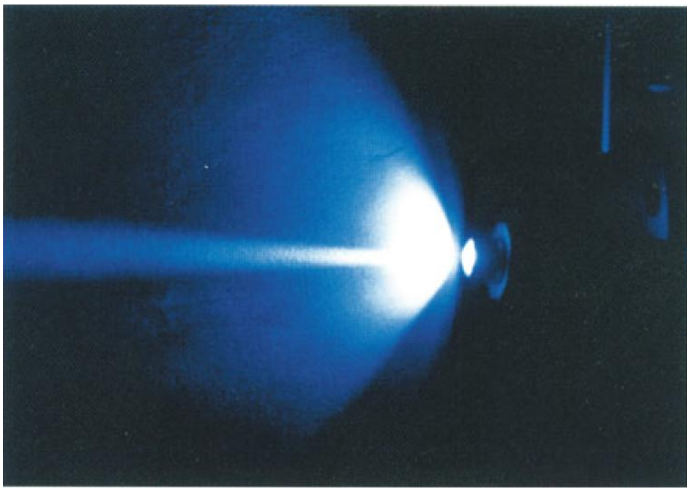

Figure 9.1: InGaN MQW structure violet LD which is operated under a pulsed current at room temperature [1].

9.1 Structure

Usually, GaN-based LDs are grown by two epitaxial method: mostly by metal-organic vapor phase epitaxy (MOVPE) [206], but also by molecular beam epitaxy (MBE) [207] on bulk GaN substrates. The growth of good quality nitride layers is a crucial issue for obtaining satisfying parameters of the device. Unfortunately, substrate problems influence epitaxial growth, leading to cracking, defects propagation and poor uniformity.

The conventional epistructure of InGaN-based laser diodes is a heterostructure consisting in 1-3 InGaN QWs. A typical structure of a nitride laser diode epitaxial structure is reported in Figure 9.2.

A p-type AlGaN layer is put on top of the active layers, acting as EBL. The active region is covered by waveguides formed usually by GaN layers. These layers may be Si- or Mg-doped, but they can be also left undoped. n- and p-doped AlGaN calddings contain the whole structure, in order to avoid optical mode leakage.

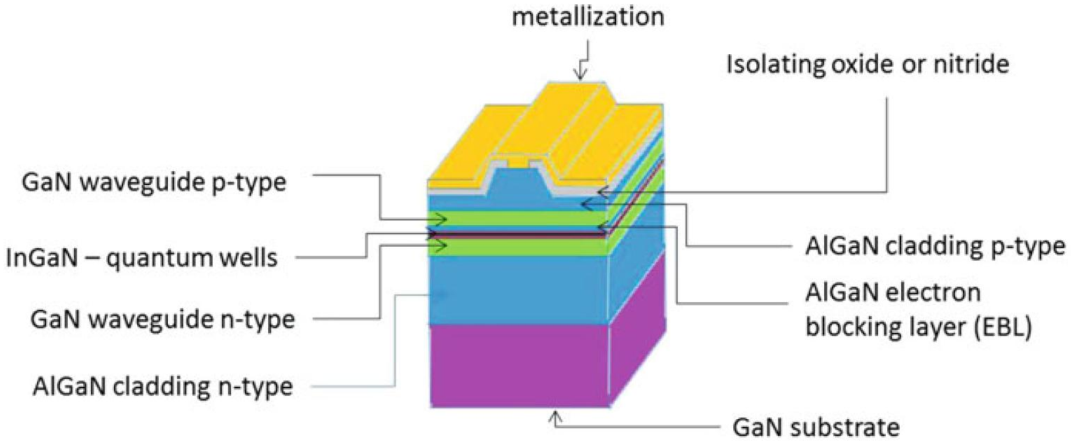

Figure 9.2: Scheme of nitride laser diode epitaxial structure [208].

9.2 Degradation of InGaN-based laser diodes

Degradation may occur in different regions of the laser diode structure. These regions are the facet, the active region and the contact region.

Degradation at the facets is a well known phenomenon and we can divide it into two main classes:

- catastrophic optical mirror damage;
- mirror degradation related to the formation of carbon deposits on the surface of the output mirror.

The first process manifests itself through the sudden increase in the mirror's temperature, that causes the melting of the facets. The temperature increase is usually caused by an optical absorption in the near-facet area of a device. This mechanism is still under investigation in nitride system.

Regarding the second mechanism, it was observed that under operation in the oxygen-free atmosphere, a process of photo-assisted hydrocarbons decomposition occurs, leading to the formation of carbon deposit and fast laser diode degradation. In particular, the carbon deposit formation may limit the lifetime of devices from few tens up to hundreds of hours [208].

Particularly important is the degradation that occurs in the whole volume of the active region. Usually, an increase in the threshold current is observed, as reported in Figure 9.3. In this case, the increase of the threshold current is not accompanied by the proportional change in the slope efficiency. This suggest an increase in the non radiative recombination within the active layer [14]. The constant slope efficiency during the operation means a constant injection efficiency and no increase in optical losses. In fact, the slope efficiency can be expressed by:

$$SE = \eta_j \frac{\alpha_m}{\alpha_i + \alpha_m} \tag{9.1}$$

where η_j is the injection efficiency, α_m mirror losses, and α_i internal losses.

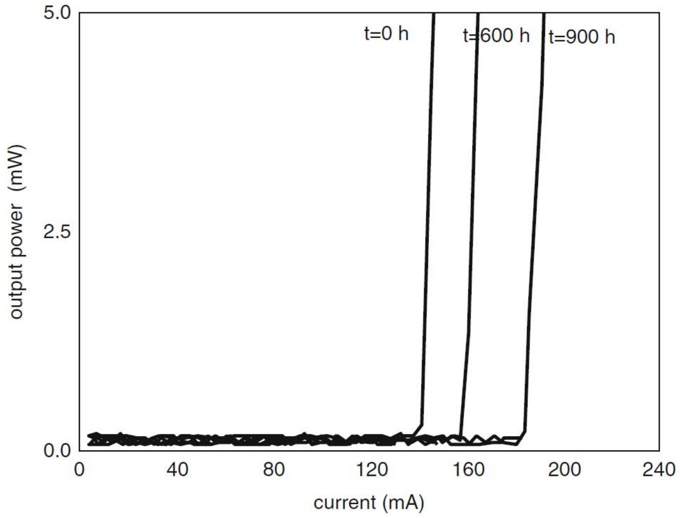

Figure 9.3: Evolution of the L-I characteristics with the degradation time [14, 17].

Some reports [14, 17, 209] have shown an increase in the threshold current with the square root of time, that is frequently associated with diffusion according to the Einstein-Smoluchowski formula:

$$\Delta x = \sqrt{Dt} \tag{9.2}$$

where Δx is change of the stoichiometry along one direction, D is diffusion coefficient and t is time. It is important to understand what actually diffuses. The interdiffusion of magnesium was a first candidate to the degradation mechanisms, but other results reported in [210], based on SIMS measurements of some dopants like Mg, H and Si over a stressed area of a LD, show no magnesium or hydrogen profile changes with the degradation, implying that these two elements are not directly involved in the diffusion process, though this does not exclude a local rearrangements of atoms around defects.

In some cases, also linear behavior of the current as function of the time is observed, but it is still not so clear what kind of degradation mechanism is involved.

Usually, degradation of laser diodes is described by the so-called activation energy E_A, value that can be estimated by using Arrhenius formula

$$D = C \exp\left(\frac{E_A}{kT}\right) \tag{9.3}$$

where D is the degradation rate, C is a constant and E_A the activation energy. Degradation rate can be defined in different ways, as, for example, change of the threshold current in the unit of time or a number of accumulated failures as function of time. This equation shows that degradation is thermally activated.

Another relevant degradation process is the increase in the non-radiative recombination rate within the active region due to the generation of defects [211, 17]. One possible methods suitable for determining the concentration of these non-radiative recombination centers is the DLTS. Meneghini et al. [118] performed DLTS measurements during stress of an InGaN laser diode, detecting a signal increasing with the degradation time. However, the identification of the defects involved in the degradation process can be quite complex.

Takeya et al. [209] demonstrated very steep dependence of the laser diodes lifetime on the number of threading dislocations in the laser diode structure. Again, the physical interpretation of this relation is not yet clear.

In general, degradation of InGaN-based laser diodes seems to be dominated by the increase in non-radiative recombination in the QWs, that leads to an increase in the threshold current. This increase can be ascribed to the generation of point defects within the active region. Moreover, also dislocations may have an important role in the degradation, but it is not yet clear. The following chapters report the works on a group of InGaN-based laser diodes, where we studied in particular the role of the defects and the impact of the dislocations on the degradation of the samples.

Chapter 10

Long-term degradation of InGaN-based laser diodes: role of defects

In this chapter we give an extensive presentation of the defect-related degradation of InGaN-based laser diodes (LDs) submitted to constant current stress, at room temperature. The analysis is based on combined electrical-optical characterization, capacitance-temperature analysis, and deep-level transient spectroscopy (DLTS). The results reported in this chapter were published in [212].

10.1 Introduction

As already mentioned in the previous chapter, an important degradation process in InGaN-based LDs is the increase in non radiative recombination due to the presence of defects. The aim of this work is to investigate the correlation between the optical degradation of InGaN laser diodes and the generation of point defects within the active region and to describe the properties of the deep levels involved. Our approach is based on combining electrical-optical (L-I) characterization with deep-level transient spectroscopy (DLTS) analysis and capacitance-temperature (C-T) measurements. In particular, we show that: (i) constant current stress induces an increase in the threshold current (I_{th}) of the devices; (ii) capacitance-temperature measurements highlight the presence of two main defects, one activated at low temperature and one at room temperature; (iii) DLTS analysis identifies the physical origin of these traps as acceptor-like defects, associated with dislocations.

10.2 Experimental details

The analysis has been carried out on a set of InGaN-based LDs, with a peak wavelength around 418 nm. The structure (Figure 10.1) consists of a Si-doped n-AlGaN cladding layer, a n-GaN guiding layer, a 2x InGaN QWs of 3.6 nm, a Mg-doped p-AlGaN EBL, of 20 nm thickness, and a Mg-doped p-AlGaN layer with a p-GaN contact layer on top. The junction area is 3×10^{-3} cm^2, and the area below the ridge is 2000 μm^2. Device were submitted to stress at constant current, $20-30$ mA higher than the Ith measured before stress, at room temperature (25°C). Stress duration was over 500 h, and a limited set of devices was stressed up to 1500 h. During the stress, the electrical and optical parameters were continuously monitored. L-I, C-T and DLTS measurements were executed without removing the devices from the stress chamber, in order to ensure good reproducibility of the results.

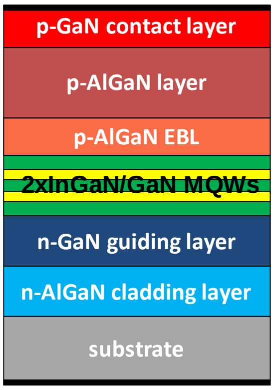

Figure 10.1: Structure of the analyzed samples.

10.3 Optical characterization and spectral analysis

Figure 10.2(a) shows the L-I curves measured during the stress at 4.075 kA/cm^2 ($I =$ 81.50 mA) and 25°C on one of the samples. Stress induced an increase in the threshold current I$_{\text{th}}$, without a strong change in the slope efficiency. From the theory we know that the slope efficiency is proportional to the differential quantum efficiency, that can be expressed by the following equation [213]

$$\eta_d = \eta_0 \frac{\alpha_m}{\alpha_m + \alpha_i} \tag{10.1}$$

where α_m represents the mirror losses and α_i the internal losses. Therefore, we may assume that stress does not modify the injection efficiency and, in turn, the mirror and absorption losses. Figure 10.2(b) shows better this increase during the aging of the device. It is possible to observe that, in the first 60 h of stress, the threshold current increases with the square root of time: this behavior suggests that degradation is promoted by a diffusion process of point defects towards the active region, that takes place most in the first hours of the device aging [214, 14]. When a diffusion process is present, theoretically the distribution of the defects has a square root dependence on Dt [200], where D is the diffusion constant of the impurity/defect involved in the degradation process and t is time.

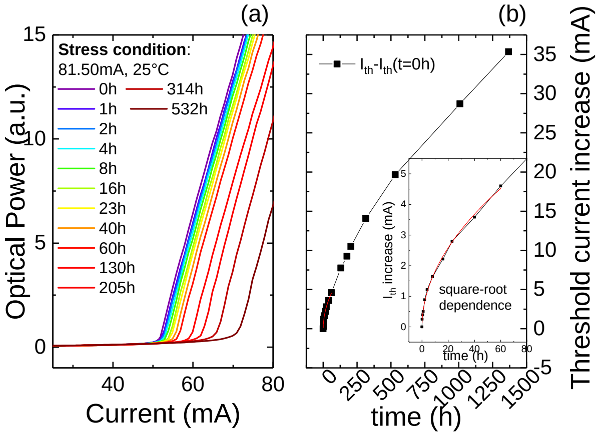

Figure 10.2: (a) L-I characteristics of one of the analyzed sample during stress. (b) Increase of the threshold current during stress.

10.4 Electrical characterization

To better analyze the degradation of the devices, the electrical characteristics were measured after each stage of the stress test. From the I-V characteristics made on another sample stressed at 3.5 kA/cm^2 ($I = 70$ mA), reported in Figure 10.3, it is possible to observe a slight increase in the reverse leakage current. This effect can be attributed to parasitic current paths across the active region and/or at the sidewalls of the junction [215]. Before stress, in the low forward-bias regime ($V < 2$ V), the I-V curve of the devices is dominated by defect-assisted conduction, possibly promoted by tunneling [137, 103]. With increasing stress time, the I-V curves show significant changes in the low current regime, namely an increase in the sub-threshold forward current. This change in the slope could be related to the creation of defects within the active region of the devices, which can enhance the trap-assisted tunneling components.

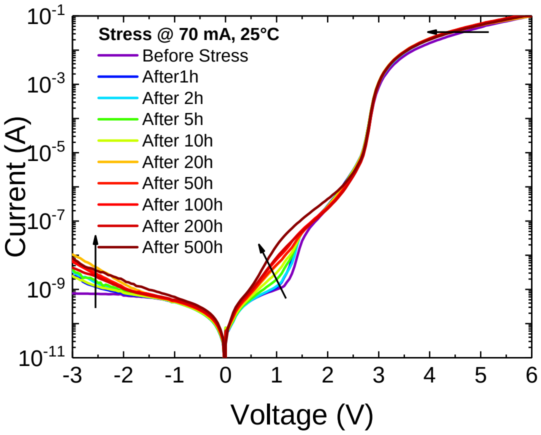

Figure 10.3: I-V characteristics of one of the analyzed sample.

In order to characterize the properties of the deep levels involved in the degradation of laser diodes, we carried out capacitance measurements and DLTS analysis. Figure 10.4(a) reports the capacitance measured as function of temperature. From this analysis, we observed an increase in the junction capacitance with device aging, indicating an increase of the free charge. A first important information regarding the defects related to the degradation is given by the capacitance derivative as function of temperature (Figure 10.4(b)): the curves revealed the presence of two defects at different temperature, one around 200 K and one around 300 K (room temperature). Here each peak represents a defect active in a particular temperature range. As can be noticed, the signal associated to the deep levels increases after stress, thus confirming that stress induced the generation of non-radiative centers in the active region.

Information on the origin of the defects was obtained by DLTS. Figure 10.5 shows the DLTS signal measured at different stress times. The measurements were carried out with a filling voltage of $V_{fill} = 1.5$ V and a reverse measuring voltage of $V_{meas} = 0$ V (in order to explore the region next to the junction). During stress, two positive peaks appear, labeled as "h_1" and "h_2". From the DLTS theory [66],we know that a positive peak is related to a minority carrier trap: in fact, the model used for these LDs assumes the junction to be unilateral, with the p-type region heavily doped with respect to the n-type region. For this reason, the space charge region (SCR) extends principally in the low doped n-type layer.

By extrapolating the Arrhenius plot before and after stress, we obtained the activation energies of the two traps: during the stress, trap "h_1" presents an activation energy in the range between 0.25 and 0.35 eV, and trap "h_2" an activation energy between 0.30 and 0.59 eV. In order to better understand the nature of these deep levels,

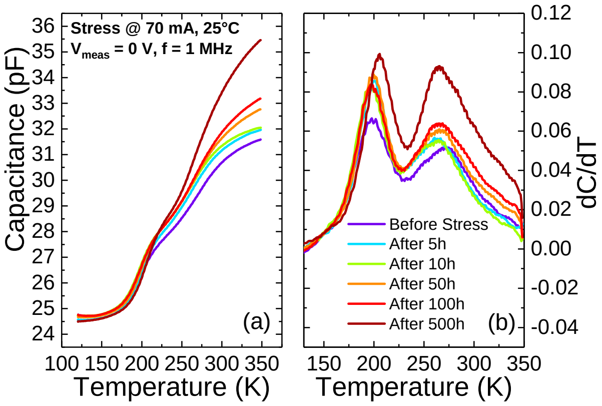

Figure 10.4: (a) Capacitance as function of temperature measurements at different stress times, showing the increase of the capacitance during stress. (b) capacitance derivative as function of temperature, revealing the presence of two peaks related to traps.

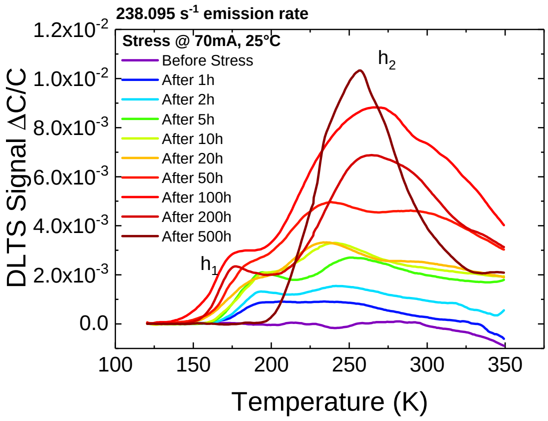

Figure 10.5: DLTS spectra obtained during stress for $V_{meas} = 0V$ and $V_{fill} = 1.5V$.

we compared our Arrhenius plots with several reports reported in literature. Results indicate that the positive peak "h_2" could be ascribed to acceptor-like traps, associated with "line defects" [216, 217]: in this case, traps are not randomly distributed throughout the crystal, but are arranged along dislocation. Also the physical origin of deep level "h_1" could be related to dislocations [218]. In Table 10.1 are reported the activation energy and cross section of the traps revealed by the DLTS spectra during stress. These results are consistent with the presence of a diffusion process of defects through dislocations in the active layer, shown by the increase in the I_{th}.

Table 10.1: Summary of the main parameters of the deep level defects deduced from the DLTS data during the stress and their possible origins; E_a is the activation energy and σ is the cross section.

Deep levels	**Ea (eV)**	$\boldsymbol{\sigma (cm^2)}$	**Possible origins**
h_1	0.25-0.35	$1.3 \cdot 10^{-17}$-$9.72 \cdot 10^{-16}$	Dislocations
h_2	0.25-0.59	$3.9 \cdot 10^{-14}$-$3.6 \cdot 10^{-19}$	Acceptor-like traps

10.5 Conclusion

In conclusion, we analyzed a group of InGaN-based laser diodes, by carrying out a stress at fixed current and temperature. Stress induced an increase in the threshold current, with the square root dependence on time in the first hours of stress, indicating the presence of a diffusion process. Capacitance-temperature and DLTS analysis allowed us to reveal two main traps related to the degradation of the device and to identify their possible physical origin. In particular, trap h_2 is probably ascribed to acceptor-like traps associated with dislocations. The presence of these dislocations is consistent with the diffusion process observed by the optical characterization.

Chapter 11

Impact of dislocations on DLTS spectra and degradation of InGaN-based laser didoes

This chapter illustrates the dependence of DLTS characteristics and degradation of InGaN-based laser diodes (LDs) on the density of dislocations. The analysis is based on combined electrical-optical measurements and DLTS investigation was made before and after stress. The data reported in this chapter were published in [219].

11.1 Introduction

The aim of this work was to study the impact of different dislocation density on the degradation of InGaN-based LDs, since the role of dislocations in GaN-based devices is still an open question. In particular, we show that: (i) DLTS analysis allows us to identify the presence of a hole trap in each sample, whose concentration increases with increasing dislocation density; (ii) constant current stress induces the degradation of the optical power in all three samples; (iii) moreover, stress may induce the generation of an electron trap, whose generation rate may be related to the dislocation density of the samples.

11.2 Experimental details

The analysis has been carried out on three groups of InGaN-based LDs, each of them with a different dislocation density: the first group has a dislocation density of $2 \cdot 10^{7}$ cm^{-2}, the second one a dislocation density of $1.5 \cdot 10^{6}$ cm^{-2}, and the third group in a range between $10^4 - 10^5$ cm^{-2}. The three groups have a peak wavelength between $422 - 426$ nm. The structure consists of InGaN multi-quantum wells (MQWs), a Mg-doped p-AlGaN electron blocking layer (EBL), of 20 nm thickness, and a Mg-doped p-type layer with a p-AlGaN top cladding layer. The junction area is $3 \cdot 10^{-3}$ cm^2, and the ridge area is $2.2 \cdot 10^{-5}$ cm^2. Figure 11.1 reports the structure of the analyzed samples. Devices were submitted to stress at constant current of 50 mA, at room temperature. The stress conditions were conservative in order to avoid a strong increase in the leakage current of the devices, since we were interested in monitoring the DLTS spectra before/after stress (DLTS characterization is strongly influenced by leakage).

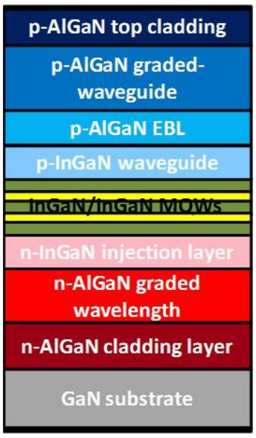

Figure 11.1: Structure of the analyzed samples.

11.3 Analysis of the DLTS results before stress

Figure 11.2 reports the DLTS signals for the three untreated samples, for a measuring voltage $V_{\text{meas}} = 0$ V and a filling pulse $V_{\text{fill}} = 1.5$ V, and a rate window of 2.38 s^{-1}. The choice of these voltages was made in order to probe the region next to the junction. We can observe the presence of a positive peak in each sample in a temperature range between 250 K and 300 K. Since we are considering that in our samples the p-type region is heavily doped, we can assume that the space charge region (SCR) extends mostly in the n-type region, thus the appearance of a positive peak in the DLTS signal means the presence of a minority carrier trap, that in our case is a hole trap. Moreover, the peak amplitude is related to the trap concentration [66]. In this case, considering the peak in the temperature range $250 - 300$ K, we observe that with the increase in the dislocation density, the amplitude of the peak increases, meaning an increase in the trap concentration associated to that deep level. The detected hole trap could be ascribed to a dislocation-related defect.

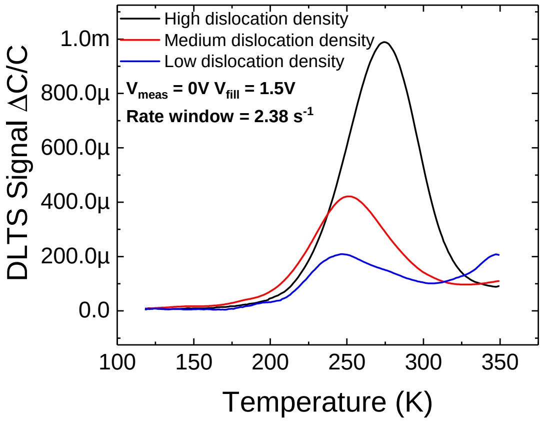

Figure 11.2: DLTS signal measured on the untreated samples for a $V_{meas} = 0$ V and $V_{fill} = 1.5$ V, and a rate window of 2.38 s^{-1}.

Figure 11.3 reports the Arrhenius plot extrapolated by the DLTS signals obtained by the previous measurements, where we can observe that samples with high and medium dislocation density present similar activation energies, meaning that the hole traps in these samples are probably the same. These results suggest that, the increase in the dislocation density in these samples causes an increase in the hole trap concentration. Sample with low dislocation density still presents a hole trap, but with a different activation energy.

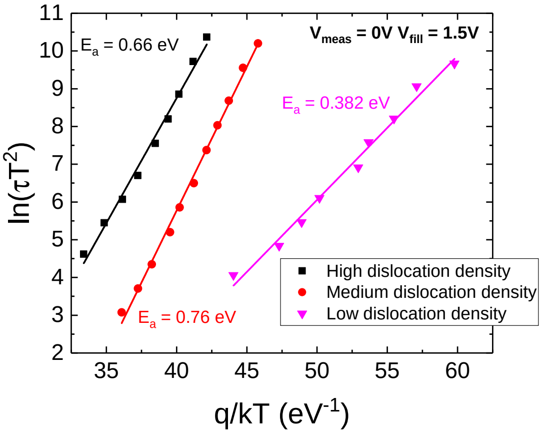

Figure 11.3: Arrhenius plot extrapolated by the DLTS measurement with $V_{meas} = 0$ V and $V_{fill} = 1.5$ V.

From a comparison with previous reports in the literature, we were able to give a first hypothesis regarding the physical origin of the traps related to the high and medium dislocation density samples: Cho et al. in [120] report nitrogen antisite point defects, and Arehart et al. [220] report that these defects may be point defects that cluster around dislocation, that means traps are arranged along dislocation. Regarding the trap in the sample with low dislocation, the physical origin is still not so clear and further investigations are required.

Figure 11.4 reports the DLTS signal for the sample with the highest dislocation density, at different applied voltages. When a measuring voltage of -2 V and a filling voltage of 0 V are applied, we are able to probe regions far away from the active region. With increasing voltages, instead, we start to approach the active region. From this figure we can observe a decrease of the positive peak amplitude related to the hole trap with increasing voltage, that means a decrease of the trap concentration approaching the active region. In general, this defect could be a point defect associated to the dislocation.

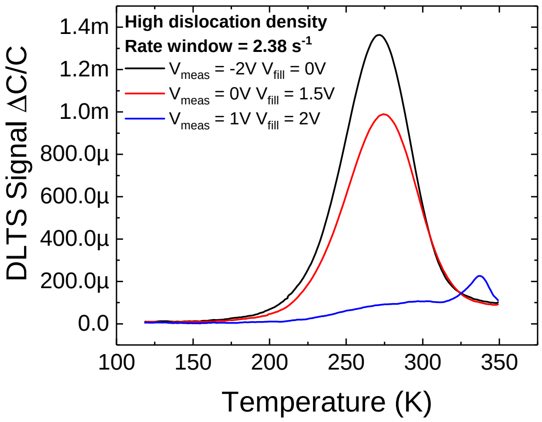

Figure 11.4: DLTS signal at different applied voltages for the sample with the highest dislocation density.

11.4 Constant current stress and DLTS analysis after stress

After this first characterization, the three samples were stressed for 100 hours at a constant current of 50 mA. The samples show similar optical power loss after the stress. With the analysis performed in this work we can say that, in our case, there is no strong relation between the different dislocation density and the degradation of the samples. This is possibly due to the fact that the average number of dislocations that cross the active region is between 440 (when TDD $= 2 \cdot 10^7$ cm^{-2}) and 2 (when TDD =

$10^4 - 10^5$ cm^{-2}), i.e. too small to favor the degradation process. Figure 11.5 shows the I-V characteristics during the stress for one of the analyzed samples (sample with the medium dislocation density). From the analysis of the electrical characterizations, we were able to notice that in all the three samples the reverse leakage current stays stable during the stress. Analyzing the voltage in forward bias at a current of 20 mA, as reported in Figure 11.6, we observed a small variation of this parameter during the stress for all samples.

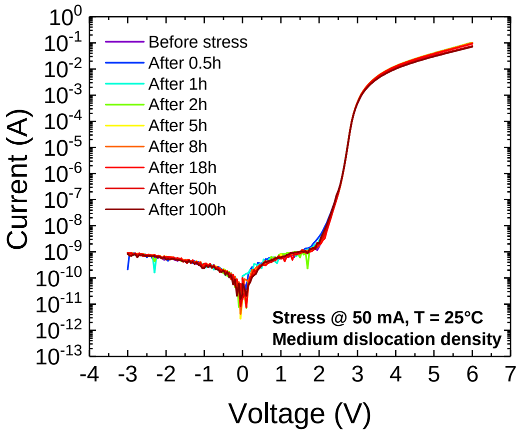

Figure 11.5: I-V characteristics of one of the analyzed sample during the stress.

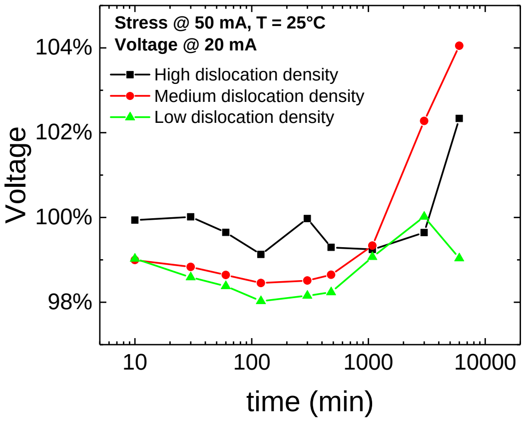

Figure 11.6: Variation during stress of the voltage at 20 mA (normalized at the value at 0 hour) for the three samples.

After stress, we performed again DLTS spectroscopy on the three samples. Figure 11.7 reports the DLTS signal before and after stress for the sample with the highest dislocation density, for $V_{\text{meas}} = 0$ V and $V_{\text{fill}} = 1.5$ V, and a rate window of 2.38 s^{-1}. After stress, we are still able to observe the positive peak now presenting a decreased amplitude. The inset in the same figure shows the DLTS signal for the sample with the medium dislocation density with the same measurement parameters. It is interesting to observe that, the signal after stress goes at negative values around the same region of the positive peak, indicating the presence of a negative peak, i.e. an electron trap. The origin of this deep level is still under investigation. This behavior is evident for all the three samples. This suggests that stress induces the generation of an electron trap in the same region of the hole trap. In particular, since we observed a decrease of the hole trap concentration for the sample with the highest dislocation density, the generation rate of this electron level may be related to the dislocation density. Probably, we are able to observe a stronger change in the DLTS spectra in the sample with the highest dislocation density since the signal may be derived mostly from the dislocation itself.

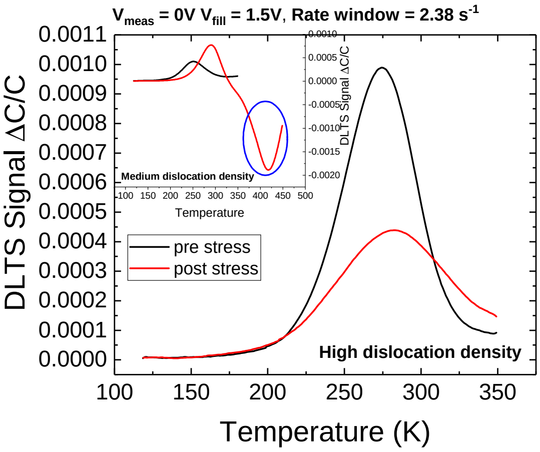

Figure 11.7: DLTS signal before and after stress for the sample with the highest dislocation density; the inset shows the DLTS signal before and after stress for the sample with the medium dislocation density.

In order to study in deep the physical nature of the observed defects, we measured the capture kinetics of the main defects observed around $T = 330$ K, with $V_{meas} = 0$ V and $V_{fill} = 1.5$ V, in sample with the medium dislocation density. The analysis consists in measuring the DLTS signal, in particular the initial ΔC capacitance peak, at varying filling pulse width, while keeping the sample at the temperature corresponding to the peak in the DLTS signal associated to the deep level under investigation [221, 222]. Figure 11.8 reports the results obtained by this measurement. As can be noticed, signal has a logarithmic dependence on filling time, indicating that it originates from to extended defects and not to simple point defects.

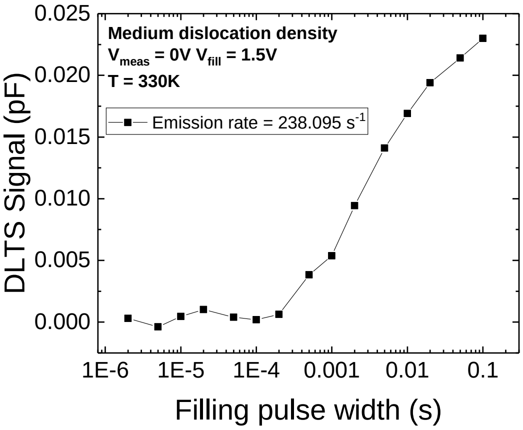

Figure 11.8: DLTS peak height (ΔC) as function of the filling pulse width.

11.5 Conclusion

In conclusion, we analyzed three groups of InGaN-based laser diodes, with different dislocation density, carrying out a stress at fixed current and temperature and carrying out before and after stress DLTS spectra. Stress induced a degradation of the optical power, with no particular dependence on the dislocation density; for this reason, we can exclude that the degradation is due to only the dislocation density. DLTS spectroscopy highlighted the presence of a hole trap in all three samples, which may be related to point defects associated to the dislocations. Stress at constant current caused the generation of an electron trap, causing in the sample with the highest dislocation density a decrease in the hole trap concentration. Capture kinetics measurements were performed and confirmed the fact that the observed traps may be related to extended defects.

Chapter 12

Conclusions

The aim of this thesis was to identify and analyze the physical mechanisms responsible for the degradation of UV-LEDs and InGaN-based laser diodes. The reliability of these devices was extensively investigated by means of accelerated life tests and thermal charatcerizations. Whereas, the role of defects in the device degradation was analyzed by means of advanced techniques such Deep-Level Transient Spectroscopy (DLTS) and Photocurrent (PC) Spectroscopy.

After a first teoretical part, the thesis was dedicated to the presentation of the most relevant results obtained during the research activity, split in two main sections.

In the first section, an extensive analysis on the degradation mechanisms affecting UV-LEDs was reported. Initially, a description of the wide range of applications of these devices, the state of the art and their performance issue is given. In particular, some limiting factor such the low external and internal quantum efficiency, the problematics in having a high value in the light extraction efficiency and the degradation of these devices are discussed. This section continues with the work carried out on four groups of UV-A LEDs, whose emission wavelength ranged from 385 nm to 420 nm. The aim of this activity was to study the impact of the emission wavelength, i.e. the structure of the active layer, on the device degradation and the physical mechanisms responsible for the degradation of UV-A power LEDs. In particular, electrical and optical characterizations were carried out at different temperatures; from these measurements, it was possible to observe a stronger dependence on the temperature of the current at low forward bias for the LED emitting at the shorter wavelength, as expected by the shallower quantum wells. In fact, due to the small band offset with respect to the barriers, a more pronounced carrier escape is promoted. The increase in reverse leakage current with the temperature was ascribed to the increase in thermally assisted multi-step tunneling component. Optical characterization as function of temperature allowed us to analyze a stronger thermal droop for the devices with shorter emission wavelength, due to a stronger thermal escape of the carriers from the QWs in these samples. The devices were stressed at different current levels, and from these accelerated tests we observed that the degradation process is ascribed to the generation of point defects within the active region. Moreover, the degradation was found to be faster for higher stress current levels, demonstrating that current is a relevant driving force for the degradation process. The emission wavelength has also a strong influence on the degradation, since devices with longer emission wavelength exhibit a weaker degradation: in fact, devices with shorter wavelength show a stronger self-heating, that accelerate the degradation kinetics. Stress carried out at a fixed current level and different temperatures showed that the degradation has a dependence on temperature.

The second part of this section is focused on the work carried out on a group of UV-B LEDs emitting at 308 nm. The aim was to understand the role of the defects in the device degradation and the physical origin of this defects, by means of electrical and optical characterizations, DLTS analysis and PC spectroscopy. Stress at constant current level induces an increase in the defectiveness of the active layer, causing an increase in SRH recombination centers. The electroluminescence spectra revealed the presence of a parasitic peak between $330 - 380$ nm related to electron overflow. Electrical characterizations show an increase in the reverse leakage current ascribed to the generation of point defects, and an increase in the current below the turn-on voltage, due to the TAT mechanisms. Since TAT model assumes the presence of mid-gap defects, we were able to demonstrate the presence of this mechanism thanks to PC spectroscopy measurements, that highlighted the existence of a mid-gap band of defects, located $2 - 2.5$ eV below the conduction band energy. DLTS investigation identified the presence of three defects, one of whom was ascribed to Mg-related acceptor traps, whose concentration is correlated with the change in the electrical characteristics of the p-type region and/or of the ohmic contacts.

The work on UV-B LEDs was carried on with an analysis of the origin of the EL peaks observed on these samples and of the thermal droop phenomenom. We were able to extract information regarding the physical origin of the different parasitic bands observed in the EL spectra. In particular, the parasitic peak defined as peak 3 was found to originate from the escape of carriers that recombine by intra-bangap radiative transitions in the last quantum barrier next to the EBL, and is influenced by the enhanced hole injection with increasing temperature at high current levels. The second parasitic band, labeled as peak 4, could be attributed to a parasitic radiative transition in the p-AlGaN superlattice, assisted by a charge transfer mechanism. Concerning the dependence on temperature of the QW emission, this showed three different behavior: at low temperatures and high current levels it was possible to observe an increase in the optical power, due to an increase in the hole injection from the p side to the n side; at high temperatures, the optical power showed a reduction due to an enhanced SRH recombination rate; finally, at low temperatures and low current levels, we observed a reduction, probably due to the exciton delocalization from the potential minima inside the QWs. A new model based on the SRH recombination lifetime and on the ABC model was developed in order to fit the decrease of the optical power with increasing temperature.

The work on AlGaN-based UV-B LEDs was then concluded with an investigation of the degradation affecting the devices when submitted to constant current stress under highly accelerated conditions, i.e. using a current stress higher than the nominal current. A careful analysis of the optical power degradation and the EL spectra during the stress, we were able to identify two main degradation mechanisms. The first degradation mechanism takes place during the first 50 hours of stress, where we observed a decrease in the intensity of the main peak of the EL spectra (the one related to the QW emission), and an increase in the intensity of the parasitic peak centered around 340 nm, whose origin was already studied in the previous chapter. For this reason, this first process could be ascribed to an increase in the carrier escape from the quantum wells, due to the generation of a positive charge density at the interface between tha last quantum barrier and the EBL. The second degradation mechanism takes place after 50 hours of stress and could be ascribed to a defect-diffusion process; as a consequence, an increase in the non-radiative recombination is observed. The analysis of the I-V characteristics revealed the increase in the reverse leakage current, ascribed to the generation of point defects. Moreover, the analysis highlighted the increase in the current below the turn-on voltage, ascribed to the TAT mechanism, with a square root dependence on time; this last evidence confirmed the presence of a diffusion process. Photocurrent spectroscopy was employed to study the presence of defects: in this case two main absorption bands were identified, one of which was attributed to defects creating states near the mid-gap, whose concentration was found to increase during the stress.

The second part of the thesis investigate on the impact of dislocation density on InGaN-based laser diodes (LDs) with a nominal emission wavelength around 418 nm and between $422 - 426$ nm. The analysis on the first group of samples was carried out by means of constant current stress. During this stress the electrical and optical parameters were monitored, and the presence of the defects was studied thanks to the capacitance-temperature measurements and DLTS analysis. The L-I characteristics showed an increase in the threshold current during the stress with a square root dependence on time, suggesting the presence of a diffusion process involved in the optical degradation of the device. Increase in defect concentration was detected from the electrical characterizations, which showed an increase in the reverse leakage current, attributed to parasitic current paths generated by defects, and an increase in the subthreshold forward current, again related to the TAT components. The presence of deep levels was studied by means of capacitance-temperature measurements, from which we were able to identify two main defects (h_1 and h_2) at different temperatures. DLTS analysis allowed then to further investigate on their physical origin. The comparison of our results with previous results in literature suggest a relation between level h_2 and an acceptor-like traps associated with line defects; level h_1 instead could be ascribed to GaN dislocations.

For the second part, three groups of LDs with different dislocation density were first submitted to DLTS analysis in order to identify the defects present in the material. A hole trap was observed in each sample, with a concentration increasing with the dislocation density; this could indicate that this defect is related to the dislocations. Stress at constant current induced a decrease in the optical power, with no particular dependence on the dislocation density, indicating degradation is not mainly related to the dislocation density. After the stress, DLTS also revealed the presence of an electron trap was observed, that caused a decrease in the hole trap concentration in the sample with the highest dislocation density. Together with DLTS analysis, we carried out capture kinetics, which confirmed the fact that the observed traps may be realted to extended defects.

Bibliography

[1] S. Nakamura and G. Fasol, *The Blue Laser Diode.* Berlin, Heidelberg: Springer Berlin Heidelberg, 1997.

[2] C. Moe, “UV-C Light Emitting Diodes,” *Radtech Report Issue 1*, pp. 45–49, 2014.

[3] M. Moseley, A. Allerman, M. Crawford, J. J. Wierer, M. Smith, and L. Biedermann, “Electrical current leakage and open-core threading dislocations in AlGaN-based deep ultraviolet light-emitting diodes,” *Journal of Applied Physics*, vol. 116, no. 5, p. 053104, 2014.

[4] M. Meneghini, D. Barbisan, Y. Bilenko, M. Shatalov, J. Yang, R. Gaska, G. Meneghesso, and E. Zanoni, “Defect-related degradation of Deep-UV-LEDs,” *Microelectronics Reliability*, vol. 50, no. 9-11, pp. 1538–1542, 2010.

[5] T. Kolbe, A. Knauer, C. Chua, Z. Yang, V. Kueller, S. Einfeldt, P. Vogt, N. M. Johnson, M. Weyers, and M. Kneissl, “Effect of temperature and strain on the optical polarization of (In)(Al)GaN ultraviolet light emitting diodes,” *Applied Physics Letters*, vol. 261105, pp. 1–5, 2011.

[6] T. Kolbe, A. Knauer, C. Chua, Z. Yang, S. Einfeldt, P. Vogt, N. M. Johnson, M. Weyers, and M. Kneissl, “Optical polarization characteristics of ultraviolet (In)(Al)GaN multiple quantum well light emitting diodes,” *Applied Physics Letters*, vol. 97, no. 17, pp. 5–8, 2010.

[7] T. Takano, T. Mino, J. Sakai, N. Noguchi, K. Tsubaki, and H. Hirayama, “Deep-ultraviolet light-emitting diodes with external quantum efficiency higher than 20% at 275 nm achieved by improving light-extraction efficiency,” *Applied Physics Express*, vol. 10, no. 3, 2017.

[8] N. Maeda, M. Jo, and H. Hirayama, “Improving the Efficiency of AlGaN Deep-UV LEDs by Using Highly Reflective Ni/Al p-Type Electrodes,” *Physica Status Solidi (A) Applications and Materials Science*, vol. 215, no. 8, pp. 1–5, 2018.

[9] M. Khizar, Z. Y. Fan, K. H. Kim, J. Y. Lin, and H. X. Jiang, "Nitride deep-ultraviolet light-emitting diodes with microlens array," *Applied Physics Letters*, vol. 86, no. 17, pp. 1–3, 2005.

[10] M. Kneissl and J. Rass, eds., *III-Nitride Ultraviolet Emitters - Technology & Applications.* Cham, Heidelberg, New York, London: Springer International Publishing, 2015.

[11] S. P. Denbaars, D. Feezell, K. Kelchner, S. Pimputkar, C. C. Pan, C. C. Yen, S. Tanaka, Y. Zhao, N. Pfaff, R. Farrell, M. Iza, S. Keller, U. Mishra, J. S. Speck, and S. Nakamura, "Development of gallium-nitride-based light-emitting diodes (LEDs) and laser diodes for energy-efficient lighting and displays," *Acta Materialia*, vol. 61, no. 3, pp. 945–951, 2013.

[12] A. A. Bergh, "Blue laser diode (LD) and light emitting diode (LED) applications," *Physica Status Solidi (A) Applied Research*, vol. 201, no. 12, pp. 2740–2754, 2004.

[13] A. Bojarska, G. Muziol, C. Skierbiszewski, E. Grzanka, P. Wiśniewski, I. Makarowa, R. Czernecki, T. Suski, and P. Perlin, "Influence of the growth method on degradation of InGaN laser diodes," *Applied Physics Express*, vol. 10, no. 9, 2017.

[14] L. Marona, P. Wisniewski, P. Prystawko, I. Grzegory, T. Suski, S. Porowski, and P. Perlin, "Degradation mechanisms in InGaN laser diodes grown on bulk GaN," vol. 201111, no. 2006, pp. 3–5, 2006.

[15] C. C. Kim, Y. Choi, Y. H. Jang, M. K. Kang, M. Joo, and M. S. Noh, "Degradation modes of high-power InGaN/GaN laser diodes on low-defect GaN substrates," vol. 6894, p. 68940O, International Society for Optics and Photonics, feb 2008.

[16] M. Furitsch, A. Avramescu, C. Eichler, K. Engl, A. Leber, A. Miler, C. Rumbolz, G. Brüderl, U. Strauß, A. Lell, and V. Härle, "Comparison of degradation mechanisms of blue-violet laser diodes grown on SiC and GaN substrates," *Physica Status Solidi (A) Applications and Materials Science*, vol. 203, no. 7, pp. 1797–1801, 2006.

[17] M. Meneghini, N. Trivellin, K. Orita, S. Takigawa, T. Tanaka, D. Ueda, G. Meneghesso, and E. Zanoni, "Degradation of InGaN-based laser diodes analyzed by means of electrical and optical measurements," *Applied Physics Letters*, vol. 97, no. 26, pp. 10–13, 2010.

[18] S. Tomiya, T. Hino, S. Goto, M. Takeya, and M. Ikeda, “Dislocation related issues in the degradation of GaN-based laser diodes,” *IEEE Journal on Selected Topics in Quantum Electronics*, vol. 10, no. 6, pp. 1277–1286, 2004.

[19] E. F. Schubert, *Light-Eitting Diodes.* 2006.

[20] H. Morkoç, *Handbook of nitride semiconductors and devices. Volume 1, Materials, properties, physics and growth.* Wiley-VCH, 2008.

[21] G. A. Slack, L. J. Schowalter, D. Morelli, and J. A. Freitas, “Some effects of oxygen impurities on AlN and GaN,” *Journal of Crystal Growth*, vol. 246, pp. 287–298, dec 2002.

[22] F. Yun, M. A. Reshchikov, L. He, T. King, H. Morkoç, S. W. Novak, and L. Wei, “Energy band bowing parameter in AlxGa1xN alloys,” *Journal of Applied Physics*, vol. 92, pp. 4837–4839, oct 2002.

[23] M. A. Khan, J. M. Van Hove, J. N. Kuznia, and D. T. Olson, “High electron mobility GaN/Al _{<i>x</i>} Ga _{1 <i>x</i>} N heterostructures grown by low-pressure metalorganic chemical vapor deposition,” *Applied Physics Letters*, vol. 58, pp. 2408–2410, may 1991.

[24] T. Tanaka, A. Watanabe, H. Amano, Y. Kobayashi, I. Akasaki, S. Yamazaki, and M. Koike, “P-type conduction in Mg-doped GaN and Al0.08Ga0.92N grown by metalorganic vapor phase epitaxy,” *Applied Physics Letters*, vol. 65, no. 5, pp. 593–594, 1994.

[25] K. B. Nam, J. Li, M. L. Nakarmi, J. Y. Lin, and H. X. Jiang, “Unique optical properties of AlGaN alloys and related ultraviolet emitters,” *Applied Physics Letters*, vol. 84, pp. 5264–5266, jun 2004.

[26] D. A. B. Miller, D. S. Chemla, T. C. Damen, A. C. Gossard, W. Wiegmann, T. H. Wood, and C. A. Burrus, “Band-Edge Electroabsorption in Quantum Well Structures: The Quantum-Confined Stark Effect,” *Physical Review Letters*, vol. 53, pp. 2173–2176, nov 1984.

[27] A. Hangleiter, “Optical properties of nitride heterostructures,” *Physica Status Solidi C: Conferences*, vol. 0, no. 6 SPEC. ISS., pp. 1816–1834, 2003.

[28] M. Kanamura, T. Kikkawa, and K. Joshin, “A 100-W high-gain A1GaNIGaN HEMT power amplifier on a conductive N-SiC substrate for wireless base station

applications," in *IEDM Technical Digest. IEEE International Electron Devices Meeting, 2004.*, pp. 799–802, IEEE, 2004.

[29] R. Quay, *Gallium nitride electronics.* Springer, 2008.

[30] S. Nakamura, "InGaN/GaN/AIGaN-Based Laser Diodes With an Estimated Lifetime of Longer Than 10,000 Hours," *MRS Bulletin*, vol. 23, pp. 37–43, may 1998.

[31] S. N. Mohammad, A. A. Salvador, and H. Morkoc, "Emerging gallium nitride based devices," *Proceedings of the IEEE*, vol. 83, no. 10, pp. 1306–1355, 1995.

[32] H. Amano, M. Kito, K. Hiramatsu, and I. Akasaki, "P-Type Conduction in Mg-Doped GaN Treated with Low-Energy Electron Beam Irradiation (LEEBI)," *Japanese Journal of Applied Physics*, vol. 28, pp. L2112–L2114, dec 1989.

[33] I. Akasaki, H. Amano, M. Kito, and K. Hiramatsu, "Photoluminescence of Mg-doped p-type GaN and electroluminescence of GaN p-n junction LED," *Journal of Luminescence*, vol. 48-49, pp. 666–670, jan 1991.

[34] S. Nakamura, T. Mukai, M. Senoh, and N. Iwasa, "Thermal Annealing Effects on P-Type Mg-Doped GaN Films," *Japanese Journal of Applied Physics*, vol. 31, pp. L139–L142, feb 1992.

[35] I. Akasaki and H. Amano, "Widegap Column-III Nitride Semiconductors for UV/Blue Light Emitting Devices," *Journal of The Electrochemical Society*, vol. 141, p. 2266, aug 1994.

[36] W. Götz, N. M. Johnson, J. Walker, D. P. Bour, and R. A. Street, "Activation of acceptors in Mg-doped GaN grown by metalorganic chemical vapor deposition," *Applied Physics Letters*, vol. 68, p. 667, aug 1998.

[37] P. Kozodoy, H. Xing, S. P. DenBaars, U. K. Mishra, A. Saxler, R. Perrin, S. Elhamri, and W. C. Mitchel, "Heavy doping effects in Mg-doped GaN," *Journal of Applied Physics*, vol. 87, p. 1832, jan 2000.

[38] S. Nakamura, N. Iwasa, M. Senoh, and T. Mukai, "Hole Compensation Mechanism of P-Type GaN Films," *Japanese Journal of Applied Physics*, vol. 31, pp. 1258–1266, may 1992.

[39] U. Kaufmann, M. Kunzer, M. Maier, H. Obloh, A. Ramakrishnan, B. Santic, and P. Schlotter, "Nature of the 2.8 eV photoluminescence band in Mg doped GaN," *Applied Physics Letters*, vol. 72, p. 1326, jul 1998.

[40] S. Nakamura, T. Mukai, and M. Senoh, "High-Power GaN P-N Junction Blue-Light-Emitting Diodes," *Japanese Journal of Applied Physics*, vol. 30, p. L1998, 1991.

[41] C. Chu, C. C. Yu, Y. K. Wang, J. Y. Tsai, F. I. Lai, and S. C. Wang, "Low-resistance ohmic contacts on p-type GaN using Ni/Pd/Au metallization," *Applied Physics Letters*, vol. 77, no. 2000, p. 3423, 2000.

[42] C. G. Van De Walle and J. Neugebauer, "First-principles calculations for defects and impurities: Applications to III-nitrides," *Journal of Applied Physics*, vol. 95, no. 8, pp. 3851–3879, 2004.

[43] D. C. Look, D. C. Reynolds, J. W. Hemsky, J. R. Sizelove, R. L. Jones, and R. J. Molnar, "Defect Donor and Acceptor in GaN," *Physical Review Letters*, vol. 79, pp. 2273–2276, sep 1997.

[44] J. L. Lyons, A. Alkauskas, A. Janotti, and C. G. Van de Walle, "First-principles theory of acceptors in nitride semiconductors," *physica status solidi (b)*, vol. 252, pp. 900–908, may 2015.

[45] W. Götz, R. S. Kern, C. H. Chen, H. Liu, D. A. Steigerwald, and R. M. Fletcher, "Hall-effect characterization of III–V nitride semiconductors for high efficiency light emitting diodes," *Materials Science and Engineering: B*, vol. 59, pp. 211–217, may 1999.

[46] J. Neugebauer and C. G. Van de Walle, "Hydrogen in GaN: Novel Aspects of a Common Impurity," *Physical Review Letters*, vol. 75, pp. 4452–4455, dec 1995.

[47] J. Neugebauer and C. G. Van De Walle, "Role of hydrogen in doping of GaN," *Applied Physics Letters*, vol. 68, p. 1829, jun 1998.

[48] P. Perlin, T. Suski, H. Teisseyre, M. Leszczynski, I. Grzegory, J. Jun, S. Porowski, P. Bogusławski, J. Bernholc, J. C. Chervin, A. Polian, and T. D. Moustakas, "Towards the Identification of the Dominant Donor in GaN," *Physical Review Letters*, vol. 75, pp. 296–299, jul 1995.

[49] P. Perlin, T. Suski, A. Polian, J. C. Chervin, E. Litwin-Staszewska, I. Grzegory, S. Porowski, and J. W. Erickson, "Spatial distribution of electron concentration and strain in bulk GaN single crystals - relation to growth mechanism," *MRS Proceedings*, vol. 449, p. 519, jan 1996.

[50] J. Speck and S. Rosner, “The role of threading dislocations in the physical properties of GaN and its alloys,” *Physica B: Condensed Matter*, vol. 273-274, pp. 24–32, dec 1999.

[51] T. Hino, S. Tomiya, T. Miyajima, K. Yanashima, S. Hashimoto, and M. Ikeda, “Characterization of threading dislocations in GaN epitaxial layers,” *Applied Physics Letters*, vol. 76, p. 3421, may 2000.

[52] N. G. Weimann, L. F. Eastman, D. Doppalapudi, H. M. Ng, and T. D. Moustakas, “Scattering of electrons at threading dislocations in GaN,” *Journal of Applied Physics*, vol. 83, p. 3656, jun 1998.

[53] T. Kehagias, P. Komninou, G. Nouet, P. Ruterana, and T. Karakostas, “Misfit relaxation of the AlN/Al2O3 (0001) interface,” *Physical Review B - Condensed Matter and Materials Physics*, vol. 64, p. 195329, oct 2001.

[54] P. Ruterana, A. M. Sánchez, and G. Nouet, “Extended Defects in Wurtzite GaN Layers: Atomic Structure, Formation, and Interaction Mechanisms,” in *Nitride Semiconductors - Handbook on Materials and Devices*, pp. 379–438, Weinheim, FRG: Wiley-VCH Verlag GmbH & Co. KGaA, jun 2003.

[55] G. P. Dimitrakopulos, P. Komninou, T. Karakostas, and R. C. Pond, “Topological Analysis of Defects in Nitride Semiconductors,” in *Nitride Semiconductors - Handbook on Materials and Devices*, pp. 319–377, Weinheim, FRG: Wiley-VCH Verlag GmbH & Co. KGaA, jun 2003.

[56] J. Elsner, R. Jones, P. K. Sitch, V. D. Porezag, M. Elstner, T. Frauenheim, M. I. Heggie, S. Öberg, and P. R. Briddon, “Theory of Threading Edge and Screw Dislocations in GaN,” *Physical Review Letters*, vol. 79, pp. 3672–3675, nov 1997.

[57] W. Qian, G. S. Rohrer, M. Skowronski, K. Doverspike, L. B. Rowland, and D. K. Gaskill, “Open-core screw dislocations in GaN epilayers observed by scanning force microscopy and high-resolution transmission electron microscopy,” *Applied Physics Letters*, vol. 67, pp. 2284–2286, oct 1995.

[58] J. Elsner, R. Jones, M. I. Heggie, P. K. Sitch, M. Haugk, T. Frauenheim, S. Öberg, and P. R. Briddon, “Deep acceptors trapped at threading-edge dislocations in GaN,” *Physical Review B*, vol. 58, pp. 12571–12574, nov 1998.

[59] I. Arslan and N. D. Browning, “Role of Oxygen at Screw Dislocations in GaN,” *Physical Review Letters*, vol. 91, p. 165501, oct 2003.

[60] J. E. Northrup, “Screw dislocations in GaN: The Ga-filled core model,” *Applied Physics Letters*, vol. 78, pp. 2288–2290, apr 2001.

[61] S. M. Lee, M. A. Belkhir, X. Y. Zhu, Y. H. Lee, Y. G. Hwang, and T. Frauenheim, “Electronic structures of GaN edge dislocations,” *Physical Review B*, vol. 61, pp. 16033–16039, jun 2000.

[62] A. Y. Polyakov and I. Lee, “Deep traps in GaN-based structures as affecting the performance of GaN devices,” *Materials Science and Engineering: R: Reports*, vol. 94, pp. 1–56, aug 2015.

[63] U. K. Mishra and J. Singh, *Semiconductor Device Physics and Design*. Springer, 2008.

[64] D. Sands, *Diode Lasers*. CRC Press, 2004.

[65] S. O. Kasap, *Optoelectronics and Photonics: Principles and Practices*. Pearson, 2013.

[66] D. Lang, “Deep-level transient spectroscopy: A new method to characterized traps in semiconductors,” *Journal of Applied Physics*, vol. 45, no. 7, pp. 3023–3032, 1974.

[67] D. V. Lang, “Space-charge spectroscopy in semiconductors,” pp. 93–133, Springer, Berlin, Heidelberg, 1979.

[68] D. Monti, M. Meneghini, C. De Santi, G. Meneghesso, E. Zanoni, J. Glaab, J. Rass, S. Einfeldt, F. Mehnke, T. Wernicke, and M. Kneissl, “Defect generation in deep-UV AlGaN-based LEDs investigated by electrical and spectroscopic characterisation,” *Proceedings of SPIE*, vol. 10124, pp. 1–9, 2017.

[69] J. Rass, T. Kolbe, N. Lobo Ploch, T. Wernicke, F. Mehnke, C. Kuhn, J. Enslin, M. Guttmann, C. Reich, A. Mogilatenko, J. Glaab, C. Stoelmacker, M. Lapeyrade, S. Einfeldt, M. Weyers, and M. Kneissl, “High power UV-B LEDs with long lifetime,” *Proceedings of SPIE*, vol. 9363, pp. 9363K–1–13, 2015.

[70] Y. Muramoto, M. Kimura, and S. Nouda, “Development and future of ultraviolet light-emitting diodes: UV-LED will replace the UV lamp,” *Semiconductor Science and Technology*, vol. 29, no. 8, p. 084004, 2014.

[71] H. Hönigsmann, “History of phototherapy in dermatology,” *Photochemical & Photobiological Sciences*, vol. 12, no. 1, pp. 16–21, 2012.

[72] J. A. Parrish, "Phototherapy and Photochemotherapy of Skin Diseases," *Journal of Investigative Dermatology*, vol. 77, pp. 167–171, jul 1981.

[73] S. Vilhunen, H. Särkkä, and M. Sillanpää, "Ultraviolet light-emitting diodes in water disinfection," *Environmental Science and Pollution Research*, vol. 16, pp. 439–442, jun 2009.

[74] M. A. Würtele, T. Kolbe, M. Lipsz, A. Külberg, M. Weyers, M. Kneissl, and M. Jekel, "Application of GaN-based ultraviolet-C light emitting diodes - UV LEDs - for water disinfection," *Water Research*, vol. 45, no. 3, pp. 1481–1489, 2011.

[75] W. Kowalski, *Ultraviolet Germicidal Irradiation Handbook*. Berlin, Heidelberg: Springer Berlin Heidelberg, 2009.

[76] J. Mellqvist and A. Rosén, "DOAS for flue gas monitoring-I. Temperature effects in the U.V./visible absorption spectra of NO, NO2, SO2 and NH3," *Journal of Quantitative Spectroscopy and Radiative Transfer*, vol. 56, pp. 187–208, aug 1996.

[77] J. Hodgkinson and R. P. Tatam, "Optical gas sensing: a review," *Measurement Science and Technology*, vol. 24, p. 012004, jan 2013.

[78] P. J. Hargis, Jr., T. J. Sobering, G. C. Tisone, J. S. Wagner, S. A. Young, and R. J. Radloff, "Ultraviolet fluorescence identification of protein, DNA, and bacteria," vol. 2366, p. 147, International Society for Optics and Photonics, feb 1995.

[79] M. Lapeyrade, A. Muhin, S. Einfeldt, U. Zeimer, A. Mogilatenko, M. Weyers, and M. Kneissl, "Electrical properties and microstructure of vanadium-based contacts on ICP plasma etched n-type AlGaN:Si and GaN:Si surfaces," *Semiconductor Science and Technology*, vol. 28, p. 125015, dec 2013.

[80] S. F. Chichibu, A. Uedono, T. Onuma, B. A. Haskell, A. Chakraborty, T. Koyama, P. Fini, S. Keller, S. P. DenBaars, J. S. Speck, U. K. Mishra, S. Nakamura, S. Yamaguchi, S. Kamiyama, H. Amano, I. Akasaki, J. Han, and T. Sota, "Origin of defect-insensitive emission probability in In-containing (Al,In,Ga)N alloy semiconductors," *Nature Materials*, vol. 5, pp. 810–816, oct 2006.

[81] S. Y. Karpov and Y. N. Makarov, "Dislocation effect on light emission efficiency in gallium nitride," *Applied Physics Letters*, vol. 81, no. 25, p. 4721, 2002.

[82] H. Hirayama, Y. Tsukada, T. Maeda, and N. Kamata, “Marked enhancement in the efficiency of deep-ultraviolet AlGaN light-emitting diodes by using a multiquantum-barrier electron blocking layer,” *Applied Physics Express*, vol. 3, pp. 3–6, 2010.

[83] T. Kolbe, F. Mehnke, M. Guttmann, C. Kuhn, J. Rass, T. Wernicke, and M. Kneissl, “Improved injection efficiency in 290 nm light emitting diodes with Al(Ga)N electron blocking heterostructure,” *Applied Physics Letters*, vol. 103, no. 3, p. 031109, 2013.

[84] M. S. Shur and R. Gaska, “Deep-Ultraviolet Light-Emitting Diodes,” *IEEE Transactions on Electron Devices*, vol. 57, no. 1, pp. 12–25, 2010.

[85] T. N. Oder, K. H. Kim, J. Y. Lin, and H. X. Jiang, “III-nitride blue and ultraviolet photonic crystal light emitting diodes,” *Applied Physics Letters*, vol. 84, pp. 466–468, jan 2004.

[86] A. Khan, K. Balakrishnan, and T. Katona, “Ultraviolet light-emitting diodes based on group three nitrides,” *Nature Photonics*, vol. 2, pp. 77–84, feb 2008.

[87] V. Adivarahan, A. Heidari, B. Zhang, Q. Fareed, S. Hwang, M. Islam, and A. Khan, “280 nm Deep Ultraviolet Light Emitting Diode Lamp with an AlGaN Multiple Quantum Well Active Region,” *Applied Physics Express*, vol. 2, p. 102101, sep 2009.

[88] L. Zhou, J. E. Epler, M. R. Krames, W. Goetz, M. Gherasimova, Z. Ren, J. Han, M. Kneissl, and N. M. Johnson, “Vertical injection thin-film AlGaN/AlGaN multiple-quantum-well deep ultraviolet light-emitting diodes,” *Applied Physics Letters*, vol. 89, no. 24, p. 241113, 2006.

[89] T. Gessmann, E. Schubert, J. Graff, K. Streubel, and C. Karnutsch, “Omnidirectional reflective contacts for light-emitting diodes,” *IEEE Electron Device Letters*, vol. 24, pp. 683–685, nov 2003.

[90] N. Lobo, H. Rodriguez, A. Knauer, M. Hoppe, S. Einfeldt, P. Vogt, M. Weyers, and M. Kneissl, “Enhancement of light extraction in ultraviolet light-emitting diodes using nanopixel contact design with Al reflector,” *Applied Physics Letters*, vol. 96, p. 081109, feb 2010.

[91] J. DeGroot, Jr., A. Norris, S. Glover, and T. Clapp, “Highly transparent silicone materials,” in *Linear and Nonlinear Optics of Organic Materials IV*, p. 8,

Bellingham, Wash.: SPIE - The International Society of Optical Engineering, 2004.

[92] J. J. Wierer, D. A. Steigerwald, M. R. Krames, J. J. O'Shea, M. J. Ludowise, G. Christenson, Y.-C. Shen, C. Lowery, P. S. Martin, S. Subramanya, W. Götz, N. F. Gardner, R. S. Kern, and S. A. Stockman, "High-power AlGaInN flip-chip light-emitting diodes," *Applied Physics Letters*, vol. 78, pp. 3379–3381, may 2001.

[93] G. Y. Lui, D. Roser, R. Corkish, N. Ashbolt, P. Jagals, and R. Stuetz, "Photovoltaic powered ultraviolet and visible light-emitting diodes for sustainable point-of-use disinfection of drinking waters," *Science of The Total Environment*, vol. 493, pp. 185–196, sep 2014.

[94] J. Glaab, C. Ploch, R. Kelz, C. Stölmacker, M. Lapeyrade, N. Lobo Ploch, J. Rass, T. Kolbe, S. Einfeldt, F. Mehnke, C. Kuhn, T. Wernicke, M. Weyers, and M. Kneissl, "Temperature induced degradation of InAlGaN multiple-quantum well UV-B LEDs," *MRS Proceedings*, vol. 1792, no. JANUARY, pp. mrss15–2102646, 2015.

[95] J. Glaab, C. Ploch, R. Kelz, C. Stölmacker, M. Lapeyrade, N. Lobo Ploch, J. Rass, T. Kolbe, S. Einfeldt, F. Mehnke, C. Kuhn, T. Wernicke, M. Weyers, and M. Kneissl, "Degradation of (InAlGa)N-based UV-B light emitting diodes stressed by current and temperature," *Journal of Applied Physics*, vol. 118, no. 9, p. 094504, 2015.

[96] A. Fujioka, K. Asada, H. Yamada, T. Ohtsuka, T. Ogawa, T. Kosugi, D. Kishikawa, and T. Mukai, "High-output-power 255/280/310 nm deep ultraviolet light-emitting diodes and their lifetime characteristics," *Semiconductor Science and Technology*, vol. 29, p. 084005, jun 2014.

[97] C. G. Moe, J. R. Grandusky, J. Chen, K. Kitamura, M. C. Mendrick, M. Jamil, M. Toita, S. R. Gibb, and L. J. Schowalter, "High-power pseudomorphic mid-ultraviolet light-emitting diodes with improved efficiency and lifetime," p. 89861V, mar 2014.

[98] N. Lobo Ploch, H. Rodriguez, C. Stolmacker, M. Hoppe, M. Lapeyrade, J. Stellmach, F. Mehnke, T. Wernicke, A. Knauer, V. Kueller, M. Weyers, S. Einfeldt, and M. Kneissl, "Effective Thermal Management in Ultraviolet Light-Emitting Diodes With Micro-LED Arrays," *IEEE Transactions on Electron Devices*, vol. 60, pp. 782–786, feb 2013.

[99] N. L. Ploch, S. Einfeldt, M. Frentrup, J. Rass, T. Wernicke, A. Knauer, V. Kueller, M. Weyers, and M. Kneissl, "Investigation of the temperature dependent efficiency droop in UV LEDs," *Semiconductor Science and Technology*, vol. 28, no. 12, 2013.

[100] M. Shatalov, W. Sun, R. Jain, A. Lunev, X. Hu, A. Dobrinsky, Y. Bilenko, J. Yang, G. A. Garrett, L. E. Rodak, M. Wraback, M. Shur, and R. Gaska, "High power AlGaN ultraviolet light emitters," *Semiconductor Science and Technology*, vol. 29, p. 084007, jun 2014.

[101] D. Monti, M. Meneghini, C. De Santi, G. Meneghesso, and E. Zanoni, "Degradation of UV-A LEDs: Physical Origin and Dependence on Stress Conditions," *IEEE Transactions on Device and Materials Reliability*, vol. 16, no. 2, pp. 213–219, 2016.

[102] Y. Xi and E. F. Schubert, "Junction–temperature measurement in GaN ultraviolet light-emitting diodes using diode forward voltage method," *Applied Physics Letters*, vol. 85, no. 12, pp. 2163–2165, 2004.

[103] M. Mandurrino, G. Verzellesi, M. Goano, M. Vallone, F. Bertazzi, G. Ghione, M. Meneghini, G. Meneghesso, and E. Zanoni, "Physics-based modeling and experimental implications of trap-assisted tunneling in InGaN/GaN light-emitting diodes," *Physica Status Solidi (a)*, vol. 953, no. 5, pp. 947–953, 2015.

[104] J. Kim, J.-Y. Kim, Y. Tak, J. Kim, H.-G. Hong, M. Yang, S. Chae, J. Park, Y. Park, and U. Chung, "Investigation of Reverse Leakage Characteristics of InGaN/GaN Light-Emitting Diodes on Silicon," *IEEE Electron Device Letters*, vol. 33, no. 12, pp. 1741–1743, 2012.

[105] Q. Shan, D. S. Meyaard, Q. Dai, J. Cho, F. E. Schubert, J. Kon Son, and C. Sone, "Transport-mechanism analysis of the reverse leakage current in GaInN light-emitting diodes," *Applied Physics Letters*, vol. 99, no. 25, p. 253506, 2011.

[106] X. A. Cao, S. F. LeBoeuf, and T. E. Stecher, "Temperature-dependent electroluminescence of AlGaN-based UV LEDs," *Ieee Electron Device Letters*, vol. 27, no. 5, pp. 329–331, 2006.

[107] S. Moon and J. Kwak, "High-current Electro-optical Degradation of InGaN / GaN Light-emitting Diodes Fabricated with Ag-based Reflectors," *Journal of the Korean Physical Society*, vol. 55, no. 3, pp. 1128–1131, 2009.

[108] M. S. Ferdous, X. Wang, M. N. Fairchild, and S. D. Hersee, “Effect of threading defects on InGaNGaN multiple quantum well light emitting diodes,” *Applied Physics Letters*, vol. 91, no. 23, pp. 11–13, 2007.

[109] C. Sah, R. Noyce, and W. Shockley, “Carrier Generation and Recombination in P-N Junctions and P-N Junction Characteristics,” *Proceedings of the IRE*, vol. 45, no. 9, pp. 1228–1243, 1957.

[110] J. M. Shah, Y. L. Li, T. Gessmann, and E. F. Schubert, “Experimental analysis and theoretical model for anomalously high ideality factors (n>>2.0) in AlGaN/GaN p-n junction diodes,” *Journal of Applied Physics*, vol. 94, no. 4, pp. 2627–2630, 2003.

[111] X. A. Cao, J. M. Teetsov, M. P. D’Evelyn, D. W. Merfeld, and C. H. Yan, “Electrical characteristics of InGaN/GaN light-emitting diodes grown on GaN and sapphire substrates,” *Applied Physics Letters*, vol. 85, no. 1, p. 7, 2004.

[112] H. C. Casey, J. Muth, S. Krishnankutty, and J. M. Zavada, “Dominance of tunneling current and band filling in InGaN/AlGaN double heterostructure blue light-emitting diodes,” *Applied Physics Letters*, vol. 68, no. 20, pp. 2867–2869, 1996.

[113] P. Perlin, M. Osiński, P. G. Eliseev, V. A. Smagley, J. Mu, M. Banas, and P. Sartori, “Low-temperature study of current and electroluminescence in InGaN/AlGaN/GaN double-heterostructure blue light-emitting diodes,” *Applied Physics Letters*, vol. 69, pp. 1680–1682, 1996.

[114] H. Chen, A. Keppens, P. Hanselaer, Y. Lu, Y. Gao, R. Zhuang, and Z. Chen, “Failure analysis of electrical-thermal-optical characteristics of LEDs based on AlGaInP and InGaN/GaN,” *Semiconductor Physics and Technology*, vol. 46, no. 10, pp. 1333–1338, 2012.

[115] J. Xu, M. F. Schubert, A. N. Noemaun, D. Zhu, J. K. Kim, E. F. Schubert, M. H. Kim, H. J. Chung, S. Yoon, C. Sone, and Y. Park, “Reduction in efficiency droop, forward voltage, ideality factor, and wavelength shift in polarization-matched GaInN/GaInN multi-quantum-well light-emitting diodes,” *Applied Physics Letters*, vol. 94, no. 1, pp. 92–95, 2009.

[116] C. M. Tan and P. Singh, “Time evolution degradation physics in high power white LEDs under high temperature-humidity conditions,” *IEEE Transactions on Device and Materials Reliability*, vol. 14, no. 2, pp. 742–750, 2014.

[117] A. E. Y. F. Manyakhin, A. Kovalev, “Aging Mechanisms of InGaN/AlGaN/GaN Light Emitting Diodes Operating at High Currents,” *MRS Internet J. Nitride Semicond. Res.*, vol. 53, no. 1998, pp. 1–6, 1999.

[118] M. Meneghini, C. De Santi, N. Trivellin, K. Orita, S. Takigawa, T. Tanaka, D. Ueda, G. Meneghesso, and E. Zanoni, “Investigation of the deep level involved in InGaN laser degradation by deep level transient spectroscopy,” *Applied Physics Letters*, vol. 99, no. 9, pp. 97–100, 2011.

[119] H. M. Chung, W. C. Chuang, Y. C. Pan, C. C. Tsai, M. C. Lee, W. H. Chen, W. K. Chen, C. I. Chiang, C. H. Lin, and H. Chang, “Electrical characterization of isoelectronic In-doping effects in GaN films grown by metalorganic vapor phase epitaxy,” *Applied Physics Letters*, vol. 76, no. 7, p. 897, 2000.

[120] H. K. Cho, C. S. Kim, and C. H. Hong, “Electron capture behaviors of deep level traps in unintentionally doped and intentionally doped n-type GaN,” *Journal of Applied Physics*, vol. 94, no. 3, pp. 1485–1489, 2003.

[121] M. A. Reshchikov and H. Morkoç, “Luminescence properties of defects in GaN,” *Journal of Applied Physics*, vol. 97, no. 6, 2005.

[122] H. Cho, F. Khan, I. Adesida, Z.-Q. Fang, and D. Look, “Deep level characteristics in n-GaN with inductively coupled plasma damage,” *Journal of Physics D: Applied Physics*, vol. 41, no. 15, p. 155314, 2008.

[123] M. Meneghini, D. Barbisan, L. Rodighiero, G. Meneghesso, and E. Zanoni, “Analysis of the physical processes responsible for the degradation of deep-ultraviolet light emitting diodes,” *Applied Physics Letters*, vol. 97, no. 14, pp. 1–4, 2010.

[124] M. Ikeda, T. Mizuno, M. Takeya, S. Goto, S. Ikeda, T. Fujimoto, Y. Ohfuji, and T. Hashizu, “High-power GaN-based semiconductor lasers,” *Physica Status Solidi (C)*, vol. 1, no. 6, pp. 1461–1467, 2004.

[125] T. Asano, M. Takeya, T. Mizuno, S. Ikeda, Y. Ohfuji, T. Fujimoto, K. Oikawa, S. Goto, T. Hashizu, K. Aga, and M. Ikeda, “Over 100-mW blue-violet laser diodes for Blu-ray Disc system,” *Proceedings of SPIE*, vol. 5365, pp. 297–305, 2004.

[126] S. Nakamura, “InGaN-based laser diodes with an estimated lifetime of longer than 10,000 hours,” *SPIE Conference on Physics and Simulation of Optoelectronic Devices VI*, vol. 3283, no. January, pp. 2–13, 1998.

[127] M. Kneissl, D. P. Bour, L. Romano, C. G. Van de Walle, J. E. Northrup, W. S. Wong, D. W. Treat, M. Teepe, T. Schmidt, and N. M. Johnson, "Performance and degradation of continuous-wave InGaN multiple-quantum-well laser diodes on epitaxially laterally overgrown GaN substrates," *Applied Physics Letters*, vol. 77, no. 13, p. 1931, 2000.

[128] M. Meneghini, M. Dal Lago, N. Trivellin, G. Mura, M. Vanzi, G. Meneghesso, and E. Zanoni, "Chip and package-related degradation of high power white LEDs," *Microelectronics Reliability*, vol. 52, no. 5, pp. 804–812, 2012.

[129] L. Trevisanello, M. Meneghini, G. Mura, M. Vanzi, M. Pavesi, G. Meneghesso, and E. Zanoni, "Accelerated Life Test of High Brightness Light Emitting Diodes," *IEEE Transactions on Device and Materials Reliability*, vol. 8, no. 2, pp. 304–311, 2008.

[130] D. Monti, M. Meneghini, C. De Santi, G. Meneghesso, E. Zanoni, J. Glaab, J. Rass, S. Einfeldt, F. Mehnke, J. Enslin, T. Wernicke, and M. Kneissl, "Defect-Related Degradation of AlGaN-Based UV-B LEDs," *IEEE Transactions on Electron Devices*, vol. 64, no. 1, pp. 200–205, 2017.

[131] Z. Gong, M. Gaevski, V. Adivarahan, W. Sun, M. Shatalov, and M. Asif Khan, "Optical power degradation mechanisms in AlGaN-based 280 nm deep ultraviolet light-emitting diodes on sapphire," *Applied Physics Letters*, vol. 88, no. 12, pp. 2004–2007, 2006.

[132] C. G. Moe, M. L. Reed, G. A. Garrett, A. V. Sampath, T. Alexander, H. Shen, M. Wraback, Y. Bilenko, M. Shatalov, J. Yang, W. Sun, J. Deng, and R. Gaska, "Current-induced Degradation of High Performance Deep Ultraviolet Light Emitting Diodes," *Applied Physics Letters*, vol. 96, no. 21, p. 213512, 2010.

[133] F. Mehnke, C. Kuhn, J. Stellmach, T. Kolbe, N. Lobo-Ploch, J. Rass, M.-A. Rothe, C. Reich, N. Ledentsov, M. Pristovsek, T. Wernicke, and M. Kneissl, "Effect of heterostructure design on carrier injection and emission characteristics of 295 nm light emitting diodes," *Journal of Applied Physics*, vol. 117, no. 19, p. 195704, 2015.

[134] M. Meneghini, N. Trivellin, L. Trevisanello, A. Lunev, J. Yang, Y. Bilenko, W. Sun, M. Shatalov, R. Gaska, E. Zanoni, and G. Meneghesso, "Combined optical and electrical analysis of AlGaN-based deep-UV LEDs reliability," *IEEE*

CFP08RPS-CDR 46th Annual International Reliability, Physics Symposium, pp. 441–445, 2008.

[135] T. Kolbe, J. Stellmach, F. Mehnke, M. A. Rothe, V. Kueller, A. Knauer, S. Einfeldt, T. Wernicke, M. Weyers, and M. Kneissl, "Efficient carrier-injection and electron-confinement in UV-B light-emitting diodes," *Physica Status Solidi (A) Applications and Materials Science*, vol. 213, no. 1, pp. 210–214, 2016.

[136] J. C. Zhang, Y. H. Zhu, T. Egawa, S. Sumiya, M. Miyoshi, and M. Tanaka, "Suppression of the subband parasitic peak by 1 nm i-AlN interlayer in AlGaN deep ultraviolet light-emitting diodes," *Applied Physics Letters*, vol. 93, no. 13, 2008.

[137] M. Auf Der Maur, B. Galler, I. Pietzonka, M. Strassburg, H. Lugauer, and A. Di Carlo, "Trap-assisted tunneling in InGaN/GaN single-quantum-well light-emitting diodes," *Applied Physics Letters*, vol. 105, no. 13, pp. 133504–1 – 133504–4, 2014.

[138] A. Y. Polyakov, N. B. Smirnov, A. V. Govorkov, E. A. Kozhukhova, A. M. Dabiran, P. P. Chow, A. M. Wowchak, I.-H. Lee, J.-W. Ju, and S. J. Pearton, "Comparison of electrical properties and deep traps in p-Al[x]Ga[1x]N grown by molecular beam epitaxy and metal organic chemical vapor deposition," *Journal of Applied Physics*, vol. 106, no. 7, p. 073706, 2009.

[139] D. Seghier and H. P. Gislason, "Electrical characterization of Mg-related energy levels and the compensation mechanism in GaN:Mg," *Journal of Applied Physics*, vol. 88, no. 2000, pp. 6483–6487, 2000.

[140] C. Johnson, J. Y. Lin, H. X. Jiang, M. A. Khan, and C. J. Sun, "Metastability and persistent photoconductivity in Mg-doped p-type GaN," *Applied Physics Letters*, vol. 68, no. 13, pp. 1808–1810, 1996.

[141] S. N. Lee, H. S. Paek, J. K. Son, H. Kim, K. K. Kim, K. H. Ha, O. H. Nam, and Y. Park, "Effects of Mg dopant on the degradation of InGaN multiple quantum wells in AlInGaN-based light emitting devices," *Journal of Electroceramics*, vol. 23, no. 2-4, pp. 406–409, 2009.

[142] Z.-Q. Fang, D. C. Look, W. Kim, and Z. Fan, "Deep centers in n -GaN grown by reactive molecular beam epitaxy," *Applied Physics Letters*, vol. 72, no. 18, pp. 2277–2279, 1998.

[143] Y. S. Park, M. Lee, K. Jeon, I. T. Yoon, Y. Shon, H. Im, C. J. Park, H. Y. Cho, and M.-S. Han, "Deep level transient spectroscopy in plasma-assisted molecular beam epitaxy grown Al0.2Ga0.8N/GaN interface and the rapid thermal annealing effect," *Applied Physics Letters*, vol. 97, no. 11, p. 112110, 2010.

[144] C. De Santi, M. Meneghini, D. Monti, J. Glaab, M. Guttmann, J. Rass, S. Einfeldt, F. Mehnke, J. Enslin, T. Wernicke, M. Kneissl, G. Meneghesso, and E. Zanoni, "Recombination mechanisms and thermal droop in AlGaN-based UV-B LEDs," *Photonics Research*, vol. 5, no. 2, pp. 44–51, 2017.

[145] K. H. Lee, H. J. Park, S. H. Kim, M. Asadirad, Y.-T. Moon, J. S. Kwak, and J.-H. Ryou, "Light-extraction efficiency control in AlGaN-based deep-ultraviolet flip-chip light-emitting diodes: a comparison to InGaN-based visible flip-chip light-emitting diodes," *Optics Express*, vol. 23, no. 16, p. 20340, 2015.

[146] C. De Santi, M. Meneghini, M. La Grassa, B. Galler, M. Goano, S. Dominici, M. Mandurrino, F. Bertazzi, G. Meneghesso, and E. Zanoni, "Role of defects in the thermal droop of InGaN-based Light Emitting Diodes," *Journal of Applied Physics*, vol. 119, no. 094501, pp. 094501–1 – 094501–10, 2016.

[147] V. Adivarahan, S. Wu, A. Chitnis, R. Pachipulusu, V. Mandavilli, M. Shatalov, J. P. Zhang, M. A. Khan, G. Tamulaitis, A. A. Sereika, I. Yilmaz, M. S. Shur, and R. Gaska, "AlGaN single-quantum-well light-emitting diodes with emission at 285 nm," *Applied Physics Letters*, vol. 81, no. 19, pp. 3666–3668, 2002.

[148] M. A. Khan, M. Shatalov, H. P. Maruska, H. M. Wang, and E. Kuokstis, "III-nitride UV devices," *Japanese Journal of Applied Physics, Part 1: Regular Papers and Short Notes and Review Papers*, vol. 44, no. 10, pp. 7191–7206, 2005.

[149] A. Pinos, S. Marcinkevičius, J. Yang, Y. Bilenko, M. Shatalov, R. Gaska, and M. S. Shur, "Aging of AlGaN quantum well light emitting diode studied by scanning near-field optical spectroscopy," *Applied Physics Letters*, vol. 95, no. 18, pp. 1–4, 2009.

[150] A. Pinos, S. Marcinkevičius, J. Yang, R. Gaska, M. Shatalov, and M. S. Shur, "Optical studies of degradation of AlGaN quantum well based deep ultraviolet light emitting diodes.pdf," *Journal of Applied Physics*, vol. 108, no. 093113, pp. 093113–1 – 093113–6, 2010.

[151] A. Pinos, S. Marcinkevičius, and M. S. Shur, "High current-induced degradation of AlGaN ultraviolet light emitting diodes," *Journal of Applied Physics*, vol. 109, no. 10, pp. 1–10, 2011.

[152] N. Grandjean, J. Massies, I. Grzegory, and S. Porowski, "GaN/AlGaN quantum wells for UV emission: Heteroepitaxy versus homoepitaxy," *Semiconductor Science and Technology*, vol. 16, no. 5, pp. 358–361, 2001.

[153] S. Chichibu, T. Sota, K. Wada, and S. Nakamura, "Exciton localization in InGaN quantum well devices," *Journal of Vacuum Science & Technology B: Microelectronics and Nanometer Structures Processing, Measurement, and Phenomena*, vol. 16, p. 2204, oct 1998.

[154] S. Fan, Z. Qin, C. He, M. Hou, X. Wang, B. Shen, W. Li, W. Wang, D. Mao, P. Jin, J. Yan, and P. Dong, "Optical investigation of strong exciton localization in high Al composition AlxGa1-xN alloys," *Optics Express*, vol. 21, p. 24497, oct 2013.

[155] J. Brault, D. Rosales, B. Damilano, M. Leroux, A. Courville, M. Korytov, S. Chenot, P. Vennéguès, B. Vinter, P. De Mierry, A. Kahouli, J. Massies, T. Bretagnon, and B. Gil, "Polar and semipolar GaN/Al0.5Ga0.5N nanostructures for UV light emitters," *Semiconductor Science and Technology*, vol. 29, no. 8, 2014.

[156] N. Can, S. Okur, M. Monavarian, F. Zhang, V. Avrutin, H. Morkoç, A. Teke, and Ü. Özgür, "Active region dimensionality and quantum efficiencies of InGaN LEDs from temperature dependent photoluminescence transients," vol. 9363, p. 93632U, International Society for Optics and Photonics, mar 2015.

[157] T. Li, A. M. Fischer, Q. Y. Wei, F. A. Ponce, T. Detchprohm, and C. Wetzel, "Carrier localization and nonradiative recombination in yellow emitting InGaN quantum wells," *Applied Physics Letters*, vol. 96, no. 3, 2010.

[158] G. Steude, B. K. Meyer, A. Göldner, A. Hoffmann, F. Bertram, J. Christen, H. Amano, and I. Akasaki, "Optical investigations of AlGaN on GaN epitaxial films," *Applied Physics Letters*, vol. 74, no. 17, pp. 2456–2458, 1999.

[159] N. Nepal, J. Li, M. L. Nakarmi, J. Y. Lin, and H. X. Jiang, "Exciton localization in AlGaN alloys," *Applied Physics Letters*, vol. 88, no. 6, pp. 2004–2007, 2006.

[160] H. Murotani, Y. Yamada, T. Taguchi, A. Ishibashi, Y. Kawaguchi, and T. Yokogawa, “Temperature dependence of localized exciton transitions in AlGaN ternary alloy epitaxial layers,” *Journal of Applied Physics*, vol. 104, no. 5, 2008.

[161] Y. Iwata, T. Oto, D. Gachet, R. G. Banal, M. Funato, and Y. Kawakami, “Coexistence of a few and sub micron inhomogeneities in Al-rich AlGaN/AlN quantum wells,” *Journal of Applied Physics*, vol. 117, no. 11, 2015.

[162] H. Jiang and J. Lin, “AlGaN and InAlGaN alloys epitaxial growth, optical and electrical properties, and applications,” *Opto-Electronics Review*, vol. 10, no. 4, pp. 271–286, 2002.

[163] G. Martínez-Criado, C. R. Miskys, A. Cros, O. Ambacher, A. Cantarero, and M. Stutzmann, “Photoluminescence study of excitons in homoepitaxial GaN,” *Journal of Applied Physics*, vol. 90, no. 11, pp. 5627–5631, 2001.

[164] S. O. Usov, A. F. Tsatsul’nikov, V. V. Lundin, A. V. Sakharov, E. E. Zavarin, M. A. Sinitsyn, and N. N. Ledentsov, “Energy characteristics of excitons in structures based on InGaN alloys,” *Semiconductors*, vol. 42, no. 6, pp. 720–725, 2008.

[165] P. P. Paskov, T. Paskova, P. O. Holtz, and B. Monemar, “Polarized photoluminescence study of free and bound excitons in free-standing GaN,” *Physical Review B - Condensed Matter and Materials Physics*, vol. 70, no. 3, pp. 83–86, 2004.

[166] X. B. Chen, J. Huso, J. L. Morrison, and L. Bergman, “Dynamics of GaN band edge photoluminescence at near-room-temperature regime,” *Journal of Applied Physics*, vol. 99, no. 4, pp. 1–4, 2006.

[167] D. Banerjee, S. Sankaranarayanan, D. Khachariya, M. B. Nadar, S. Ganguly, and D. Saha, “Superluminescent light emitting diodes on naturally survived InGaN/GaN lateral nanowires,” *Applied Physics Letters*, vol. 109, no. 3, 2016.

[168] I. V. Osinnykh, T. V. Malin, V. F. Plyusnin, A. S. Suranov, A. M. Gilinsky, and K. S. Zhuravlev, “Characterization of the green band in photoluminescence spectra of heavily doped Al x Ga 1 x N:Si with the Al content x $>$ 0.5,” *Japanese Journal of Applied Physics*, vol. 55, no. 5S, p. 05FG09, 2016.

[169] L. Zhang, K. Cheng, S. Degroote, M. Leys, M. Germain, and G. Borghs, “Strain effects in GaN epilayers grown on different substrates by metal organic vapor phase epitaxy,” *Journal of Applied Physics*, vol. 108, no. 7, 2010.

[170] X. A. Cao, S. F. LeBoeuf, L. B. Rowland, C. H. Yan, and H. Liu, "Temperature-dependent emission intensity and energy shift in InGaN/GaN multiple-quantum-well light-emitting diodes," *Applied Physics Letters*, vol. 82, no. 21, pp. 3614–3616, 2003.

[171] D. O. Demchenko, I. C. Diallo, and M. A. Reshchikov, "Yellow luminescence of gallium nitride generated by carbon defect complexes," *Physical Review Letters*, vol. 110, no. 8, pp. 1–5, 2013.

[172] J. S. Colton, P. Y. Yu, K. L. Teo, P. Perlin, E. R. Weber, I. Grzegory, and K. Uchida, "Selective excitation of the yellow luminescence of GaN," *Physica B: Condensed Matter*, vol. 273-274, pp. 75–79, 1999.

[173] D. Bimberg, M. Sondergeld, and E. Grobe, "Thermal dissociation of excitons bounds to neutral acceptors in high-purity GaAs," *Physical Review B*, vol. 4, no. 10, pp. 3451–3455, 1971.

[174] J. Piprek, "Unified model for the GaN LED efficiency droop," vol. 7939, p. 793916, International Society for Optics and Photonics, feb 2011.

[175] S. Karpov, "ABC-Model for Interpretation of Intemal Quantum Efficiency and Its Droop in III-Nitride LEDs," *Nusod 2014*, pp. 17 – 18, 2014.

[176] D. S. Meyaard, Q. Shan, Q. Dai, J. Cho, E. F. Schubert, M. H. Kim, and C. Sone, "On the temperature dependence of electron leakage from the active region of GaInN/GaN light-emitting diodes," *Applied Physics Letters*, vol. 99, no. 4, pp. 2009–2012, 2011.

[177] W. Liu, R. Butté, A. Dussaigne, N. Grandjean, B. Deveaud, and G. Jacopin, "Carrier-density-dependent recombination dynamics of excitons and electron-hole plasma in m -plane InGaN/GaN quantum wells," *Physical Review B*, vol. 94, no. 19, pp. 1–10, 2016.

[178] Ž. Podlipskas, R. Aleksiejunas, A. Kadys, J. Mickevičius, J. Jurkevičius, G. Tamulaitis, M. Shur, M. Shatalov, J. Yang, and R. Gaska, "Dependence of radiative and nonradiative recombination on carrier density and Al content in thick AlGaN epilayers," *Journal of Physics D: Applied Physics*, vol. 49, no. 14, 2016.

[179] E. Kioupakis, Q. Yan, D. Steiauf, and C. G. Van De Walle, "Temperature and carrier-density dependence of Auger and radiative recombination in nitride optoelectronic devices," *New Journal of Physics*, vol. 15, 2013.

[180] A. David and M. J. Grundmann, "Droop in InGaN light-emitting diodes: A differential carrier lifetime analysis," *Applied Physics Letters*, vol. 96, no. 10, pp. 1–4, 2010.

[181] J. Hader, J. V. Moloney, and S. W. Koch, "Density-activated defect recombination as a possible explanation for the efficiency droop in GaN-based diodes Density-activated defect recombination as a possible explanation for the efficiency droop in GaN-based diodes," *Applied Physics Letters*, vol. 96, no. 22, p. 221106, 2010.

[182] D. Schiavon, M. Binder, M. Peter, B. Galler, P. Drechsel, and F. Scholz, "Wavelength-dependent determination of the recombination rate coefficients in single-quantum-well GaInN/GaN light emitting diodes," *Physica Status Solidi (B) Basic Research*, vol. 250, no. 2, pp. 283–290, 2013.

[183] A. Pinos, S. Marcinkevičius, K. Liu, M. S. Shur, J. Yang, M. Shatalov, and R. Gaska, "Carrier lifetimes in AlGaN quantum wells: Electric field and excitonic effects," *Journal of Physics D: Applied Physics*, vol. 41, no. 15, 2008.

[184] A. Hangleiter, Z. Jin, M. Gerhard, D. Kalincev, T. Langer, H. Bremers, U. Rossow, M. Koch, M. Bonn, and D. Turchinovich, "Efficient formation of excitons in a dense electron-hole plasma at room temperature," *Physical Review B - Condensed Matter and Materials Physics*, vol. 92, no. 24, pp. 1–5, 2015.

[185] S. A. Goodman, F. D. Auret, F. K. Koschnick, J. M. Spaeth, B. Beaumont, and P. Gibart, "Radiation induced defects in MOVPE grown n-GaN," *Materials Science and Engineering B: Solid-State Materials for Advanced Technology*, vol. 71, pp. 100–103, 2000.

[186] F. D. Auret, W. E. Meyer, L. Wu, M. Hayes, M. J. Legodi, B. Beaumont, and P. Gibart, "Electrical characterisation of hole traps in n-type GaN," *Physica Status Solidi C: Conferences*, vol. 1, no. 9, pp. 2271–2276, 2004.

[187] C. B. Soh, D. Z. Chi, A. Ramam, H. F. Lim, and S. J. Chua, "Study of electrically active defects in n-GaN layer," *Materials Science in Semiconductor Processing*, vol. 4, no. 6, pp. 595–600, 2001.

[188] P. Kamyczek, E. Placzek-Popko, V. Kolkovsky, S. Grzanka, and R. Czernecki, "A deep acceptor defect responsible for the yellow luminescence in GaN and AlGaN," *Journal of Applied Physics*, vol. 111, no. 11, 2012.

[189] Z. Zhang, C. A. Hurni, A. R. Arehart, J. Yang, R. C. Myers, J. S. Speck, and S. A. Ringel, "Deep traps in nonpolar m-plane GaN grown by ammonia-based molecular beam epitaxy," *Applied Physics Letters*, vol. 100, no. 5, pp. 1–5, 2012.

[190] M. Shatalov, A. Chitnis, V. Mandavilli, R. Pachipulusu, J. P. Zhang, V. Adivarahan, S. Wu, G. Simin, M. A. Khan, G. Tamulaitis, A. Sereika, I. Yilmaz, M. S. Shur, and R. Gaska, "Time-resolved electroluminescence of AlGaN-based light-emitting diodes with emission at 285 nm," *Applied Physics Letters*, vol. 82, no. 2, pp. 167–169, 2003.

[191] J. Zhang, S. Wu, S. Rai, V. Mandavilli, V. Adivarahan, A. Chitnis, M. Shatalov, and M. Asif Khan, "AlGaN multiple-quantum-well-based, deep ultraviolet light-emitting diodes with significantly reduced long-wave emission," *Applied Physics Letters*, vol. 83, no. 17, pp. 3456–3458, 2003.

[192] D. Monti, M. Meneghini, C. De Santi, S. Da Ruos, G. Meneghesso, J. Zanoni, Glaab, J. Rass, S. Einfeldt, F. Mehnke, T. Wernicke, and M. Kneissl, "Defect-generation and diffusion in deep-UV (In)AlGaN-based LEDs submitted to constant current stress," *Proceeding of SPIE*, vol. 10554, 2018.

[193] H. Wang, J. Zhang, C. Chen, Q. Fareed, J. Yang, and M. A. Khan, "AlN/AlGaN superlattices as dislocation filter for low-threading-dislocation thick AlGaN layers on sapphire," *Applied Physics Letters*, vol. 81, pp. 604–606, jul 2002.

[194] H. Hirayama, "Quaternary InAlGaN-based high-efficiency ultraviolet light-emitting diodes," *Journal of Applied Physics*, vol. 97, no. 9, 2005.

[195] M. W. Moseley, A. A. Allerman, M. H. Crawford, J. J. Wierer, M. L. Smith, and A. M. Armstrong, "Detection and modeling of leakage current in AlGaN-based deep ultraviolet light-emitting diodes," *Journal of Applied Physics*, vol. 117, no. 9, 2015.

[196] K. Orita, S. Takigawa, M. Yuri, T. Tanaka, M. Meneghini, N. Trivellin, L. R. Trevisanello, E. Zanoni, and G. Meneghesso, "Analysis of diffusion involved in degradation of InGaN-based laser diodes," in *2009 IEEE International Reliability Physics Symposium*, pp. 736–740, IEEE, 2009.

[197] A. Hierro, S. A. Ringel, M. Hansen, J. S. Speck, U. K. Mishra, and S. P. DenBaars, “Hydrogen passivation of deep levels in n–GaN,” *Applied Physics Letters*, vol. 77, no. 10, p. 1499, 2000.

[198] J. Neugebauer and C. G. Van De Walle, “Gallium vacancies and the yellow luminescence in GaN,” *Applied Physics Letters*, vol. 69, p. 503, jun 1998.

[199] A. Armstrong, A. R. Arehart, B. Moran, S. P. DenBaars, U. K. Mishra, J. S. Speck, and S. A. Ringel, “Impact of carbon on trap states in n-type GaN grown by metalorganic chemical vapor deposition,” *Applied Physics Letters*, vol. 84, pp. 374–376, jan 2004.

[200] K. Orita, M. Meneghini, H. Ohno, N. Trivellin, N. Ikedo, S. Takigawa, M. Yuri, T. Tanaka, E. Zanoni, and G. Meneghesso, “Analysis of diffusion-related gradual degradation of InGaN-based laser diodes,” *IEEE Journal of Quantum Electronics*, vol. 48, no. 9, pp. 1169–1176, 2012.

[201] S. Nakamura, T. Mukai, and M. Senoh, “Candela-class high-brightness InGaN/AlGaN double-heterostructure blue-light-emitting diodes,” *Applied Physics Letters*, vol. 64, pp. 1687–1689, mar 1994.

[202] S. Nakamura, M. Senoh, S. Nagahama, N. Iwasa, T. Yamada, T. Matsushita, H. Kiyoku, and Y. Sugimoto, “InGaN-Based Multi-Quantum-Well-Structure Laser Diodes,” *Japanese Journal of Applied Physics*, vol. 35, no. 1B, pp. L74–L76, 1996.

[203] S. Brüninghoff, C. Eichler, S. Tautz, A. Lell, M. Sabathil, S. Lutgen, and U. Strauß, “8 W single-emitter InGaN laser in pulsed operation,” *physica status solidi (a)*, vol. 206, pp. 1149–1152, jun 2009.

[204] M. Adachi, Y. Yoshizumi, Y. Enya, T. Kyono, T. Sumitomo, S. Tokuyama, S. Takagi, K. Sumiyoshi, N. Saga, T. Ikegami, M. Ueno, K. Katayama, and T. Nakamura, “Low Threshold Current Density InGaN Based 520–530 nm Green Laser Diodes on Semi-Polar (20\bar21) Free-Standing GaN Substrates,” *Applied Physics Express*, vol. 3, p. 121001, nov 2010.

[205] H. Morkoç, *Nitride Semiconductors and Devices.* Springer Berlin Heidelberg, 1999.

[206] S. Nakamura, "InGaN/GaN/AlGaN-based laser diodes grown on epitaxially laterally overgrown GaN," *Journal of Materials Research*, vol. 14, pp. 2716–2731, jul 1999.

[207] C. Skierbiszewski, P. Wiśniewski, M. Siekacz, P. Perlin, A. Feduniewicz-Zmuda, G. Nowak, I. Grzegory, M. Leszczyński, and S. Porowski, "60mW continuous-wave operation of InGaN laser diodes made by plasma-assisted molecular-beam epitaxy," *Applied Physics Letters*, vol. 88, p. 221108, may 2006.

[208] P. Perlin and Ł. Marona, "InGaN Laser Diode Degradation," in *Materials and Reliability Handbook for Semiconductor Optical and Electron Devices*, pp. 247–261, New York, NY: Springer New York, 2013.

[209] M. Takeya, T. Mizuno, T. Sasaki, S. Ikeda, T. Fujimoto, Y. Ohfuji, K. Oikawa, Y. Yabuki, S. Uchida, and M. Ikeda, "Degradation in AlGaInN lasers," *physica status solidi (c)*, vol. 0, pp. 2292–2295, dec 2003.

[210] L. Marona, P. Perlin, R. Czernecki, M. Leszczyński, M. Boćkowski, R. Jakiela, T. Suski, and S. P. Najda, "Secondary ions mass spectroscopy measurements of dopant impurities in highly stressed InGaN laser diodes," *Applied Physics Letters*, vol. 98, p. 241115, jun 2011.

[211] N. Trivellin, M. Meneghini, G. Meneghesso, E. Zanoni, K. Orita, M. Yuri, T. Tanaka, and D. Ueda, "Reliability analysis of InGaN Blu-Ray laser diode," *Microelectronics Reliability*, vol. 49, no. 9-11, pp. 1236–1239, 2009.

[212] D. Monti, M. Meneghini, C. De Santi, G. Meneghesso, E. Zanoni, A. Bojarska, and P. Perlin, "Long-term degradation of InGaN-based laser diodes: Role of defects," *Microelectronics Reliability*, vol. 76-77, pp. 584–587, 2017.

[213] L. A. Coldren, S. W. Corzine, and M. Mashanovitch, *Diode lasers and photonic integrated circuits*. Wiley, 2012.

[214] S. Tomiya, O. Goto, and M. Ikeda, "Structural Defects and Degradation Phenomena in High-Power Pure-Blue InGaN-Based Laser Diodes," *Proceedings of the IEEE*, vol. 98, pp. 1208–1213, jul 2010.

[215] F. Rossi, M. Pavesi, M. Meneghini, G. Salviati, M. Manfredi, G. Meneghesso, A. Castaldini, A. Cavallini, L. Rigutti, U. Strass, U. Zehnder, and E. Zanoni,

"Influence of short-term low current dc aging on the electrical and optical properties of InGaN blue light-emitting diodes," *Journal of Applied Physics*, vol. 99, no. 5, pp. 10–17, 2006.

[216] Z.-Q. Fang, L. Polenta, J. Hemsky, and D. Look, "Deep centers in as-grown and electron-irradiated n-GaN," in *2000 International Semiconducting and Insulating Materials Conference. SIMC-XI (Cat. No.00CH37046)*, pp. 35–42, IEEE, 2000.

[217] G. Verzellesi, A. Mazzanti, C. Canali, G. Meneghesso, A. Chini, and E. Zanoni, "Study on the origin of dc-to-RF dispersion effects in GaAs- and GaN-based beterostructure FETs," in *Proceedings GaAs Reliability Workshop, 2003.*, pp. 155–156, IEEE, 2003.

[218] J. Osaka, Y. Ohno, S. Kishimoto, K. Maezawa, and T. Mizutani, "Deep levels in n-type AlGaN grown by hydride vapor-phase epitaxy on sapphire characterized by deep-level transient spectroscopy," *Applied Physics Letters*, vol. 87, p. 222112, nov 2005.

[219] D. Monti, M. Meneghini, C. De Santi, A. Bojarska, P. Perlin, G. Meneghesso, and E. Zanoni, "Impact of dislocations on DLTS spectra and degradation of InGaN-based laser diodes," *Microelectronics Reliability*, vol. 88-90, pp. 864–867, 2018.

[220] A. R. Arehart, A. Corrion, C. Poblenz, J. S. Speck, U. K. Mishra, S. P. DenBaars, and S. A. Ringel, "Comparison of deep level incorporation in ammonia and rf-plasma assisted molecular beam epitaxy n-GaN films," *Physica Status Solidi (C) Current Topics in Solid State Physics*, vol. 5, no. 6, pp. 1750–1752, 2008.

[221] A. Hierro, A. R. Arehart, B. Heying, M. Hansen, J. S. Speck, U. K. Mishra, S. P. DenBaars, and S. A. Ringel, "Capture kinetics of electron traps in MBE-grown n-GaN," *Physica Status Solidi (B) Basic Research*, vol. 228, no. 1, pp. 309–313, 2001.

[222] A. R. Arehart, *Investigation of electrically active defects in GaN, AlGaN, and AlGaN/GaN high electron mobility transistors.* PhD thesis, The Ohio State University, 2009.